

DTIC FILE COPY

AD-A226 021

RADC-TR-90-42, Vol I (of two)  
In-House Report  
March 1990



2

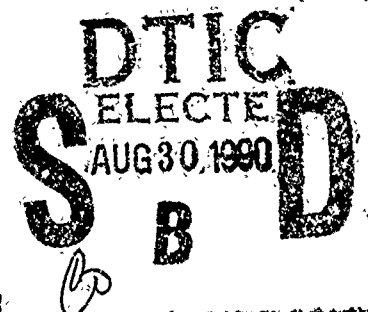
# PROCEEDINGS OF THE 1989 ANTENNA APPLICATIONS SYMPOSIUM

Paul Mayes, et al

Sponsored by  
Directorate of Electromagnetics  
Rome Air Development Center  
Hanscom Air Force Base  
Air Force Systems Command

and

Electromagnetics Laboratory  
Department of Electrical and Computer Engineering  
College of Engineering  
University of Illinois  
Urbana-Champaign, Illinois 61801



APPROVED FOR PUBLIC RELEASE; DISTRIBUTION UNLIMITED.

Rome Air Development Center  
Air Force Systems Command  
Griffiss Air Force Base, NY 13441-5700

20 06 20 1994

This report has been reviewed by the RADC Public Affairs Division (PA) and is releasable to the National Technical Information Service (NTIS). At NTIS it will be releasable to the general public, including foreign nations.

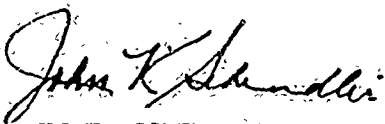
RADC-TR-90-42, Volume I (of two) has been reviewed and is approved for publication.

APPROVED:



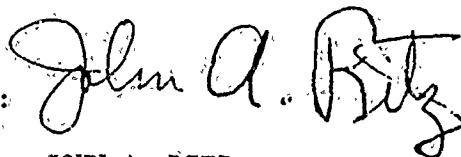
ROBERT J. MAILLOUX  
Chief, Antennas and Components Division  
Directorate of Electromagnetics

APPROVED:



JOHN K. SCHINDLER  
Director of Electromagnetics

FOR THE COMMANDER:



JOHN A. RITZ  
Directorate of Plans and Programs

If your address has changed or if you wish to be removed from the RADC mailing list, or if the addressee is no longer employed by your organization, please notify RADC (EEAS) Hanscom AFB MA 01731-5000. This will assist us in maintaining a current mailing list.

Do not return copies of this report unless contractual obligations or notices on a specific document require that it be returned.

REPORT DOCUMENTATION PAGE			Form Approved OMB No 0704-0188	
<small>Public reporting burden for this collection of information is estimated to average 1 hour per response, including the time for reviewing instructions, searching existing data sources, gathering and maintaining the data needed, and completing and reviewing the collection of information. Send comments regarding this burden estimate or any other aspect of this collection of information, including suggestions for reducing this burden, to Washington Headquarters Services, Directorate for Information Operations and Reports, 1215 Jefferson Davis Highway, Suite 1204 Arlington, VA 22202-4302, and to the Office of Management and Budget, Paperwork Reduction Project (0704-0188), Washington, DC 20503.</small>				
1. AGENCY USE ONLY (Leave blank)	2. REPORT DATE March 1990	3. REPORT TYPE AND DATES COVERED In-house		
4. TITLE AND SUBTITLE Proceedings of the 1989 Antenna Applications Symposium		5. FUNDING NUMBERS PE 62702F PR 4600 TA 14 WU PD		
6. AUTHOR(S) Paul Mayes et al				
7. PERFORMING ORGANIZATION NAME(S) AND ADDRESS(ES) Rome Air Development Center Hanscom AFB, MA 01731-5000  Responsible Individual: John Antonucci (EEAS)		8. PERFORMING ORGANIZATION REPORT NUMBER RADC-TR-90-42 Volume I		
9. SPONSORING/MONITORING AGENCY NAME(S) AND ADDRESS(ES)		10. SPONSORING/MONITORING AGENCY REPORT NUMBER		
11. SUPPLEMENTARY NOTES Volume I consists of pages 1 through 342; Volume II consists of pages 343 through 611				
12a. DISTRIBUTION/AVAILABILITY STATEMENT  Approved for public release; distribution unlimited			12b. DISTRIBUTION CODE	
13. ABSTRACT (Maximum 200 words)  The Proceedings of the 1989 Antenna Applications Symposium is a collection of state-of-the-art papers relating to phased array antennas, multibeam antennas, satellite antennas, microstrip antennas, reflector antennas, HF, VHF, UHF and various other antennas.				
14. SUBJECT TERMS Antennas, Satellite antennas, Broadband antennas,		Microstrip, Reflector, HF, VHF,	UHF, Multibeam antennas, Array antennas,	15. NUMBER OF PAGES 348
17. SECURITY CLASSIFICATION OF REPORT Unclassified		18. SECURITY CLASSIFICATION OF THIS PAGE Unclassified	19. SECURITY CLASSIFICATION OF ABSTRACT Unclassified	16. PRICE CODE SAR

Accession For	
NTIS GRA&I	<input checked="" type="checkbox"/>
DTIC TAB	<input type="checkbox"/>
Unannounced	<input type="checkbox"/>
Justification	
By	
Distribution/	
Availability Codes	
Dist.	Avail and/or Special
A-1	



## CONTENTS

- \* Keynote: "Future deirection in Solid-State Millimeter-Wave Arrays," J. Kinzel, General Electric. Electronics Laboratory, Syracuse, NY

WEDNESDAY, 20 SEPTEMBER 1989

### ANTENNA ELEMENTS AND CPSS

- |      |   |    |
|------|---|----|
| 1.   | "Microstrip Antennas in Composite Layers," D. R. Jackson, N. G. Alexopoulos, and A. A. Oliner                                     | 1  |
| 2.   | "A Compact Multi-Polarized Broadband Antenna," Dean A. Hofer, Oren B. Kesler, and Lowell L. Loyet                                 | 23 |
| 3.   | "A Simple Circularly Polarized Primary Antenna for Direct Broadcast From Satellite Receivers," Takashi Nakamura and Kamel Maamria | 47 |
| 4.   | "Closed Loop Performance of an Adaptive Polarization Combiner," Kyle A. Dallabetta, Bernard J. Lamberty, and Kenneth G. Voyce     | 63 |
| * 5. | "A Dual Polarized Horn With a Scanning Beam," Z. Frank  |    |
| 6.   | "A New Circular Polarization Selective Surface (CPSS), Gilbert A. Morin   | 79 |

### REFLECTOR AND LENS ANTENNAS

- |      |  |     |
|------|--|-----|
| * 7. | "Design and Analysis of a dual Reflector Multibeam Torus Antenna," S. Carrillo                                 |     |
| 8.   | "The ARSR-4 Antenna, a Unique Combination of Array and Antenna Technology," Richard S. White, and Daniel Davis | 105 |

\* NOT INCLUDED IN THIS VOLUME



## Contents

9.	"A Segmented Mirror Antenna for Radiometers," S. W. Lee, B. Houshmand, M. Zimmerman, and R. Acosta	121
10.	"Reflector Performance Degradation Due to an Arcjet Plume," H. Ling, G. A. Hallock, H. Kim, B. W. Birkner, and A. Zaman	163
11.	"Parametric Estimation of the J-Band Radiation Properties of Cylindrical Feeds With or Without External Coaxial Cups," Constantinos J. Papathomas	185
12.	"Impedance-Matched coaxial-Probe Feed for a Rotman Lens- Fed Array with 4.5:1 Bandwidth and Sector Pattern Coverage," Joseph A. Troychak, Peter S. Simon	213
13.	"Ku-Band Antenna for VSAT Applications," Nicholas Moldovan	223

THURSDAY, 21 SEPTEMBER 1989

## ARRAYS

14.	"Electromagnetic Coupler," Peter R. Franchi and Nicholas P. Kernweis	239
15.	"Design of a Planar Array of Parasitic Microstrip Patch Antennas," R. W. Shaw, J. K. Kovitz, I. Paz, L. Johnson and G. D. Arndt	251
16.	"Advances in Monolithic Horn-Antenna Imaging Arrays, Philip Stimson, Yong Guo, Karen Lee and David Rutledge	271
17.	"Wideband dual Polarized Apertures Utilizing Closely Spaced Printed Circuit Flared Slot Antenna Elements for Active Transmit and Receive Phased Array Demonstration," Mark J. Povinelli	283
18.	"Design, Performance Characterization and Hybrid Finite Element Boundary Element Analysis of a Linearly Polarized Printed Circuit Tapered Notch Array," Mark J. Povinelli and John D'Angelo	311
19.	"EHF Active Array," Joe Kobus	343
20.	"Unique Joint Stars Phased-Array Antenna," H. Shnitkin	360

## Contents

### ARRAYS AND NUMERICAL TECHNIQUES

- 21. "An Octive Band High Gain Receive Cylindrical Array Antenna With Full Azimuth Coverage," J. C. Herper, A. M. bucceri and J. J. Stangel 381
- 22. "Conformal Active Phased Array Demonstration," Jerome D. Hanfling 411
- 23. "High Precision Frequency Locking technique for Active Microstrip Antenna Arrays," Gabriel Colef, George Eichmann, Raymand L. Camisa and Aly E. Fathy 441
- \* 24. "EHF Polyrød Array Antenna," P. W. Brock and R. W. Major
- 25. "PHEDRE: A Computer Package for the Study of Electromagnetic Radiation," Christian Renard, Fabrice Clerk and Louis Beaulieu 463
- \* 26. "A Novel Technique for the Synthesis of Separable Aperture Distributions Over Arbitrarily-Shaped Array Surfaces," W. W. Milroy
- 27. "Moment Method Analysis of a Stripline-Fed Finite Slot Using Subdomain Basis Functions," Peter S. Simon, Kim McInturff, Deron L. Johnson, and Joseph A. Troychak 477
- 28. (No Paper)

FRIDAY, 22 SEPTEMBER 1989

### EXPERIMENT AND THEORY

- 29. "A Technique to Measure Large Antenna Arrays That Contain Random Amplitude Errors," Peter R. Franchi and Harvey Tobin 507
- 30. "An Incident Field Sensor for EMP Measurements," Everett G. Farr and Joseph S. Hofstra 527
- 31. "Quantifying Simultaneous V and H Coverage From an Underside Aircraft Location," George Monser and Leonard T. Surette 549

\* NOT INCLUDED IN THIS VOLUME

## Contents

- |   |     |
|---|-----|
| 32. "Polarization Determination in a DF System at MM Wavelengths Without a Rotary Joint," Harry B. Sefton, Jr | 572 |
| 33. "The Effect of Feed on the Input Impedance of a Microstrip Antenna," W. C. Chew, Z. Nie and Y. T. Lo      | 597 |

## MICROSTRIP ANTENNAS IN COMPOSITE LAYERS

D. R. Jackson  
Department of Electrical Engineering  
University of Houston  
Houston, TX 77204-4793

N. G. Alexopoulos  
Department of Electrical Engineering  
University of California  
Los Angeles, CA 90024

A. A. Oliner  
Department of Electrical Engineering  
Polytechnic University  
333 Jay Street  
Brooklyn, NY 11201

**ABSTRACT** - Embedding a microstrip antenna within a composite of multiple dielectric layers may significantly affect both the radiation and the scattering properties of the antenna. One of the most significant ways in which a composite may influence the radiation pattern of a microstrip antenna is by the excitation of weakly attenuated leaky waves on the composite structure, resulting in narrow-beam radiation patterns. A discussion of a composite structure which produces such narrow-beam patterns is given, along with an analysis in terms of leaky-wave antenna concepts. This allows for formulas to predict the radiation patterns of such composite leaky-wave antennas accurately, both for the infinite structure and for the practical case of a finite structure. An experimental leaky-wave antenna is tested, with the measured pattern showing good agreement with the theoretical pattern. It is then shown that the radar cross section (RCS) of a microstrip antenna within a composite is directly related to the radiation efficiency of the antenna. Results are presented to show how both lossless and lossy composite layers may affect the RCS.

# 1 A MULTIPLE LAYER LEAKY-WAVE ANTENNA

## 1.1 INTRODUCTION

One of the fundamental ways in which multiple layer composites can affect the radiation pattern of a microstrip element is in the creation of narrow beam patterns. If the layer thicknesses are chosen properly, narrow beam patterns may be produced about any desired scan angle  $\theta_p$  in space, with the beam angle becoming smaller as the number of layers increases [1,2]. The configuration for producing these narrow beam patterns is shown in Fig. 1. In this structure a stacked arrangement of alternating layers is used, with the odd-numbered layers above the ground plane having a relative permittivity  $\epsilon_1$ , and the even-numbered layers having a higher value of relative permittivity  $\epsilon_2$ . There is an even number of  $N$  layers in the composite structure, with the top layer being a high permittivity layer. All even layers have the same thickness, as do all odd layers, with the exception of the bottom layer which is twice as thick as the other odd layers. A narrow beam conical pattern will be produced at angle  $\theta_p$  when the layer thicknesses satisfy the conditions

$$\frac{n_1 b}{\lambda_0} \sqrt{1 - \sin^2(\theta_p)/n_1^2} = .5 \quad (1)$$

$$\frac{n_2 t}{\lambda_0} \sqrt{1 - \sin^2(\theta_p)/n_2^2} = .25 \quad (2)$$

where  $n_i = \sqrt{\epsilon_i \mu_i}$ .

An explanation for this phenomenon may be given from a ray optics point of view. In calculating the radiation from a source in such a layered structure, each layer may be modeled as a transmission line, with a propagation constant  $k_{zi} = (k_i^2 - k_x^2 - k_y^2)^{1/2}$  where  $k_x$  and  $k_y$  are the Fourier transform variables in a spectral domain solution. Each of the transmission lines becomes a  $\lambda/4$  resonant section for wave propagation at angle  $\theta_p$  in free space, when Eqs. (1,2) are satisfied. At this wave angle the composite structure then behaves as a multiple section resonant filter, creating a low impedance boundary condition at  $z = b$ . This, in effect, causes spectral rays which are launched by a source within the bottom layer to be significantly trapped within the bottom layer, provided the wave angle within the bottom layer corresponds to a propagation angle  $\theta_p$  in free space through Snell's law. The wave component at this angle thus propagates outward from the source for a large distance, creating a large radiating aperture, and hence the narrow-beam effect.

## 1.2 LEAKY-WAVE ANTENNA CONCEPT

A more elegant, and useful, explanation of the dielectric layer leaky-wave antenna is provided by considering the radiation to be attributable to weakly attenuated leaky waves which are supported on the composite structure. When Eqs. (1-2) are satisfied, two leaky waves become dominant (weakly attenuated) on the structure, a  $TE$  leaky wave and a  $TM$  leaky wave [3]. The  $TE$  wave is responsible for producing a narrow-beam  $E_\phi$  field, while the  $TM$  wave produces a narrow-beam  $E_\theta$  field [4]. Formulas for the leaky wave contribution to the radiation pattern as a function of the leaky wave complex propagation constant  $k_\rho = \beta - j\alpha$  have been derived in [4].

To derive the radiation formulas for the multiple-layered leaky-wave antenna, the general structure of Fig. 2 is first considered, which consists of an arbitrary planar surface which can support the propagation of leaky waves. This planar surface is above a ground plane, which results in radiation only into the half-space  $z > 0$ . A finite-sized source is assumed to reside somewhere within this structure, and it is this source which launches the leaky wave on the planar surface. In a classical leaky-wave antenna, this planar surface would typically consist of a metallic grating or periodically perforated conducting sheet. However, for the composite layered structure, the dielectric layers above the ground plane take the place of the planar surface. The top of the composite structure is then regarded as the planar surface. By the equivalence principle, the radiation from a leaky wave on such a composite structure will be the same as that from the same leaky wave on the structure of Fig. 2, since only the fields existing at the aperture surface determine the radiation into the upper half-space.

One of the novel features about the leaky-wave antenna of Fig. 2 is that the source is assumed to be of finite size, so that a cylindrical leaky wave is launched from the source, as opposed to a one-directional (planar) leaky wave which propagates in a fixed direction along the surface. The cylindrical  $TM$  and  $TE$  leaky waves thus propagate outward from the source with a magnetic or electric vector potential given by

$$\psi = A H_n^{(2)}(k_\rho \rho) \begin{pmatrix} \cos n\phi \\ \sin n\phi \end{pmatrix} e^{-jk_z z} \quad (3)$$

where  $\psi$  denotes either  $A_z$  or  $F_z$  for the  $TM_z$  or  $TE_z$  case, respectively.

In general, the amplitude  $A$  as well as the wavenumber  $k_\rho$  may be different for each leaky wave. The wavenumber  $k_z$  is determined as  $k_z =$

$(k_0^2 - k_\rho^2)^{1/2}$  where the improper branch interpretation of  $k_z$  is assumed, since the leaky wave is always improper [5,6]. The index  $n$  in Eq. (3) determines the  $\phi$  variation of the leaky wave, which is independent of the  $k_\rho$  wavenumber. The method of excitation will determine which  $n$  value modes will be excited, and the relative amplitudes of excitation. For example, an infinitesimal vertical electric dipole will only excite an  $n = 0$   $TM_z$  leaky wave. An infinitesimal horizontal electric dipole will only excite  $n = 1$   $TM_z$  and  $TE_z$  leaky waves. Although leaky waves with higher values of  $n$  could in principle be excited, the  $n = 0$  and  $n = 1$  mode types are the most important, since the radiation from microstrip antennas can always be regarded as coming from the superposition of horizontal and vertical sources.

A summary of the radiation formulas for these two mode types, derived in [4], is presented in the next section.

### 1.3 RADIATION FROM CYLINDRICAL LEAKY WAVES

A summary of the radiation formulas for a cylindrical leaky wave having the form of Eq. (3), propagating on the planar structure on Fig. 2, are given below. For consistency in notation, the normalizing constant factor  $A$  in Eq. (3) is chosen to agree with the derivation of [4]. These formulas were derived by using the equivalence principle, in which the entire planar structure of Fig. 2 is replaced with an equivalent electric current  $\mathbf{J}_e = 2\hat{\mathbf{z}} \times \mathbf{H}$  in free space at the aperture plane  $z = 0$ . Standard radiation theory is then used to find the far field from the resulting current. By considering only the equivalent current within the region  $a < \rho < b$ , formulas for the radiation from a finite aperture are obtained, which are useful in determining the radiation from a practical finite size leaky-wave antenna.

#### $n = 0$ case

(a)  $TM_z$ :

$$A_z = \frac{1}{2} H_0^{(2)}(k_\rho \rho) e^{-jk_z z} \quad (4)$$

$$E_\theta = R(r) \cos \theta P^{(0)}(\theta) \quad (5)$$

$$E_\phi = 0 \quad (6)$$

(b)  $TE_z$ :

$$F_z = \frac{1}{2} \frac{\omega \mu_0}{k_z} H_0^{(2)}(k_\rho \rho) e^{-jk_z z} \quad (7)$$

$$E_\theta = 0 \quad (8)$$

$$E_\phi = -R(r) P^{(0)}(\theta) \quad (9)$$

where

$$R(r) = -\frac{j\omega\mu_0 r}{4\pi r} e^{-jk_0 r}$$

$$P^{(0)}(\theta) = -\frac{j2\pi k_\rho}{k_\rho^2 - \xi^2} \left[ \xi \rho' J_0(\xi \rho') H_1^{(2)}(k_\rho \rho') - k_\rho \rho' J_1(\xi \rho') H_0^{(2)}(k_\rho \rho') \right]_{\rho'=a}^{\rho'=b}$$

and

$$\xi = k_0 \sin \theta.$$

$n = 1$  case

(a)  $TM_z$ :

$$A_z = \frac{1}{2} H_1^{(2)}(k_\rho \rho) \cos \phi e^{-jk_z z} \quad (10)$$

$$E_\theta = R(r) \cos \phi \cos \theta P^{(1)}(\theta) \quad (11)$$

$$E_\phi = -R(r) \sin \phi C(\theta) \quad (12)$$

(b)  $TE_z$ :

$$F_z = \frac{1}{2} \frac{\omega \mu_0}{k_z} H_1^{(2)}(k_\rho \rho) \sin \phi e^{-jk_z z} \quad (13)$$

$$E_\theta = R(r) \cos \phi \cos \theta C(\theta) \quad (14)$$

$$E_\phi = -R(r) \sin \phi P^{(1)}(\theta) \quad (15)$$

where

$$P^{(1)}(\theta) = \frac{2\pi k_\rho}{k_\rho^2 - \xi^2} \left[ k_\rho \rho' H_1^{(2)}(k_\rho \rho') J_0(\xi \rho') - \xi \rho' H_0^{(2)}(k_\rho \rho') J_1(\xi \rho') \right]_{\rho'=a}^{\rho'=b} = C(\theta)$$

and

$$C(\theta) = \frac{2\pi}{\xi} \left[ H_1^{(2)}(k_\rho \rho') J_1(\xi \rho') \right]_{\rho'=a}^{\rho'=b}$$



The  $P^{(0)}(\theta)$  and  $P^{(1)}(\theta)$  terms in Eqs. (5,9,11,15) become sharply peaked at angle  $\theta_p$  given by

$$\beta = k_0 \sin \theta_p \quad (16)$$

as the attenuation constant  $\alpha$  becomes small. From Eqs. (4-9) it is then apparent that an  $n = 0$   $TM_z$  leaky wave will radiate a peaked beam with only an  $E_\theta$  component, while an  $n = 0$   $TE_z$  wave will radiate a peaked beam with only an  $E_\phi$  component. The  $n = 1$  waves radiate both an  $E_\theta$  and an  $E_\phi$  component, seen from Eqs. (10-15). However, the  $C(\theta)$  function does not become sharply peaked as  $\alpha \rightarrow 0$ . Hence a  $TM_z$  wave still predominantly radiates an  $E_\theta$  component, while a  $TE_z$  wave predominantly radiates an  $E_\phi$  component.

#### 1.4 LEAKY-WAVE PROPAGATION CONSTANTS

In order to use the radiation formulas of the preceding section, the phase and attenuation constants,  $\beta$  and  $\alpha$ , must be known for both the  $TM$  and the  $TE$  dominant leaky waves which contribute significantly to the radiation pattern.

The value of the complex propagation constant  $k_p$  for the  $TM_z$  and the  $TE_z$  leaky waves may be found numerically, using, for example, a secant method search in the complex plane to find the zeros of the  $TM$  and  $TE$  transverse resonance equations for the layered structure [3]. In the limit of narrow beamwidths ( $\alpha/k_0 \ll 1$ ), it is also possible to derive asymptotic expressions for the attenuation constant  $\alpha$  however, which become increasingly accurate as the beamwidth decreases [7]. The results are summarized below.

##### A) Scanned beam ( $\theta_p > 0$ )

$$\alpha = \frac{1}{2} \frac{P_r}{P_f} \quad (17)$$

where

$$P_r = \frac{2}{\eta_0} \cos \theta_p \quad (18)$$

and

$$P_f = \frac{1}{k_0} F_{TE} \sin \theta_p \quad (TE_z \text{ wave}) \quad (19)$$

$$P_f = \frac{1}{k_0} F_{TM} \sin \theta_p \quad (TM_z \text{ wave}) \quad (20)$$

with

$$F_{TE} = \frac{1}{\eta_0} p^{-N} \left[ \frac{1}{1-p^2} \left( \frac{k_0 b}{2\mu_1} + p^2 \frac{k_0 t}{\mu_2} \right) + \frac{k_0 b}{2\mu_1} \right] \quad (21)$$

$$F_{TM} = \eta_0 p^{-N} \frac{\cos^2 \theta_p}{Z_{c1}^2} \left[ \frac{1}{1-p^2} \left( \frac{k_0 b}{2\epsilon_1} + \frac{k_0 t}{\epsilon_2} \right) + \frac{k_0 b}{2\epsilon_1} \right]. \quad (22)$$

The term  $p$  is the ratio of the characteristic impedances for the transmission lines which represent the dielectric layers, for wave propagation at an angle  $\theta_p$  in free space. Specifically,

$$p = \frac{Z_{c2}}{Z_{c1}} \quad (23)$$

where

$$Z_{ci} = \eta_0 N_i(\theta) / \epsilon_i \quad TM_z \text{ wave}, i = 1, 2 \quad (24)$$

$$Z_{ci} = \eta_0 \mu_i / N_i(\theta) \quad TE_z \text{ wave}, i = 1, 2 \quad (25)$$

with

$$N_i(\theta) = \sqrt{n_i^2 - \sin^2 \theta}$$

and  $n_i = \sqrt{\epsilon_i \mu_i}$ .

## B) Broadside beam ( $\theta_p = 0$ )

$$\alpha = k_0 \sqrt{\frac{1}{\eta_0 F}} \quad (26)$$

where

$$F = F_{TE} = F_{TM} \quad \text{at } \theta_p = 0. \quad (27)$$

## 1.5 RESULTS FOR INFINITE STRUCTURE

To illustrate the patterns which may be produced with a microstrip antenna embedded within the composite structure of Fig. 1, results are shown for the case where an infinitesimal vertical or horizontal electric dipole is used as the source. For the horizontal dipole, the dipole is placed at  $z_0 = b/2$ . For the vertical dipole, the dipole is placed at the ground plane, at  $z_0 = 0$ .

The choice of dipole location does not significantly influence the shape of the beam near the peak, since this is determined by the leaky wave propagation constants, which are not affected by the source location. However, the choice of dipole location just described results in a maximum radiated power from the dipole [1].

Fig. 3 shows the  $\phi$ -symmetric pattern for a vertical dipole within a six-layered structure having  $\epsilon_1 = 2.2$  and  $\epsilon_2 = 10.0$ , where the scan angle is  $\theta_p = 45^\circ$ . The exact radiation pattern is found from a reciprocity method [1]. For comparison, the leaky-wave pattern due to the  $TM$  leaky wave alone is also shown, found from Eq. (5) with  $a = 0$  and  $b = \infty$ . Near the beam peak, the agreement is excellent.

In Fig. 4 the E-plane patterns ( $\phi = 0$ ) for a horizontal dipole within a six-layered structure are shown. The layer permittivities are the same as for Fig. 3, but the thicknesses are chosen from Eqs. (1,2) to produce a broadside beam.

## 1.6 RADIATION FROM A FINITE LEAKY-WAVE ANTENNA

One of the most important practical concerns is the ability to accurately predict the radiation pattern for a leaky-wave antenna of finite size. For the cylindrical leaky-wave antenna of Fig. 2, the radius  $R$  is assumed to be finite. To calculate the pattern in this case, the total pattern  $R(\theta, \phi)$  is written as the sum of three parts:

$$R(\theta, \phi) = R_{sp}(\theta, \phi) + R_{lw}^{(0,R)}(\theta, \phi) + R_d(\theta, \phi). \quad (28)$$

The term  $R_{sp}(\theta, \phi)$  is the space-wave contribution, which is defined as the total radiation field minus the leaky-wave field. Because this component is essentially a near-field contribution of the source, it may be taken as the space-wave contribution for the infinite aperture case with little error. The term  $R_{lw}^{(0,R)}(\theta, \phi)$  is the contribution due to the leaky wave with a finite radiating aperture extending from  $\rho = 0$  to  $\rho = R$ . This term may be calculated from Eqs. (4-15). Finally, the term  $R_d(\theta, \phi)$  is due to edge diffraction from both the leaky wave and any existing surface waves, at the boundary  $\rho = R$ . Although this term would be difficult to predict, it can be minimized by placing absorber around the perimeter of the antenna. This has been done in the experimental design shown later, so this term will be neglected in the following derivation.

The difficulty with using Eq. (28) directly is that the term  $R_{sp}(\theta, \phi)$  is difficult to calculate. To avoid having to calculate this term, the total radiation pattern for the infinite aperture case is first written as

$$R_{\infty}(\theta, \phi) = R_{sp}(\theta, \phi) + R_{lw}^{(0,\infty)}(\theta, \phi) \quad (29)$$

and this equation is subtracted from Eq. (28). Assuming that  $R_d(\theta, \phi) = 0$ , the result is

$$R(\theta, \phi) = R_{\infty}(\theta, \phi) - R_{lw}^{(R,\infty)}(\theta, \phi). \quad (30)$$

The term  $R_{\infty}(\theta, \phi)$  is easy to calculate, since it is the total pattern of the source within an infinite layered structure. The term  $R_{lw}^{(R,\infty)}(\theta, \phi)$  may be calculated from Eqs. (4-15), once the amplitudes of the propagating leaky waves are known (discussed further in the next section).

## 1.7 EXPERIMENTAL DESIGN AND RESULTS

An experimental leaky-wave antenna using air ( $\epsilon_1 = 1.0$ ) and polyethylene ( $\epsilon_2 = 2.2$ ) is shown in Fig. 5. The radius  $R$  is 30.0 cm, corresponding to  $1.208 \lambda_0$  at a frequency of 12.08 GHz. This frequency was chosen to provide a scanned beam at  $\theta_p = 45^\circ$  from Eq. (2), using a layer thickness of  $t = .476$  cm for the polyethylene. The source was a bent coaxial feed probe. The vertical part of the feed probe radiates only an  $E_\theta$  field component. Furthermore, in the H-plane ( $\phi = 90^\circ$ ), the length of the horizontal part of the feed probe does not affect the radiation pattern. Therefore, if only the  $E_\phi$  field component in the H-plane is considered, the pattern will be exactly the same as that of an infinitesimal horizontal electric dipole. An easy comparison can then be made with the theoretical pattern, using  $R(\theta, \phi) = E_\phi(\theta, \phi)$ .

The theoretical H-plane pattern  $R_{\infty}(\theta, \phi)$  for an infinite layered structure corresponding to Fig. 5 is shown in Fig. 6a, for a dipole height  $z_0 = .124$  cm. This dipole height corresponds to an electrical height of  $n_1 z_0 / \lambda_0 = .5$ , which produces a null in the pattern at broadside. The value of  $z_0$  has little effect on the beam shape near the peak, however. In the H-plane, the radiation field  $R_{\infty}(\theta, \phi)$  from the x-directed dipole has only an  $E_\phi$  component.

Figure 6b shows the theoretical pattern  $R_{lw}^{(0,\infty)}$  for the dominant  $TE_{n=1}$  leaky wave, calculated from Eq. (15). The  $TE$ -mode leaky wave is the one responsible for the narrow beam in the H-plane, since this wave produces the narrow beam  $E_\phi$  pattern. The values of  $\alpha$  and  $\beta$  used in Eq. (15) were

obtained numerically as  $\beta/k_0 = .7084$ ,  $\alpha/k_0 = .0157$ . It is seen that the leaky wave pattern of Fig. 6b agrees fairly well with the total pattern of Fig. 6a near the beam peak.

Figure 6c shows the theoretical pattern  $R_{lw}^{(R,\infty)}(\theta, \phi)$  for the  $TE$  leaky wave. The beamwidth of this pattern is noticeably broader than that of the infinite leaky-wave pattern of Fig. 6b. Because of this, this term has the dominant effect on the beamwidth of the total pattern for the finite leaky-wave antenna.

To determine the pattern  $R(\theta, \phi)$  of the finite leaky-wave antenna from Eq. (30), the complex amplitude  $A$  in Eq. (3) for the  $TE$ -mode leaky wave must be determined, so that the amplitude of  $R_{lw}^{(R,\infty)}(\theta, \phi)$  can be found. This may be done from the normalizing condition

$$R_{lw}^{(0,\infty)}(\theta_p, \pi/2) = R_{\infty}(\theta_p, \pi/2) \quad (31)$$

which equates the total pattern with that of the leaky wave at the beam peak in the H-plane, for an infinite structure. This condition provides for an accurate calculation of  $A$ , since the exact and leaky wave patterns agree very closely at the beam peak. The resulting theoretical pattern  $R(\theta, \phi)$  for the finite leaky-wave antenna is shown in Fig. 6d.

In figure 7, the experimental pattern is shown. The agreement with the pattern of Fig. 6d is fairly good except for the back radiation which is probably attributable to spurious ground plane diffraction which was not completely eliminated by the absorber. The beam peak in the experimental pattern is also shifted slightly away from  $45^\circ$ , with the peak on the left lower in amplitude than the one on the right. These effects could possibly be due to tolerance errors in the layer spacings, since some warping of the polyethylene layers was observed between the styrofoam spacers.

## 2 SCATTERING FROM A MICROSTRIP ANTENNA

In addition to modifying the radiation pattern, a composite structure may also significantly affect the radar cross section (RCS) of a microstrip antenna. A general equation for the RCS of an arbitrary body such as a microstrip

antenna within a composite structure is [8]

$$A_{uv} = \frac{\lambda_0^2}{\pi} \left( \frac{R_s}{|Z_s|} \right)^2 e_r^2 G_u(\theta_1, \phi_1) G_v(\theta_2, \phi_2) \quad (32)$$

where  $A_{uv}$  is the RCS for the  $\hat{v}$  component of the scattered field, due to an incident wave in the  $\hat{u}$  polarization.  $Z_s$  is the body impedance, defined as minus the self reaction of the scattered current,

$$Z_s = R_s + jX_s = - \langle \mathbf{J}_s, \mathbf{J}_s \rangle. \quad (33)$$

$G_u$  and  $G_v$  are the partial antenna gains in the direction of the incident field and scattered field, respectively, when considering the  $\hat{u}$  or  $\hat{v}$  component of radiation from the body current  $\mathbf{J}_s$ . The radiation efficiency  $e_r$  is the ratio of power radiated into space by the body current  $\mathbf{J}_s$  to the total power delivered by the body current (which includes surface wave and conduction losses).

Because of the term  $e_r^2$  in Eq. (32), the RCS may be reduced by lowering the radiation efficiency. This may be done in three different ways: by introducing loss into the substrate beneath the patch, by using a lossy layer or layers above the patch, or by using multiple lossless layers above the patch. This is illustrated for the two-layered case of Fig. 8, where  $\ell$  denotes dielectric loss tangent. Results for monostatic RCS with broadside incidence in the  $\hat{x}$  polarization are shown in Figs. (9-11). All results are for a rectangular patch of dimensions  $L = 1.27 \text{ cm}$  and  $W = 1.5 L$ , where  $L$  is the  $x$  dimension, chosen to be of resonant length for all calculations. The layers are assumed to be nonmagnetic ( $\mu_i = 1.0$ ) in all cases. The RCS component  $A_{xx}$  is normalized to  $1.0 \text{ m}^2$  and is expressed in dB.

Fig. (9a) shows the effect of introducing loss in the substrate for a patch on a single layer ( $t = 0$ ). Figure (9b) shows that the radiation efficiency is lowered along with the RCS. Fig. (10) demonstrates the effect of a lossless superstrate layer on the RCS. A superstrate with a high permittivity may substantially reduce the RCS when the thickness is approximately a half wavelength in the substrate. Using multiple layers permits an even greater reduction in RCS, and results for this case will be presented. Figure (11) shows how the RCS may be reduced by using a lossy layer above the patch.

## References

- [1] D. R. Jackson and N. G. Alexopoulos, "Gain enhancement methods for printed circuit antennas", IEEE Trans. Antennas Propagat., vol. AP-33, pp. 976-987, Sept. 1985.
- [2] H. Y. Yang and N. G. Alexopoulos, "Gain enhancement methods for printed antennas through multiple superstrates", IEEE Trans. Antennas Propagat., vol. AP-35, pp. 860-863.
- [3] D. R. Jackson and A. A. Oliner, "A leaky wave analysis of the high-gain printed antenna configuration", IEEE Trans. Antennas Propagat., vol. AP-36, pp. 905-910, July 1988.
- [4] A. Ip and D. R. Jackson, "Radiation from cylindrical Leaky waves", IEEE Trans. Antennas Propagat., accepted for publication.
- [5] T. Tamir and A. A. Oliner, "Guided complex waves: part 1, fields at an Interface", Proc. IEE, vol. 110, pp. 310-324, Feb. 1963.
- [6] T. Tamir and A. A. Oliner, "Guided complex waves: part 2, relation to radiation patterns", Proc. IEE, vol. 110, pp. 325-334, Feb. 1963.
- [7] D. R. Jackson, A. A. Oliner, and A. Ip, "Leaky-wave propagation and radiation for a multiple-layer dielectric structure", submitted to IEEE Trans. Antennas Propagat.
- [8] D. R. Jackson and N. G. Alexopoulos, "The RCS of a rectangular microstrip patch in a substrate-superstrate geometry", IEEE Trans. Antennas Propagat., accepted for publication.

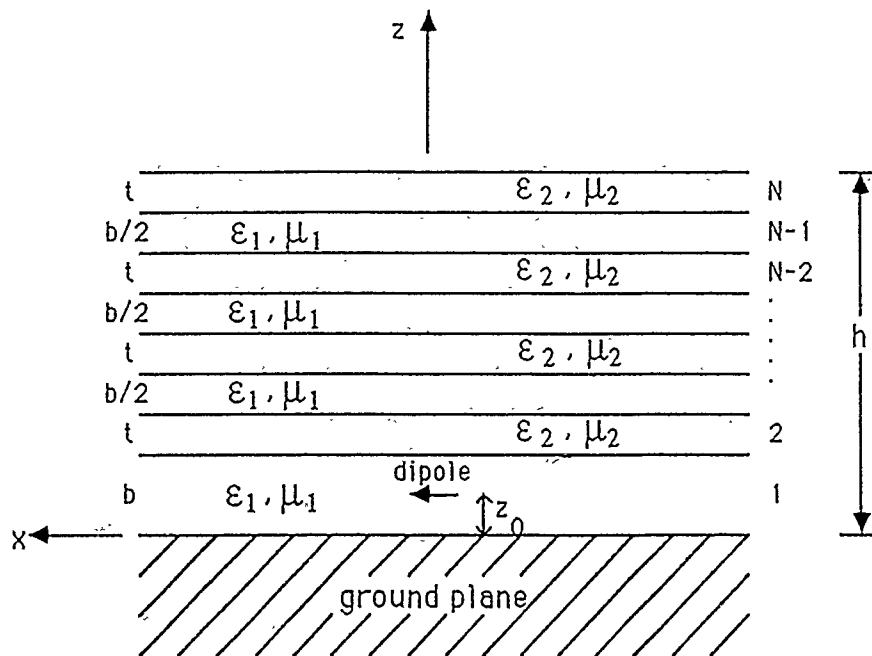


Fig. 1 A multiple layer composite-structure for producing narrow-beam radiation patterns.  $\epsilon_i$  and  $\mu_i$  are the relative permittivity and permeability, respectively.

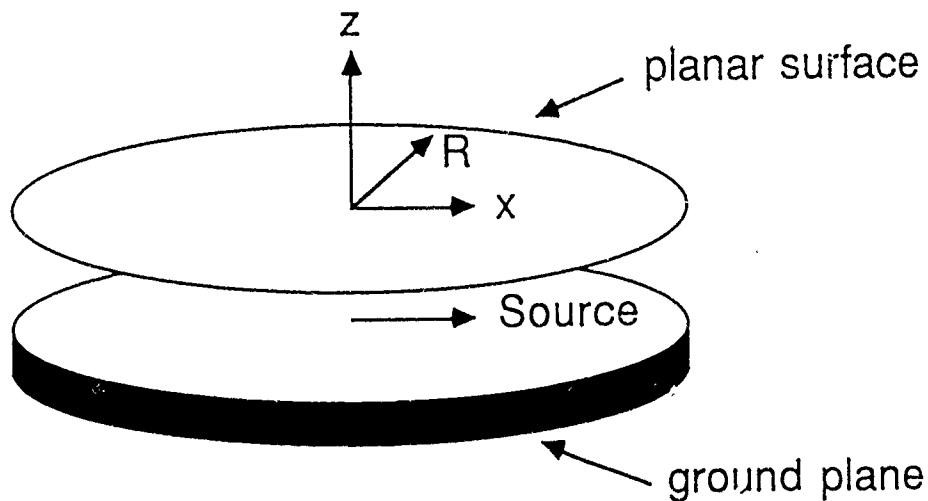


Fig. 2 A general representation of a finite-size cylindrical leaky-wave antenna, consisting of a planar surface which can support leaky wave propagation over a ground plane.



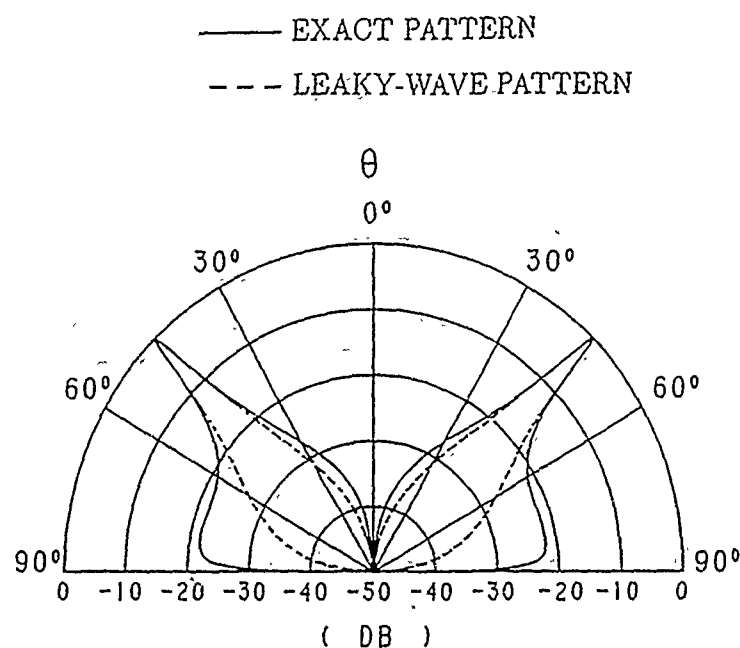


Fig. 3 A comparison of exact and leaky-wave radiation patterns for an infinitesimal vertical electric dipole within a six-layered structure with a scan angle of  $\theta_p = 45^\circ$ . The dipole is at the ground plane ( $z_0 = 0$ ).  $\epsilon_1 = 2.2$ ,  $\mu_1 = 1.0$ ,  $\epsilon_2 = 10.0$ ,  $\mu_2 = 1.0$ .

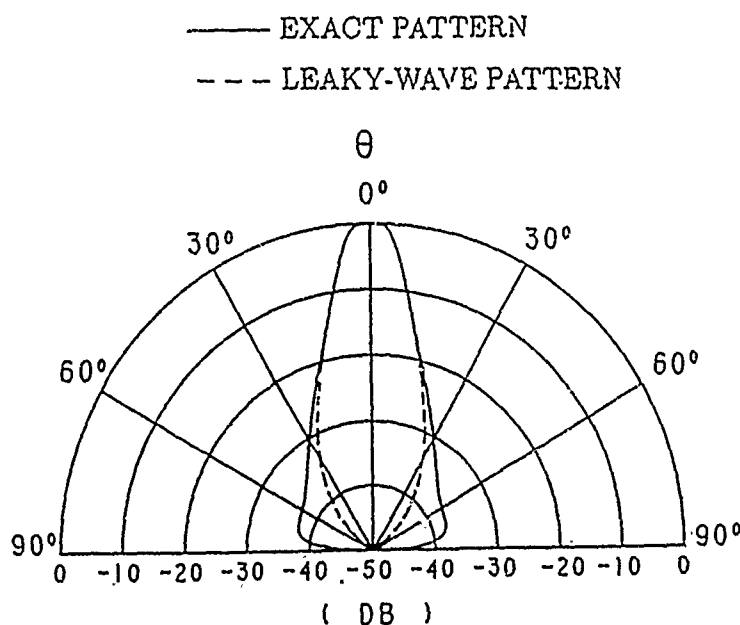


Fig. 4 A comparison of exact and leaky-wave E-plane radiation patterns for an infinitesimal horizontal electric dipole within a six-layered structure with a broadside scan angle ( $\theta_p = 0^\circ$ ). The dipole is oriented in the x direction and is in the middle of the bottom layer.  $\epsilon_1 = 2.2$ ,  $\mu_1 = 1.0$ ,  $\epsilon_2 = 10.0$ ,  $\mu_2 = 1.0$ .

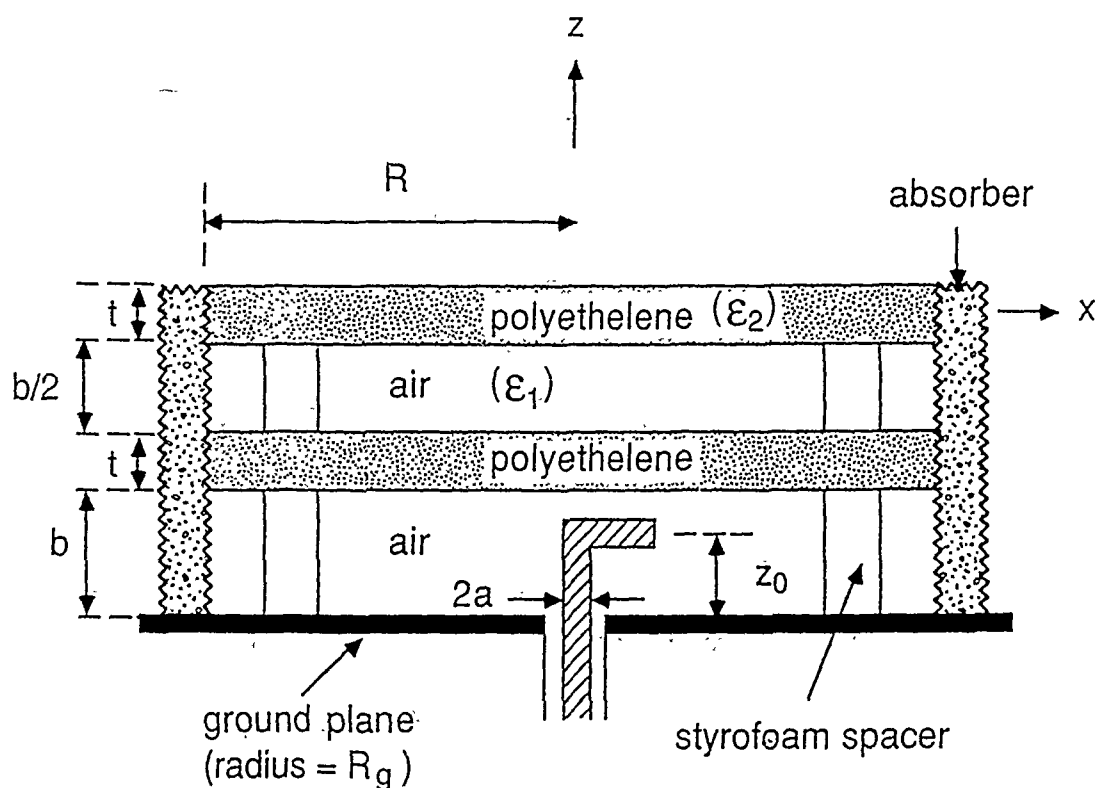


Fig. 5 The experimental leaky-wave antenna, designed for operation at 12.08 GHz with a beam angle at  $\theta_p = 45^\circ$ .  $b = 1.76$  cm,  $t = .476$  cm,  $R = 30.0$  cm,  $R_g = 50.8$  cm,  $z_0 = 1.24$  cm,  $a = .16$  cm (probe radius),  $\epsilon_2 = 2.2$ .

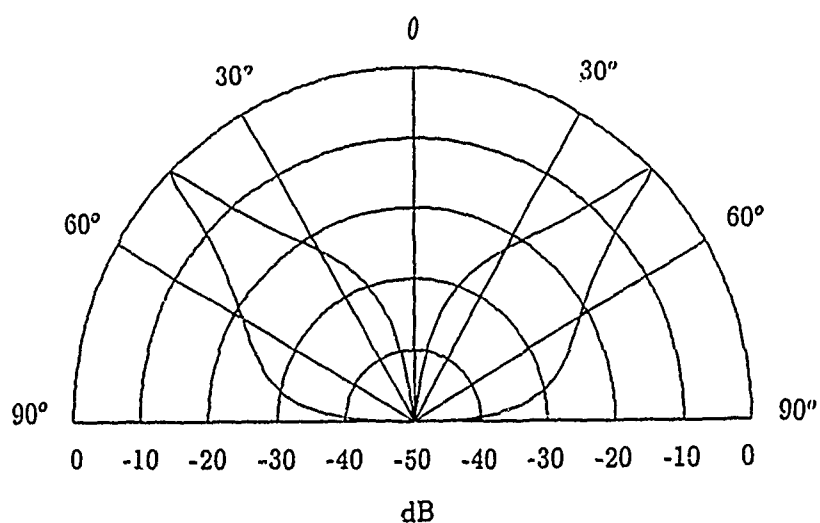


Fig. 6a Theoretical H-plane pattern for an infinitesimal horizontal electric dipole in the structure of Fig. 5, if the layers extend to infinity.

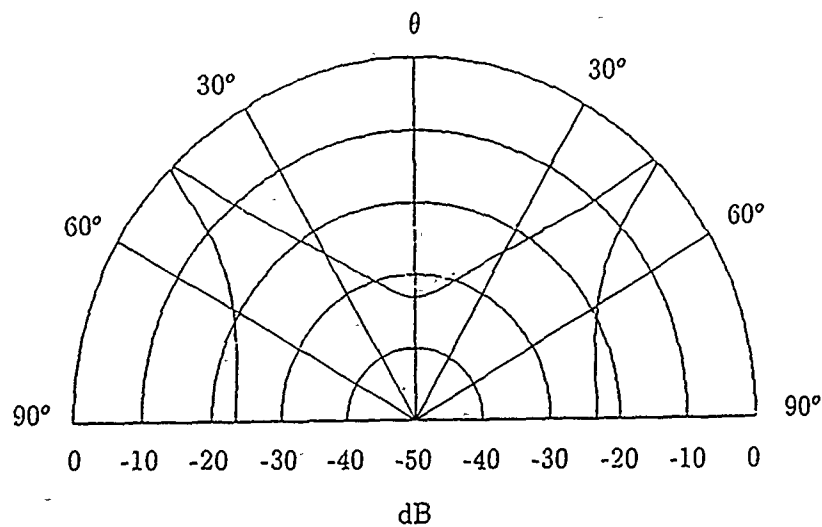


Fig. 6b Theoretical pattern due to the TE leaky wave for the structure of Fig. 5, assuming the layers extend to infinity. The leaky-wave phase and attenuation constants are found numerically as  $\beta/k_0 = .7084$ ,  $\alpha/k_0 = .0157$ . The pattern is calculated from Eq. (15).

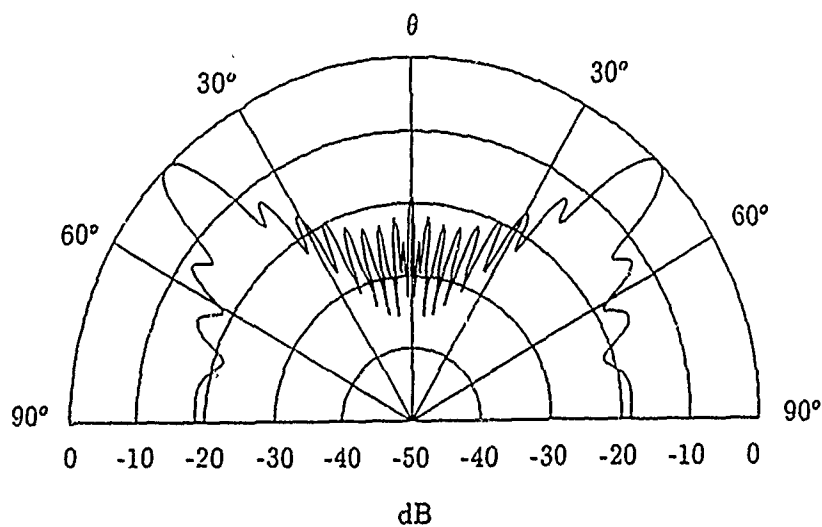


Fig. 6c Theoretical pattern due to the same TE leaky wave as in Fig. 6b, but with a radiating aperture starting at  $a = R = 12.08\lambda_0$  and extending to  $b = \infty$ .

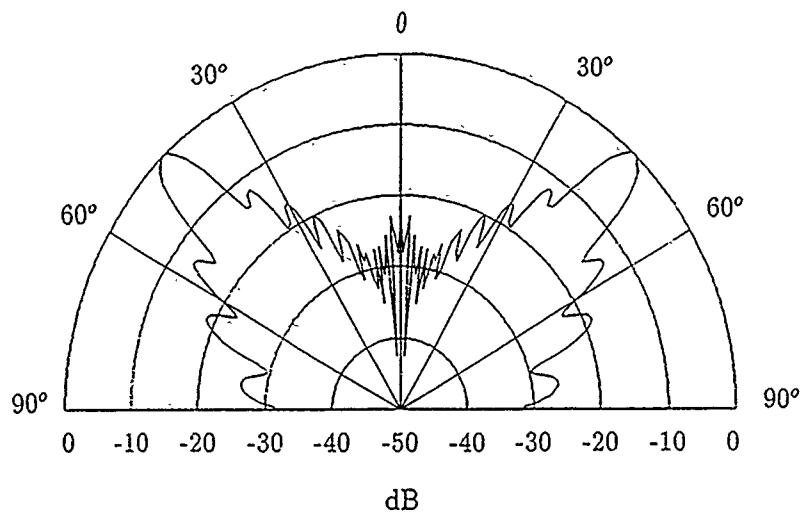


Fig. 6d Theoretical pattern for the finite-size leaky-wave antenna of Fig. 5, obtained from Eq. (30).

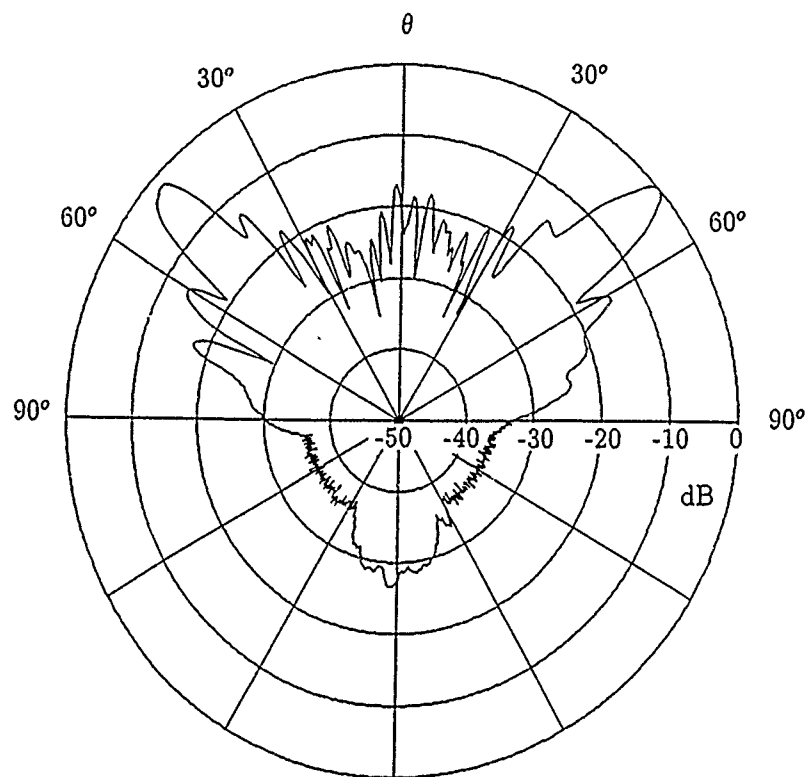


Fig. 7 measured radiation pattern for the leaky-wave antenna of Fig. 5.  $f = 12.08$  GHz.

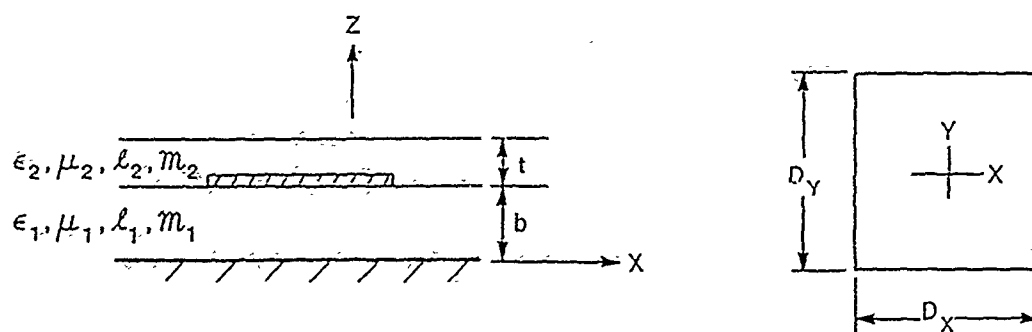


Fig. 8 Patch antenna within a substrate-superstrate configuration.

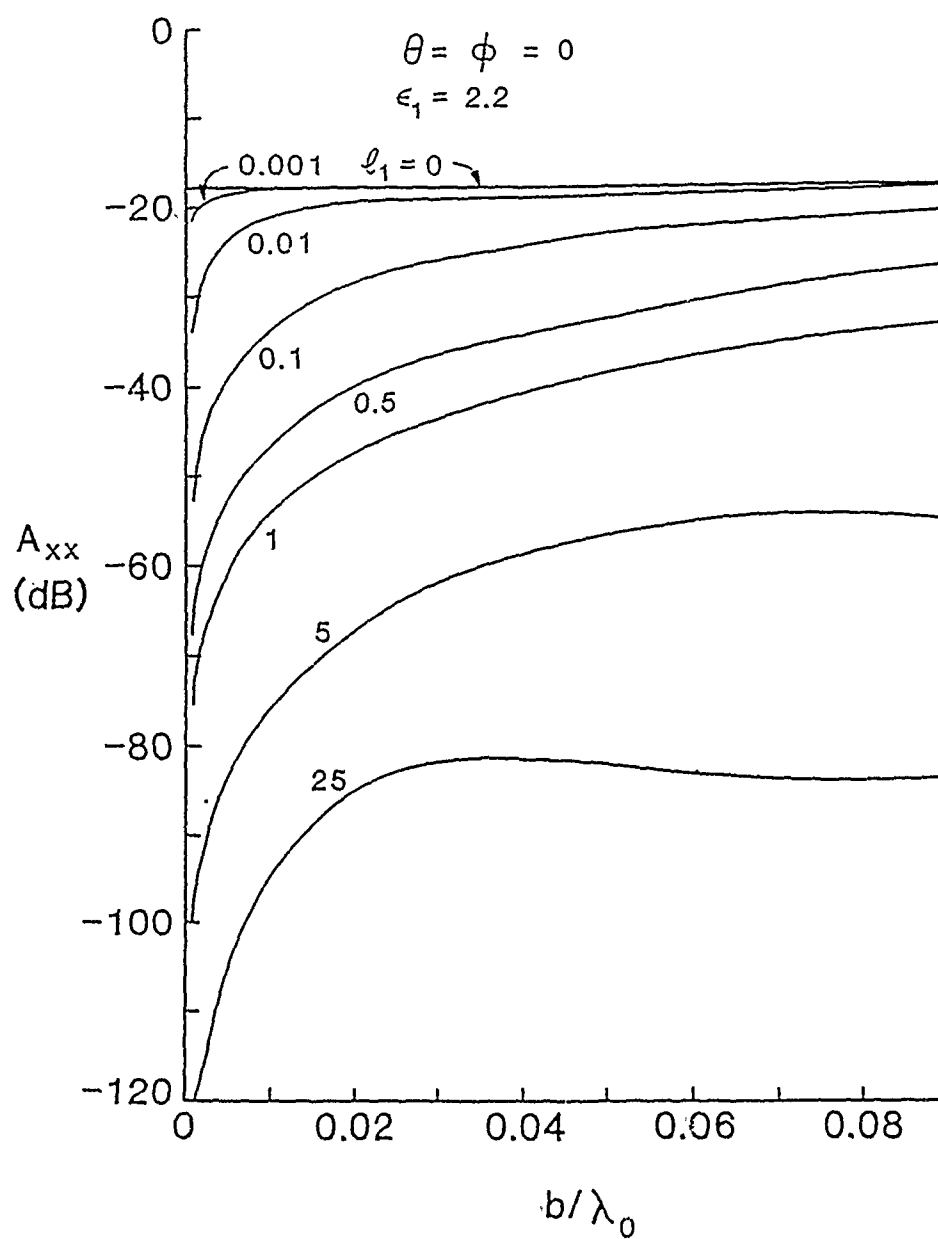


Fig. 9a  $A_{xx}$  vs. substrate thickness for a patch on a single substrate with different loss tangents.

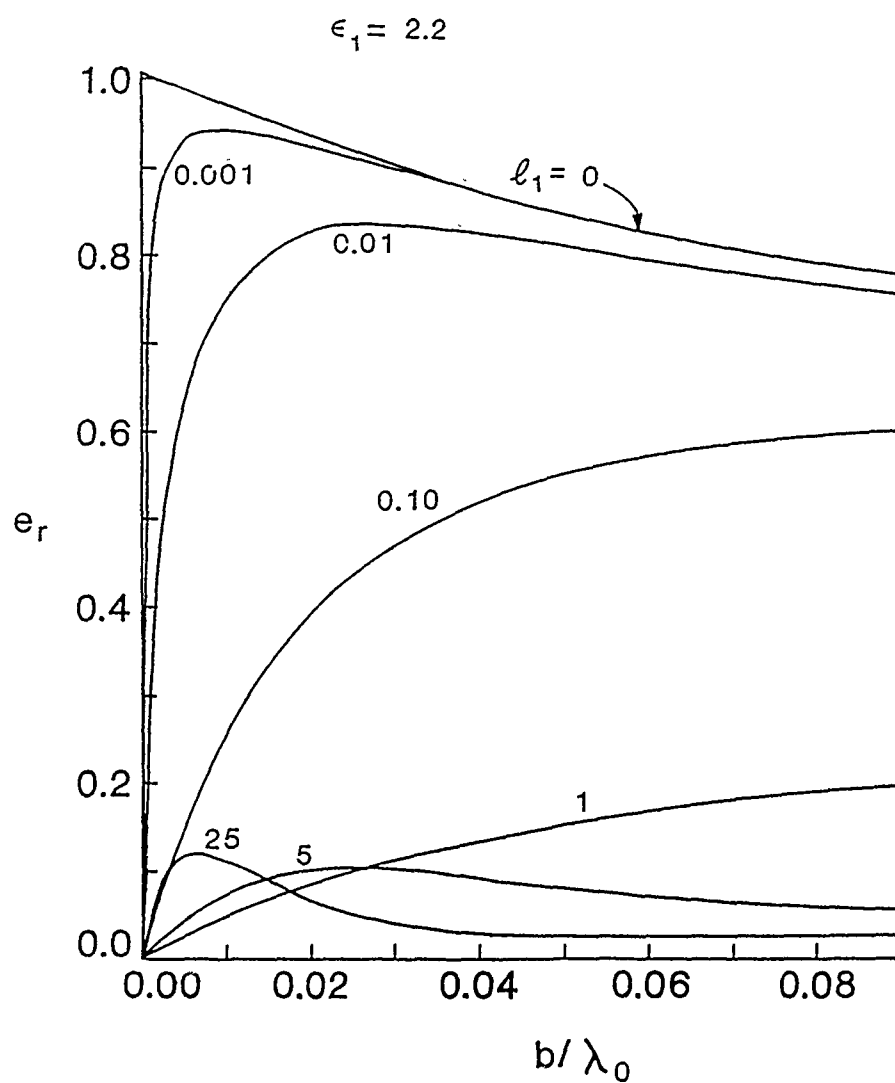


Fig. 9b  $e_r$  vs. substrate thickness for a patch on a single substrate with different loss tangents.

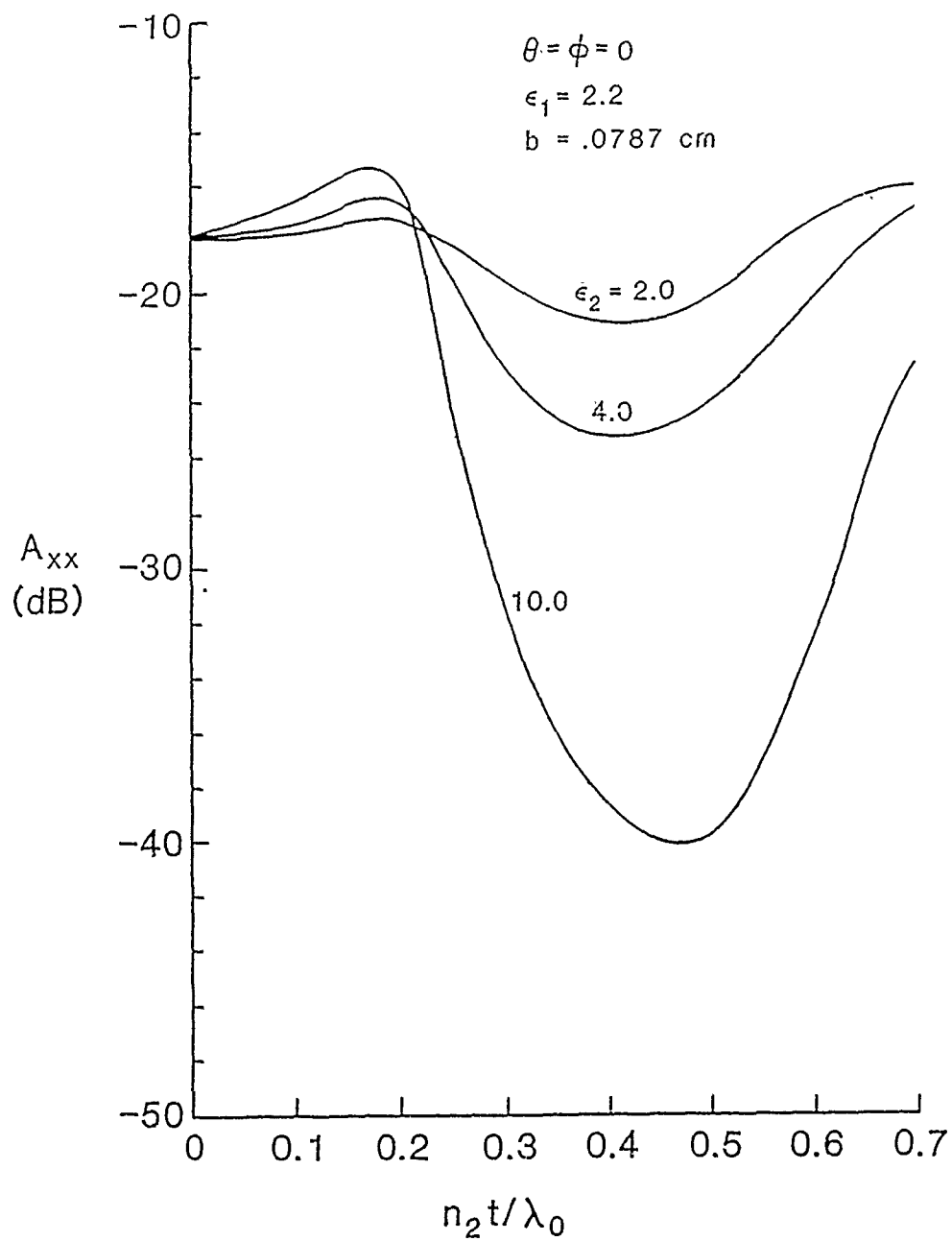


Fig. 10  $A_{xx}$  vs. superstrate thickness for different superstrate permittivities.

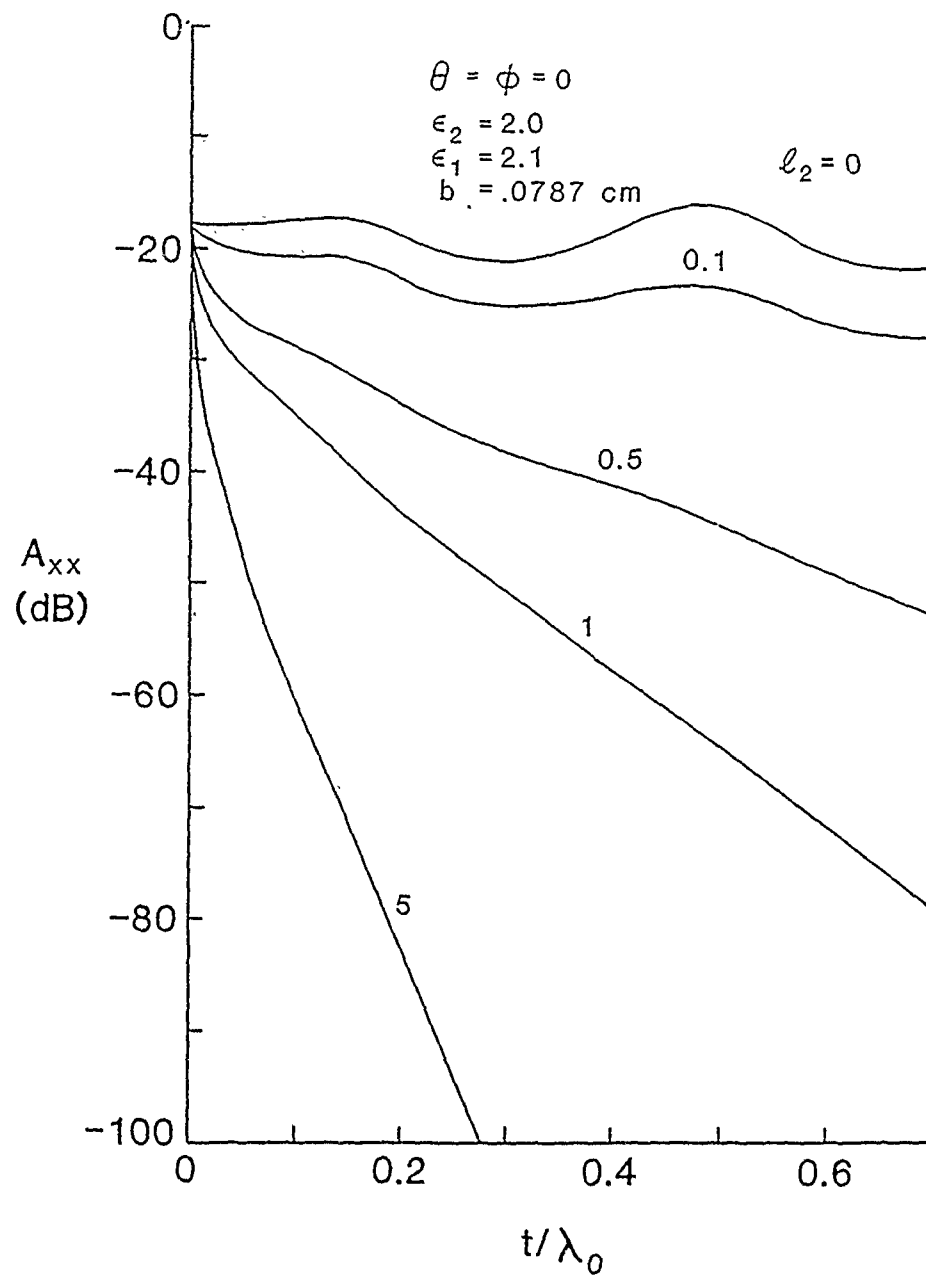


Fig. 11  $A_{xx}$  vs. superstrate thickness for different loss tangents of superstrate.



## **A COMPACT MULTI-POLARIZED BROADBAND ANTENNA**

Dean A. Hofer, Dr. Oren B. Kesler and Lowell L. Loyet

Texas Instruments Incorporated  
Defense Systems and Electronics Group  
Antenna Department  
McKinney, Texas 75070

### **Abstract**

A spiral antenna has served as the standard circularly polarized multi-octave element since its inception. Antenna systems using the right or left hand sense spiral are ineffective when receiving the opposite sense polarization. Hence, a dual circularly polarized antenna with the same aperture area is desired to receive all polarizations over a broad band. Recently, efforts have resulted in the demonstration of an innovative concept to meet the multi-octave, polarization diverse challenge. Equal right and left hand polarization performance has been achieved from a single radiating aperture using an inherent symmetry. This concept employs an edge fed, interleaved log-periodic antenna referred to as the InterLog antenna. The edge fed geometry improves antenna reliability over that of the center fed spiral due to mechanical and thermal stability. The antenna consists of four interleaved, curved dipole, log-periodic elements placed over an absorber-loaded cavity. Opposite elements are excited 180 degrees out-of-phase using a printed circuit infinite balun approach. Orthogonal circular polarizations are achieved by connecting the balun outputs to an integral stripline 90 degree coupler. Analysis, measured pattern, VSWR and isolation data are given, demonstrating the effectiveness of the antenna approach.

**1.0 INTRODUCTION** With the rising complexity of EW threats, radar polarizations have become switchable. Thus, EW, radar warning and DF systems must respond to signals having any polarization over multi-octave bandwidths. Any sense polarization can be received with two opposite sense circular polarized antennas. This however, requires two antenna apertures, which is often not acceptable due to space constraints. Thus, a polarization diverse antenna using a single aperture is desired. Table 1 summarizes the advantages and disadvantages of some polarization diverse approaches that have been considered. Of the approaches shown in Table 1, the InterLog was chosen as the preferred approach because it has the best broad band performance and reliability potential obtainable in a compact package. The inherent symmetry of the InterLog aperture offers balanced circular polarization response. Key technical features together with theory of operation, analysis, and test results of the InterLog design are presented in the following sections.

**2.0 TECHNICAL APPROACH** The InterLog antenna approach is a novel array of orthogonal interleaved log periodic elements with radial baluns integral to the etched antenna aperture. The edge fed structure is planar, broadband and equally sensitive to either left hand or right hand circular polarization. This is uniquely different from many past polarization diverse approaches.

The interleaved log periodic elements form a circular pattern and are placed over an absorber loaded cavity for uni-directional broadband performance. A typical InterLog antenna is shown in Figure 1. Figure 2 details the basic geometry from which the interleaved structure is made. The basic geometry of Figure 2a may be rotated through 90, 180 and 270 degrees to produce the interleaved aperture shown in Figure 2b. A 90 degree hybrid is located in the antenna cavity base. This hybrid, together with the two infinite baluns (integral to the antenna aperture) provides the necessary RF processing

to obtain simultaneous left hand and right hand circular polarization response.

Key technical features of the InterLog antenna include: 1) Dual circular or dual linear polarization capability from a single radiating aperture. Inherent aperture symmetry responds equally well to either right hand or left hand senses of circular polarization, 2) Various polarization output options. Figure 3, illustrates dual circular or dual linear capability. With an internal switch, dual circular or dual linear may be obtained from a single output port. 3) Orthogonal edge fed infinite baluns, integral to the printed circuit antenna aperture. This offers the advantage for reduced cost and potential improved reliability. 4) Wideband performance (9:1) similar to spiral antennas. 5) Broad, fixed beam radiation patterns and gain similar to spiral antennas. 6) May be packaged similar to existing spiral antennas for retro-fitting existing systems.

**3.0 DESIGN DESCRIPTION** Key antenna components are packaged in a single antenna housing. This includes: 1) Dual polarized antenna aperture with integral infinite baluns, 2) 90 degree hybrid and 3) Polarization selection switch. Interface between the edge fed antenna and 90 degree hybrid is obtained via coaxial lines passing along the inner perimeter of the antenna housing. The foam spacer and graded absorbers provide broadband antenna cavity loading similar to cavity backed spiral antennas.

**3.1 EXCITATION REQUIREMENTS** To achieve polarization diversity from a four port antenna, each of the feed ports must be excited with equal amplitudes and the proper phasing as shown in Figure 4a. One of the physical methods of realizing this excitation is shown in Figure 4b. The 180 degree phase shift may be obtained by discrete Marchand baluns or 180 degree hybrids while the 90 degree phase shift is normally obtained through a 90 degree structure. Figure 4c shows a broadband 90 degree coupler designed for the InterLog antenna. The polarization selection switch allows dual

polarized outputs from a single antenna output port. In the InterLog design, the 180 degree phase shift is achieved with orthogonal printed circuit infinite baluns integrated into the antenna aperture. This eliminates the external 180 degree balun normally required. Figure 5 shows a printed circuit microstrip balun integrated into the log periodic structure. A stripline version of this balun is shown in Figure 6. This arrangement employs three dielectric layers. The top and bottom layers contain the same log periodic element etched pattern. The orthogonal stripline feed conductors are on each side of the very thin center dielectric layer. Interdec pins, or plated through holes connect conductors 9, 3 and 12 at point (a), and conductors 11, 7 and 13 at point (b).

**3.2 ANALYSIS AND THEORY OF OPERATION** A preliminary analysis model of the InterLog element aperture was analyzed using the PATCH code. This is a general purpose method of moments (MOM) code based on the solutions of the electric field integral equation that was developed by Johnson, Wilton and Sharpe.<sup>[1]</sup> The simple model assumed a perfectly conducting element in free space using rooftop basis functions for the currents on the triangulation of the element shown in Figure 7. Although the model does not include the feed, termination, substrate, or cavity loading effects, it still shows a strong correlation with the measured data and is useful in determining the trades for the geometric parameters of the aperture, alpha, tau, sigma, feed line width, and radius. A representative set of results is shown in Figures 8 through 10 at 10 GHz for a circularly polarized excitation. As can be seen in Figure 10, the approximate analysis model shows good correlation of pattern shape and axial ratios. The figures

---

[1] Johnson, W.A., D.R. Wilton and R.M. Sharpe, "Patch Code User's Manual", Sandia National Laboratories, Sandia Report SAND87-2991, May 1988

show the amplitude and phase of the currents on the feedline and the curvilinear elements. In Figure a, the numbered curves refer to element number beginning with the smallest center element and progressing outward. From the data the following conclusions can be made,

- 1) The currents are resonant on the dipole arms that are approximately one half wavelength in length. On each arm the amplitude and phase are approximately cosine shaped and constant respectively.

- 2) The phase on the feed line tends to delay from the feed tip to the outer diameter. From the feed to the first resonant dipoles the phase slope is approximately a constant. At the locations of the resonant dipoles the phase is perturbed by the loading of the resonant arms.

Computed vertical and horizontal patterns from the currents are shown in Figure 10 and can be compared with the measured data. This calculation was made for an antenna having parameters of  $\tau = 0.8$ ,  $\alpha = 60$  degrees,  $\sigma = \sqrt{\tau}$ ,  $w = 0.047$  inches, and radius = 1.2 inches.\*

**4.0 TEST RESULTS** To validate and refine performance of the InterLog aperture, preliminary development was done with the aperture connected to an external four port RF processor. The antenna was fed at the center with four phase matched coaxial cables. Section 4.1 presents test results of the coaxial fed InterLog aperture fed with a hardware and software RF processor. Section 4.2 presents test results of an infinite balun (both coaxial and printed circuit) integrated into the InterLog aperture.

---

\* The authors would like to acknowledge Jim Prewitt and Richard Smith for the computations using the PATCH code.

4.1 EXTERNAL RF PROCESSOR FED ANTENNA The initial development objective was to determine an acceptable scale factor,  $\tau$ , and  $\alpha$  angle for a 2.4 inch cavity backed InterLog antenna. Antennas having a  $\tau$  ranging from 0.5 to 0.94 were evaluated while connected to a external RF processor via four phase matched coaxial cables. A  $\tau$  of 0.8 was determined to have the best overall performance. Figures 11 and 12 show measured antenna patterns in dB for RHC, LHC and rotating linear source polarizations for the RHC port and LHC ports respectively.

Conical cut radiation patterns taken at 30 degrees off boresight are shown in Figure 13a and 13b. These patterns show excellent circular coverage for both senses of circular polarization. The large axial ratio and cross polarizations are a result of the non optimum RF processor coupling errors and noise floor limits due to processor insertion loss at 18 GHz. These losses are expected to be significantly reduced when the external four port processor is replaced with an internal processor consisting of orthogonal infinite baluns and 90 a degree hybrid.

In order to verify the RF processor as an error source, the antenna aperture data was collected and processed with the software method (simulated RF processor). For the software processing method, the anechoic chamber source antenna radiated two orthogonal linear polarizations while the received amplitude and phase were recorded at each of the four antenna arms (no RF processor) as a function of polarization, spatial angle and frequency. This data as then combined through a computer routine simulating a "perfect" RF processor with software to produce RHC and LHC and rotating linear polarization responses for the InterLog antenna aperture. Figure 14 shows measured InterLog antenna response using the perfect software RF processor for the LHC port. Note that the axial ratio and cross polarizations have significantly improved with respect to the non optimum RF (external) processor data. This technique is a

useful method for establishing error budgets for the aperture, infinite balun, and 90 degree hybrid.

Figure 15 shows a plot of gain vs frequency for RHC, LHC polarizations and the respective cross polarizations. Both RHC and LHC polarizations track well with good cross polarization rejection. Gain tracking between RHC and LHC can be further improved with optimization of the RF processor design. The inherent symmetry of the aperture dictates that both polarizations should perform identically.

**4.2 INFINITE BALUN FED APERTURE** This section discusses integration of orthogonal infinite baluns into the antenna aperture, thus eliminating two 180 degree hybrids in the RF processor. The data presented in Section 4.1 is for an InterLog antenna externally fed with a four port (external) RF processor using four phase matched coaxial cables.

The excitation requirements for the InterLog antenna are shown in Figure 4 where opposite ports of the structure require equal amplitude and 180 degree phase shift. Only some log periodic structures are suitable for excitation with an infinite balun. For example, a cavity backed log periodic Zig Zag antenna is not suitable for an infinite balun because of the long acute angled path from the central feed point to the outer perimeter region. The infinite balun concept, employing a non radiating transmission line (coax, stripline or properly designed microstrip) to transport RF energy to the antenna feedpoint is frequently used on log periodic dipole antennas. A linear polarized element was fed with a coax infinite balun as shown in Figure 16. Gain of this configuration for a ( $\tau = 0.8$ ,  $\alpha = 60$  degrees,  $Dia = 2.4"$ ) is shown in Figure 17. The infinite balun fed structure operates in a broadband fashion. The low frequency gain rolls off due to constrained diameter and non-optimum (open circuit) termination. In practice, an orthogonal pair of microstrip or stripline infinite baluns, shown in Figure 5 and 6 could be used. Figure 18 shows VSWR of two orthogonal microstrip baluns integrated into a InterLog

aperture. Broadband characteristics with well behaved VSWR over most of the band are observed with the InterLog antenna. High VSWR at the lower band edge band is attributed to the element being unterminated. Further improvement in VSWR can be achieved by adjusting the impedance of the infinite balun transmission line and the feed point impedance of the log periodic structure.

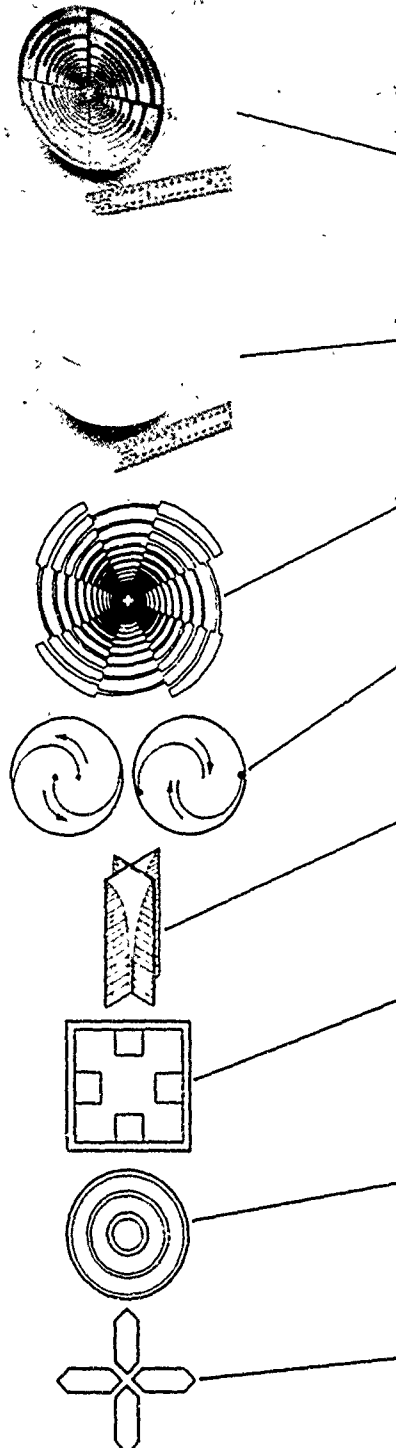
**5.0 FUTURE REFINEMENTS AND APPLICATIONS** The material presented in the foregoing sections has demonstrated feasibility of the InterLog concept. While much progress has been made, there are some tasks which remain. Future refinements must include: 1) Optimization of the antenna design parameters. 2) Optimization and integration of the printed circuit balun into the antenna aperture, 3) Interfacing the antenna/balun assembly with the 90 degree hybrid and 4) Integration of the polarization switch. Planned parameter variations include: 1) Optimization of the aperture design parameter  $\tau$ ,  $\alpha$ ,  $\sigma$ , feeder impedance, balun impedance and feedpoint impedance. Analytical modeling described in Section 3.2 will play an important role in optimizing these parameters, particularly when evaluating design parameter sensitivities such as  $\tau$  vs  $\alpha$  angle. Other areas for design optimization are the antenna termination for improved low frequency performance and cavity loading.

Figure 19 illustrates several applications for the InterLog antenna ranging from flush and conformal mounts to 3-D projections. Experience shown that spiral antennas are rather forgiving of non planar shape changes. Similarly, it is expected that the InterLog may work equally well in non planar applications.



Table 1

Comparison of Various Multi-polarized  
Broadband Antenna Approaches



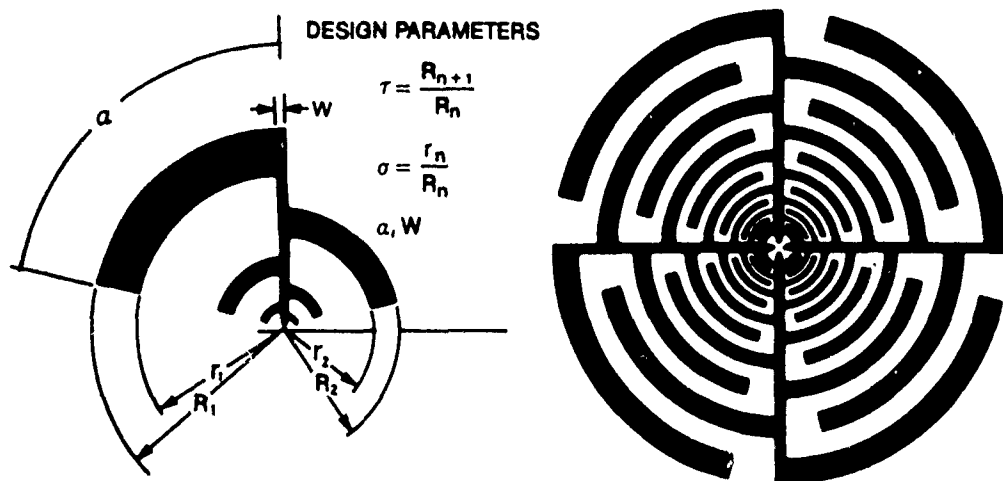
APPROACH	ADVANTAGE	DISADVANTAGE
EDGE FED LOG PERIODIC (INTERLOG)	SIZE, BANDWIDTH, PLANAR, SIMPLE MODE FORMER	CONTINUED DEVELOPMENT REQUIRED BUT APPROACH HAS BEEN VALIDATED
CENTER FED LOG PERIODIC ZIG ZAG	SIZE, BANDWIDTH, PLANAR	MODEFORMER COMPLEXITY, COST
MODULATED ARM WIDTH (MAW) SPIRAL	BANDWIDTH, PLANAR, GEOMETRY	VERY COMPLEX FEED NETWORK, SIZE, COST
DUAL FED SPIRAL	PLANER GEOMETRY	MODE FORMER COMPLEXITY, LIMITED BANDWIDTH
CROSSED NOTCH	SIMPLE MODE FORMER	DEPTH, 3:1 BANDWIDTH, IMPEDANCE MATCHING
QUAD RIDGE WAVEGUIDE	GAIN	DEPTH, BANDWIDTH, SIZE, WEIGHT, MODE FORMER, COMPLEXITY, DIFFICULT TO FAB
COAXIAL WAVEGUIDE	GAIN	DEPTH, BANDWIDTH, SIZE, WEIGHT, MODE FORMER, COMPLEXITY, DIFFICULT TO FAB
ELECTRICALLY SMALL TURNSTILE	SIMPLE MODE FORMER	BANDWIDTH, LOW GAIN, SIZE

M96415001



W96415002 (98-308)

Figure 1. Cavity Backed InterLog Antenna

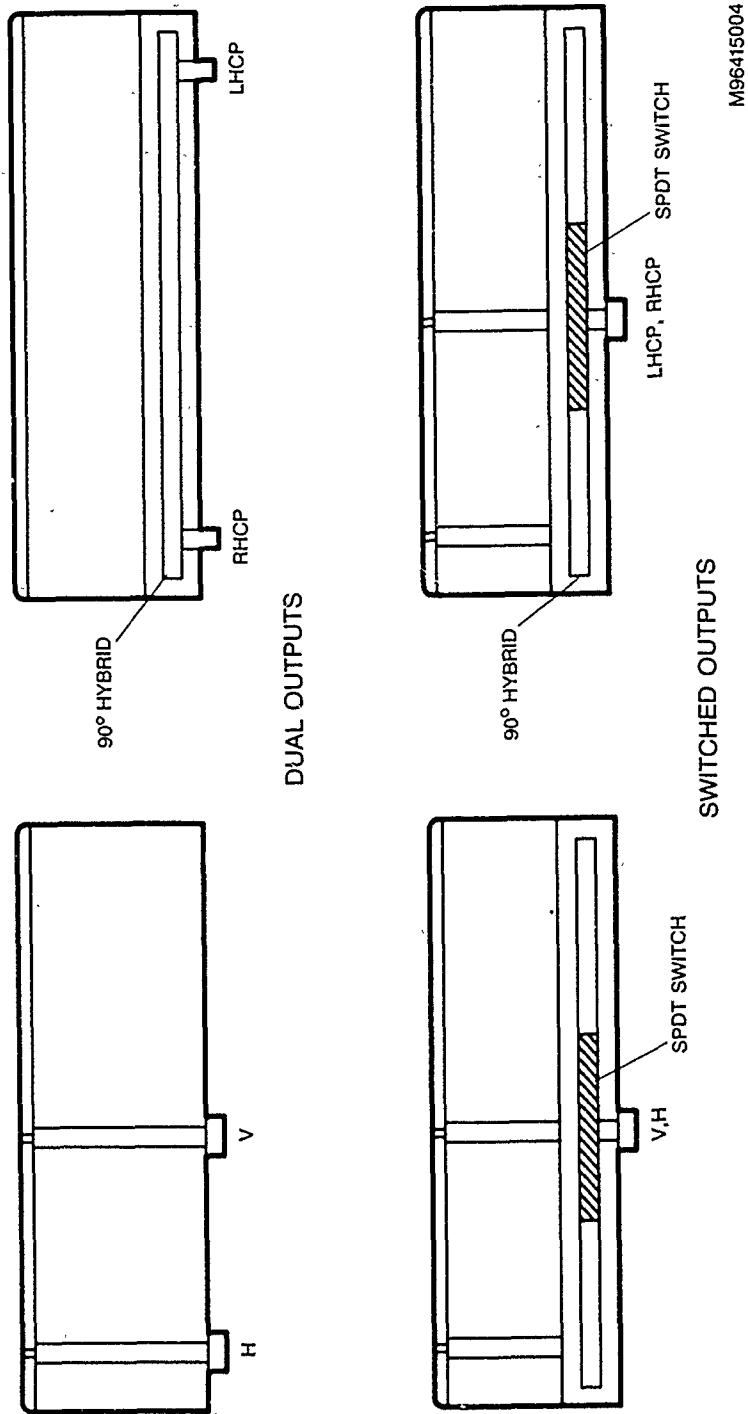


The basic geometry of the InterLog antenna is rotated through 90, 180, and 270 degrees to produce the interleaved aperture

Interleaved log periodic Aperture of the InterLog antenna

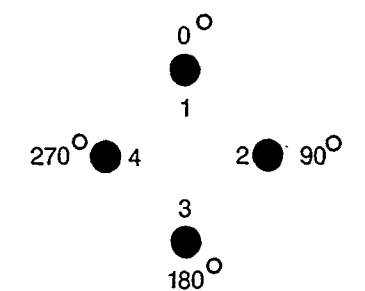
W96415003

Figure 2. InterLog Antenna Geometry

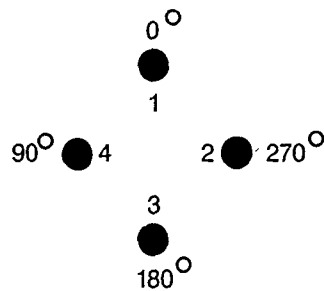


M96415004

Figure 3. InterLog Antenna Polarization Output Options

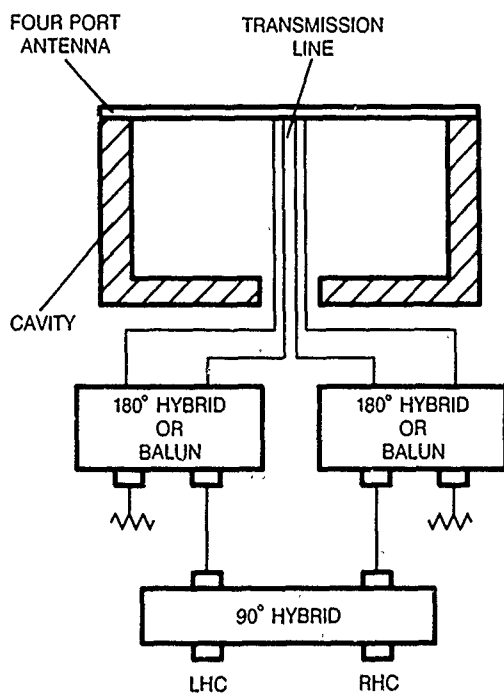


LEFT HAND  
CIRCULAR POLARIZATION

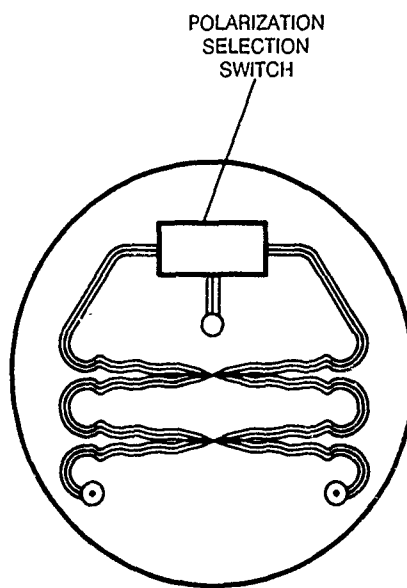


RIGHT HAND  
CIRCULAR POLARIZATION

(a)



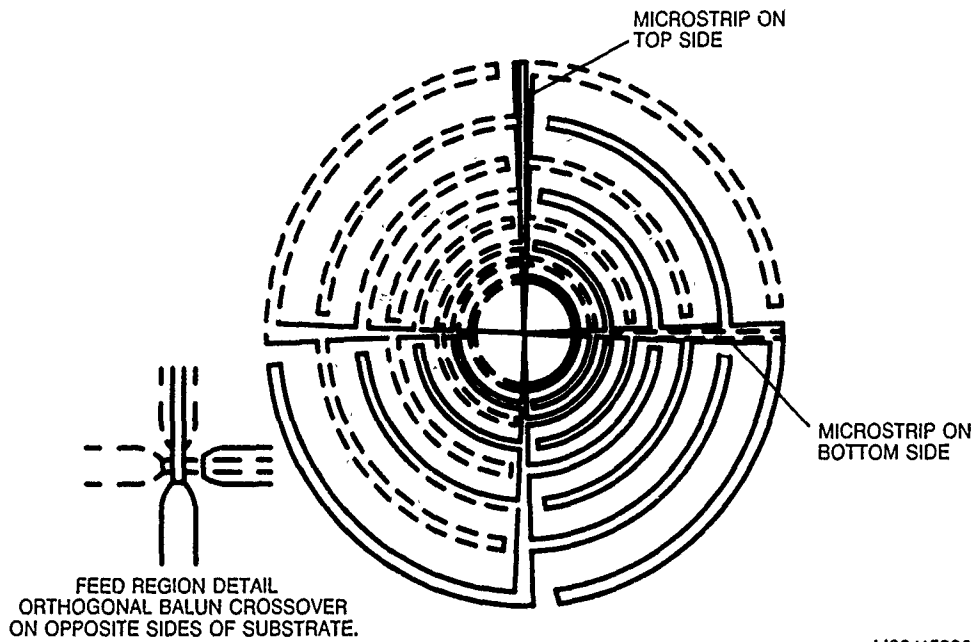
(b)



(c)

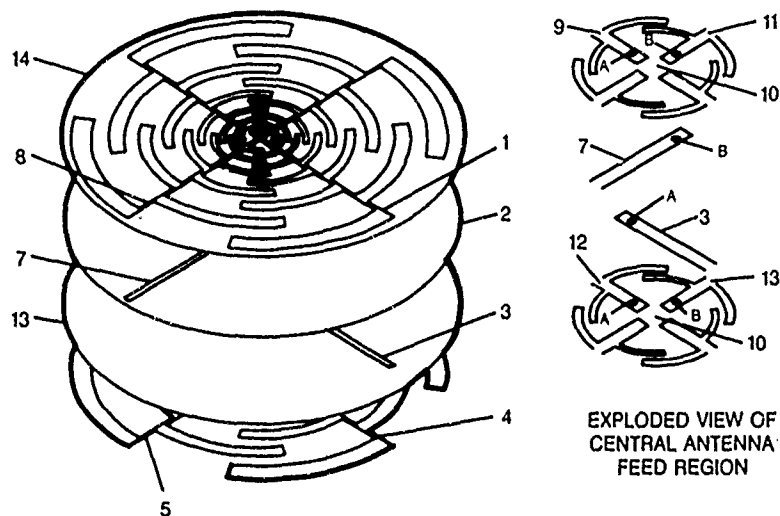
M96415005

Figure 4. Excitation Requirements for Dual Sense Circular Polarization (a), Hardware Implementation (b), and 90 Degree Coupler With Polarization Selection Switch (c)



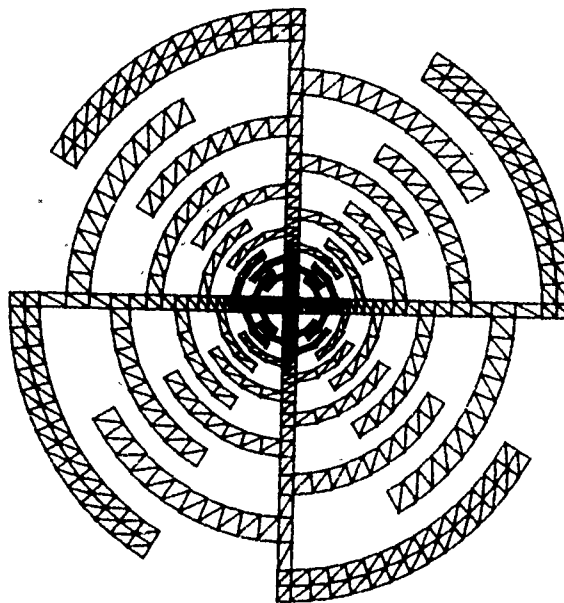
M96415006

Figure 5. Dual polarized Microstrip Fed Antenna.  
Solid Lines Represent Circuit on Top Side of Substrate.  
Dashed Lines Represent Circuit on Bottom Side of Substrate



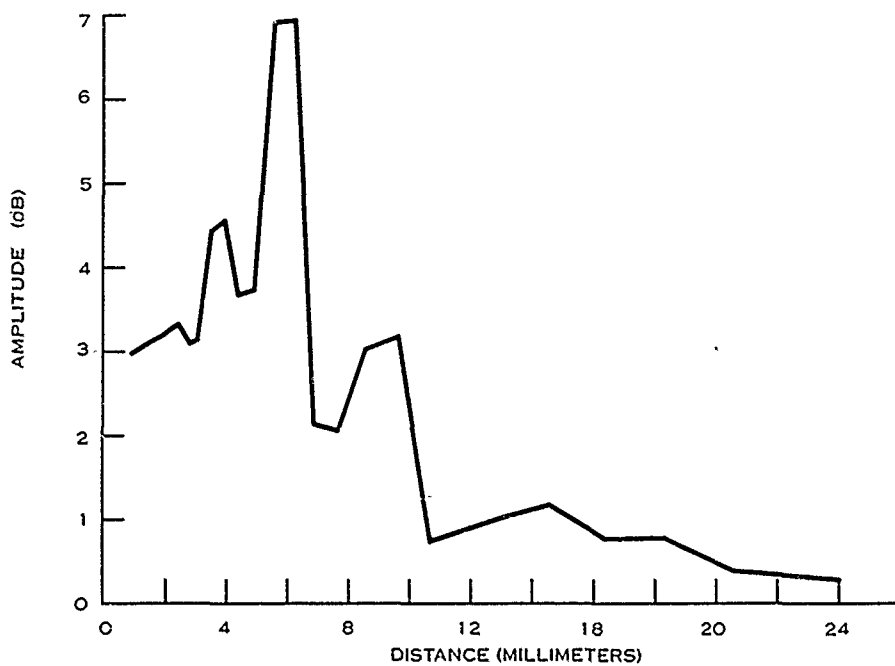
M96415007

Figure 6. Dual Polarized Interleaved Log Periodic Antenna Employing Orthogonal Infinite Baluns in Stripline Form

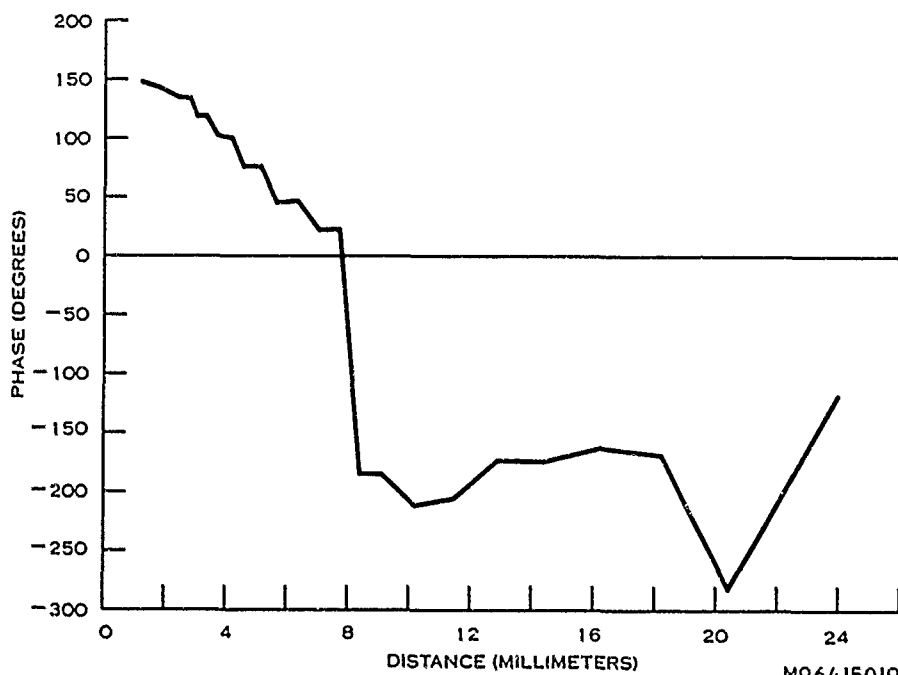


W96415018

Figure 7. InterLog Patch Code (MOM) Geometry

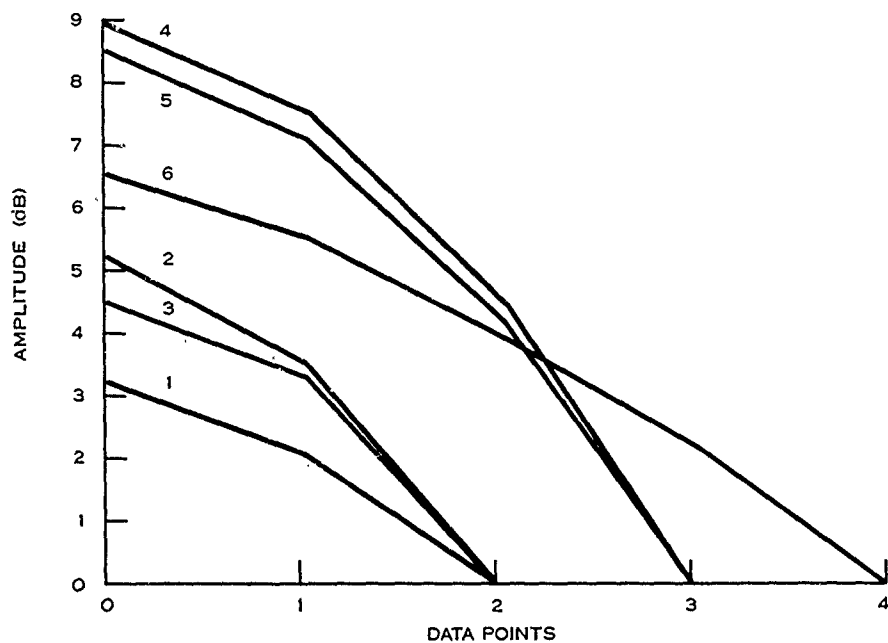


(a) Feedline Current Amplitude vs Distance From Center

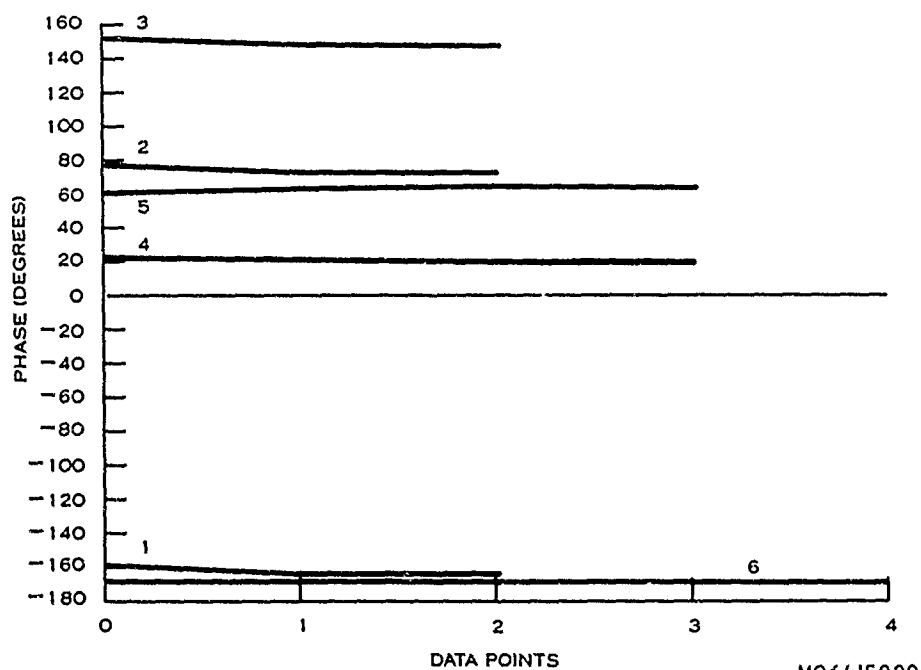


(b) Feedline Current Phase vs Distance From Center

Figure 8. Feedline Current Amplitude and Phase



(a) Curvilinear Dipole Current Amplitude Along Arms



(b) Curvilinear Dipole Current Phase Along Arms

M96415020

Figure 9. Curvilinear Dipole Current Amplitude and Phase



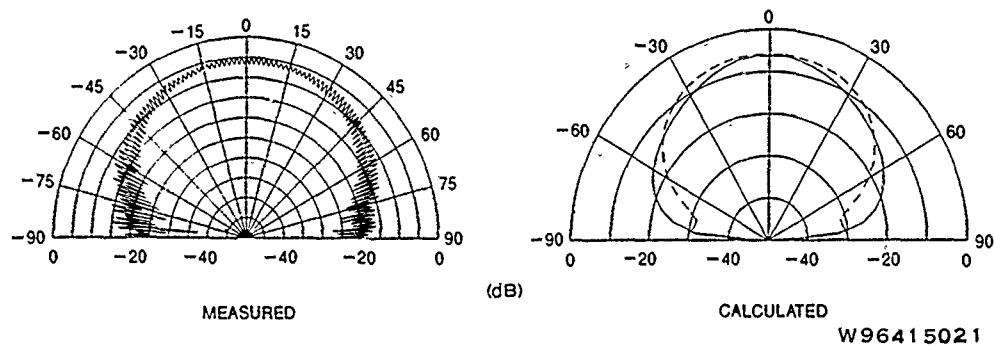
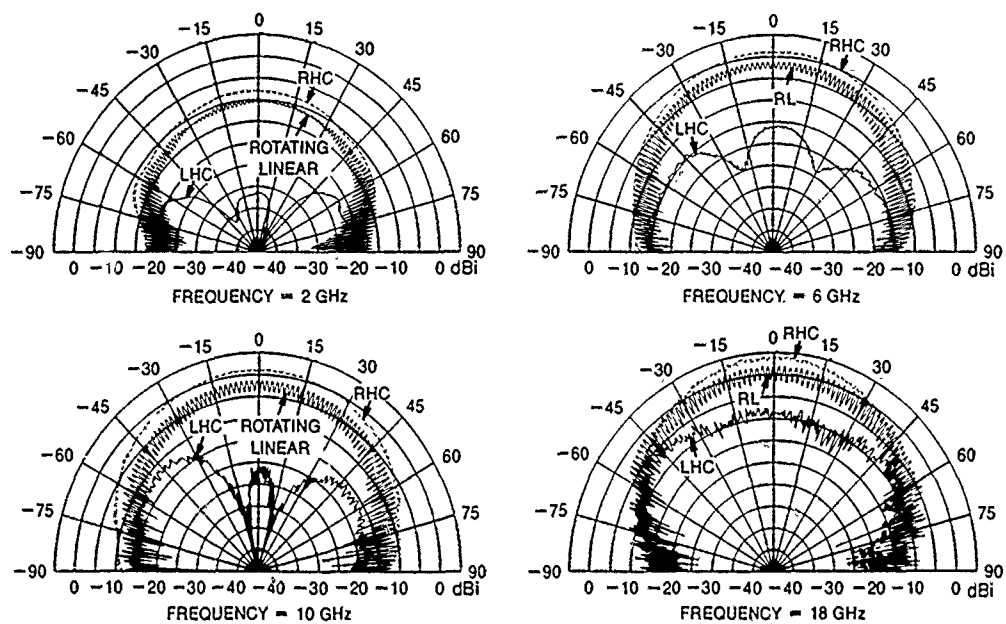
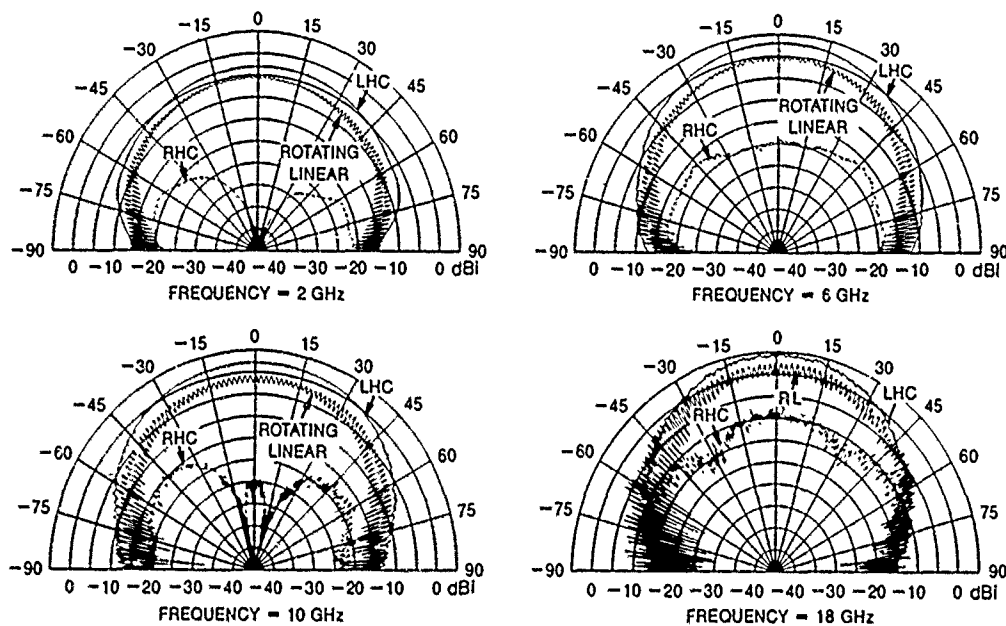


Figure 10. Measured vs Calculated Amplitude Radiation Pattern



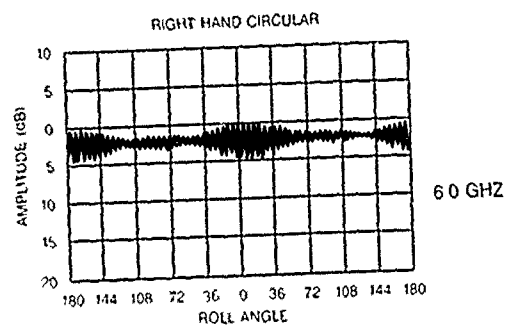
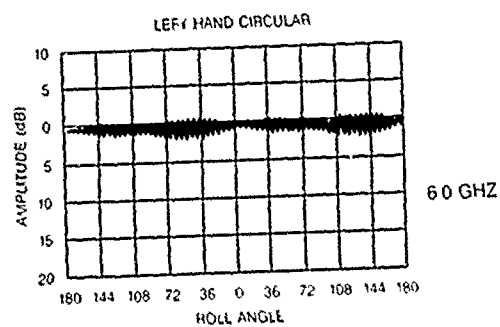
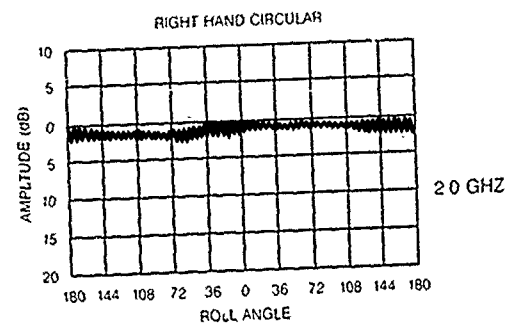
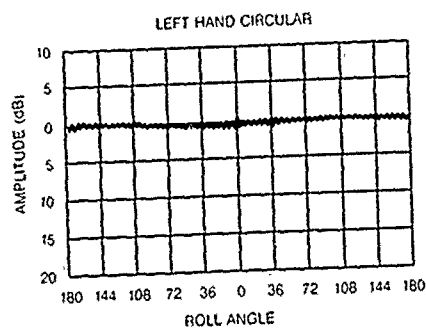
W9651 5009

Figure 11. Right Hand Circular Principal Plane Patterns for InterLog Antenna



W9641 5008

Figure 12. Left Hand Circular Principal Plane Patterns for InterLog Antenna



M96415010

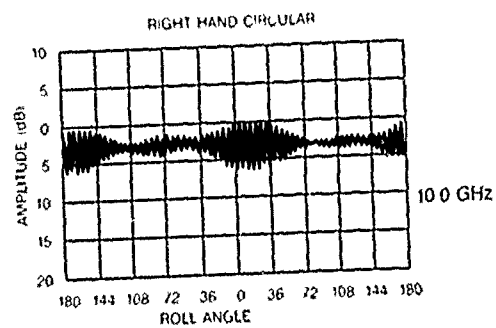
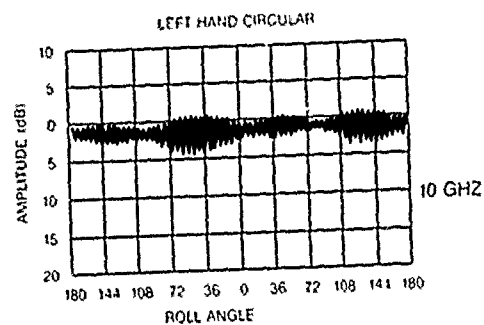


Figure 13(a). Conical Amplitude Patterns at 30 Degrees From Antenna Axis, InterLog Antenna

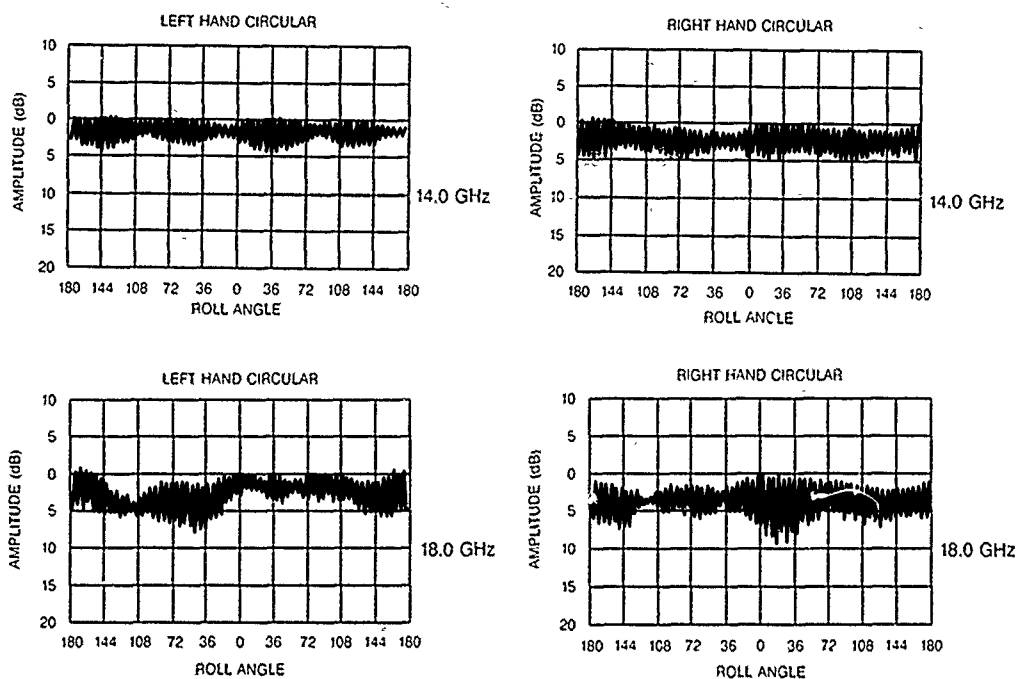
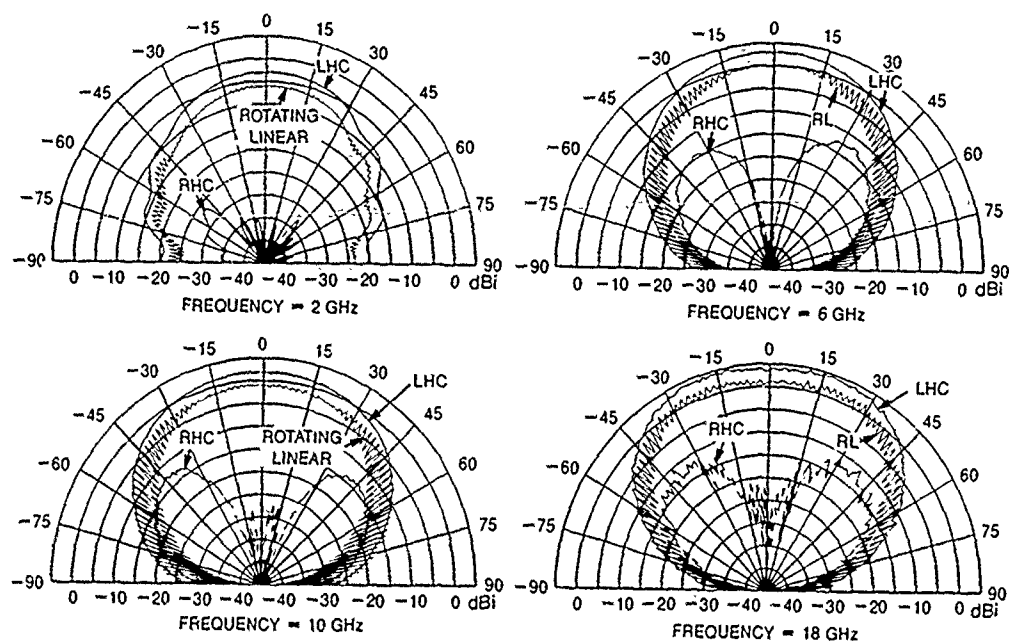


Figure 13(b). Conical Amplitude Patterns at 30 Degrees From Antenna Axis, InterLog Antenna



W96415013

Figure 14. Measured InterLog Antenna Data Using a Simulated (Software) RF Processor

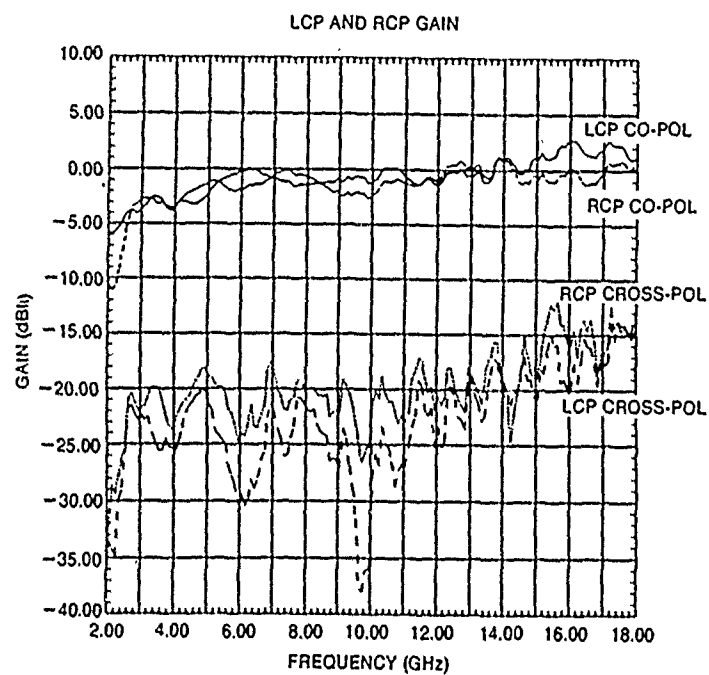
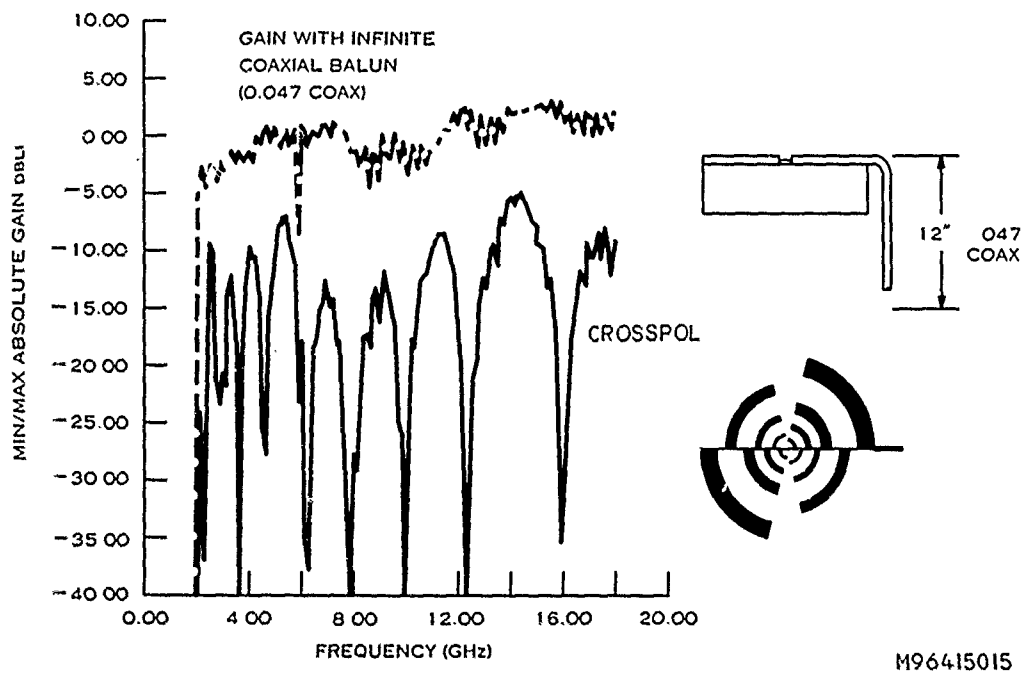


Figure 15. Gain vs. Frequency For LHC And RHC Polarizations



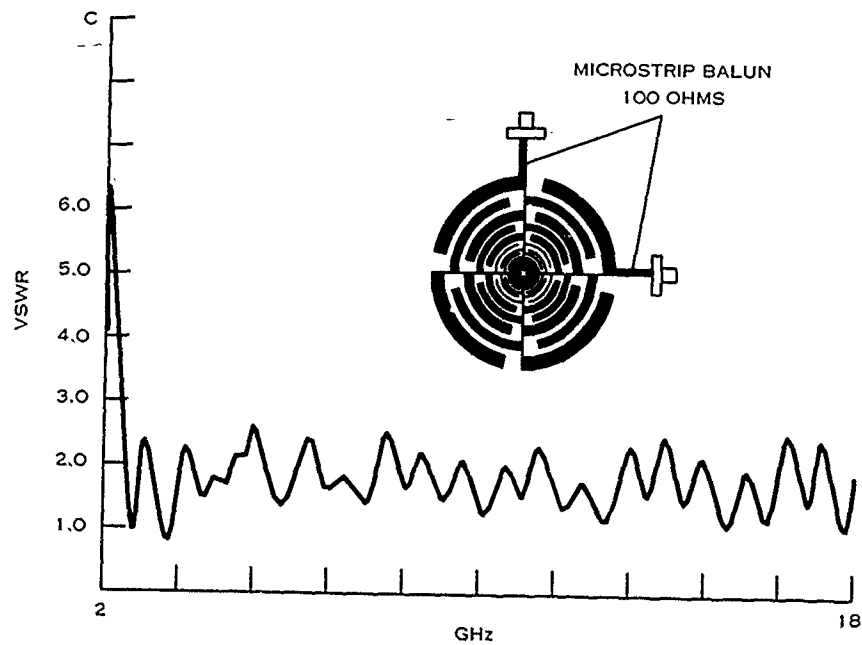
W96415014 (96-416)

Figure 16. Cavity Backed Log Periodic Antenna Fed With Conical Infinite Balun



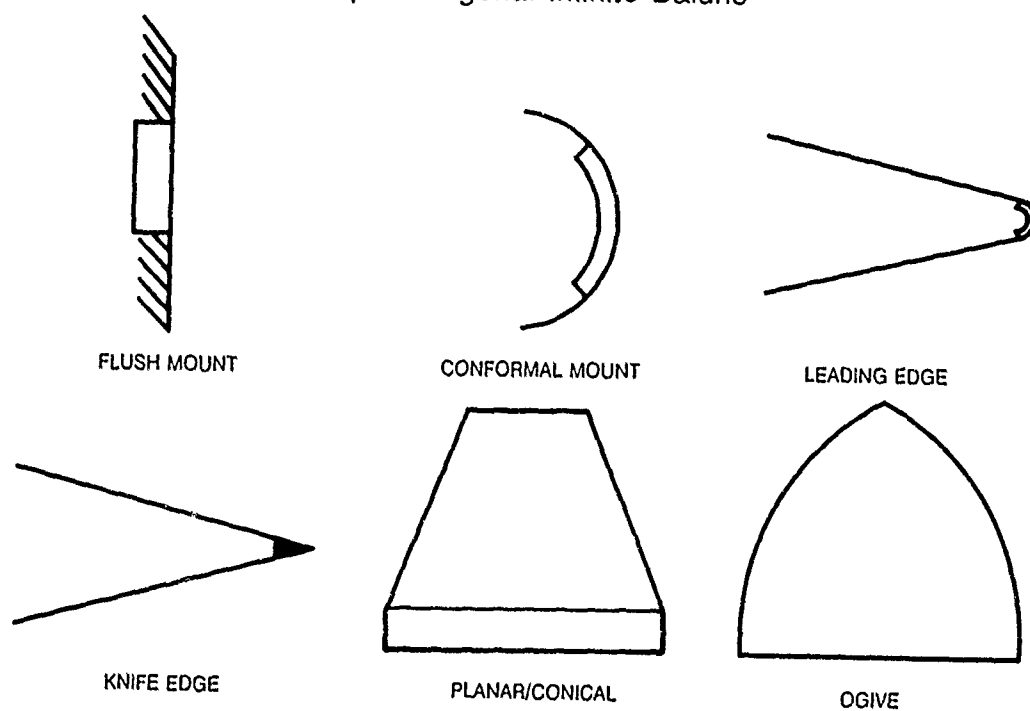
M96415015

Figure 17. MIN/MAX Gain vs Frequency With Infinite Balun



M96415016

Figure 18. VSWR vs Frequency of InterLog Antenna With Microstrip Orthogonal Infinite Baluns



M96415017

Figure 19. Potential Installation Configurations For InterLog Antenna

# A SIMPLE CIRCULARLY POLARIZED PRIMARY ANTENNA FOR DIRECT BROADCAST FROM SATELLITE RECEIVERS

Takashi Nakamura and Kamel Maamria

Gifu University, Japan

## ABSTRACT

In this paper we propose a small and simple printed antenna which easily produces circular polarization and can be used as a primary antenna for reflectors used for the 12 GHz band direct broadcast from satellite (DBS) reception. The design concept idea of this antenna is based on the turnstile type antenna configuration. It is a single fed structure consisting of a pair of crossed dipoles connected with two angular branches, which easily generates circularly polarized waves. This antenna, with a director, placed over an infinite ground plane is analyzed as a primary antenna for illuminating parabolic reflectors used for DBS reception. A design example is realized and measured at 2 GHz, and the validity of the theoretical results is confirmed with the experiments.

## 1. INTRODUCTION

DBS receivers are now gaining popularity in Japan, and are increasingly receiving considerable attention [1]. A wide variety of parabolic reflector antennas are now being used for domestic reception. Since the shape of the reflectors used for these antennas is fixed, the characteristics of the receivers depend primarily on their feeds. The commonly used feeds are horns, as they produce most of the de-



sired specifications. However, horns are expensive to manufacture and are heavy. Recently, microstrip feeds have also come into use. These antennas have the advantage of having low profile structures; however, wide bandwidths are difficult to achieve using these antennas.

In this paper, we propose a small, light weight, inexpensive and simple wire antenna for circular polarization which can also be used as a primary antenna for reflectors used for direct broadcast from satellite reception. The design concept of this antenna is based on the turnstile type antenna configuration. It is a single fed structure consisting of a pair of crossed dipoles connected with angular branches. With this configuration, the functions of the power divider and the phase shifter required in the conventional crossed dipole antenna are achieved and the circular polarization is easily produced. A theoretical approach for the circular polarization condition is given. Based on the fact that the mutual coupling between the two dipoles is minimal, the equivalent circuit of the antenna is determined, and the circular polarization condition is then derived.

This antenna is used in the structure shown in Fig.1, which consists of the circularly polarized radiator with a director, placed over a perfectly conducting ground plane, and studied as a primary antenna for reflectors used for DBS reception. At 12 GHz, this antenna is designed to be manufactured as a printed antenna. The less than 1 dB axial ratio bandwidths realized by different structures of this antenna are given. The variation of the beam shape as a function of the structure of the antenna is also studied. It is shown that this antenna can be used for reflectors of various shapes, since the desired beam width of this feed for a particular reflector is obtained by adjusting the structural parameters of this antenna. A design example

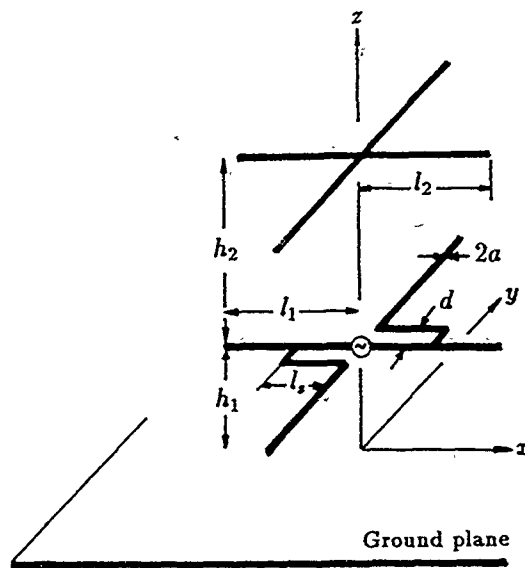


Fig.1. The configuration and structural parameters of the antenna.

is realized and its characteristics are measured at 2 GHz. The computed axial ratio, field pattern and input impedance of the antenna are compared to the measured data. Good agreement between the theoretical predictions and the experiments is found.

## 2. THEORETICAL ANALYSIS

The turnstile antenna [2], which consists of two crossed dipoles with equal lengths and oriented at a right angle, has been used for a long time as an omnidirectional or a circularly polarized antenna because of its simple element configuration and its simplicity in forming an array. However, to generate the circular polarization in the axial direction, the currents in the dipoles must be equal and in phase quadrature. This is generally achieved by using a power divider and a phase shifter. This however results in a complexity in the feeding system. The antenna structure shown

in Fig.2(a) is a simple flat configuration, consisting of a single fed pair of crossed dipoles connected through two angular branches, is designed to produce circularly polarized waves in the axial direction. Following, is a theoretical approach for the analysis of this antenna:

Since the two dipoles are oriented at a right angle, the mutual coupling between the elements is very small. Therefore, the horizontal element consisting of the horizontal dipole with the angular branches, and the vertical element which consists of the vertical dipole, are treated separately. Considering the horizontal element, the sum and difference of the currents flowing in this element can be used to decompose the current into the balanced mode current  $I_b$ , and the unbalanced mode current  $I_u$  [3]. When the terminal voltage is applied so as to excite only one of these modes, the impedance of each mode is obtained. Let  $Z_b$  and  $Z_u$  the impedance of the balanced and unbalanced mode of the horizontal element. On the vertical element, an unbalanced current  $I_d$  is flowing through an input impedance  $Z_d$ . For the unbalanced mode, element 1 is equivalent to a dipole with an equivalent radius which depends on the width of the angular branch. For simplicity, and since the width  $d$  is small, we approximate the radius to be the same. Therefore, since the two crossed dipoles have the same length, the two elements have the same impedance for the unbalanced mode  $Z_d = Z_u$ .

From the foregoing, the equivalent circuit of the antenna shown in Fig.2(a) is given by Fig.2(b), where  $Z_b$  is the input impedance of the short-circuited stub formed by the angular branch, and  $Z_d$  is the input impedance of the dipoles. On the other hand, since the stub does not radiate in the balanced mode, the two dipoles are the only elements contributing to the radiation. Therefore, the radiated electromagnetic

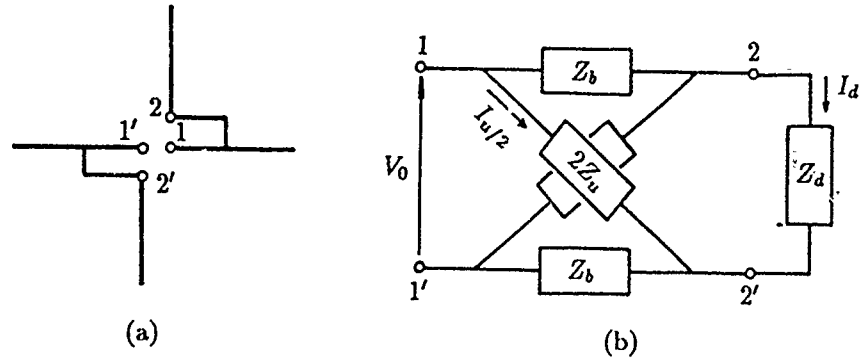


Fig.2. (a) Considered structure. (b) Equivalent circuit.

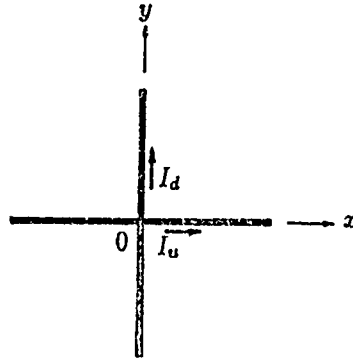


Fig.3. Approximated equivalent crossed dipoles.

field of the present antenna is equivalent to that radiated by the crossed dipoles of Fig.3. The currents  $I_u$  and  $I_d$  can be obtained easily from the equivalent circuit.

If  $E_x$  and  $E_y$  are the x and y component of the electric far field, the condition of generation of the circular polarization in the z axis is:

$$\frac{E_y}{E_x} = \frac{I_d}{I_u} = \frac{2Z_d - Z_b}{Z_d + Z_b} = \pm j, \quad (1)$$

where the upper and lower signs of  $\pm j$  indicate respectively the left and right circular polarization. Using the fact that  $Z_b$  is imaginary, and decomposing the above equation to the real and imaginary parts, we obtain the condition of generation of the circular polarization:

$$R_d = \pm 3X_d \quad (2)$$

$$X_b = \mp 4R_d/3 \quad (3)$$

with  $R_d + jX_d = Z_d$  and  $jX_b = Z_b$ ,

where  $X_b$  depends on the distance of the branch location  $l_s$ , and is given by:

$$\frac{l_s}{\lambda} = \frac{1}{2\pi} \tan^{-1} \left( \frac{X_b}{Z_0} \right), \quad Z_0 = 120 \ln \left( \frac{d}{a} \right) \quad (4)$$

$\lambda$  is the wavelength and  $Z_0$  is the characteristic impedance of the stub.

Eq.(2) is satisfied for many values of the dipole length. The lengths of about one half wavelength used in the conventional crossed dipoles are considered. From the approximation of the input impedance of an about half wavelength antenna [3]:

$$Z_d \simeq 73.13 + j42.55 + j120\pi \frac{2\Delta l}{\lambda} \ln \left( \frac{2l_1}{a} \right), \quad (5)$$

where  $2\Delta l = 2(l_1 - \lambda/4)$  and indicates the deviation from the half wavelength; the existence of a solution satisfying the two signs of eq.(2) around the half wavelength is verified. Hence, if  $l_1 < \lambda/4$ , one obtains  $X_b > 0$  from the structural constraint

$l_s < l_1$ ; and the lower sign of eq.(3) for the right hand circular polarization can easily be satisfied. To produce the left hand circular polarization, the antenna is simply turned over so the positions of the two angular branches are reversed.

It is thus shown, that the circular polarization can always be produced by an appropriate choice of  $Z_b$  and  $Z_d$  to provide the necessary amplitude ratio and phase difference to the currents  $I_u$  and  $I_d$ . This is achieved by adjusting the length of the dipoles  $l_1$  and  $l_s$ .

### 3. DESIGN

The antenna above an infinite ground plane was first considered. The results obtained show that with this configuration the antenna can not be used as a feed for parabolic reflectors designed to receive direct broadcasts from satellite mainly because of its relatively large beamwidth compared to those of the feeds for reflectors used for DBS reception in Japan. A director is then used for narrowing the beamwidth of the antenna and giving new parameters for changing the dimensions of the antenna to obtain the desired specifications for different reflectors.

The designed antenna with its structural parameters is shown in Fig.1. The conductor radius used for the different elements of the antenna is the same and is denoted by  $a$ . The width  $d$  of the folded branch is also fixed, for simplicity, to a value, taking into account the theoretical approximation and the ease of fabrication of the antenna. The two crossed dipoles of the radiator are set to have the same length  $l_1$ . The crossed elements of the director also have the same length  $l_2$ . The distance between the radiator and the ground plane  $h_1$  is fixed and for various values of  $l_2$  and the height  $h_2$  the antenna characteristics are computed. The computation is carried out by adjusting for every configuration the values of  $l_1$  and  $l_s$  to minimize

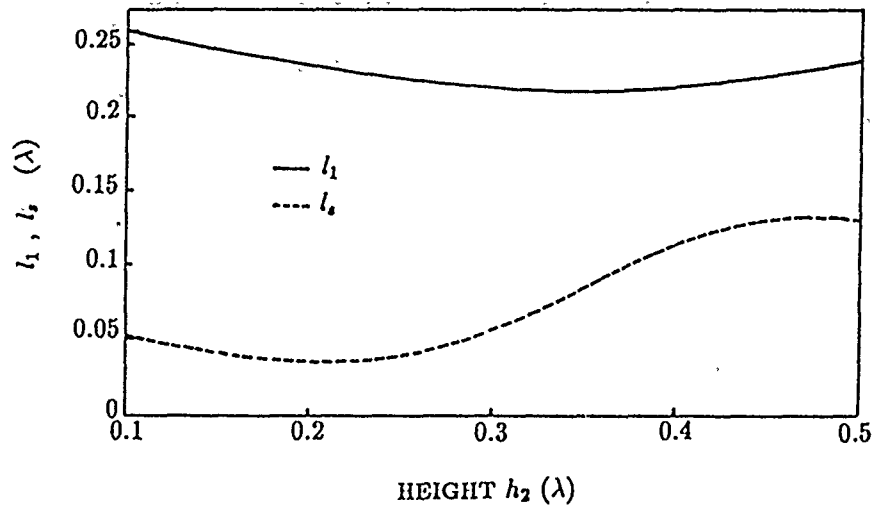


Fig.4. Values of  $l_1$  and  $l_s$  that produce the circular polarization. Variation with  $h_2$  for  $l_2 = 0.22\lambda$ .

the axial ratio on the axial direction. The moment method with the pulse function as an expansion function, and the delta function as a weighting function, has been used for the computation [4].

When the radiator is considered without ground plane or director, the circular polarization is found easily for values of  $l_1$  around  $\lambda/4$ ; and from eqs. (3) and (4), the theoretical value of  $l_s$  is found to be approximately  $0.075\lambda$ . With the ground plane and director,  $l_1$  is still around  $\lambda/4$ , but  $l_s$  varies with the position of the director as shown in Fig.4. This figure illustrates a representative example of the variations of  $l_1$  and  $l_s$  as a function of  $h_2$  for  $l_2 = 0.22\lambda$ . These results are obtained for  $a = 0.006\lambda$ ,  $d = 0.03\lambda$  and  $h_1 = 0.25\lambda$ .

#### 4. RESULTS AND DISCUSSION

To receive the Japan allocated band of 11.7 - 12 GHz, a 2.5% frequency bandwidth antenna is needed. The axial ratio bandwidth for circular polarization of

this antenna is determined for an axial ratio of less than 0.97 dB giving a cross polarization discrimination level of less than  $-25\text{dB}$  as fixed by the 1977 WARC requirements for DBS reception [5].

The variation of the bandwidth as a function of  $l_2$  and  $h_2$  is shown in Fig.5. When the director is placed close to the radiator, narrow bandwidths are found. This is due to the coupling between the radiator, the ground plane, and the director. For higher positions of the director, the bandwidths increase to reach the 2.5% around  $h_2 = 0.4 \lambda$ . The bandwidth continues to increase as  $h_2$  increases, it then starts decreasing for higher values of  $h_2$  to a value of 4% which corresponds to the antenna bandwidth without director. The curves shown in Fig.5 are for values of  $l_2$  that give significant variation of the beamwidth of the antenna around the values that are generally required for reflectors used for DBS reception since we consider beamwidths given by antenna structures achieving the necessary 2.5% bandwidth.

Since the reflector's geometry is fixed, the receiving antenna performance depends primarily on its feed characteristics. The beamwidth of the feed necessary to produce the desired illumination on a particular reflector is generally given as a specification for parabolic reflector feeds. This is expressed by the beamwidth of the feed at a certain decibel level [6].

Fig.6 shows the variation of the beamwidth of this antenna at 10 dB level as a function of  $l_2$  and  $h_2$ . It shows that when  $h_2$  is smaller than  $0.2 \lambda$ , the beamwidths are large due to the high sidelobe levels. For these values of  $h_2$  the sidelobe levels are higher than 10 dB, resulting in high values of the beamwidth at this level. When the position of the director is higher than  $0.4 \lambda$ , the beamwidths become larger. This is due to the decreasing effect of the director when placed away from the radiator.



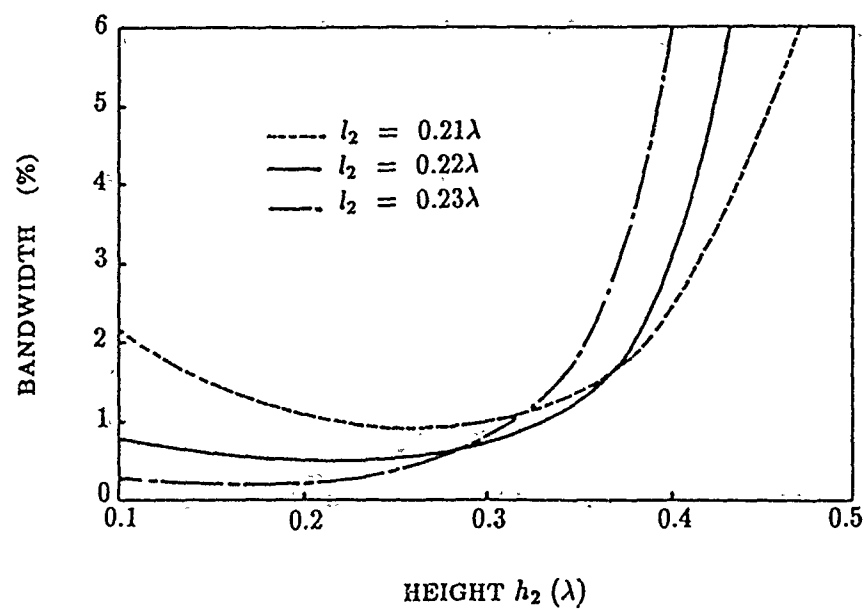


Fig.5. Variation of the less than 1dB axial ratio bandwidth of the antenna as a function of the length and position of the director.

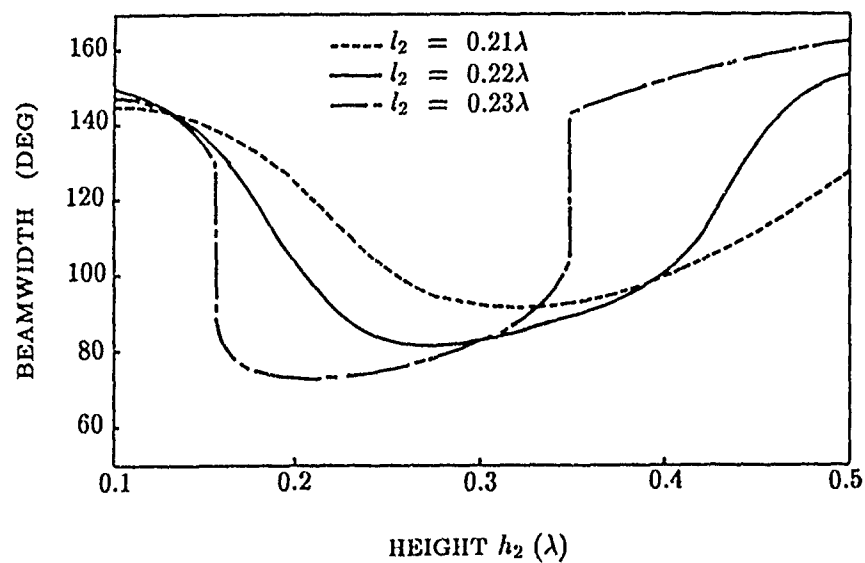


Fig.6. Variation of the -10dB beamwidth of the antenna as a function of the length and position of the director.

Narrower beamwidths at 10 dB level are observed as the length  $l_2$  increases, however it is noticed that when  $l_2$  is longer than  $0.23 \lambda$ , the sidelobe levels become higher and wide beamwidths for high values of  $h_2$  are also observed. When the length  $l_2$  is shorter than  $0.21 \lambda$ , the sidelobe levels are lower; however, the narrowest beamwidths realized using these structures are relatively large. For  $l_2$  and  $h_2$ , ranging between the values mentioned above, narrower beamwidths with relatively low sidelobe levels are found.

From Figs. 5 and 6, we can see that for bandwidths of 2.5% or higher, it is possible to realize beamwidths varying in a range from less than  $90^\circ$  to  $160^\circ$  at 10dB level by varying the structural parameters of the antenna. Therefore, this antenna can be used as a feed for various shapes of reflectors, as we can find the antenna structure which gives the desired beamwidth for a particular reflector.

## 5. DESIGN EXAMPLE

To demonstrate the validity of the computed data, a design example is fabricated and its characteristics are measured at 2 GHz. The structure of the designed antenna is for  $l_2 = 0.22 \lambda$  and  $h_2 = 0.4 \lambda$ . For this structure the bandwidth of the antenna is about 3% and the beamwidth at 10 dB level is approximately  $100^\circ$ . The remaining parameters are:  $l_1 = 0.2218 \lambda$ ,  $l_s = 0.1147 \lambda$ ,  $h_1 = 0.25 \lambda$ ,  $d = 0.03 \lambda$ , and  $a = 0.06 \lambda$ . The center frequency of design is set at  $f_0$  and the axial ratio, the radiation pattern and the input admittance are computed using the moment method already described.

The antenna is then designed and fabricated for the center frequency of 2 GHz. A  $1m \times 1m$  reflector is used. A splitted coaxial balun is used to provide the balanced feed for the antenna. The structural dimensions are set at the theoretical values and

the measurements are carried out to find first the practical dimensions of the antenna that generate the circular polarization on the axial direction. This is accomplished by adjusting  $l_1$  and  $l_2$  to find the minimum axial ratio at the center frequency. The new values of  $l_1$  and  $l_2$  are respectively 3.3 cm and 1.95 cm instead of the theoretical values 3.32 cm and 1.72 cm. We notice that  $l_1$  is almost the same as the theoretical value, however,  $l_2$  has changed. This is due to the fact that in the theoretical calculations, the feed's diameter is neglected. In fact it is found that  $l_2$  has shifted on each side a distance which is approximately equal to the radius of the balun. The radiation pattern and the frequency dependence of the input admittance of the antenna are then measured.

Fig.7 shows the frequency dependence of the axial ratio. The experimental minimum axial ratio is found to be approximately 0.3 dB. The less than 1 dB axial ratio bandwidth is found to be almost the same as the theoretical value of 3%. The figure shows that both results agree well, and also yield excellent circular polarization.

Fig.8 shows the co-polarized radiation pattern of this antenna, it shows a symmetric pattern. The effect of the director on the pattern is observed. On the axial direction, the cross polarization level is around 56 dB below the on axis field. Adding parasitic elements to the configuration can be considered to improve the pattern shape, if spillover problems arise. The measured pattern shows the same  $100^\circ$  beamwidth, at 10 dB level, as does the computed pattern. Considering the variation of the structure of the antenna between the theory and the experiments, it can be seen that the computed and measured data agree well.

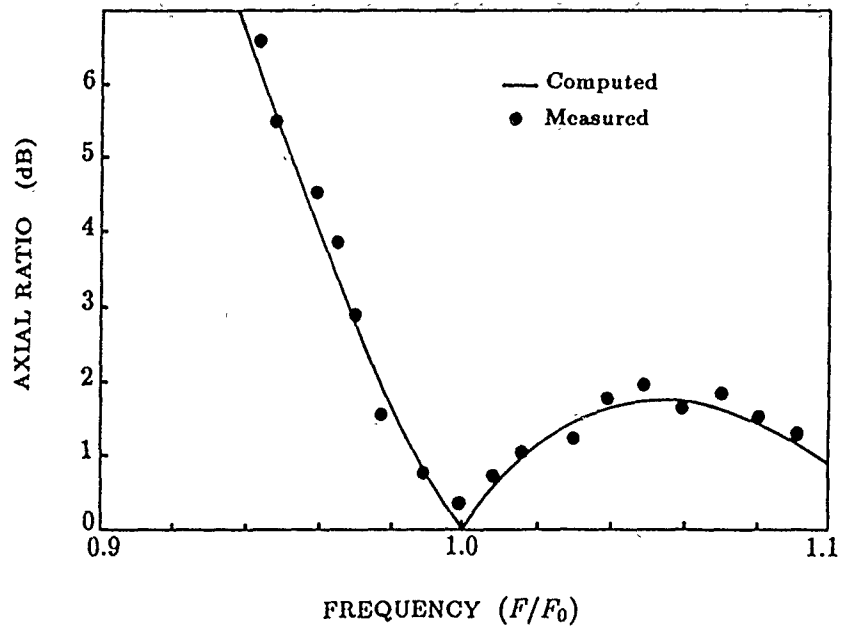


Fig.7. Theoretical and measured frequency dependence of the axial ratio of the antenna for  $l_2 = 0.22\lambda$  and  $h_2 = 0.4\lambda$ .

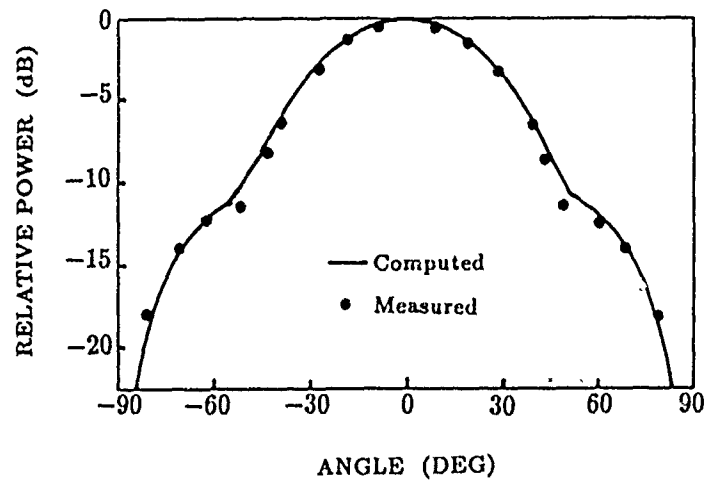


Fig.8. Theoretical and measured radiation pattern of the antenna for  $l_2 = 0.22\lambda$  and  $h_2 = 0.4\lambda$ .

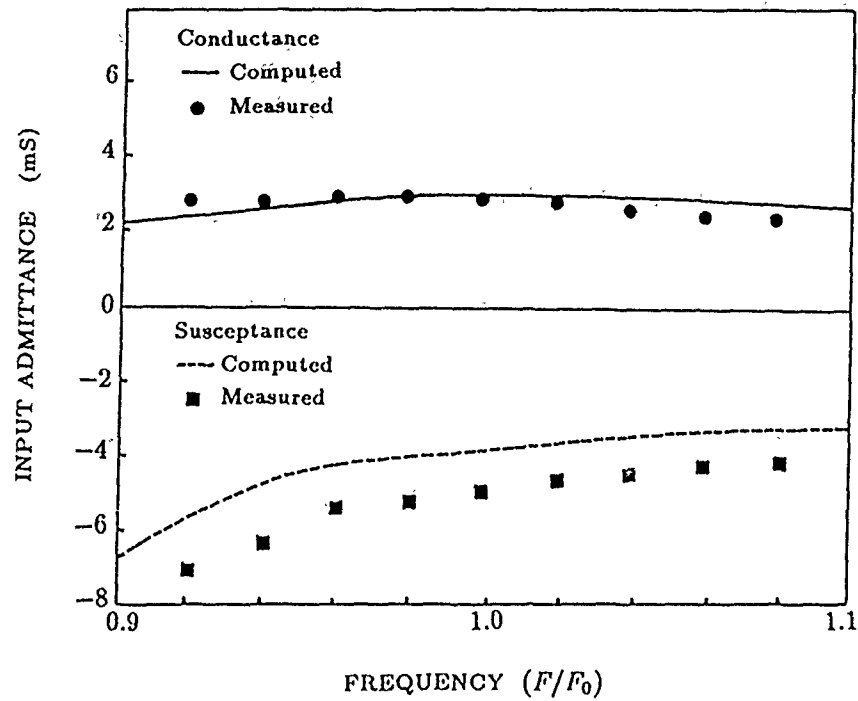


Fig.9. Theoretical and measured frequency dependence of the input admittance of the antenna for  $l_2 = 0.22\lambda$  and  $h_2 = 0.4\lambda$ .

The frequency dependence of the input admittance of the antenna is shown in Fig.9 . Although some difference in the susceptance due to the contribution of the feeding gap is observed, reasonable agreement between the calculated and measured values can be seen.

## 6. CONCLUSION

In this paper, a small wire antenna with a simple configuration was designed to produce circularly polarized waves. A theoretical approach for the analysis of this antenna was given. This antenna, with a director, placed over a ground plane, was analyzed as a primary antenna to illuminate parabolic reflectors used for DBS reception. It was shown that this antenna can be used for various reflectors by

adjusting its structural parameters. The characteristics of a design example were computed, and the antenna was fabricated and measured at 2 GHz. After comparison, good agreement between the theory and the experiments were found. The simple configuration of this antenna, along with its advantages in weight, volume, cost and ease of fabrication, makes it a promising candidate for use as a primary antenna for parabolic reflectors used in DBS reception.

#### REFERENCES

- [1] Y. Ueda, K. Ishibashi and Y. Ichikawa. (1981) Operational broadcasting satellite program in Japan. IAF, Rome, Italy.
- [2] G. H. Brown and J. Epstein. (1945) A pretuned turnstile antenna. *Electronics*, 18, pp.102-107.
- [3] H. Uchida and Y. Mushiake. (1977) Very high frequency antennas. Seisan Gijutsu Center.
- [4] R. F. Harrington. (1967) Matrix methods for field problems. *Proc. I.E.E.E.*, 55, 2, pp. 136-149.
- [5] Final Acts, World Broadcasting-satellite Administrative Radio Conference. (1977) Geneva, ITU (1977).
- [6] R. C. Johnson and H. Jasik. (1984) *Antenna Engineering Handbook*. Second Ed. McGraw-Hill, New York, pp. 17-17, 17-18.

# Closed Loop Performance of an Adaptive Polarization Combiner

Kyle A. Dallabetta      Bernard J. Lamberty  
Kenneth G. Voyce

Boeing Aerospace and Electronics  
High Technology Center  
Seattle, WA 98124-6269

August 4, 1989

## Abstract

Polarization diversity systems receive and process dual, orthogonally polarized signals. A circuit consisting of hybrids and phase shifters can be used to combine the dual signals which can be of arbitrary amplitude and phase. With the proper adjustment of the phase shifters the total power can be sent to one output port while creating a signal null at the other output port. By making the polarization combiner adaptive the circuit now has the ability to respond automatically to changes in the incident polarization. The design incorporates a unique null sensor whereby virtually all the input power is automatically directed to one output port. CW signal levels at the null port are shown to be suppressed more than 40dB for a full range of input phase relationships. Wideband input signals are shown to be suppressed by 15dB and 10dB for a 5% and 20% bandwidth signal respectively.

## 1 Introduction

Polarization diversity is used in many applications including signal enhancement, interference suppression, target signal analysis, and frequency reuse. Diversity systems must be capable of receiving and processing dual, orthogonally polarized components of incident signals which may be of arbitrary relative magnitude and phase. Optimum performance depends on the ability of the system to adjust to rapid changes in polarization without degrading system sensitivity. Several adaptive polarization tracking circuits have been described in the literature[1][2][3]. Limitations of previous approaches include: a requirement for pilot tones in each channel; maintaining the two channels at equal magnitudes using automatic gain control (AGC) circuits, which could result in a sacrifice in sensitivity; or an inability to track rapidly scintillating polarizations, particularly when no signal is present at one input port. This paper describes the design and test results of an adaptive polarization combiner that uses a unique null sensor, feedback, and loop compensation. This system overcomes the limitations of previous approaches.

## 2 The Polarization Combiner

The following sections describe the polarization combiner and the control loops.

### 2.1 Operation

The basic polarization combiner shown in Figure 1 consists of two  $90^\circ$  hybrids and two variable  $360^\circ$  phase shifters[4]. The two input signals ( $V_1$  and  $V_2$ ) can have an arbitrary amplitude and phase relationship. The first phase shifter, PH1, is adjusted so that the two signals at the input ports of hybrid 1 are in phase. These result in two equal amplitude signals at the hybrid's output ports with a phase difference related to the amplitude ratio of the two input signals.

This phase difference is adjusted by the second phase shifter, PH2, so



that the two input signals of hybrid 2 are orthogonal. As a result the total power of the two input signals is present at one output port and no power reaches the other output port. Consequently the total energy of an arbitrarily polarized incident signal can be received by using two orthogonally polarized antennas feeding the polarization combiner of Figure 1. Sufficient information regarding the phase difference and relative amplitudes of the two input signals can be obtained from the phase shifter settings to completely characterize the incident signal polarization.

When adjusted properly, the polarization combiner exhibits predictable vector relationships between the two channels at the input and output ports of the hybrids. The circuit described in this paper takes advantage of the relationship between the signals at the output ports of hybrid 2 and, by adjusting the two phase shifters accordingly, is able to maintain the desired amplitude and phase relationships.

To better understand its operation, assume that the polarization combiner has been adjusted for optimum reception of a particular type of polarization (this assumption is used as an aid in understanding the circuit operation and is not a requirement in actual operation). Phase shifters, PH1 and PH2, have been adjusted so that the signals at the input ports of hybrid 2 are orthogonal with equal amplitudes resulting in a signal null at one output port. Then, if the incident polarization were to change, the input amplitude ratio and/or phase difference would also change. A change in the amplitude ratio at the input ports of hybrid 1 will cause a phase change at the input ports of hybrid 2. A change in the phase difference between the signals at the input ports of hybrid 1 will cause the amplitude ratio at the input ports of hybrid 2 to change. Both of these altered conditions will result in a degradation in null depth. The phase change at the input ports of hybrid 2 can be controlled by adjusting PH2. The amplitudes of the signals at the input ports of hybrid 2 can be equalized by eliminating the phase difference at the input ports of hybrid 1. This is accomplished by adjusting PH1.

Depth of the null at the output port of hybrid 2 is determined by the amplitude ratio and relative phase difference of the two signals at the input of hybrid 2. If these input signals are equal and orthogonal, they cancel at the null port (assuming an ideal hybrid). If they are not orthogonal or do not have equal amplitudes then they do not exactly cancel at the null port which results in a signal there. The adaptive polarization combiner described provides loops which detect a change in the input polarization by detecting

a signal at the output null port and adjust PH1 and PH2 to maintain equal amplitude, orthogonal signals at the input ports of hybrid 2 regardless of the incident signal polarization.

## 2.2 The Null Port Signal

When the input signals of hybrid 2 are equal and orthogonal, there will be no signal at the null output port (assuming an ideal hybrid). As the input phase and amplitude change, a signal at the null port results. This signal has a particular amplitude and phase which depends on the input conditions of hybrid 2. This section examines how a departure from orthogonality or a mismatch in amplitudes at the hybrid input is reflected in the output signal at the null port.

Consider a  $90^\circ$  hybrid with equal amplitude, orthogonal input signals as shown in Figure 2(a). The equal amplitude, orthogonal condition at the input ports results in a summation of the signal power at one output port and a null at the other output port. This is the situation for hybrid 2 in the combiner shown in Figure 1.

The vectors shown in Figure 2(b) illustrate the output signals that result when the input signals are of equal amplitude but are non-orthogonal. This condition affects both amplitude and phase of each output signal. The resulting output vectors are either in phase or  $180^\circ$  out of phase depending on whether the input phase difference,  $\alpha$ , is less than or greater than  $90^\circ$ .

The vectors shown in Figure 2(c) illustrate the output signals that result when the input signals are of unequal amplitude and orthogonal. The output ports still exhibit the sum and difference characteristics but there will be a finite signal at the null port. Its amplitude is related to the difference in amplitudes at the input ports. The phase difference at the output ports is either  $+90^\circ$  or  $-90^\circ$  depending on which input signal has the greater amplitude.

Therefore if the signals at the input ports of hybrid 2 in Figure 1 are not orthogonal with equal amplitude, there will be a signal present at the null port. The component of this signal that is orthogonal to the sum port signal is related to the amplitude ratio at the input ports of hybrid 2 which is in turn related to the relative phase difference at the input ports of the combiner. The component of the null port signal that is in phase with the

sum port signal is related to the phase difference between the signals at the input ports of hybrid 2 which is in turn related to the amplitude ratio at the combiner input ports. The phase and amplitude of the output signals, as a function of the input amplitude ratio and the relative phase difference, contain the information required to implement the adaptive control loops.

### 2.3 The Null Detector

As indicated in the previous section the signal at the null port of the polarization combiner contains information about a change in the incident polarization. By detecting the amplitudes of the vector components of the null port signal the change in the input polarization can be determined. A double balanced mixer operating as a synchronous detector is ideally suited for this function, because the dc level at the IF (intermediate frequency) port of a detector is related to the amplitude of that component of the RF (radio frequency) signal which is in-phase with the signal at the LO (local oscillator) port. The dc component at the IF port attains its maximum positive value when the RF and LO signals are in phase and attains its maximum negative value when the input signals are  $180^\circ$  out of phase. In addition, the detector is insensitive to that component of the RF signal which is in quadrature with the signal at the LO port.

The circuit shown in Figure 3 is the polarization combiner with an adaptive loop implemented to adjust PH2. The synchronous detector senses changes in the null port signal due to variations in the relative phase between the input signals of hybrid 2 and feeds back an error signal to control the phase shifter PH2.

A departure from orthogonality at the input ports of hybrid 2 will produce a signal at the null output port which results in an error signal at the IF port of the mixer. This resulting error signal at the IF port is filtered and integrated to produce a control voltage which adjusts PH2. The loop will continue to adjust PH2 until the signals at the input ports of hybrid 2 are again orthogonal.

The circuit shown in Figure 3 does not respond to amplitude changes at the input ports of hybrid 2 since the resultant signal at the null port is orthogonal to the sum port signal. A control signal derived from these

amplitude differences is needed to adjust PH1. This control signal is derived by first shifting the sum port signal by  $90^\circ$  and then applying it to the LO port as shown in Figure 4. This circuit senses changes in the null port signal which are due to amplitude mismatches at the input of hybrid 2 and feeds back a control signal related to the error signal at the IF port which is used to adjust the phase shifter PH1.

## 2.4 The Adaptive Polarization Combiner

The circuit shown in Figure 5 is the polarization combiner with adaptive loops implemented to adjust PH1 and PH2.

Hybrid 3 provides orthogonal signals for the LO ports of the two mixers. The signals driving the RF ports of the mixers are obtained by splitting the null port signal into two paths. The component of the null port signal generated by amplitude changes at the input ports of the polarization combiner is detected in mixer 1. The component of the null port signal due to variations in the relative phase between the signals at the input ports of the polarization combiner is detected in mixer 2.

# 3 Implementation and Results

## 3.1 The Circuit

Figure 6 shows the complete adaptive polarization combiner.

To maximize bandwidth, phase delays in the signal paths AB and DE as well as the paths AC and DF must be equalized. To achieve the bulk of this equalization, the circuit in Figure 8 uses four voltage controlled phase shifters PH1A, PH1B, PH2A, and PH2B, instead of two.

The signals at the output ports of hybrid 2 are the desired sum and difference signals. The signal at the null port of hybrid 2 is amplified to improve the sensitivity of the null detector circuit. The error signals at the

IF ports of the two mixers are sent to the integrator networks to obtain control voltages for the phase shifters.

Comparators  $U_1, U_2, U_3$ , and  $U_4$  are used as limit sensors. To explain, first suppose that the incident polarization causes each phase shifter control voltage to be at the midpoint of the output range of the corresponding integrators. Now suppose that the incident polarization changes in a manner that causes the control voltages to increase. Eventually the phase shifter control voltages reach the output limit of the integrators. A further change in the incident polarization would not be compensated by an adjustment in the phase shifters and the polarization combiner can no longer track the incident signal polarization. A similar situation arises as the change in the incident signal polarization drives the control voltage to its minimum limit. Comparators,  $U_1, U_2, U_3$ , and  $U_4$ , sense when the output of an operational amplifier,  $U_5, U_6, U_7$ , or  $U_8$ , is approaching the limits (maximum or minimum) and cause the control voltage to change by an amount which corresponds to  $360^\circ$  change in the two phase shifters. As a result the polarization combiner continues to track the changing input signal polarization and the control voltages are reset at a value which is not near the maximum (or minimum) limit.

Since the control voltages normally ramp through their adjustment range until an input signal is present, the limit sensing circuits could cause a problem if there is a signal at only one input port. Recall that when operating with two input signals present, the control loops drive the null signal level down to where an error cannot be detected. The phase shifters adjust the hybrid input signals to the proper phase relationship in order to maintain the null depth. As component imperfections introduce phase and amplitude errors, the loops will automatically control the phase shifters to maintain the null. The component errors manifest themselves as small errors in the phase shifter control voltages, but it is possible to calibrate out these errors (if the circuit is being used to measure polarization, for example). However, if there is no signal at one input port, amplitude imbalances in the hybrid will prevent the equal amplitude condition at the output of hybrid 1 from occurring. Consequently, the control loop will continually adjust shifters PH1A and PH1B. As a result the control loop will produce a phase modulated output signal. This could be a problem in applications where use of the sum channel is required. Solutions to this problem are:

- Detect the input signal levels and disable the phase shifter control voltages for PH1A and PH1B if there is no signal present on one of the channels.
- Detect the presence of input signals by thresholding the signal at the null port and enabling the sweep circuitry only when a specific level of error signal is present there. For example, the presence of an input signal at A or D could be sensed by thresholding the error signal at the IF output of mixer 2.

The circuit shown in Figure 7 is the adaptive polarization combiner of Figure 6 with the second suggested integrator sweep disable circuit added. The detected output signal at the IF port of mixer 2 is compared with a predetermined threshold level. If the null signal increases to a level which causes the detected IF output to exceed the threshold level then the integrator sweep circuit will be enabled. As the null signal is reduced and the detected IF level falls below the threshold, the integrator sweep will be disabled.

The threshold is set above the detected IF level that results when only one input signal is present thus preventing the phase modulation mentioned above. However, adding the disable circuitry makes it possible for changing polarizations to degrade the null to a point where the threshold is reached.

Note that there is no need to disable the control circuits for PH2A and PH2B.

### 3.2 Results

The circuit shown in Figure 6 has been implemented and results have been measured at 350MHz. The curves in Figure 8 show how the depth of the null varies as a function of the input phase difference. The input CW signals are locked in frequency while the input phase difference is varied over a full  $2\pi$  range in a controlled fashion. The input amplitude ratio is maintained constant while the signal level is adjusted in 5dB steps to generate the family of curves. The curves in Figure 8 indicate that the depth of the null remains relatively constant over the full  $2\pi$  phase difference range. The depth of the null is degraded as the input signal level is decreased. This occurs because the detected null signal can be suppressed only to a level which is limited

by offset voltages and currents in the synchronous detector and operational amplifiers. The absolute null signal level remains constant as the available power and sum level decrease. The discontinuities in the curves of Figure 8 are caused by the limit sensing circuit. As the input phase difference changes, the integrators approach the maximum level and the limit sensing circuit toggles. During the time that the comparators toggle and the loop readjusts, the depth of the null degrades. This is manifested as a spike in the null depth vs. phase curve of Figure 8. When operated as a polarization combiner or polarization tracker the spike is transitory while the adaptive loop readjusts. The null depth will therefore regain its steady state value and the spike shown in the curves can generally be ignored.

The curves in Figure 9 show the null depth vs. phase characteristics for unequal input amplitudes. The input amplitude at port A is maintained at -10dBm while the amplitude at port D is varied. Recall that the null port output signal level can only be suppressed to some fixed minimum value. Therefore, the separation between the sum port and null port power levels (null depth) is directly influenced by the variable input signal level at port D. As that signal level decreases, the null depth becomes more dominated by the input power level at port A. Eventually, port D signal level can be decreased to a level where it has no significant influence on the sum port power level and so does not affect the null depth. Then the loop acts as if there is only one input signal present. This is shown in curve (d) of Figure 9. The input power level at port D is set near the minimum level that the polarization combiner can detect as an input signal. As the input phase difference sweeps, the null depth for curve (d) remains relatively constant. Due to amplitude ripple the input level briefly drops below the minimum detectable level and the null is degraded. This null degradation would be eliminated by implementing the integrator sweep disable circuit shown in Figure 7.

The performance of the polarization combiner when a wideband signal is present at the input ports was also investigated. The experiment is performed over a 5% and 20% bandwidth centered at 325MHz. The test was performed for four different phase relationships at the input and the resulting curves are shown in Figure 10(a) and (b). As the curves indicate, the circuit is able to maintain a 15db null over a 5% bandwidth and a 10dB null over a 20% bandwidth. This is true for the four input phase relationships shown.

The ability to respond to rapidly scintillating incident polarizations is determined by the RC time constant of the integrator. A trade off exists

between the circuits ability to quickly lock on the new polarization and the accuracy to which the polarization type can be determined. No effort was made to optimize the integrator time constant for this experiment.

### 3.3 Summary

The adaptive polarization combiner discussed in this paper is a circuit with the following novel features incorporated in the design:

- A unique combination of components which provides adaptive polarization combining with maximum S/N.
- A null sensor which provides inputs to two separate feedback loops.
- Limit sensing circuits which switch the phase shifters  $360^\circ$  when a limit is approached, thus allowing the loops to track conditions which require phase adjustment in excess of the phase shifter range.
- A loop which senses the detected error level and disables the ramping output of the integrators that would otherwise result when there is a signal present at only one input port.

With the above features the result is a polarization combiner which has a capability of responding to any type of incident polarization, regardless of the previous incident signal or prior state of the combiner. For narrowband applications the null depth can be maintained to greater than 20dB for all practical input phase and amplitude relationships. When components are selected to have a flat phase vs. frequency response and minimal phase and amplitude errors, the null depth can be maintained over an appreciable bandwidth.

### References

- [1] James C. Fletcher, John E. Olsen, William F. Williams, "System for Interference Signal Nulling by Polarization Adjustment", U.S. Patent No. 3,883,872, May 13, 1975.



- [2] Shoji Soma, Ikuro Sato, "System for Comensating Cross-Polarized Waves to Attenuate Crosstalk", U.S. Patent No. 4,090,137, May 16, 1978.
- [3] Benedict P. Viglietta, Clinton and Manuel Ares, "Automatic Polarization Tracker", U.S. Patent No. 3,310,805, May 21, 1967.
- [4] Benard J. Lamberty and Robert Freidman, "Interference Suppression Using an Adaptive Polarization combiner.", Proceedings of 1987 Antenna Applications Symposium Allerton Park, Monticello, Ill., 23-25 September, 1987.

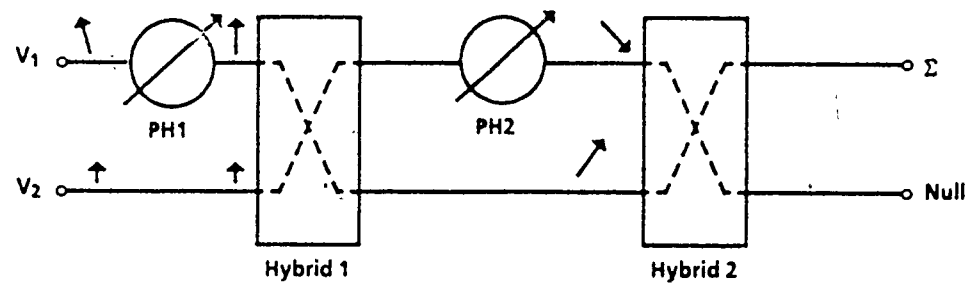


Figure 1. Polarization Combiner

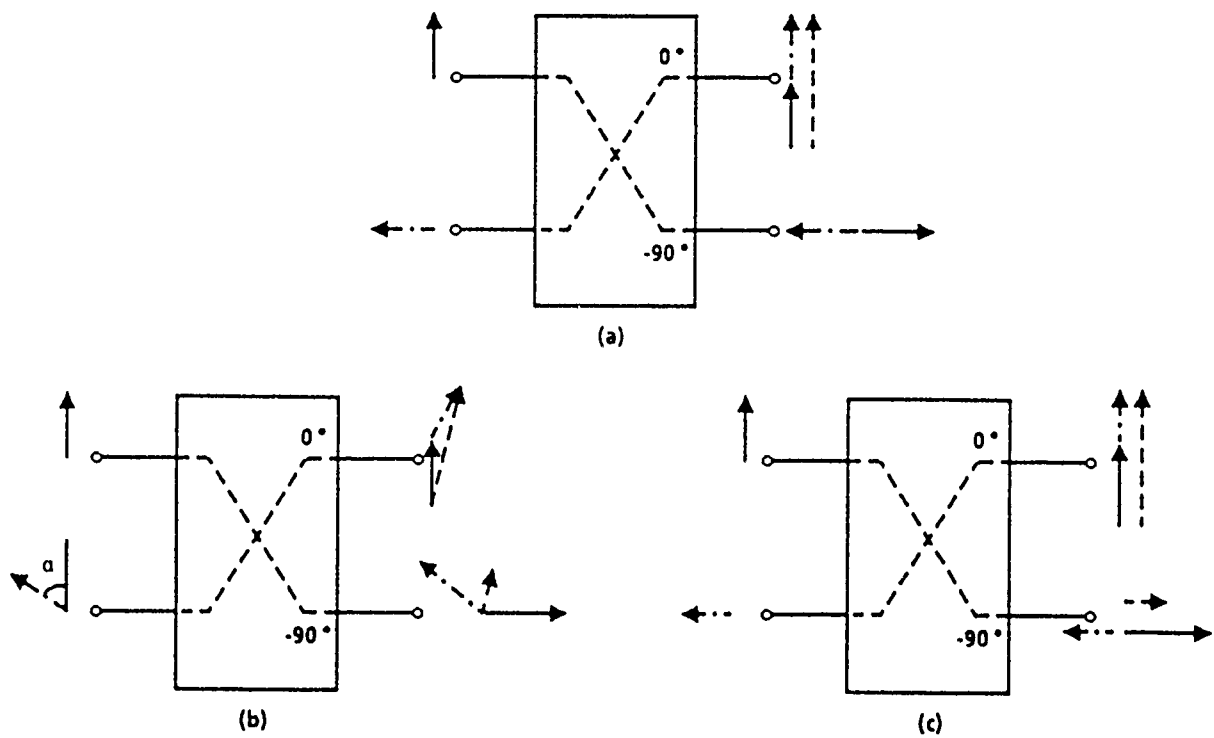


Figure 2. 90° Hybrid Vector Diagrams

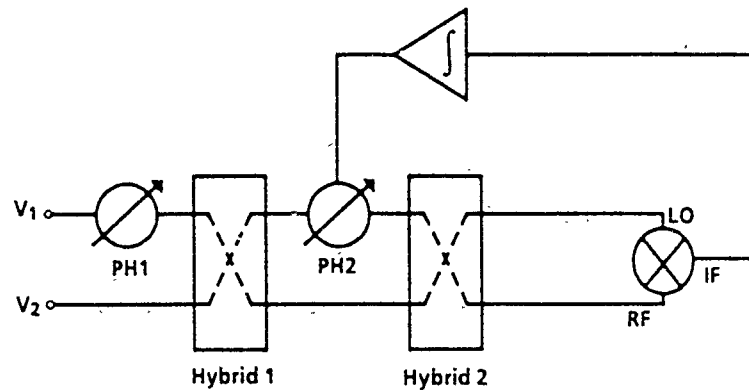


Figure 3. Polarization Combiner With PH 2 Control Loop

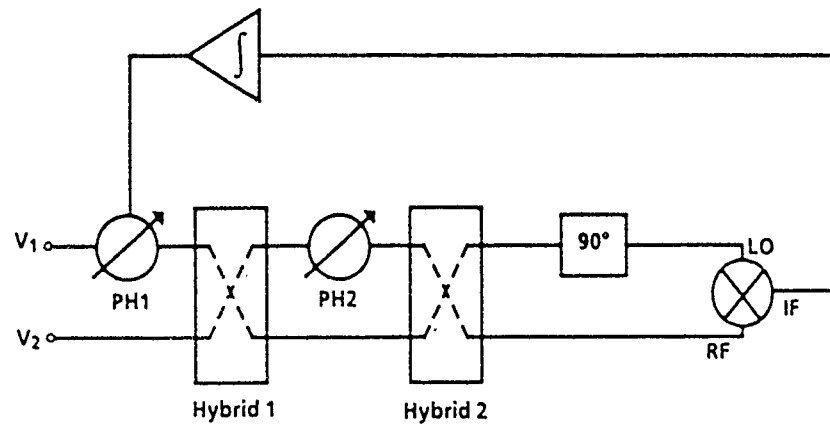


Figure 4. Polarization Combiner With PH1 Control Loop

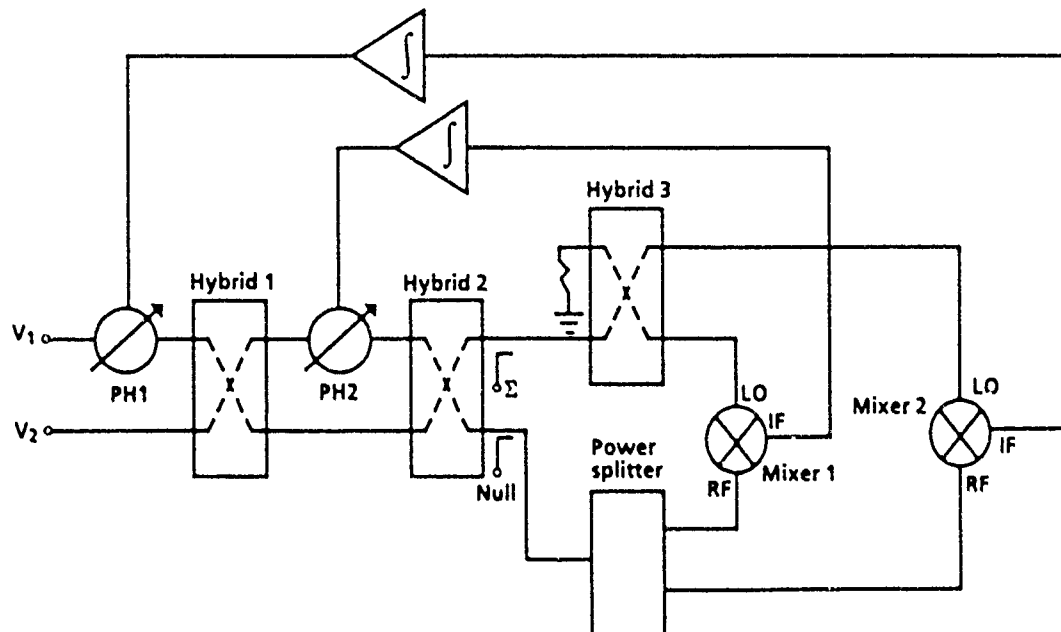


Figure 5. Adaptive Polarization Combiner

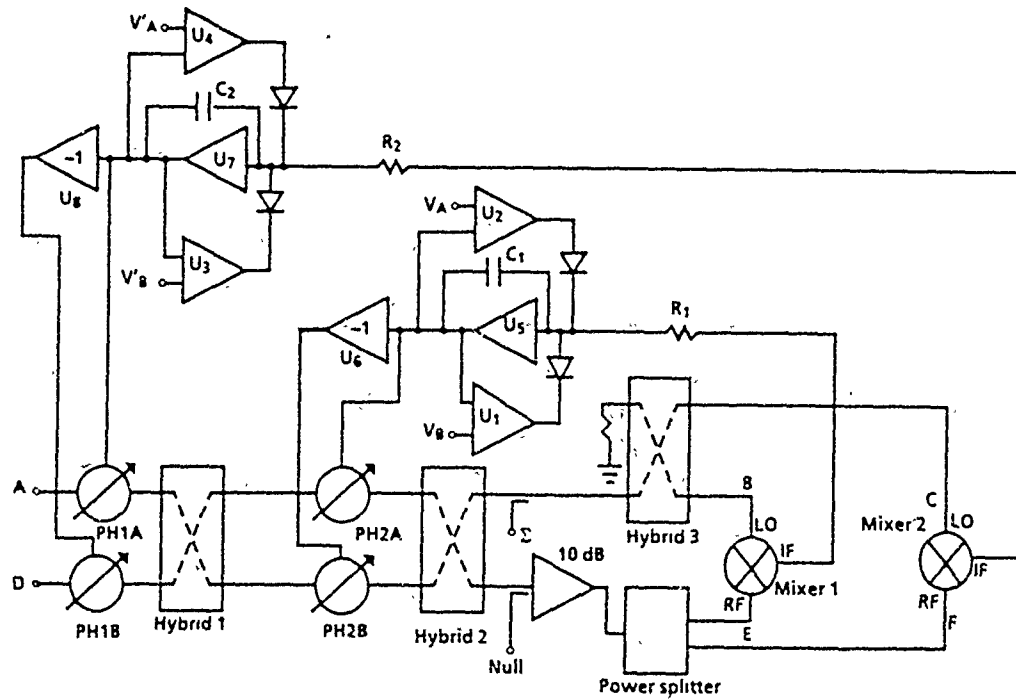


Figure 6. Preferred Embodiment of Adaptive Polarization Combiner

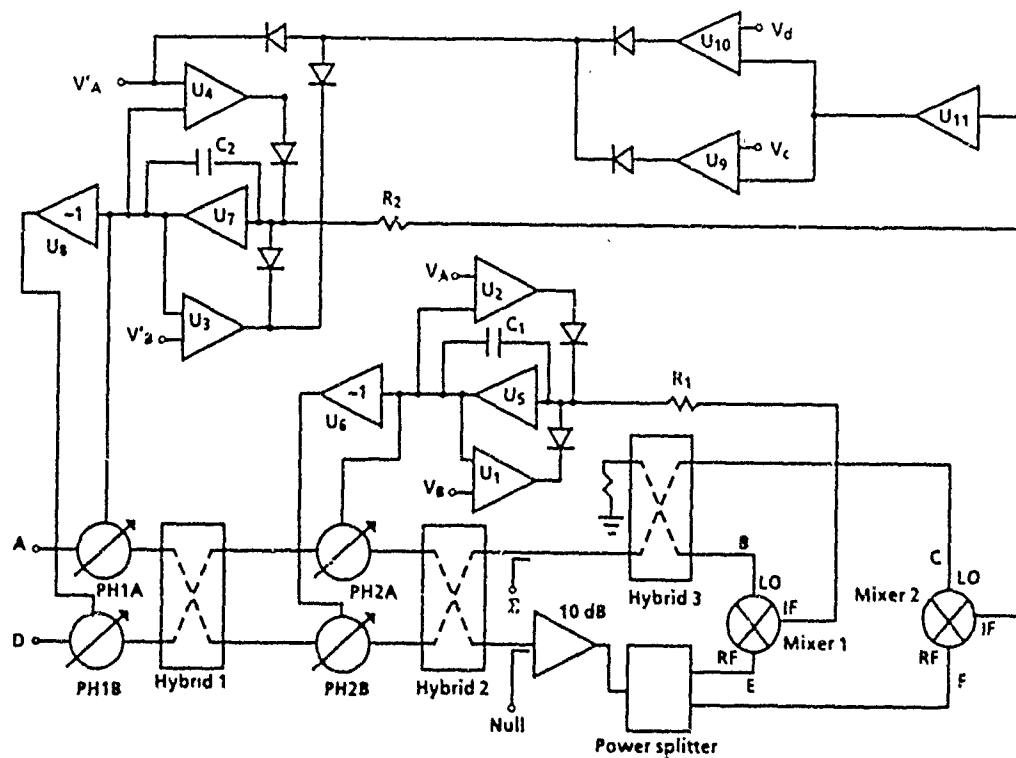


Figure 7. Adaptive Polarization Combiner With Integrator Sweep Disable Loop

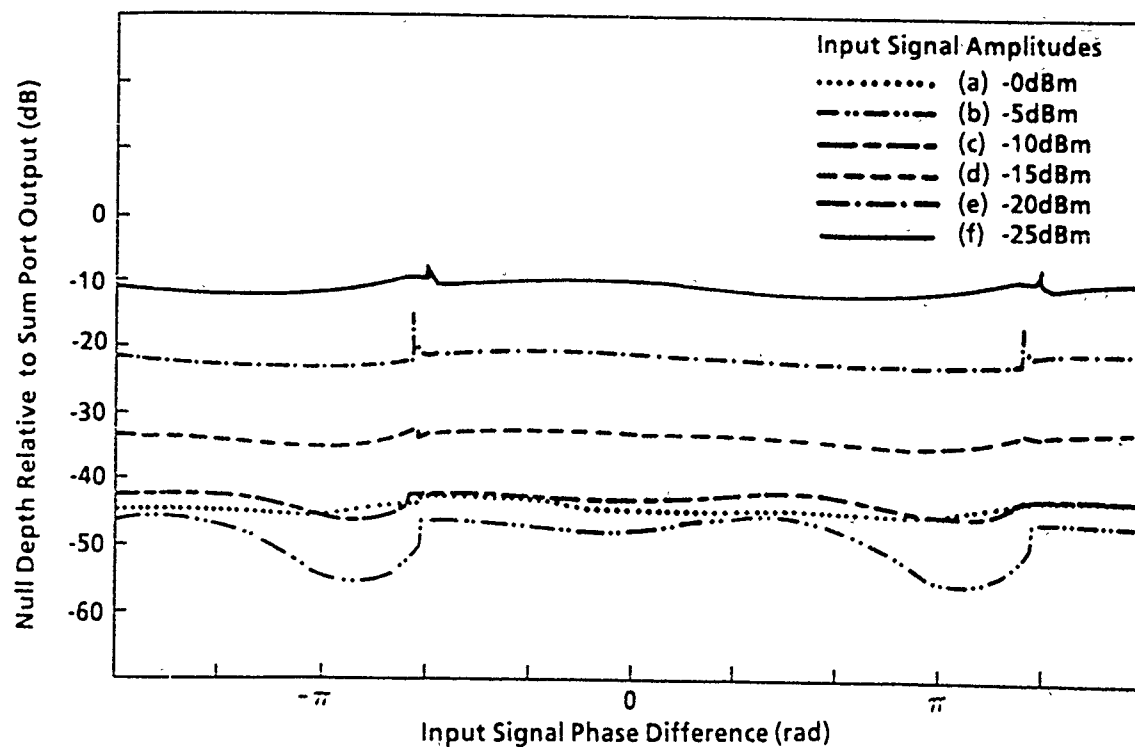


Figure 8. Null Depth as a Function of Phase Difference for Equal Amplitude Input Signals

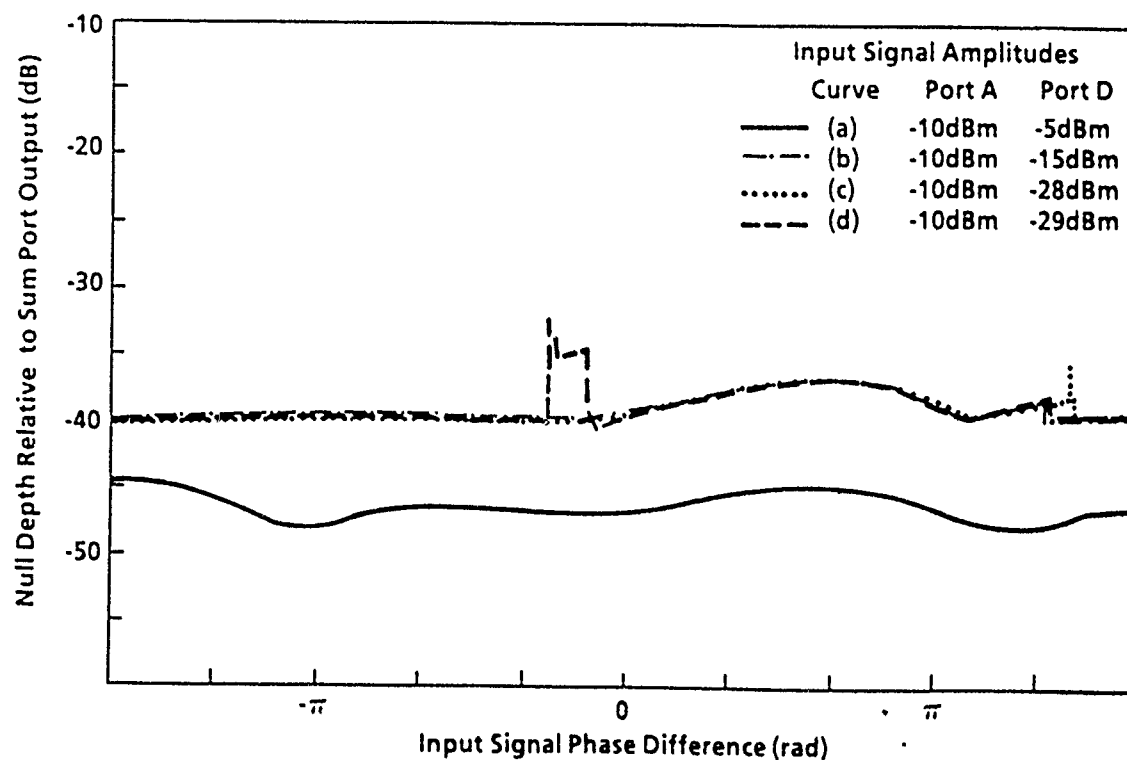


Figure 9. Null Depth as a Function of Phase Difference for Unequal Amplitude Input Signals

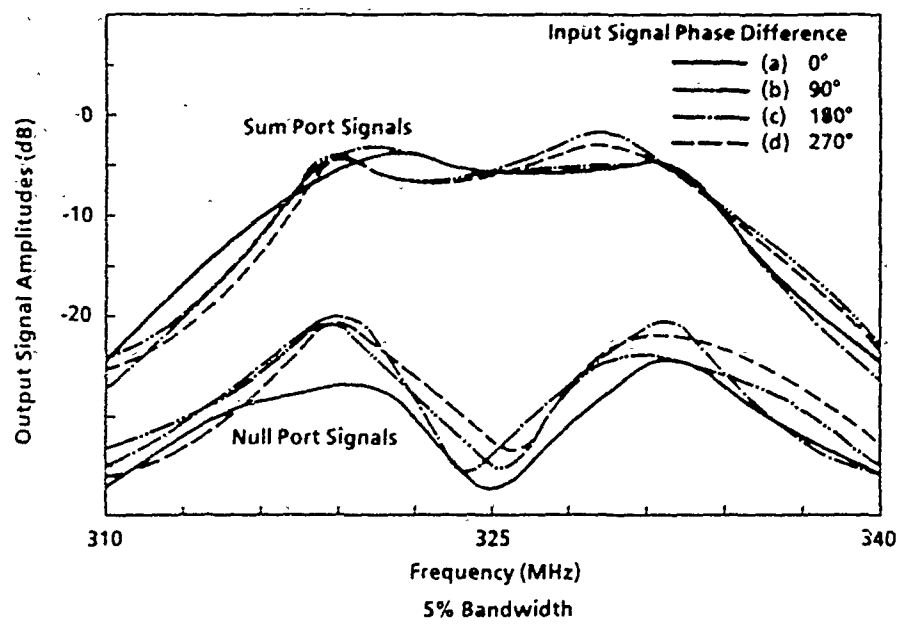


Figure (10a)

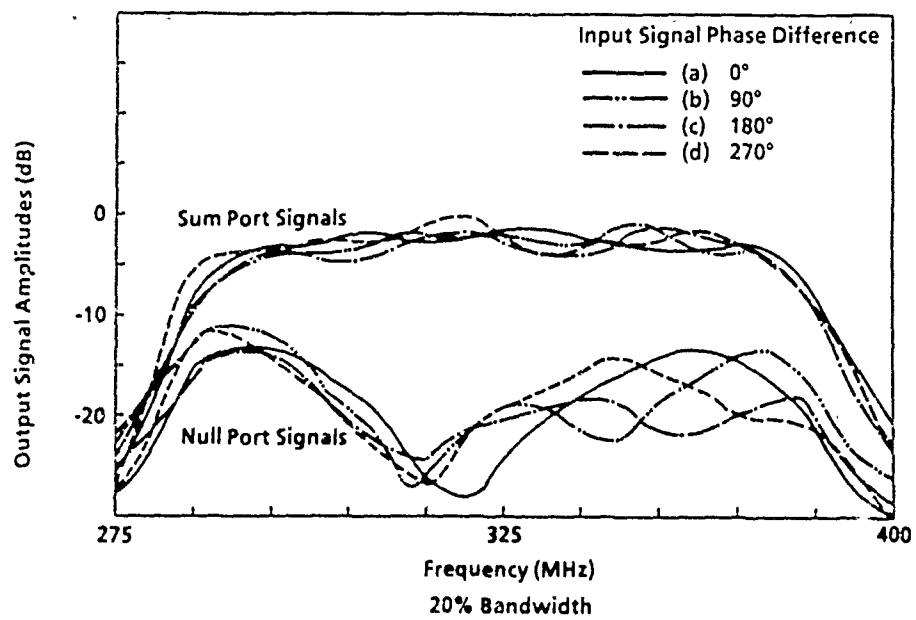


Figure (10b)

Figure 10. Performance for Wideband Equal Amplitude Input Signals with Constant Phase Difference

## A NEW CIRCULAR POLARIZATION SELECTIVE SURFACE (CPSS)

Gilbert A. Morin,  
Defence Research Establishment Ottawa,  
3701 Carling ave  
Ottawa, Ontario, Canada  
K1A 0Z4

### Abstract

A Circular Polarization Selective Surface (CPSS) is a surface that reflects one sense of circular polarization but transmits the other. While linear polarization selective surfaces are fairly common, a CPSS has been reported only recently. In this paper, a new CPSS with improved characteristics is presented.

This CPSS is made of a dielectric slab with wires printed on both surfaces and connections through the slab. It is easier to fabricate than the previously known CPSS which requires that transmission lines cross the dielectric.

The response of the CPSS to a plane wave excitation was simulated using the method of moments for thin wires. The effects of the dielectric were neglected. Mutual coupling and losses were

taken into account. Simulation results show that the scattering cross-section of the surface to one circular polarization is more than 80 times higher than to the other polarization.

A CPSS has been fabricated. Preliminary transmission measurements show that the surface permits most of one polarization to pass through while rejecting the other polarization by more than 15 dB. These results are in good agreement with the theory.

## 1. Introduction

A Circular Polarization Selective Surface (CPSS) is a surface that reflects one sense of circular polarization but transmits the other. Figure 1 illustrates the functional principle of operation of a CPSS.

While parallel-wire grids used as linear polarization selective surfaces have been known and used for a long time, a CPSS has been reported only one year ago<sup>1</sup>. In the present paper, a new CPSS is reported. Its main advantage is that it is easier and cheaper to fabricate.



Figure 2 shows a drawing of the CPSS that will be presented in this paper. It is made of a large number of identical cells distributed on a square grid. The cell element is the critical component that determines most of the electrical and mechanical characteristics of the CPSS. It will be described in section 3.

## 2. Theorems for CPSS

In the following, an infinite planar slab (of finite thickness) will be called symmetrical if it looks the same from both sides except for a rotation around an axis perpendicular to the slab.

Assuming that a CPSS is reciprocal, lossless, perfectly selective, and symmetrical, one can derive the following two theorems. The wave reflected by a CPSS will be of the same polarization as the incoming wave. The wave transmitted by a CPSS will be of the same polarization as the incoming wave.

The first theorem can be proven by showing that if there was a polarization change of the reflected wave, the surface would be a perfect conductor. Suppose a RHCP wave is reflected from a

surface as a LHCP wave, than by reciprocity, a LHCP wave will be reflected as a RHCP wave. In this case, the surface does not transmit any wave and is equivalent to a perfect conductor. Therefore, a CPSS cannot change the sense of polarization of the reflected wave.

The second theorem can be proven as follows. If a surface reflects RHCP on one side and is symmetrical, then it reflects also RHCP on the other side. Therefore, LHCP must be transmitted as LHCP otherwise it would violate reciprocity.

Another theorem states the following: an infinite CPSS cannot be made of an infinitely thin surface. In other words, an infinite CPSS must have a finite thickness. This can be shown as follows. An infinitely thin surface made of dielectric and conductors scatters identical waves on both sides except that the sense of polarization is reversed. If a RHCP wave hits such a surface, the scattered wave in the transmitted direction would have to be RHCP to cancel the incoming wave, but it would also have to be RHCP in the reflected direction according to the first theorem. The polarization would be the same in both directions which is not possible for an infinitely thin surface.

### 3. Description of the New Unit Cell Element

The previously reported CPSS element<sup>1</sup> is shown in Figure 3. The CPSS is made of a planar array of half-wave dipoles on each side of a dielectric slab that is used only for support. Crossing through the slab, transmission lines connect dipoles together. At frequencies of 1 GHz and higher, the transmission lines are increasingly difficult to fabricate because of their small size, and a simpler design is desirable. The main difficulty with the transmission lines is that they are half a wavelength long and the dielectric support is only a quarter wavelength thick. If the transmission lines are not folded, different dielectrics have to be used for the slab and the transmission lines. This is a strong disadvantage since in a practical CPSS, thousands or tens of thousands of cells are needed.

The new proposed cell element is shown in Figure 4. It is made of a single piece of wire bent in 3 dimensions. It does not use transmission lines and printed circuit technology can be used for fabrication above few GHz.

The element is made of a one-wavelength long wire bent

according to Figure 4. A LHCP plane wave propagating in the  $+z$ -direction will excite the one-wavelength resonance of the wire while a RHCP wave will not. By definition, we will call a "left CPSS" a surface that reflects LHCP waves while a "right CPSS" reflects RHCP waves. The sense of reflection instead of the sense of transmission is used to name the surface because CPSS's are used to make reflectors and it seems to make more sense to call a "left" (CPSS) reflector, a reflector that reflects left waves, the right wave seeing nothing at all. A right CPSS element is the mirror image of the element shown in Figure 4.

Figure 5 explains the behaviour of a left CPSS element in the presence of LHCP wave. It is useful to decompose the wave into two linearly polarized components as shown in the figure. Assuming the wave is propagating in the  $+z$  direction, the  $y$ -component is a quarter wavelength ahead of the  $x$ -component. Each component,  $x$ - and  $y$ -, strikes one wire segment,  $a$  and  $c$  respectively. Two full-wavelength resonances are excited, one from each end of the wire. Because of the phase relation between the  $x$ - and  $y$ -components and the position of the wire segments, both resonances are excited in phase and the currents add up. However, for a RHCP wave, the  $y$ -component is 180 degrees out of phase, compared with a LHCP wave, and the two resonances cancel each other.

To show this effect, a modified moment method program<sup>2</sup> was used to calculate the scattering cross-section (SCS) of a cell element one-wavelength long at 1.0 GHz. Figure 6 shows the result for both LHCP and RHCP waves. The SCS at resonance for LHCP is about 40 times larger than for RHCP. Resonance is shifted to higher frequencies by about 2%. The normalization of the SCS was chosen as follows. The SCS of a very large and totally reflective surface is twice the surface area. Since the CPSS is also reflective (for one sense), then its SCS will be twice its surface area. The cell dimension is half-wavelength on the side to form a "full" array. Therefore, by selecting twice the cell area as the normalization factor, the normalized element SCS must be about 1.0 to be useful. This is the result obtained in Figure 6. Of course, mutual impedance between the cells and the direction in which the scattering is made may affect the results but these factors will not be treated here.

#### 4. Simulation of a 25-Element CPSS

The cell elements can be used to form a rectangular array as shown in Figure 2. The cell size is half a wavelength by half a

wavelength. Using the same program as above, the SCS has been calculated for 25 cell array and the result is shown in Figure 7. The normalization factor is twice the array surface area as discussed above. The ratio of the left and right SCS at resonance is now 84. There is a 6% shift in the resonance frequency due in part to mutual coupling. The SCS for the LHCP wave is about 1.0 as desired.

Figure 8 shows the bistatic cross-section of the same CPSS. The scattered power is concentrated in the direction normal to the surface and there is minimal radiation in the plane of the CPSS. This is the desired result.

## 5. Experimental Results

A left CPSS made of 100 cells was fabricated and initial measurements were made. The setup used is shown in Figure 9. The CPSS was placed between two quad-ridged horns and transmission measurements were made for both RHCP and LHCP waves.

The measurement sequence proceeded as follows. First the horns are connected for LHCP waves. A transmission measurement is

made without the CPSS. Then the CPSS is inserted between the horns and a new transmission measurement is made on the same graph. The sequence is repeated for RHCP. Figure 10 shows the result for LHCP. The response when the CPSS is present shows a rejection of the signal of more than 20 dB at 7.5 GHz. In other words, the surface does not let the LHCP wave go through. In Figure 11, measurements for RHCP are shown. It is shown that the surface is almost transparent to the wave. The difference between the reference signal and the transmitted signal being less than 1 dB.

The surface behaves as expected.

## 6. Potential Applications

There are several potential applications for CPSS's. Three are presented here.

Figure 12 shows a Cassegrainian antenna with a CPSS sub-reflector that eliminates shadowing. A left wave coming out of the horn is reflected by a left sub-reflector as a left wave. This left wave bounces off the main reflector as a right wave that does not see the sub-reflector any more and shadowing is eliminated.

Figure 13 shows a mirror antenna. The left wave coming out of the horn hits the main reflector made of a left CPSS. The wave is reflected down as a left wave, is reflected off the flat plate as a right wave, and goes through the main reflector unimpeded.

Figure 14 shows a dual-reflector antenna with a CPSS sub-reflector. Both right and left polarizations could be used at the same frequency if the sub-reflector can be made to generate very little cross polarization.

## 7. Conclusion

This paper has described a new CPSS that is easy to fabricate and that has excellent electrical characteristics. Preliminary experimental results confirmed the theoretical findings. Several potential applications were presented.

## References

1. Tilston, W.V., T. Tralman, and S.M. Khanna (1988) A



Polarization Selective Surface for Circular  
Polarization, IEEE AP-S Int. Symp.: 762-765.

2. Richmond, J.H. (1974) Computer Program for Thin Wire  
Structures in a Homogenous Conductive Medium, NASA CR-  
2399.

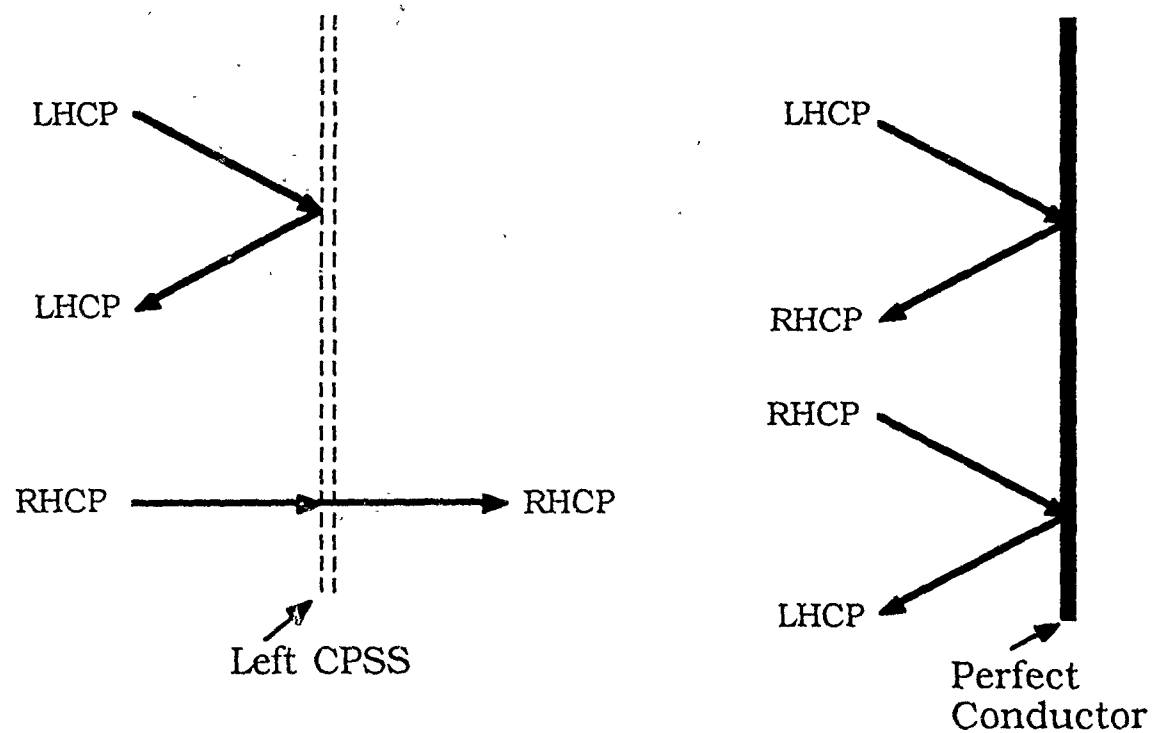


Figure 1. Interaction of circularly polarized waves with a left CPSS or a perfect conductor.  
 ( LHCP: left-hand circularly polarized )  
 ( RHCP: right-hand circularly polarized )

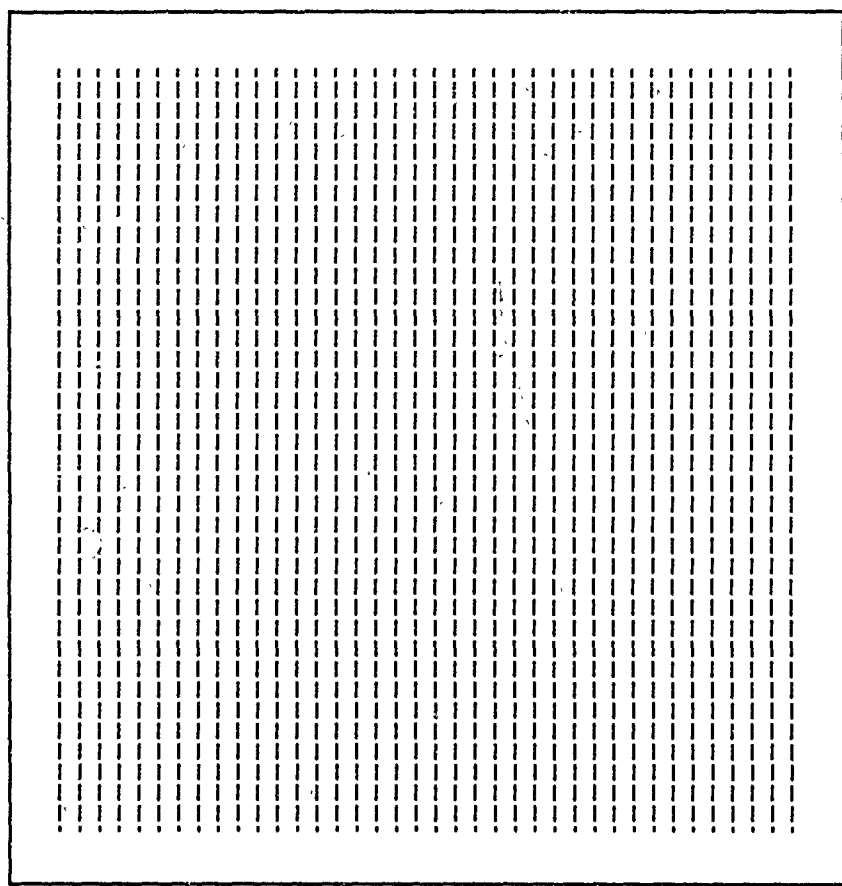


Figure 2. Drawing of the new circular polarization selective surface as seen from one side of its dielectric sheet. The other side is identical except that the wires are rotated by 90 degrees.

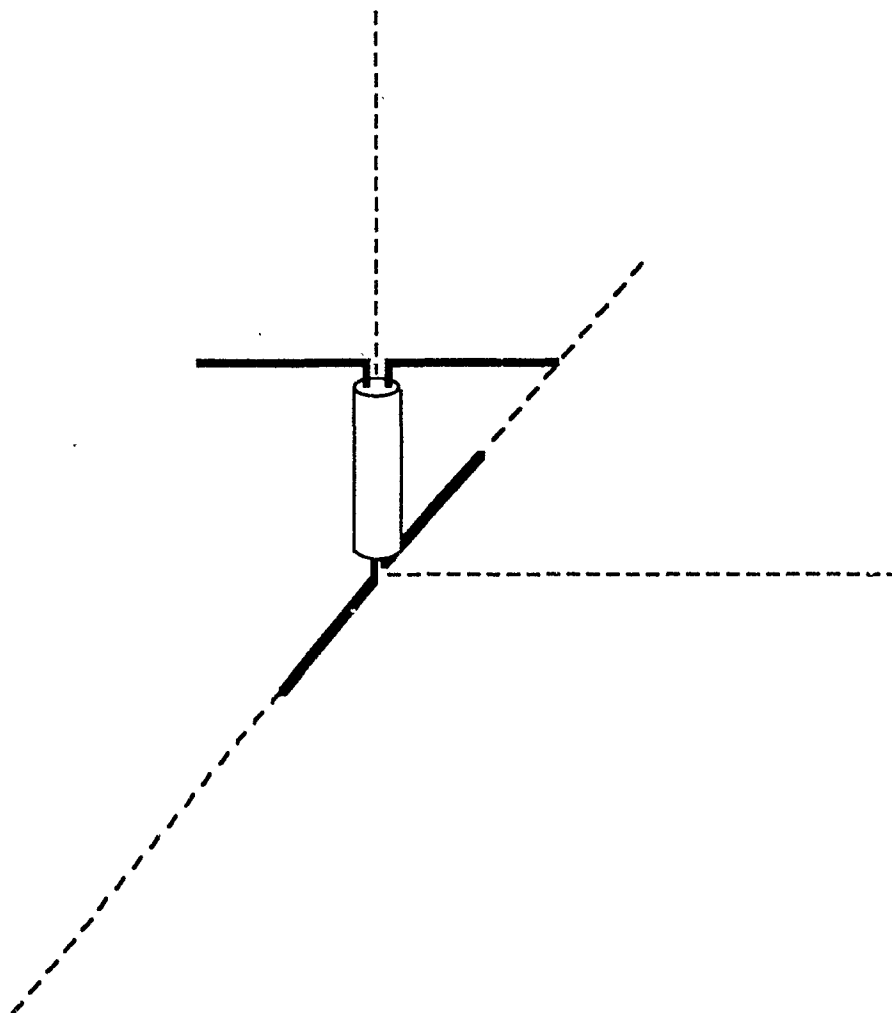


Figure 3. Tilston's CPSS element made of two dipoles and one transmission line.

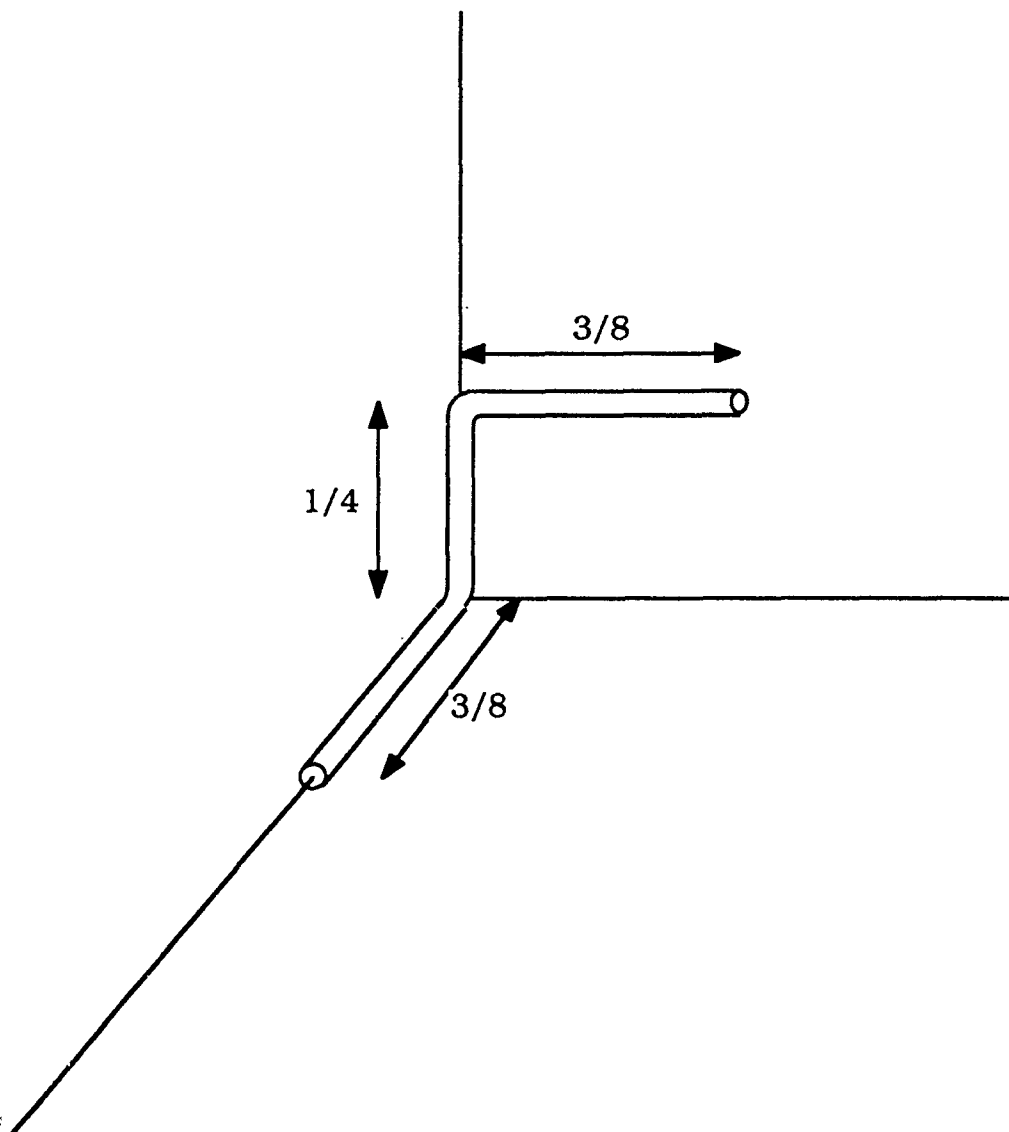


Figure 4. Left CPSS element (lengths are in wavelength).

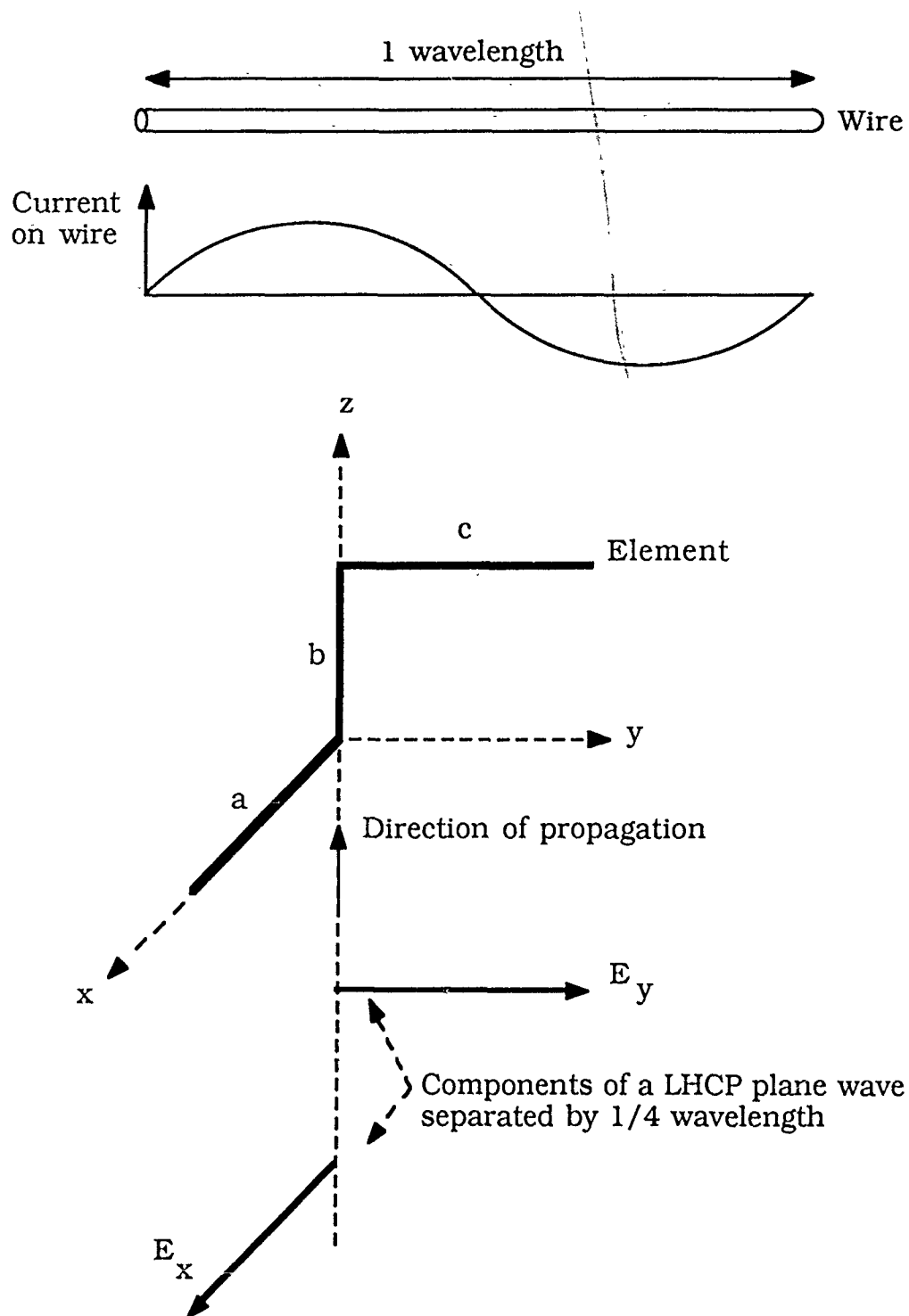


Figure 5. Full wavelength resonance of a left CPSS element.

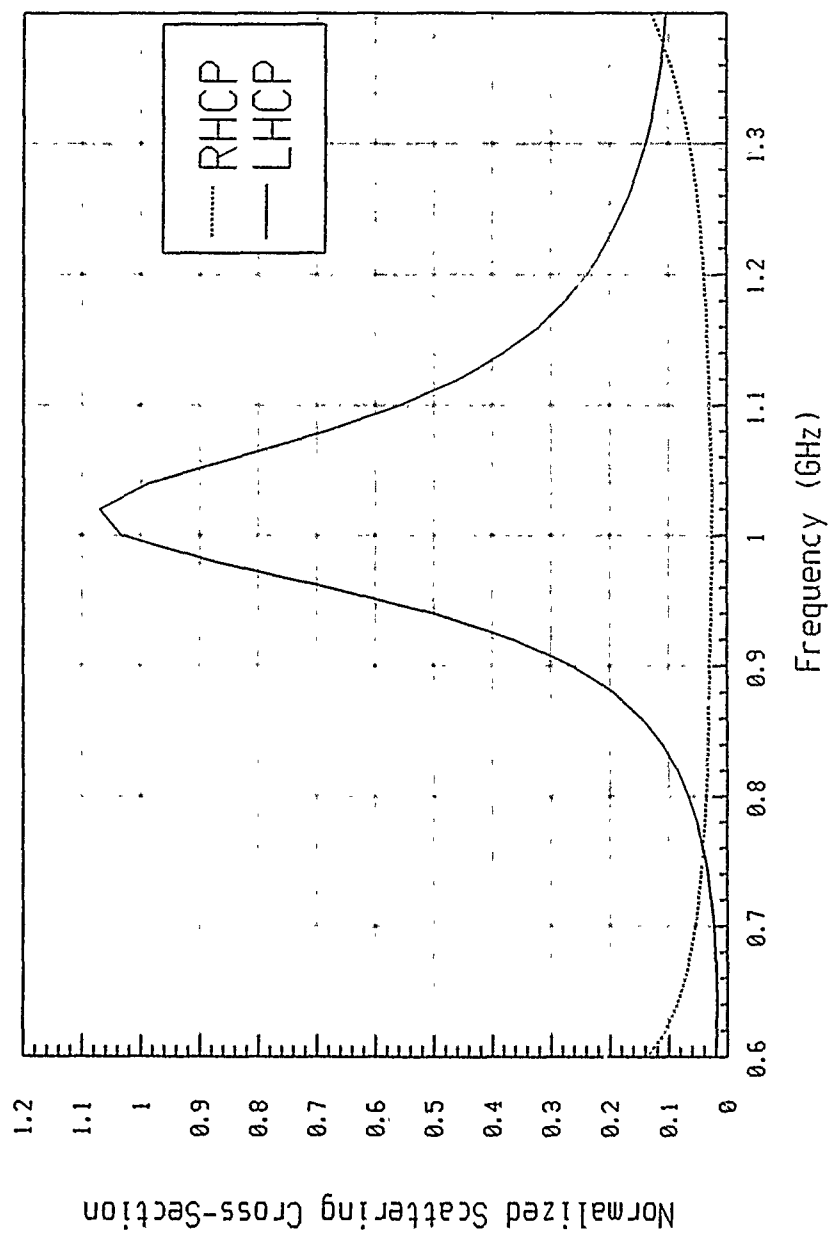


Figure 6. Scattering Cross-Section of a LHCP Cell Element

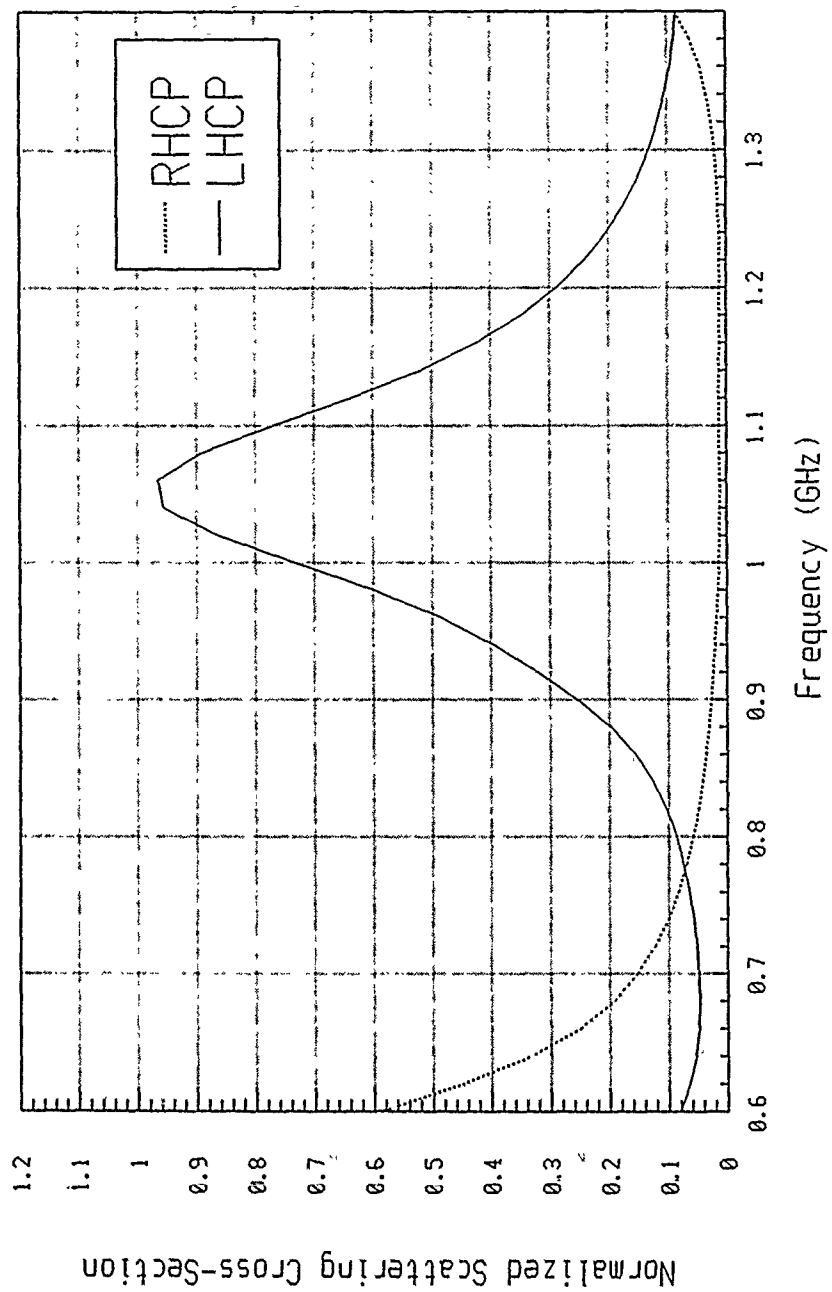


Figure 7. Scattering Cross-Section of a 25-Cell Left CPSS.



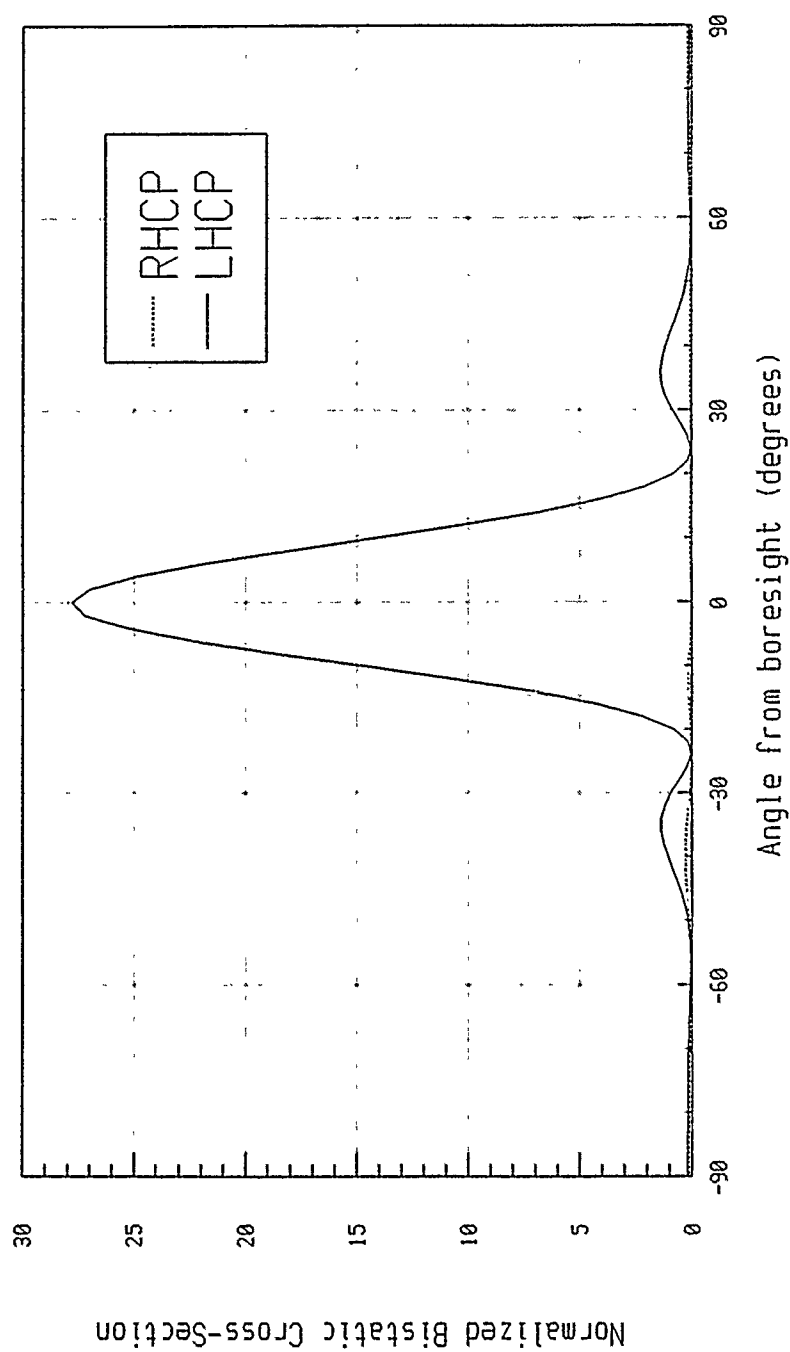


Figure 8. Bistatic Cross-Section of a 25-Cell left CPSS illuminated by an incident LHCP wave normal to the surface. Observation plane: x-y (normal to CPSS) Frequency: 1.0 GHz.

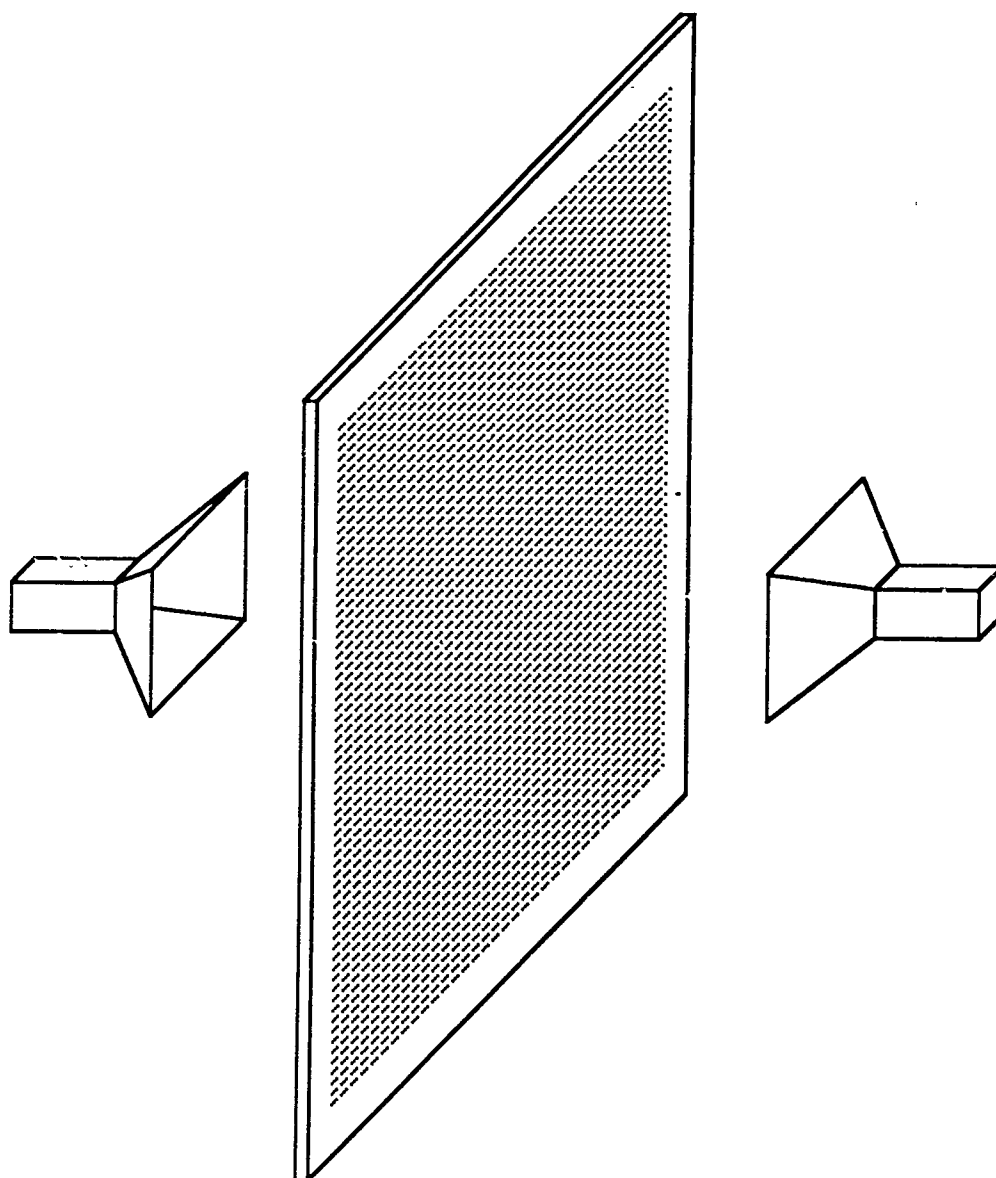


Figure 9. Experimental setup.

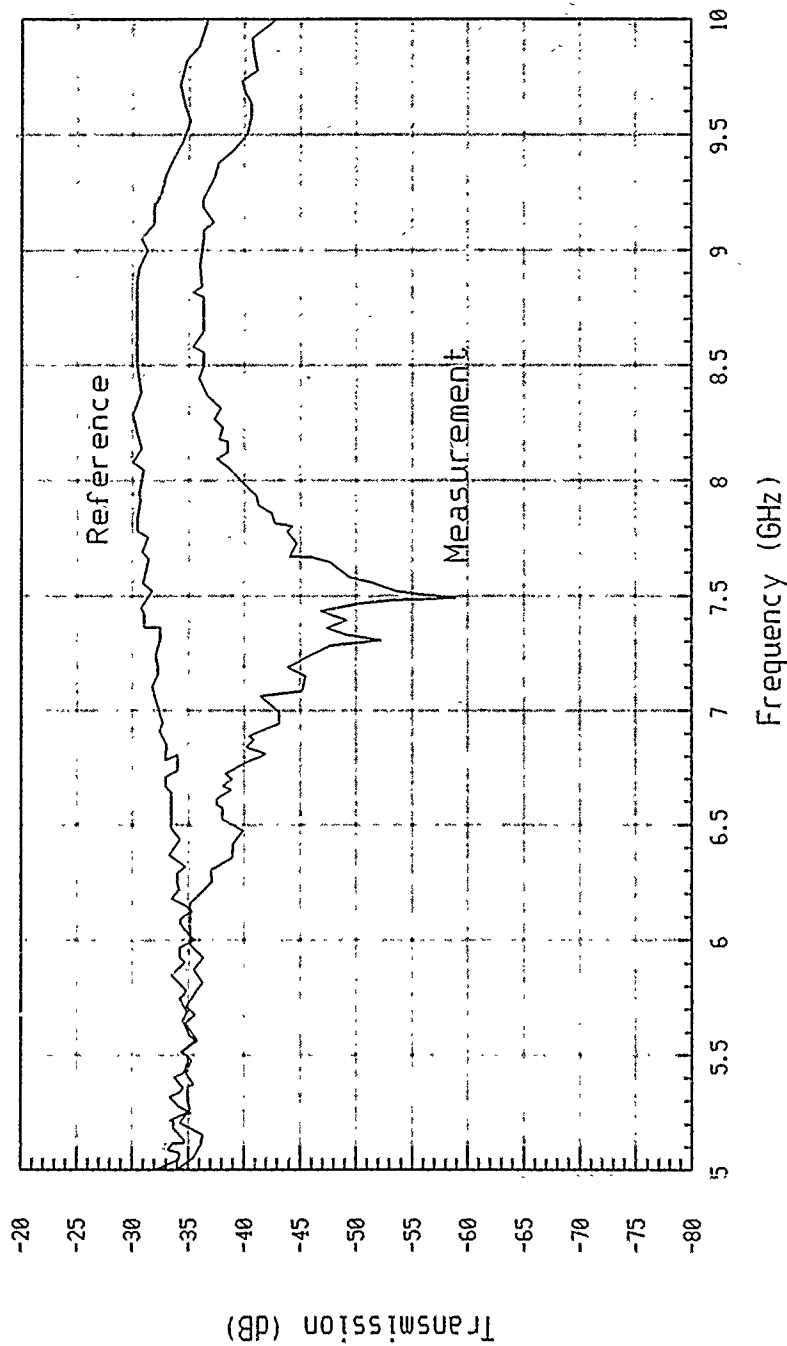


Figure 10. Transmission measurement of a LHCP wave through a left CPSS. The "reference" line is with the surface removed.

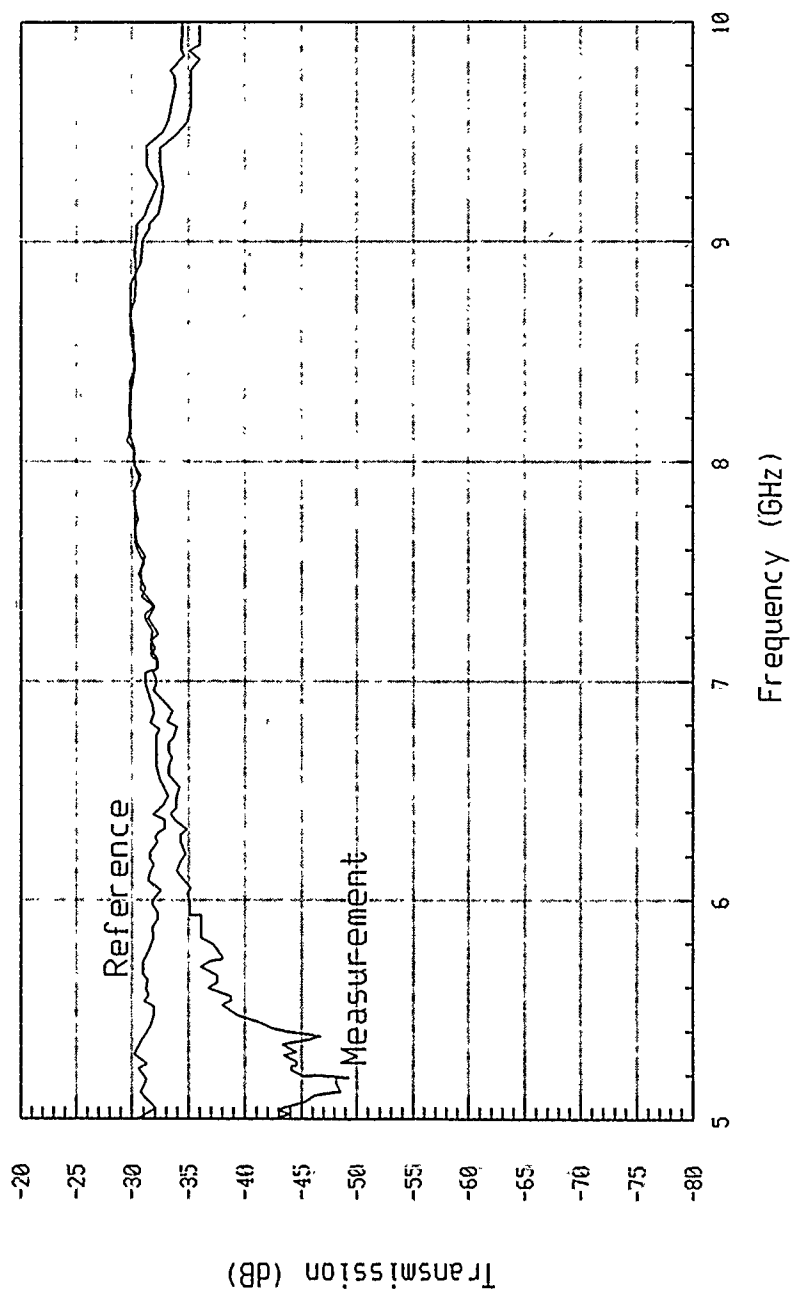


Figure 11. Transmission measurement of a RHCP wave through a left CPSS. The "reference" line is with the surface removed.

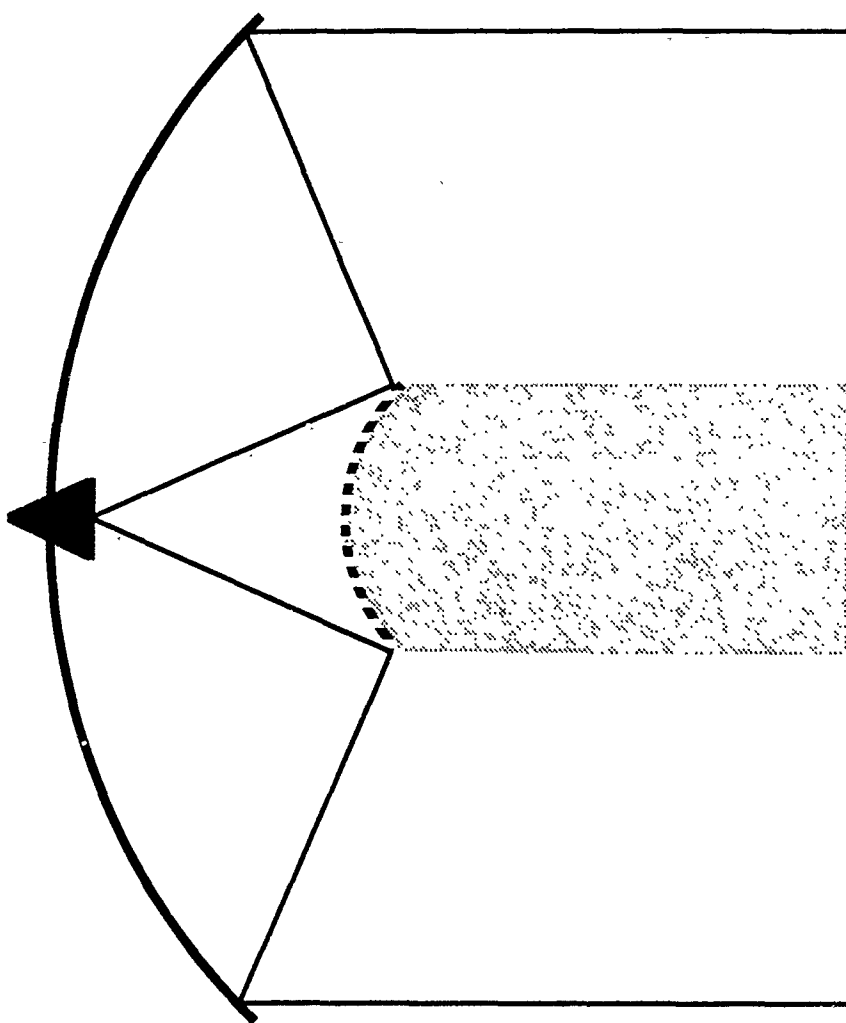


Figure 12. Cassegrain antenna with CPSS sub-reflector.

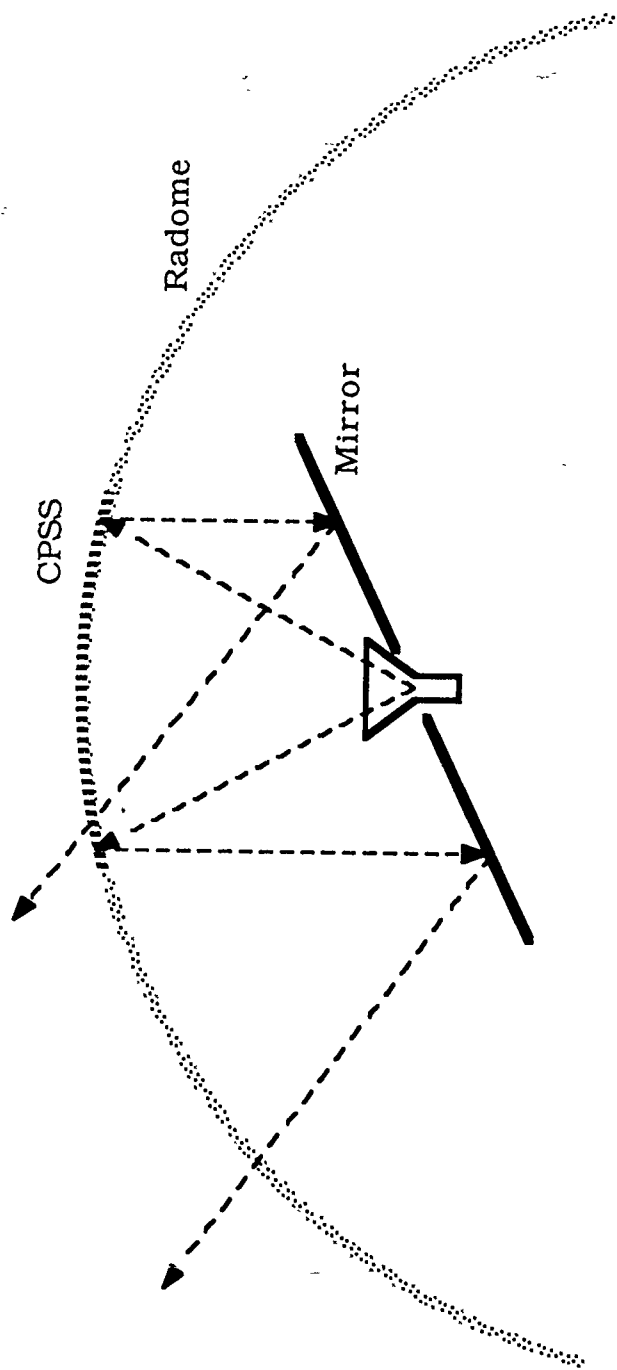


Figure 13. Mirror antenna.

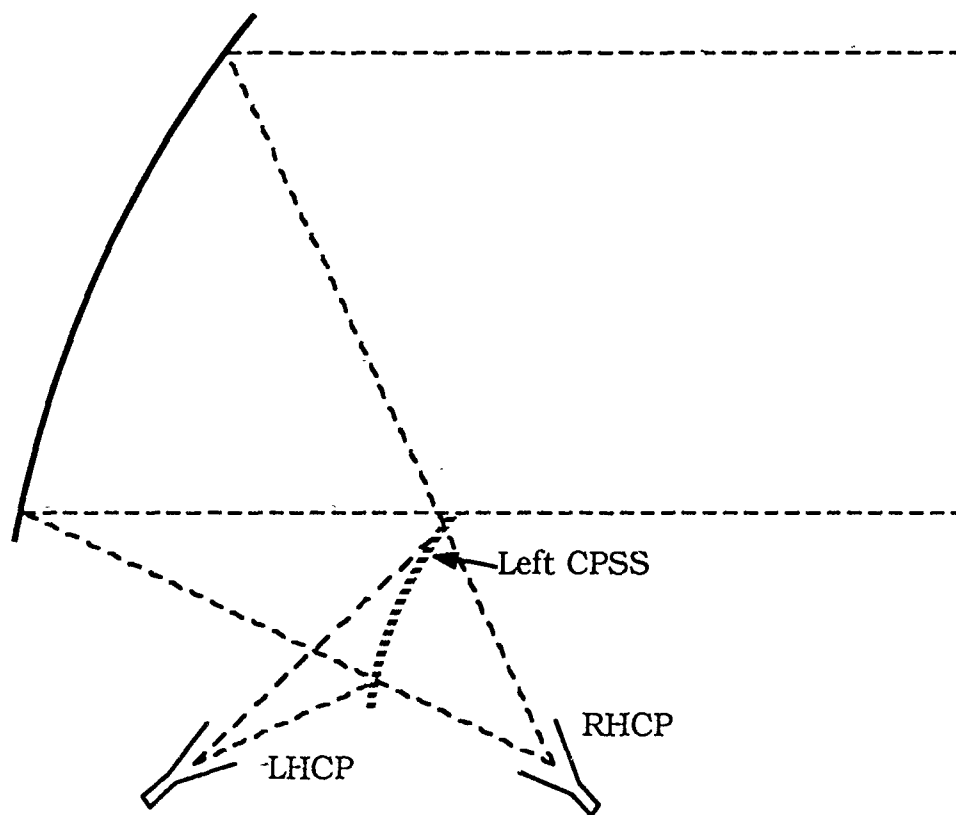


Figure 14. Frequency reuse by polarization diversity.

**The ARSR-4 Antenna,  
a Unique Combination of  
Array and Antenna Technology**

**Richard S. White and Daniel Davis**

**Westinghouse Electric Corporation  
Baltimore, Maryland**

**1989 Antenna Applications Symposium  
Allerton Park, Monticello, Illinois**

**September 20-22, 1989**



**THE ARSR-4 ANTENNA, A UNIQUE COMBINATION  
OF ARRAY AND ANTENNA TECHNOLOGY  
RICHARD S. WHITE and DANIEL DAVIS**

**WESTINGHOUSE ELECTRIC CORPORATION  
BALTIMORE, MARYLAND**

## **1.0 ABSTRACT**

The next major air route surveillance system being designed for the FAA and USAF, the ARSR-4, will include the ability to determine aircraft height, in addition to range. Cost considerations favor a rotating antenna, while performance requirements in rain make a circular polarization option practically indispensable. Timing considerations make a multiple elevation beam configuration the design of choice. Low sidelobes, and a narrow base beamwidth complicate the azimuth pattern requirements.

A unique, economical solution to all these antenna requirements has been developed and experimentally proven, and will soon be in production. The antenna uses a reflector in order to minimize the number of elements which are switchable to circular polarization. It uses multiple feeds, stacked in elevation to form multiple elevation beams. To prevent blockage, the feed system is offset. Then to remove the phase distortion that offsetting causes, the feed system is widened in azimuth. This forces a reflector design with non-equal vertical and horizontal focal lengths. To separate beams into manufacturable rows, the feed is curved.

The design logic and considerations, followed with a description of an experimental test program which proved the concept, are discussed.

## **2.0 BACKGROUND**

The requirements for next generation L-band surveillance radars, the ARSR-4, include the need for antennas with long range, high resolution, low sidelobes (-35 dB

peak in azimuth), 3-D coverage, and performance in adverse weather conditions. In addition the antenna must be capable of being used at minimally attended or unattended sites, so high reliability and low maintenance are also critical requirements. In an era of ever tightening budgets, affordability is a critical requirement, indicating that any design approach needs to be cost effective. In order to operate in clutter with a high data rate and 3-D coverage, an ideal antenna would have low sidelobes, with multiple elevation beams and selectable linear or circular polarization.

An antenna concept for a low cost approach to this high performance L-band surveillance radar system was developed. It involved a novel combination of reflector and array techniques, which some thought radical enough to warrant a full scale model to convince them of its viability. To allay all doubts a full scale breadboard or demonstration antenna was designed, built, and tested. This project was carried out in less than one year from the beginning of design to completion of test. The demonstration antenna consisted of a full size (42' x 32.5') reflector fed by a feed array consisting of 196 dual polarized radiating elements (figure 1).

Several alternate designs were initially considered, prior to settling on the array fed reflector as the optimal configuration. The candidates considered were a dual polarized corporate fed planar array, a horizontal parabolic cylinder fed by an offset array, a dual parabola reflector fed by stacked horns, and the array fed reflector. The array fed reflector is a dual paraboloid reflector fed by a polarization diverse conformal array which is offset to eliminate high azimuth sidelobes aperture blockage would cause. After reviewing anticipated performance, complexity, and relative cost, the array fed reflector was chosen for further development.

### 3.0 DESIGN

The array fed reflector consists of a precision dual-parabola reflector which is fed by an array offset below the radiating aperture. The face of the feed array is cylindrical in azimuth and tilted in elevation. It is built in azimuth rows which are fabricated out of air dielectric stripline. Each azimuth row forms a beam, albeit a high elevation sidelobe beam, at a specific elevation angle. These beams are then combined in sets and weighted to yield multiple elevation beams which are broader than the individual row patterns, have low elevation sidelobes, and are used for height finding.

The first step was to use an optical ray tracing process to determine the size and shape of the reflector, and the tilt and curvature of the feed. The reflector shape thus determined, has much longer focal length in the horizontal plane than in the vertical plane. The feed array surface passes through the vertical focal point, but is wide in the horizontal plane to correct azimuth plane phase distortion inherent in an offset configuration. To check a particular beam, rays were traced from desired wavefronts, reflected off the reflector about the normal to the surface, and down to the feed array surface (figures 2 and 3). This made it possible to choose reflector and feed geometries which align beams into rows across the feed surface, and isolates the beam feeds into independent rows, so that the beam feeds were separable. The optical mapping showed that the feed array had to increase in width as it moved further off the vertical axis to control the illumination across the reflector (figure 4). At the completion of the optical analysis, it was possible to begin work on the design of the radiating element, antenna pattern optimization, and the mechanical design of the reflector and feed array.

A new radiator was developed for the array which feeds intersecting troughs. Each trough contains an array of probes which excite the trough with the desired distribution. Intersecting horizontal troughs with vertical troughs gives the desired

dual polarization. Dual layer horizontal air dielectric stripline manifolds using Wilkinson type couplers feed elements of each polarization separately. Since a solid state transmitter with relatively low peak power is anticipated, the air dielectric stripline has adequate power handling capability. The benefit of this configuration, with dual distribution networks, is that a single active component in each row, a switch, is all that is required to switch from linear to circular polarization. This provides a dramatic improvement in reliability and maintainability.

The array element was developed in a methodical fashion using a combination of computer models, along with laboratory breadboards. After the basic concept was developed, a finite difference computer analysis program was used for numerical modeling. The results from this model were used to design the element and a simulator was built in which the element was tested and refined. This combination of techniques allowed the element to be designed and matched in both polarizations over a range of scan angles while building a minimum of hardware. The results were later borne out when the element performed as designed in pattern test with no further tuning.

The pattern optimization of the array fed reflector used extensive computer modeling starting with feed and reflector dimensions from the optical analysis. The distribution for each azimuth row was optimized individually by breaking the azimuth rows into symmetric element pairs modeled as horns, and generating individual azimuth patterns for each horn pair. The element pair patterns for each row were then used to optimize the azimuth distribution for that row. The elevation patterns were initially computed using a 2-D model which only used a narrow strip along the center line of the reflector. When the results of this model were sufficiently close, the entire reflector was used to compute the predicted pattern. The distributions arrived at in this manner were then used in the feed array design.

#### 4.0 IMPLEMENTATION

The antenna concept called for a total of 23 azimuth-rows to achieve elevation coverage of 37 degrees with 10 elevation beams. Due to limitations of resources, only eight of the 23 feed rows were built to prove the concept (figure 5). The distributions from the pattern optimization were developed in hardware as corporate feed networks made of air dielectric stripline. This medium uses numerically controlled machinery to stamp out the center conductors and ground planes thus lending itself to good accuracy and excellent repeatability (figure 3). The circuits were each breadboarded and tested through one iteration. The results of this first iteration were so good that the minor design changes were incorporated directly into the feed array design without another iteration. The accuracy of the azimuth row design was demonstrated by primary pattern testing the feed array. Figure 7 shows the theoretical pattern overlaid on the measured pattern, and they are so close that the two are indistinguishable in the main beam region, which is the region of interest since it illuminates the reflector.

The implementation of switchable linear/circular polarization required that the azimuth rows be able to feed the horizontal and vertical elements independently, and to do this each azimuth row was made up of two layers with a separate stripline power divider in each polarization. For linear polarization one of the dividers was fed with all the power. To switch to circular polarization, both dividers are fed with equal power but with a 90 degree phase difference. This will be implemented with a switch, however for the demonstration antenna a -3dB coupler with phase trimmers was used.

The mechanical design of the reflector incorporated a great deal of up front planning between manufacturing and engineering to design a structure which could be manufactured efficiently and accurately. The reflector was of such a size (42 feet wide by 32.5 feet high) that it could not be built in a model shop environment. The reflector was designed in horizontal panels approximately 6 feet high by 42 feet long to provide

the greatest possible control of the contour tolerances in the azimuth plane since the azimuth patterns require the lowest sidelobes, and so the greatest precision. These panels were assembled in precision fixtures, assuring the highest accuracy within a panel. It was designed to be fabricated on production machinery and assembled on production fixturing (figure 8). CAD/CAM techniques were used throughout with the design done on a combination of IAG and mainframe computers. The design data was transferred directly from computer file to NC controllers on the shop floor by direct computer to computer data link. Most of the structure is made of sheet metal, punched on a Wiedematic stamping machine which controls dimensional tolerances to within .005 in. The demonstration antenna was built using minimal documentation with all the hardware being fabricated directly from computer data files or engineering sketches.

## **5.0 RESULTS**

The results of pattern testing the array fed reflector antenna were excellent in that all of the original performance goals were achieved. This was remarkable in that the design effort represented a technology advance in three areas simultaneously,

- (1) novel antenna architecture for low azimuth sidelobes,
- (2) new dual polarized radiating element, and
- (3) tight contour tolerance on a large lightweight reflector.

The elevation goal was to demonstrate multiple elevation beams with moderately low sidelobes ( $-25\text{dB}$ ). Measured elevation patterns are shown in figure 9 for receive beams 2, 3, and 5. These patterns had sidelobes of  $-28\text{dB}$ , or better. The azimuth sidelobe goal of  $-35\text{dB}$  was achieved for the worst case peak sidelobes near the main beam (figure 10). The far out sidelobes were much better, being down near the  $-50\text{dB}$  level. One remarkable feature of this antenna is the absence of spillover sidelobes where energy from the feed spills past the edge of the reflector to give a

relatively high sidelobe. The absence of these sidelobes is attributed to the illumination control effected by the feed array.

The last major goal was to demonstrate circular polarization. The method of evaluating circular polarization purity was to determine the integrated cancellation ratio (ICR), that is, the ratio of power received by the circularly polarized antenna to the power received by a linearly polarized antenna of the same configuration when the antennas are completely surrounded by randomly distributed small symmetrical targets (raindrops)<sup>1</sup>. An ICR measurement of 18dB would have been considered good with anything higher being better. The measured ICR's on the array fed aperture were generally between 22 and 28dB with the worst one being 21.2dB, which corresponds to an ellipticity of approximately .75dB. An ICR of 28dB corresponds to an ellipticity of .34dB.

## 6.0 CONCLUSION

The results from the demonstration antenna prove this to be a viable antenna technology. The sidelobe performance, multiple elevation beam performance, and ICR measurements all met or exceeded the goals which had been set. Fabrication of the reflector and feed array in a manufacturing environment proved that the required tolerances can be met on a production basis. The reduction and simplification of hardware ensure that reliability and performance are maximized while cost is minimized. It is projected that the array fed aperture has a cost advantage of up to 2:1 over an array antenna capable of achieving the same performance.

## ACKNOWLEDGMENTS

The author wishes to thank Coleman Miller, M.L. "Rocky" Deal, Timothy Waterman, Ann Sullivan, Steve Syrylo, David Demers, Linda Parrish, and Hank Jiles for their efforts contributing to the success of the project.

## REFERENCES

1. Johnson, R. C. and Jasik, H. (1984) Antenna Engineering Handbook, McGraw-Hill, New York, pp. 23-30



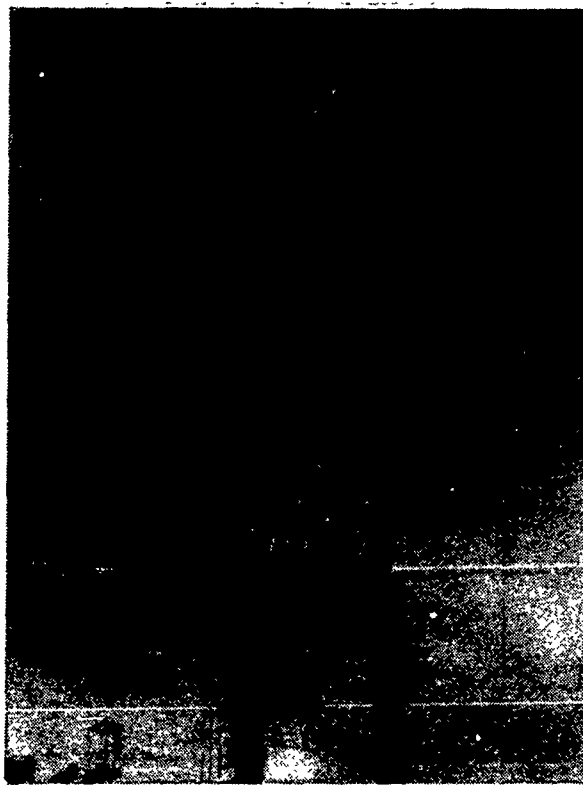


**Figure 1. Antenna Under Test**

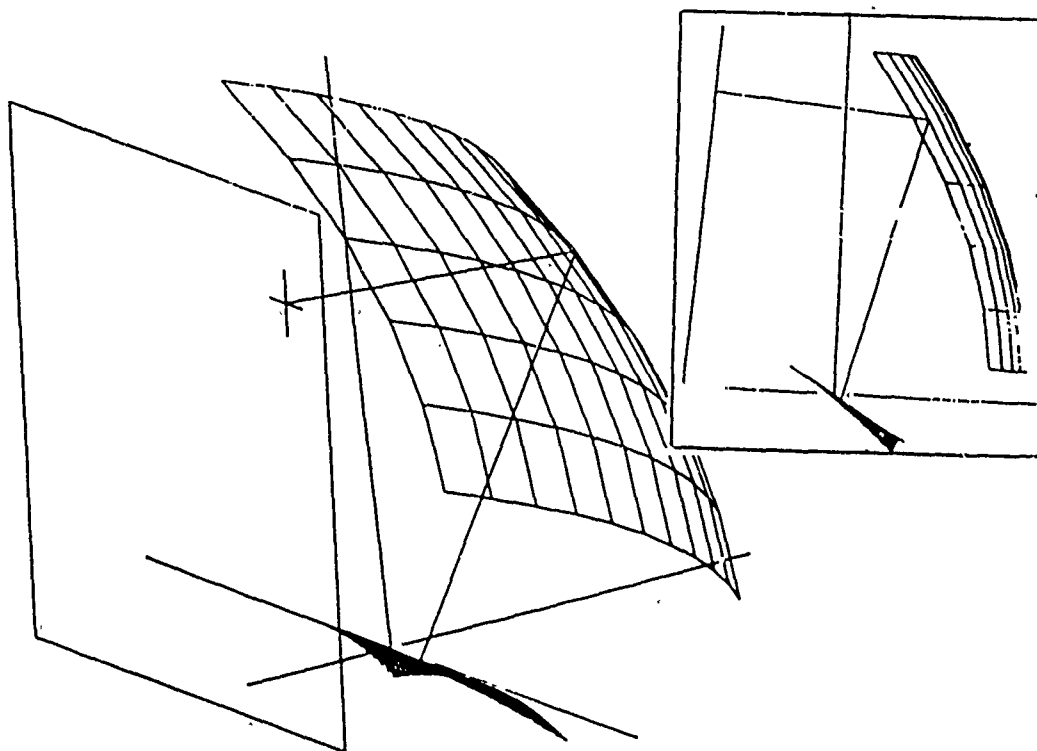


**Figure 2. Projections From Feed, Off Reflector, to Plane**

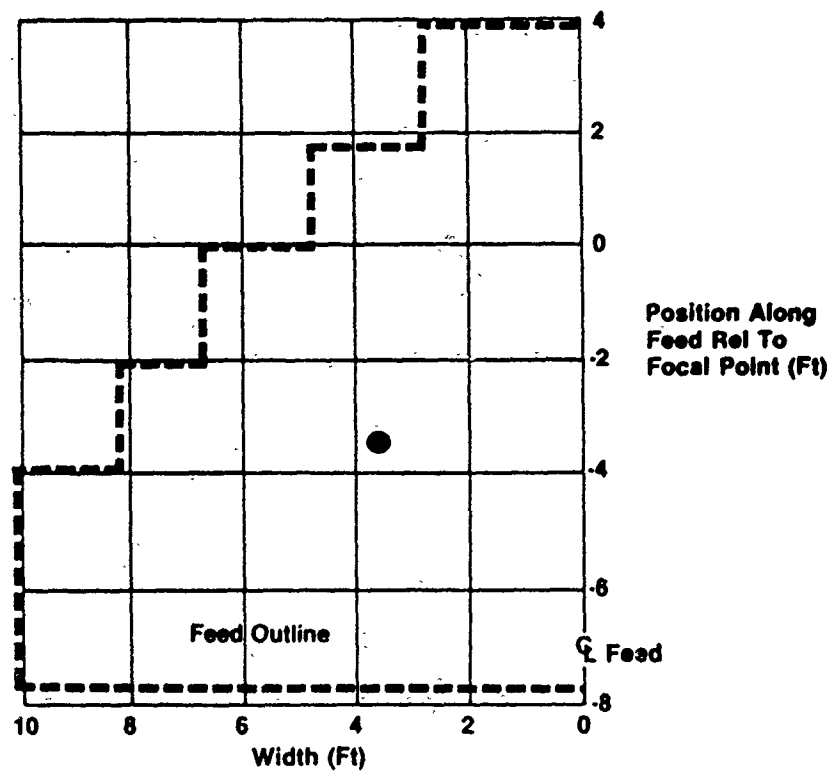


Figure 3. Point Projection to Feed

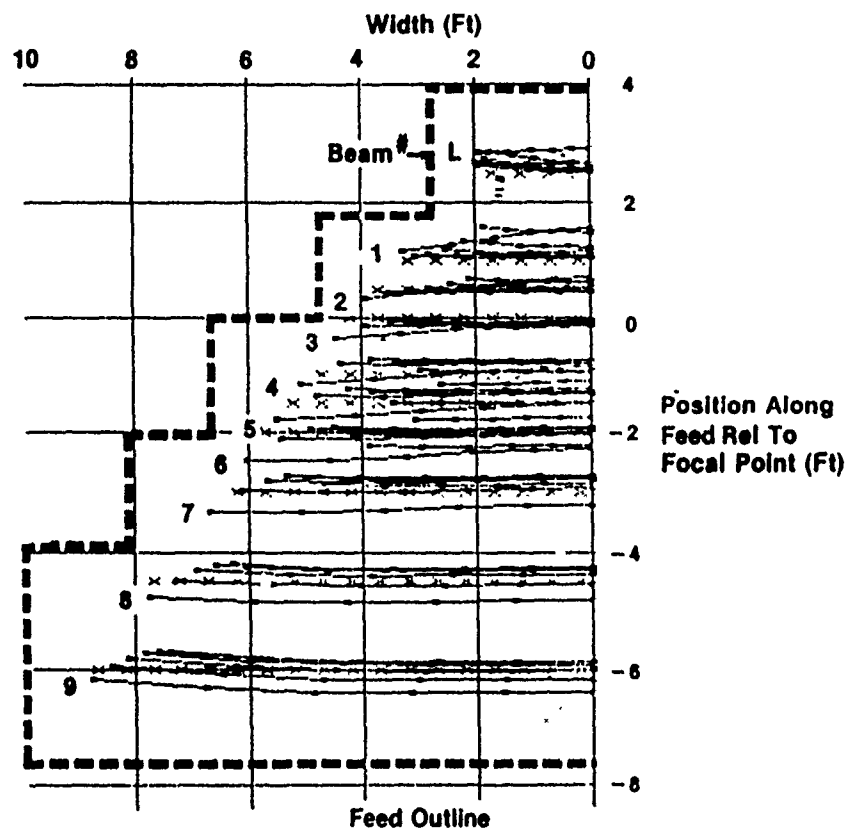
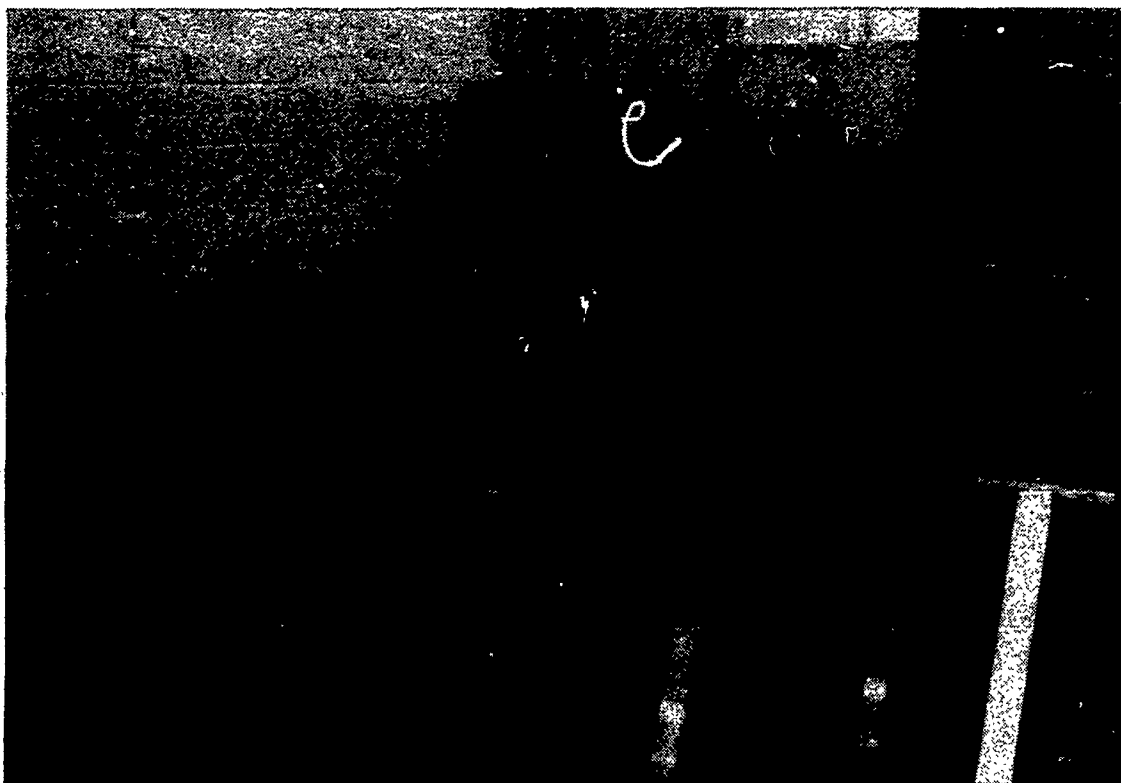


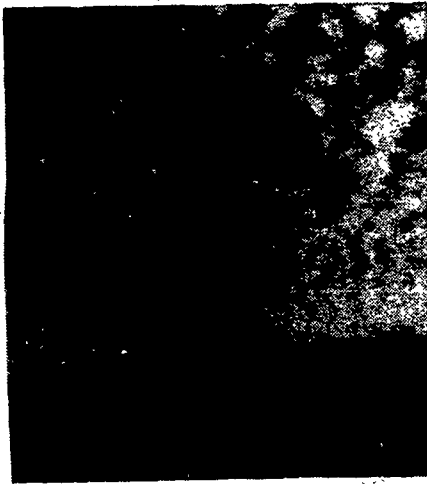
Figure 4. Multiple Beam Projections to Feed



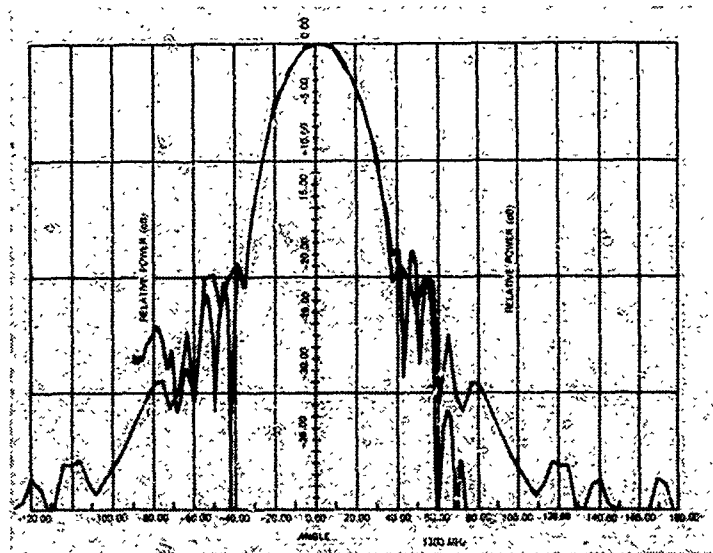
**Figure 5. Polarization Diverse Feed Array**



**Figure 6. Air Dielectric Stripline Azimuth Manifold**



a. Feed on Primary Range

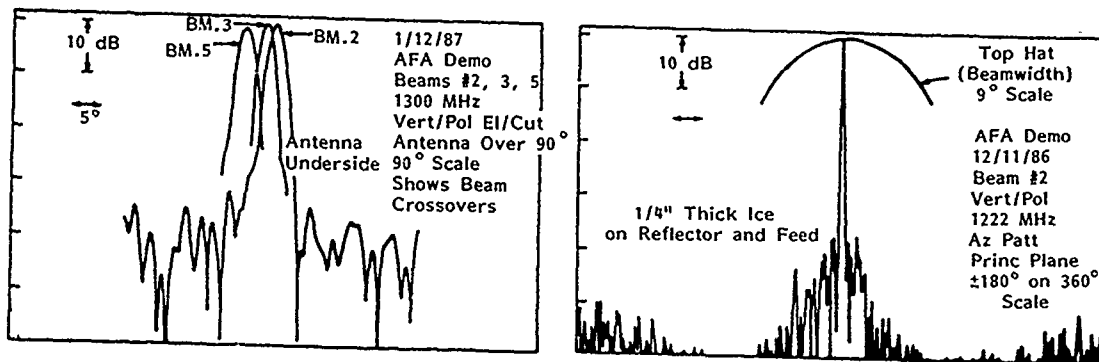


b. Predicted Primary Pattern Overlaid With Measured Pattern

Figure 7. Primary Feed and Its Pattern



Figure 8. Reflector Panel Tooling



a. Elevation Multiple Beams

b. Azimuth

Figure 9. Measured Secondary Elevation and Azimuth Patterns

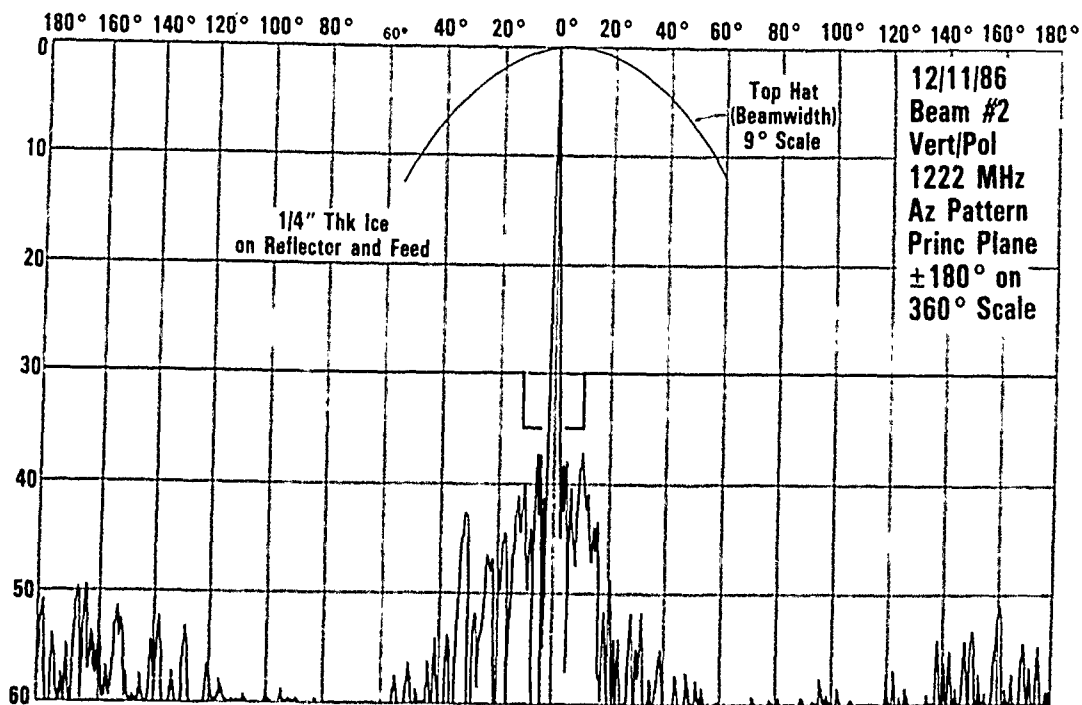
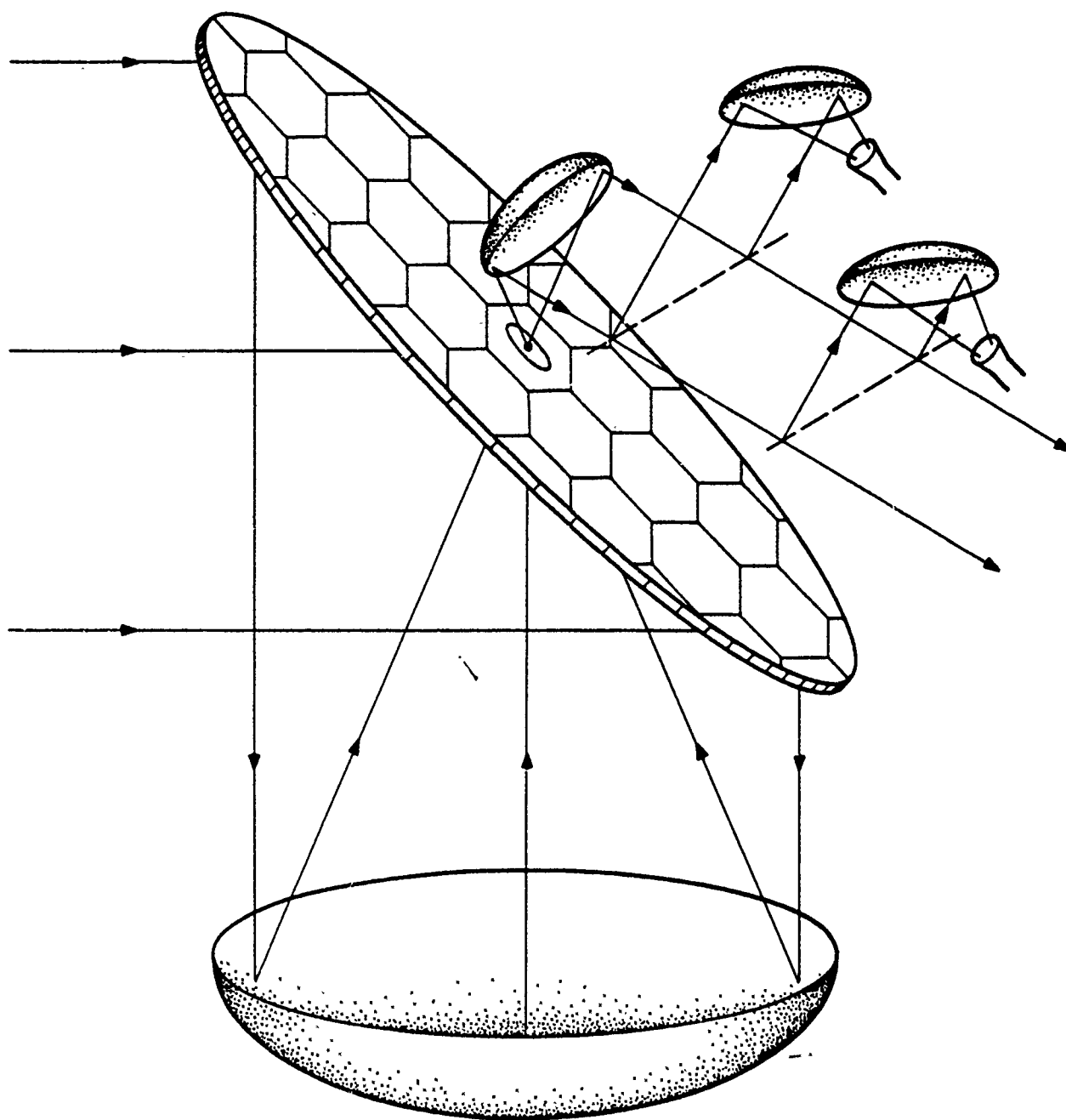


Figure 10. Measured Azimuth Pattern Expanded



**Segmented Mirror Antenna**

# **A Segmented Mirror Antenna for Radiometers\***

**S.W.Lee, B. Houshmand, M. Zimmerman and R. Acosta\*\***

## **Abstract**

The present antenna is designed for the radiometer application on the planned NASA Earth Science Geostationary Platforms in the 1990's. The antenna consists of two parts: a regular parabolic dish of 5 meters in diameter which converts the radiation from feeds into a collimated beam, and a movable mirror that redirects the beam to a prescribed scan direction. The mirror is composed of 28 segmented planar conducting plates, mostly one square meter in size. Based on a physical optics analysis, we have analyzed the secondary pattern of the antenna. For frequencies between 50 and 230 GHz, and for a scan range of  $\pm 8^\circ$  (270 beamwidths scan at 230 GHz), the worst calculated beam efficiency is 95%. To cover such a wide frequency and scan range, each of the 28 plates is individually controlled for a tilting less than  $4^\circ$ , and for a sliding less than 0.5 cm. The sliding is done at discrete steps. At 230 GHz, a step size of 2 mil is sufficient. The plate positions must be reset for each frequency and for each scan direction. Once the position is set, the frequency bandwidth of the antenna is very narrow.

---

\*This work is supported by NASA grant NAG 3-419.

\*\*The first three authors are with the Electrical and Computer Engineering Department, University of Illinois, Urbana, IL, 61801; Acosta is with NASA Lewis Research Center, Cleveland, OH, 44135.

## I. Introduction

A key instrument on the proposed NASA Earth Science Geostationary Platforms (ESGP) is a large radiometer antenna for atmospheric sounding. Even in its "near term" version, the antenna has unprecedented stringent requirements [1], namely,

- i) There are 4 to 6 operating frequency bands between 50 to 230 GHz.
- ii) The antenna diameter is about 5 meter (  $833 \lambda$  to  $3,833 \lambda$  )
- iii) The beam is to scan  $\pm 8^\circ$  for the earth-coverage in both azimuthal and elevation planes, corresponding to roughly  $\pm 60$  to  $270$  beamwidth scan.
- iii) The beam efficiency, defined by the fractional power in the main beam should exceed 95%.

The above requirements immediately rule out several antenna candidates:

- i) Currently space-qualified phase shifters are not available for frequency higher than 20-40 GHz. Even in the next ten years, any beam forming scheme relying on phase shifter is risky.
- ii) The 5:1 band makes it impractical to use arrays with discrete radiating elements.
- iii) Conventional reflector scan is achieved by feed displacement [2,3]. Such a scan normally has a range of tens of beamwidth, which is one order of magnitude short of the requirement. The use of cluster feed [3,4] for scan compensation again depends on the availability of phase shifters. Furthermore, the degree of compensation is generally not good enough to produce 95% beam efficiency .

We are left with few alternatives, one of which is the mechanically scanned reflector antenna. After all, such an antenna has been the overwhelming choice of existing radiometers [5]. In the ESGP application, however, there is one problem. As a whole, the 5-meter antenna is too large to be moved on a geostationary satellite. If we are able to



segment the reflector surface into smaller pieces, the scan motion may be more manageable. This is the motivation behind our study of a segmented mirror antenna.

The original mirror antenna concept [6-8] can be simply explained below. As sketched in Figure 1, the antenna consists two parts: a regular parabolic dish which converts a spherical wave into a plane wave, and a tilting mirror whose motion redirects the plane wave into a desired scan direction. The advantages of the mirror antenna are as follows:

- i) The antenna main beam is always collimated (no aperture phase error) for all scan angles, and for all frequencies.
- (ii) The mirror is tilted at an angle  $\theta$  to obtain a  $2\theta$  beam scan. The factor of 2 aids in mechanical motion.

Its disadvantage is that, in addition to the regular parabolic dish, the extra mirror is just as large as or larger than the dish. Tilting the mirror is not any easier than tilting the dish. Hence the mirror antenna in its original form is not suitable for the ESPG application. We propose to segment the mirror into 28 pieces, and move each piece individually. By so doing, we gain in some mechanical aspects, but we lose in other mechanical as well as some electrical aspects. Does the trade-off pay? We shall examine this question from an electrical viewpoint, namely, to what extent does the antenna radiation characteristics deteriorate because of the use of 28 small plates instead of a one-piece mirror. The mechanical question of controlling the motion of the plates is not addressed here.

## II. Mirror Antenna

The mirror antenna can be symmetrical [8], or offset. In the present application, it must be offset because of the multiple frequency band requirement. An offset mirror antenna is sketched in Figure 1. A regular parabolic reflector is to convert the incoming spherical wave from its feed into a plane wave going in the (-y) direction. A 45° mirror at position A redirects the plane wave to the +z direction, which in the far field produces the on-axis main beam. To scan the beam to a new direction  $(\theta_0, \phi_0)$ , the mirror is tilted to a new position B such that the unit normal of surface A, denoted by  $\hat{z}_{45}$ , moves to  $\hat{n}$ . Here

$$\hat{n} = \hat{x} n_1 + \hat{y} n_2 + \hat{z} n_3 \quad (2.1)$$

where

$$n_1 = \frac{u_0}{2 n_2}, \quad n_2 = \sqrt{\frac{1 + v_0}{2}}, \quad n_3 = \frac{w_0}{2 n_2}$$

$$u_0 = \sin \theta_0 \cos \phi_0, \quad v_0 = \sin \theta_0 \sin \phi_0, \quad w_0 = \cos \theta_0$$

There are different ways that  $\hat{z}_{45}$  can be tilted into  $\hat{n}$ . We choose the one sketched in Figure 2, namely,  $\hat{z}_{45}$  rotates about the  $\hat{y}_{45}$  axis by an azimuthal angle AZ, and then moves up by an elevation angle EL, where

$$AZ = \tan^{-1} \left( \frac{\sqrt{2} n_1}{n_2 + n_3} \right) \quad (2.2a)$$

$$EL = \sin^{-1} \left[ \frac{1}{\sqrt{2}} (n_2 - n_3) \right] \quad (2.2b)$$

Several remarks on the mirror antenna are in order.

(1) When the mirror is at the no-scan position A, the footprint of the incoming plane wave is an ellipse with semi-axes  $(a, \sqrt{2} a)$ , as shown in Figure 3. Normally, one may choose the mirror slightly oversized to avoid spillover loss at scanning.

(2) Apart from the possible spillover loss mentioned above, there is no scan loss due to phase error.

(3) Both the parabolic reflector and the mirror work for all frequencies. Hence, the limiting factor for the frequency bandwidth is that of the feed. For widely separated frequency bands, we may use frequency selective surfaces as multiplexier to circumvent the feed bandwidth problem. An example is sketched in Figure 4.

(4) To scan the main beam by a polar angle  $\theta_0$  from the z-axis, the mirror tilts about  $\theta_0/2$ . For the ESPG application, a typical dish diameter is 5 meter. When the beam scans  $\pm 8^\circ$  in elevation, the linear motion of the mirror edges is

$$(\pm 4^\circ) \times \frac{\pi}{180^\circ} \times \sqrt{2} a = \pm 25 \text{ cm} \quad (2.3)$$

At the intended scan rate for the radiometer, the motion distance in (2.3) is too large to be acceptable for a satellite antenna.

### III. Segmented Mirror

The motion of a large (one-piece) mirror presents mechanical problems. To circumvent this difficulty, we propose a segmented mirror, which is made of smaller flat plates. Each plate can be individually controlled for tilting and sliding motions. The segmentation can be done in different ways. An example is shown in Figure 4, where 28 rectangular plates are used. Other plate shapes such as triangles or hexagons may be just as useful. We choose the rectangles for simple analysis ( an extension to hexagons are being carried out ).

Scanning with the plate mirror is achieved in the manner described below. At the no-scan position, all the plates are aligned on the  $45^\circ$  plane (Figure 5). To scan the beam to the direction

$$\hat{k}^T = \hat{x} u_0 + \hat{y} v_0 + \hat{z} w_0 \quad (3.1)$$

Each plate is undergone two motions:

- (1) The plate is tilted to the common direction  $\hat{n}$  in (2.1) in the manner sketched in Figure 2.
- (2) Along the normal direction to the  $45^\circ$  plane, a typical plate is slid by a distance  $\Delta$  from its old center position, described by

$$\vec{r}_1 = \hat{x} x_1 + \hat{y} y_1 + \hat{z} (-y_1) \quad (3.2)$$

to a new center position described by

$$\vec{r}_2 = \hat{x} x_1 + \hat{y} \left( y_1 + \frac{\Delta}{\sqrt{2}} \right) + \hat{z} \left( -y_1 + \frac{\Delta}{\sqrt{2}} \right) \quad (3.3)$$

The sign of  $\Delta$  is positive if point 2 is in front of point 1.

The sliding distance  $\Delta$  is determined by the condition that all the reflected rays from plates must be collimated in the direction  $\hat{k}_r$ . Referring to Figure 5, we note that the difference in path length between ray 32 and a reference ray 04 is given by

$$\begin{aligned}\delta &= 32 - 04 = (-y_2) - \vec{r}_2 \cdot \hat{k}_r \\ &= (-1) \left[ u_0 x_1 + (1 + v_0 - w_0) y_1 + \frac{1}{\sqrt{2}} (1 + v_0 + w_0) \Delta \right]\end{aligned}\quad (3.4)$$

Set the path difference to zero, and the solution of  $\Delta$  from (3.4) is

$$\Delta_{\text{optical}} = \frac{-\sqrt{2}}{1 + v_0 + w_0} [u_0 x_1 + (1 + v_0 - w_0) y_1] \quad (3.5)$$

The subscript "optical" signifies the fact that, when (3.5) is satisfied, rays are collimated in the  $\hat{k}_r$  direction for all frequencies. It is a simple matter to show that by sliding a distance  $\Delta_{\text{optical}}$ , point 1 is moved to point 5, which is on the plane BB'. Then the plate mirror becomes the one-piece mirror sketched in Figure 1, which, of course, is not the case of interest.

Now, for a fixed frequency, we may set  $\delta$  in (3.4) to a multiple of wavelengths, and still maintain the perfect beam collimation. Thus, alternative solutions of  $\Delta$  are

$$\Delta = \frac{-\sqrt{2}}{1 + v_0 + w_0} [u_0 x_1 + (1 + v_0 - w_0) y_1 + m \lambda] \quad (3.6)$$

where  $m = 0, \pm 1, \pm 2, \dots$ . We choose  $m$  to obtain a minimum  $|\Delta|$ .

Let us summarize our results. Point 1 at  $(x_1, y_1, z = -y_1)$  is the center point on a plate lying on the  $45^\circ$  plane (Figure 5). In order to scan the beam in the direction of  $\hat{k}_r$  in (3.1). The plate must be tilted to the new direction  $\hat{n}$  in (2.1), and slid by a distance  $\Delta$  in (3.6). Then the reflection from the plate produces a perfectly collimated beam in direction  $\hat{k}_r$ .

The use of  $\Delta$  in (3.6), instead of that in (3.5), allows us to slide each plate by a very small distance. As a consequence, the mechanical problem of one-piece mirror is circumvented. The price that we paid, of course, is that the mirror works only for a given frequency. For wide band applications, we must slide each plate to a new position for each new frequency in a time sharing manner.

The linear motion of the plate edge due to tilting is also reduced because the plate size is smaller. For the 28-plate mirror in Figure 4, the largest plate has a dimension of  $0.2a$  instead of  $a$ . Consequently, the maximum linear motion is reduced by a factor of 5 (i.e., 5 cm instead of 25 cm; described in (2.3)).

Let us consider the possible phase error over the antenna aperture (or individual plate) due to scan. If a plate is slid by the  $\Delta_{\text{optical}}$  in (3.5), there is no phase error. In order to reduce the distance of sliding, we use  $\Delta$  in (3.6) instead. As long as there is only a fixed frequency, there is still no phase error. The range of  $\Delta$  is within  $\pm\Delta_{\text{max}}$ , where

$$2\Delta_{\text{max}} = \frac{\sqrt{2} \lambda}{1 + \cos \theta_0 - |\sin \theta_0|} \quad (3.7)$$

The above sliding range is plotted as a function of frequency and scan angle in Figure 7. For scan up to  $\pm 8^\circ$  at 50 GHz, the range is 0.46 cm, or 180 mils. Mechanically, it is desirable to have discrete, instead of continuous sliding. Analogous to the term used on phase shifters, an N-bit sliding has  $2^N$  steps in the range given in (3.7). Commonly, a 4-bit sliding (16 steps) is adequate. For a fixed sliding step  $d$ , the maximum possible phase error is given by

$$\text{Max. phase error} = 127^\circ \left( 1 + \cos \theta_0 + |\sin \theta_0| \right) \frac{d}{\lambda} \quad (3.8)$$

which is plotted in Figure 8. To avoid high sidelobes, the phase error is usually kept within  $11^\circ$  (corresponding to a 4-bit phase shifter). For scan up to  $\pm 8^\circ$  at 230 GHz, the sliding step

should not exceed 2.4 mils. We choose 2 mils a step in our later calculations. In summary, phase error for the present antenna arises from

- (i) operation at a frequency which deviates from the designed frequency
- (ii) sliding of the plates is discrete at a predetermined step instead of continuous.

In Section V, we shall examine the effect on antenna patterns due to the phase error.

A remark on segmentation is in order. Segmentation of a large antenna into smaller pieces has been known and practiced for a long time[9,10]. If a doubly curved reflector is segmented into flat plates, phase error is present with or without scan. A high beam efficiency antenna can not be achieved in such a way. Our segmentation does not have this phase error problem at all, because our reflector (mirror) is flat to begin with. This price we paid of course is to have an extra parabolic dish.

#### IV. Antenna Secondary Pattern Computation

To calculate the antenna secondary pattern, we apply the standard physical optics (PO) theory by integrating the induced PO current on all plates. To this end, it is convenient to introduce the local plate coordinate for each plate (Figure 6). The center of the plate coordinate is at point 2, which is described in (3.3). The base vectors of the plate coordinates are  $(\hat{x}_{45}, \hat{y}_{45}, \hat{z}_{45} = \hat{n})$ . By choosing the tilting motion described in Figure 2, we find

$$\begin{bmatrix} \hat{x}_{45} \\ \hat{y}_{45} \\ \hat{z}_{45} \end{bmatrix} = \bar{T} \begin{bmatrix} \hat{x} \\ \hat{y} \\ \hat{z} \end{bmatrix} \quad (4.1)$$

where matrix  $\bar{T}$  has elements

$$\begin{aligned} t_{11} &= s_1, & t_{12} &= \frac{(s_3 + s_2)}{\sqrt{2}}, & t_{13} &= \frac{(s_3 - s_2)}{\sqrt{2}} \\ t_{21} &= s_4, & t_{22} &= \frac{(s_6 + s_5)}{\sqrt{2}}, & t_{23} &= \frac{(s_6 - s_5)}{\sqrt{2}} \\ t_{31} &= s_7, & t_{32} &= \frac{(s_9 + s_8)}{\sqrt{2}}, & t_{33} &= \frac{(s_9 - s_8)}{\sqrt{2}} \\ s_1 &= \cos(AZ), & s_2 &= 0, & s_3 &= -\sin(AZ) \\ s_4 &= -\sin(EL) \sin(AZ), & s_5 &= \cos(EL), & s_6 &= -\sin(EL) \cos(AZ) \\ s_7 &= \cos(EL) \sin(AZ), & s_8 &= \sin(EL), & s_9 &= \cos(EL) \cos(AZ) \end{aligned}$$

(AZ, EL) given in (2.2)

Before tilting and sliding, let a typical point on the plate be denoted by a in Figure 7, and is described by a position vector in the main coordinate



$$\vec{r}_a = \hat{x} x_a + \hat{y} y_a + \hat{z} z_a \quad (4.2)$$

After tilting and sliding, the same point on the plate is now located at position b described by

$$\vec{r}_b = \hat{x} x_b + \hat{y} y_b + \hat{z} z_b \quad (4.3)$$

It can be shown that

$$\begin{bmatrix} x_b \\ y_b \\ z_b \end{bmatrix} = \bar{\bar{T}}^T \begin{bmatrix} x_a - x_1 \\ y_a - y_1 \\ 0 \end{bmatrix} + \begin{bmatrix} x_a \\ (y_a + \Delta)/\sqrt{2} \\ (-y_a + \Delta)/\sqrt{2} \end{bmatrix} \quad (4.4)$$

Here  $(x_1, y_1, 0)$  is the coordinator of center point 1. Matrix  $\bar{\bar{T}}$  is given in (4.1), and the subscript T is the transpose operator.

In the present pattern computation, we ignore part of the beam waveguide analysis. The feed is simply modelled by a point source located at the total point F of the parabolic reflector (Figure 1). The patterns in the E-plane, and H-plane are, respectively,

$$(\cos \theta_f)^{QE}, \text{ and } (\cos \theta_f)^{QH} \quad (4.5)$$

when  $\theta_f$  is the polar angle in the feed coordinates. It is known that (4.5) is a good approximation for common scalar feed horns used in radiometer applications. We trace the geometrical optic rays from the feed through the parabolic reflector, and then to a typical plate, which has been tilted and slid to the correct position for scanning. According to PO, the induced current on the plate is

$$\vec{J}_s = 2 \hat{n} \times \vec{H}^i \quad (4.6)$$

Next, we integrate the above current over all plates to calculate the antenna secondary pattern. In this step, results in (4.1) and (4.4) are used.

In the radiometer application, the important parameter is the beam efficiency  $e$ . Consider the antenna in transmitting mode (Figure 1),  $e$  is defined by

$$e = \frac{P_{\text{beam}}}{P_{\text{feed}}} \quad (4.7a)$$

where

$$P_{\text{feed}} = \text{total power radiated from the feed} \quad (4.7b)$$

$$P_{\text{beam}} = \text{power in the reference polarization in the main beam} \quad (4.7c)$$

The extent of the 'main beam' has been customarily defined as [4, p22-27]:

- i) the null to null beamwidths, or
- ii) "the 2.5 times half-power beamwidth".

Definition ii) is particularly useful in measured patterns where the null may not be easily identifiable. In this paper, we use definition i).

For a beam on the boresight of the antenna ( $\theta_0 = 0^\circ$  in Figure 1), the pattern is azimuthally symmetrical, and there is no ambiguity in applying (4.7). Let us denote the half null-to-null beamwidth by  $\theta_{\text{null}}$ . However, as the beam scans to a new direction ( $\theta_0, \phi_0$ ), the symmetry is lost, and the null-to-null width varies in different pattern cuts. Then, instead of using (4.7c), we define

$$P_{\text{beam}} = \text{power within a cone around the main beam direction } (\theta_0, \phi_0), \quad (4.8)$$

with the half cone angle equal to  $\theta_{\text{null}}$  obtained in the no-scan case

The present pattern computation is based on PO described in (4.6). It is known that power conservation does not hold within the PO theory. In other words, if one integrates the antenna secondary pattern over the  $4\pi$  radian space, the resultant power does not in general equal to the incident power intercepted by the reflector. For this reason, one has to be careful in calculating the beam efficiency.

For the reason just explained, a direct evaluation of (4.7a) for scanned cases often leads to inaccurate results. We use an indirect evaluation, namely,

$$e = e_{\text{spill}} * e_{\text{miss}} * e_{\text{block}} * e_{\text{pat}} \quad (4.9)$$

where (Figure 1)

$e_{\text{spill}}$  = fractional of the incident feed power intercepted by the parabolic dish (counting the spillover loss).

$e_{\text{miss}}$  = fractional of the incident power from the parabolic dish intercepted the elliptical mirror (counting the incident power missing the mirror).

$e_{\text{block}}$  = fractional of the power received by the mirror but not blocked by the feed (counting the power blocked by the feed).

$e_{\text{pat}}$  = fractional of power in the secondary pattern confined in the main beam.

Ideally,  $e_{\text{pat}}$  should be the ratio of the  $p_{\text{beam}}$  in (4.8) and  $p_{\text{pat}}$ , which is the total radiated power in the secondary pattern in the  $4\pi$  radian space. Unfortunately,  $p_{\text{pat}}$  cannot be readily calculated. The reasons are as follows:

- (i) Any PO-based pattern computation method gives accurate pattern result only in the angular region near the main beam. Means for calculating far-out lobes exist, such as adding fringe currents, using edge diffraction, etc. Their implementation is difficult, and may not be worthwhile.
- (ii) In practical antennas, far-out lobes are mostly affected by supporting struts, and near-by structures. Patterns calculated from models do not include those factors and are not realistic.

- (iii) For radiometers, far-out lobes usually point to a cold environment. Whether their power is included in  $p_{\text{pat}}$  is often not critical.

In the present analysis, we approximate  $p_{\text{pat}}$  by  $p_{\text{pat}}(\text{approx})$ , where

$p_{\text{pat}}(\text{approx})$  = power within a cone around the main beam direction  $(\theta_0, \phi_0)$ , with the half cone angle equal to  $10 * \theta_{\text{null}}$ , instead of the  $4\pi$  radian space.

As explained earlier,  $\theta_{\text{null}}$  is the half null-to-null beamwidth in the no-scan case.

## V. Numerical Results

For numerical results, we consider the ESPG radiometer antenna specified in Section I. The parameters of the antenna are chosen as follows (Figure 1):

$a$  = parabolic dish diameter = 5m

$f$  = focal length of the dish = 2 m, which makes  $f / D = 0.4$

$d$  = discrete sliding step size of the mirror = 2 mils

$QE = QH$  = feed pattern index defined in (4.5) = 2.0, which results in 17 dB edge taper in the reflector aperture.

Polarization is horizontal ( $E_x$  in the mirror aperture)

Results are summarized below.

i) **Boresight patterns.** For the no-scan case, the patterns for the lowest and the highest frequencies are plotted in Figures 9 and 10. Even with discrete sliding, there is no phase error in the mirror aperture. Hence, the pattern is smooth and sharp nulls. Sidelobes are lower than -30 dB.

ii) **Scanned Patterns.** When the beam scans, effects of both mirror segmentation and the sliding discretization come in. The worst case occurs at the highest frequency and the extreme scan angle. Patterns are shown in Figures 11 and 12. The sidelobe level is at 24 dB. In the  $\phi_0 = 90^\circ$  scan (downward scan), the pattern is characterized by grating lobe effect due to the segmentation, i.e. lobes at  $\theta = 7.91^\circ, 8.09^\circ$ , etc. The 2-mil step raises the near-in sidelobes and fills in the nulls as expected.

iii) **Beamwidth and Null Position.** For the boresight beam, the results are shown in Figure 13. Those calculated results fit approximately the following formula:

$$3 \text{ dB Beamwidth} \approx 105^\circ \lambda / D \quad (5.1)$$

$$\text{Null to Null Beamwidth} \approx 148^\circ \lambda / D \quad (5.2)$$

It follows that

$$\text{Null to Null Beamwidth} = K * (3 \text{ dB Beamwidth}) \quad (5.3)$$

where  $K = 1.4$ . These formulas are valid for the present -17 dB edge taper, which is typical for radiometer antennas. The usual definition of "2.5 times half-power beamwidth" [4] for the approximated null to null beamwidth appears to mean  $K = 2.5 / 2 = 1.25$ .

iv) **Power Distribution.** Around the main beam, a cone is defined. The percentage of total radiated power from the feed within the cone is plotted in Figures 14 and 15 for two 230 GHz cases. The losses attributed to spillover, feed blockage, and possible missing of the mirror is less than 2% of power. The rest of power is mostly confined in the main beam, even for the 8° scan case.

v) **Beam Efficiency.** We plot beam efficiency as a function of scan angle in the diagonal plane ( $\phi_0 = 45^\circ$ ). Except for the boresight beam, the efficiency in an average sense increases with the decreasing sliding step size and therefore the aperture phase error. The phase error is of the 'hit or miss' nature, which explains the uneven variation of the curves. At 230 GHz, the 95% efficiency can be met with a 2 mil step size, which is  $1/26$  of wavelength. At 50 GHz, the same is met with a 10 mil step ( $1/24$  wavelength).

vi) **Frequency Bandwidth Without Resetting Mirror Positions.** Once the mirror position is set for a center frequency, the antenna has a very narrow bandwidth. This is due to the fact that segmentation destroys the equal-path-length condition. In Figure 18, we show a 4° scanned pattern under the condition that the mirror is set for 230 GHz, but the antenna is operated at 227 GHz. The beam is shifted by about 2 beamwidths. The directivity is lowered by 3 dB, and sidelobe is increased significantly. In Figures 19 and 20, we show the beam efficiency for a band of operating frequency. The center frequencies are 50 and 230 GHz, respectively. The rapid degradation in efficiency is due to shift in the main beam away from the cone defined around the desired scan angle. The 95% beam efficiency can be maintained for  $\pm 0.4$  GHz at 4° scan, and for  $\pm 0.2$  GHz at 8° scan.

## VI. Conclusion

The radiation pattern of a segmented mirror antenna has been analyzed by a PO theory. The antenna is capable of maintaining 95% beam efficiency over the a wide frequency and scan range. The scan is achieved by tilting and sliding the mirror within a very small range. As far as the electric performance is concerned, the antenna appears to be a viable candidate for the ESGP.

The possible 'show stopper' may come from the required precision control of the segmented mirror. Specifically, in a space environment,

- i) can the mirror be moved in an increment of  $0.01^\circ$  tilting for one beamwidth scan, and 2 mil sliding for a maximum  $11^\circ$  phase error ?
- ii) can the above motion be done fast enough to meet the required scan rate?

These questions remain to be answered<sup>1</sup>.

Other than ESPG, the segmented mirror antenna is a useful antenna in its own right. Especially when the operating frequency is not as high as 230 GHz, the mechanical precision problem is eased.

**Acknowledgement:** Valuable discussions with Dr. J. Shiue, Mr. K. Moeller, Dr. A. J. Gasiewski, Dr. C. Raquet, and Dr. C. Rogers are appreciated.

---

<sup>1</sup>According to Dr. Craig Rogers of Virginia Polytechnic Institute and State University, requirement i) appears to be feasible.

## References

- [1] A. J. Gasiewski and D. H. Staelin, "Science requirements for passive microwave sensors on Earth Science Geostationary Platforms", paper presented at NASA Technology Workshop for Earth Science Geostationary Platforms, NASA Langley Research Center, Hampton, Virginia; September 21-22, 1988.
- [2] Y. Rahmat-Samii, "Reflector antennas," Chapter 15, *Antenna Handbook Theory Applications and Design*, eds. Y. T. Lo and S. W. Lee, New York: Van Nostrand Reinhold, 1988.
- [3] M. Zimmermann, S. W. Lee, R. Rahmat-Samii, B. Houshmand, and R. Acosta, "A comparison of reflector antenna designs for wide-angle scanning," paper presented at NASA Technology Workshop for Earth Science Geostationary Platforms, NASA Langley Research Center, Hampton, Virginia; September 21-22, 1988.
- [4] R. Acosta, "Active feed array compensation for reflector antenna surface distortion," Technical Report TM-100826, NASA Lewis Research Center, Cleveland, OH, June 1988.
- [5] J. C. Shiue and L. R. Dod, "Remote sensing and microwave radiometry," Chapter 22, *Antenna Handbook Theory Applications and Design*, eds. Y. T. Lo and S. W. Lee, New York: Van Nostrand Reinhold, 1988.
- [6] B. L. Lewis and J. P. Shelton, "Mirror scan antenna technology," *IEEE International Radar Conference Record*, April 1980, pp. 279-283.
- [7] D. D. Howard and D. C. Cross, "Mirror antenna dual-band lightweight mirror design," *IEEE Trans. Antennas and Propagation*, vol. AP-35, pp. 286-294, March 1985.
- [8] D. C. Cross, D. D. Howard, and J. W. Titus, "Mirror-antenna radar concept," *Microwave J.* pp. 323-335, May 1986.
- [9] S. Dasgupta and Y. T. Lo, "A study of the coma-corrected zoned mirror by diffraction theory," *IEEE Trans. Antennas and Propagation*, vol. AP-11, pp. 130-139, March 1961.
- [10] A. C. Schell, "The multiplate antenna," *IEEE Trans. Antennas and Propagation*, vol. AP-16, pp. 550-560, Sept. 1966.



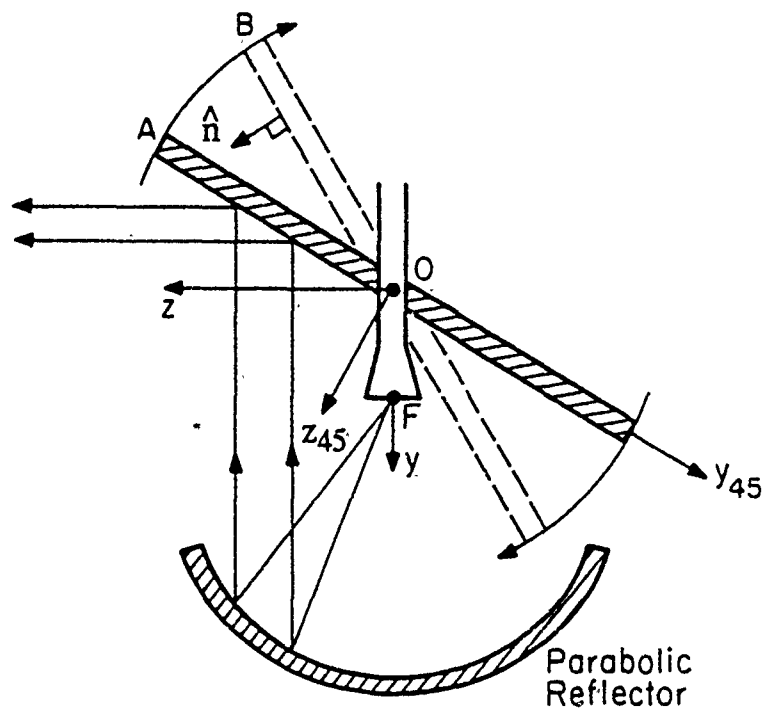


Figure 1. A conventional mirror antenna. The mirror plate is normally at position  $A$  to produce an on-axis beam ( $\theta_0 = 0$ ), and is tilted about point  $O$  for beam scanning.

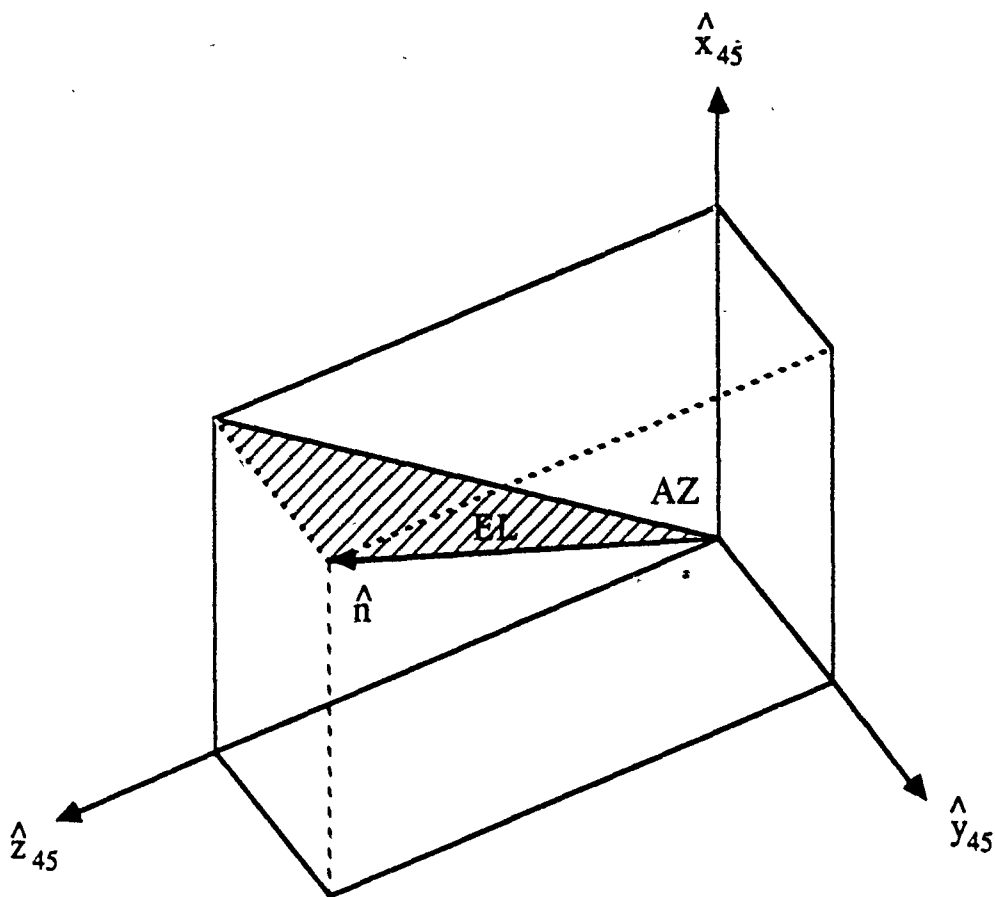


Figure 2. For no-scan case, the normal of the mirror is in the direction  $\hat{z}$ . To scan the beam, the normal is tilted to the new direction  $\hat{n}$ . The tilting is done first in the azimuthal and then the elevation direction.

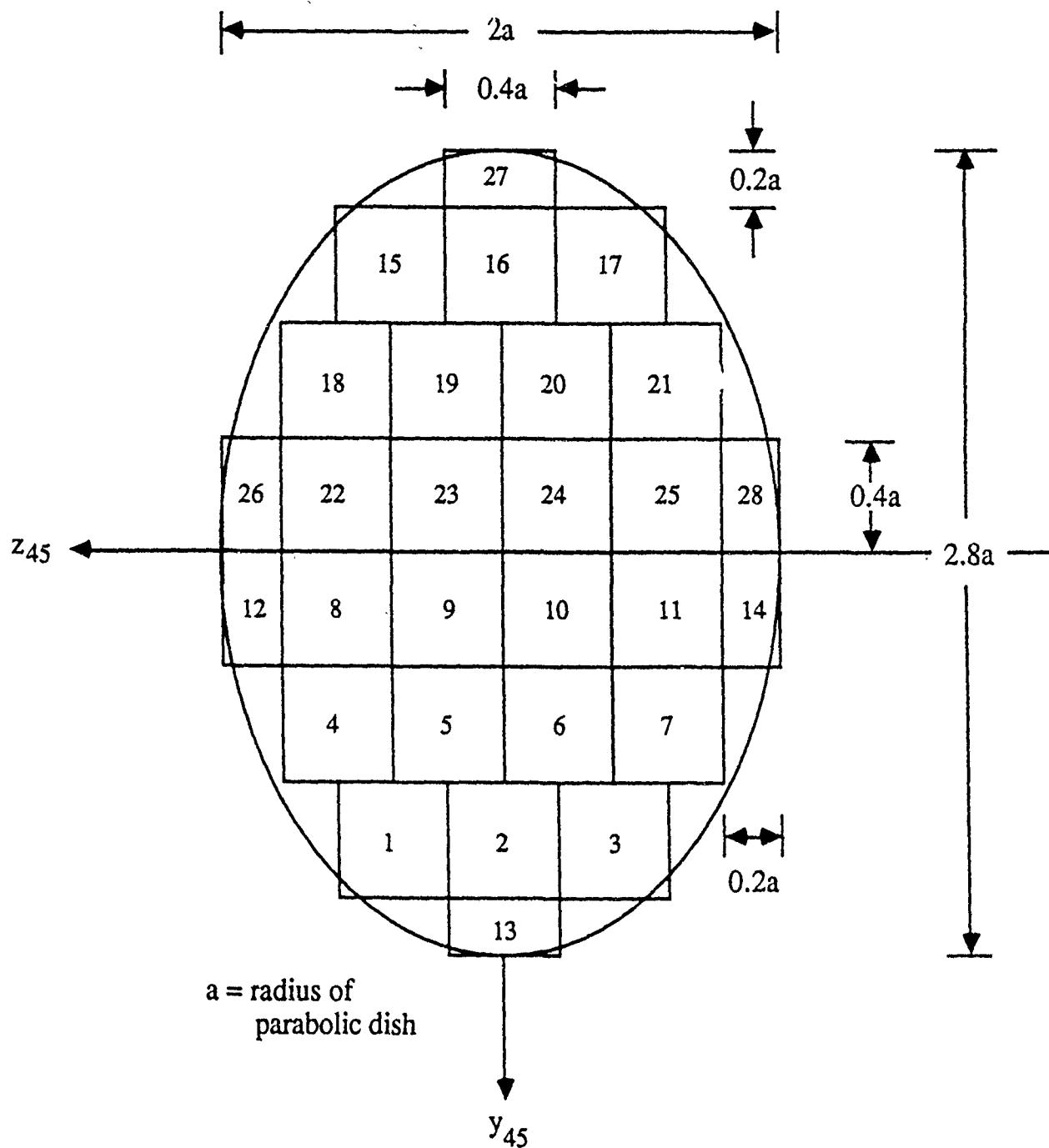


Figure 3. The elliptical mirror is divided into 28 rectangular plates, which can be individually controlled for tilting and sliding.

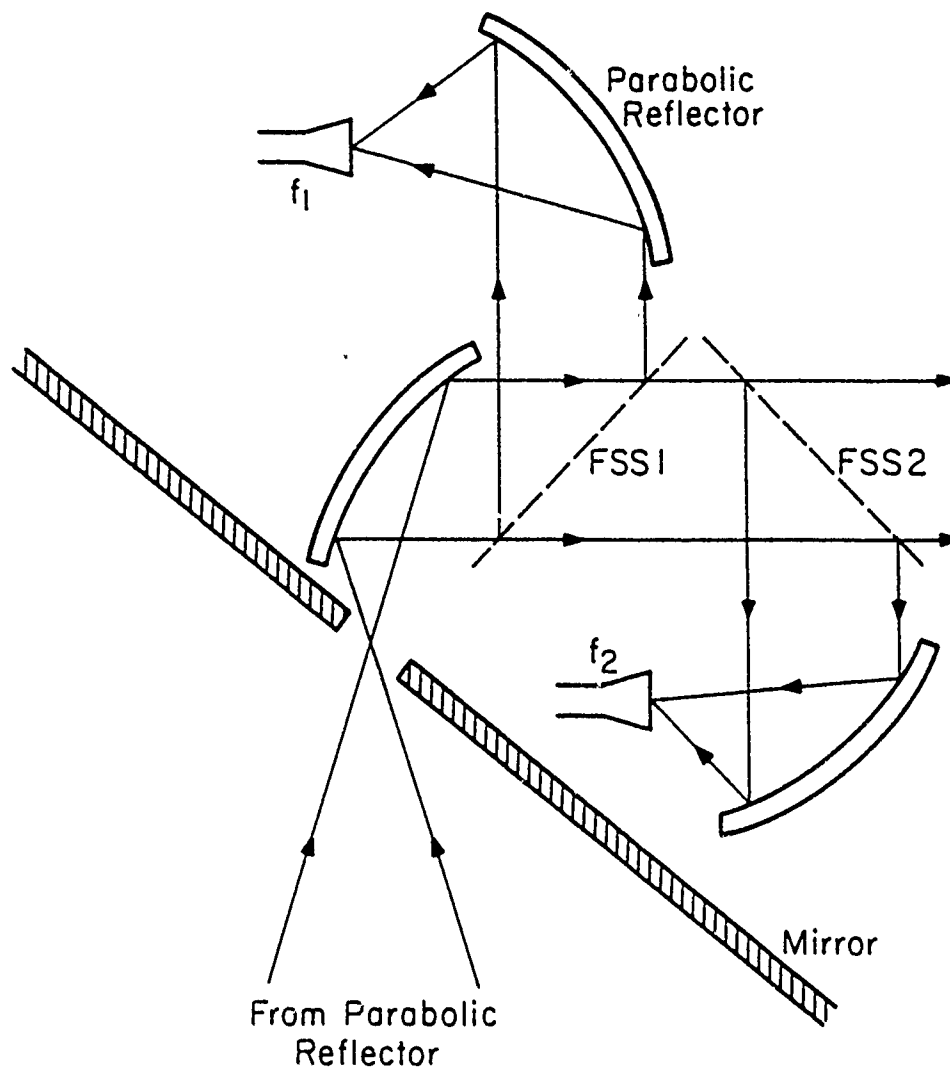


Figure 4. Multiple feeds for different frequency bands can be arranged with beam waveguides, and frequency selective surfaces.

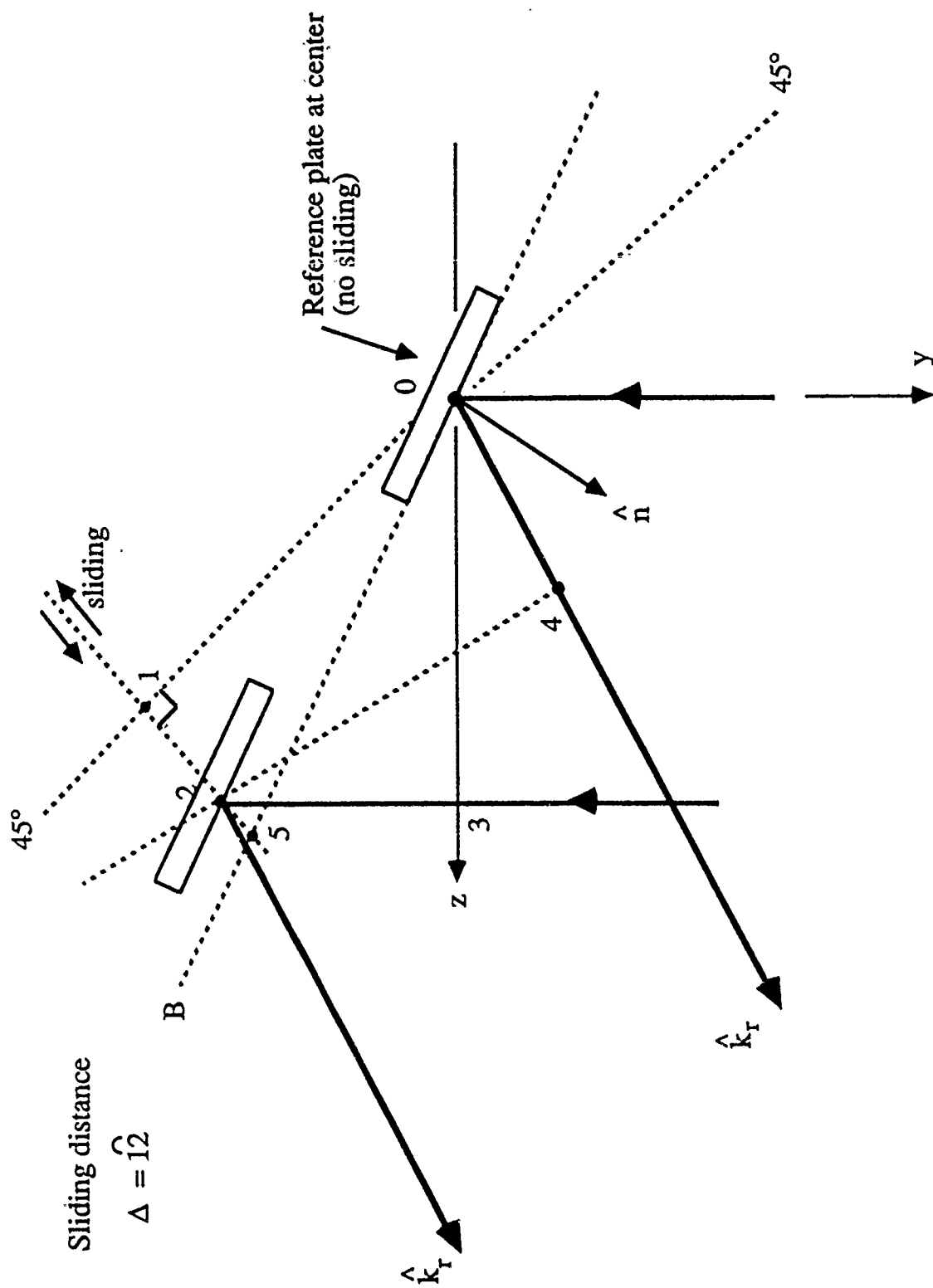


Figure 5. To scan the beam with the plate mirror, a typical plate is tilted to the common direction  $\hat{n}$  given in (2.1), and is slid from point 1 to point 2.

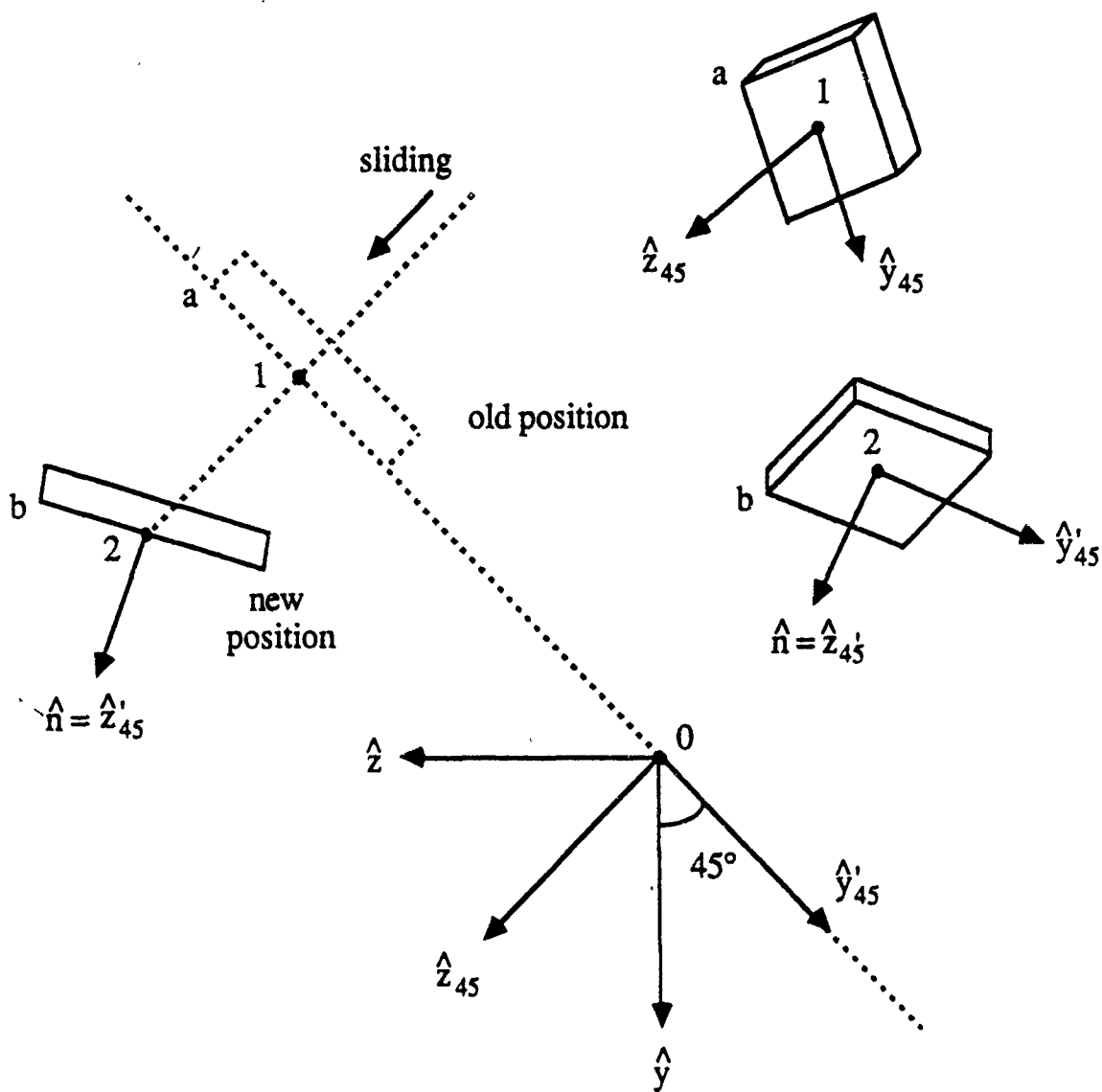


Figure 6. Main coordinate with base vectors  $(\hat{x}, \hat{y}, \hat{z})$  centered at 0.  
 For plate 2 at its new position, we introduce the local plate  
 coordinate with base vector  $(\hat{x}'_{45}, \hat{y}'_{45}, \hat{z}'_{45} = \hat{n})$ .

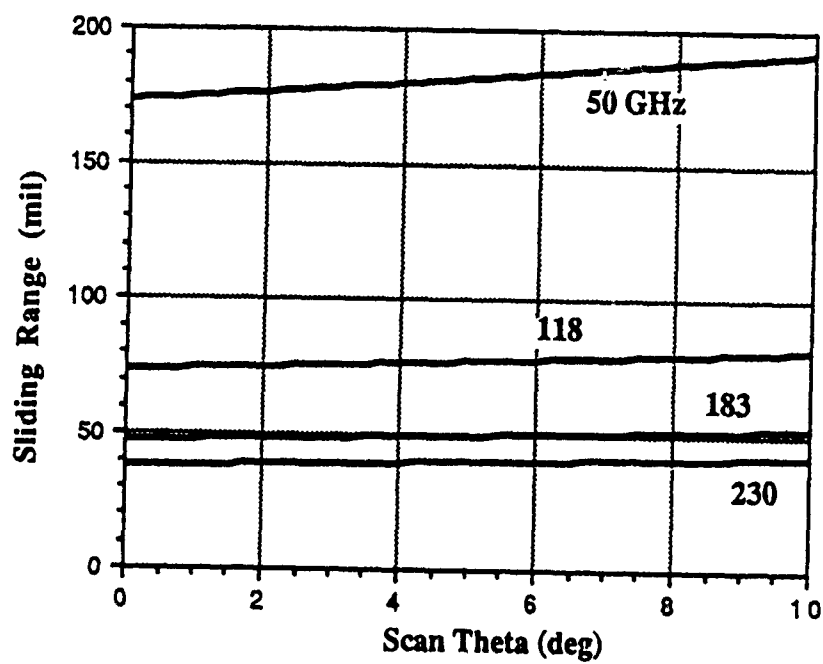


Figure 7. Sliding range as a function of scan angle calculated from Equation (3.7)

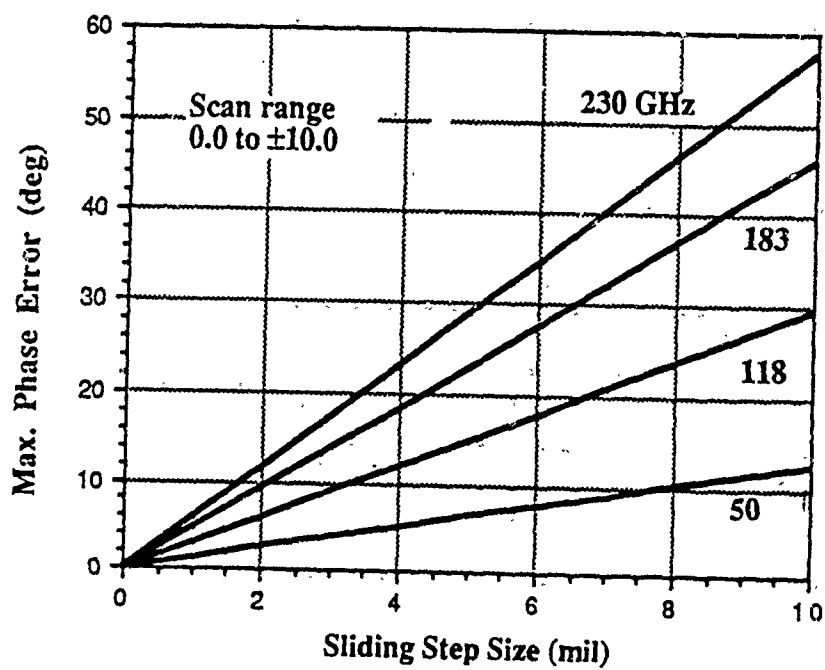


Figure 8. Maximum phase error in the mirror aperture due to the discretization of sliding.



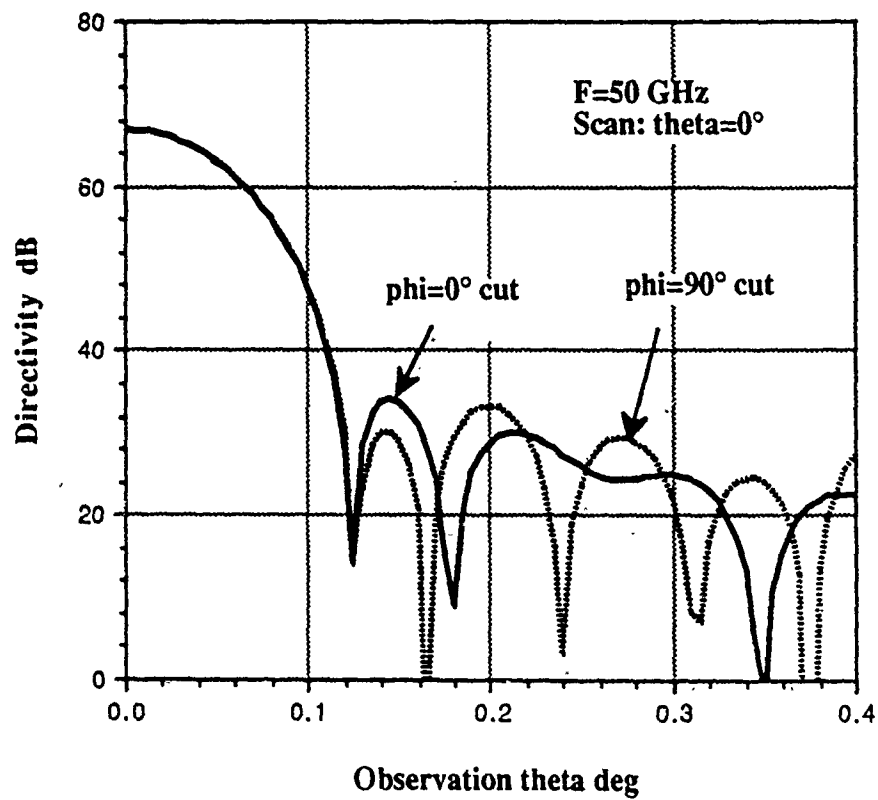


Figure 9. Secondary pattern of the segmented mirror antenna in the no-scan case.  $F = 50$  GHz.  $\Phi = 0^\circ$  is the E-plane.

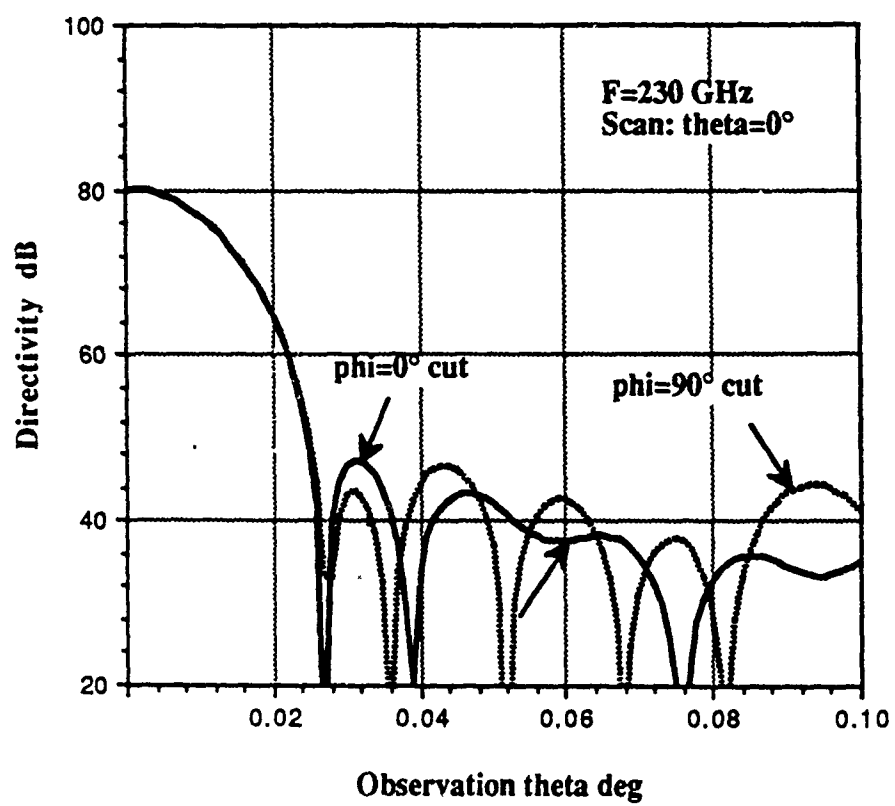


Figure 10. Same as Figure 9 except  $F = 230$  GHz.

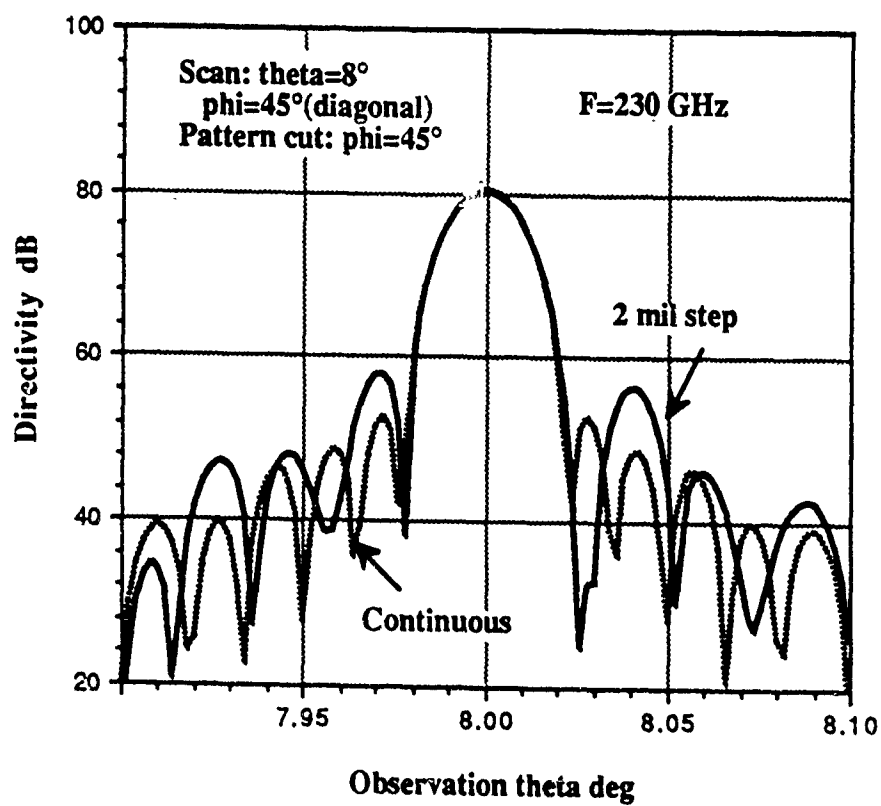


Figure 11. Secondary pattern of the segmented mirror antenna when the beam scans to  $(\theta_0 = 8^\circ, \phi_0 = 45^\circ)$ . Mirror plates sliding is either continuous or at 2-mil a step.

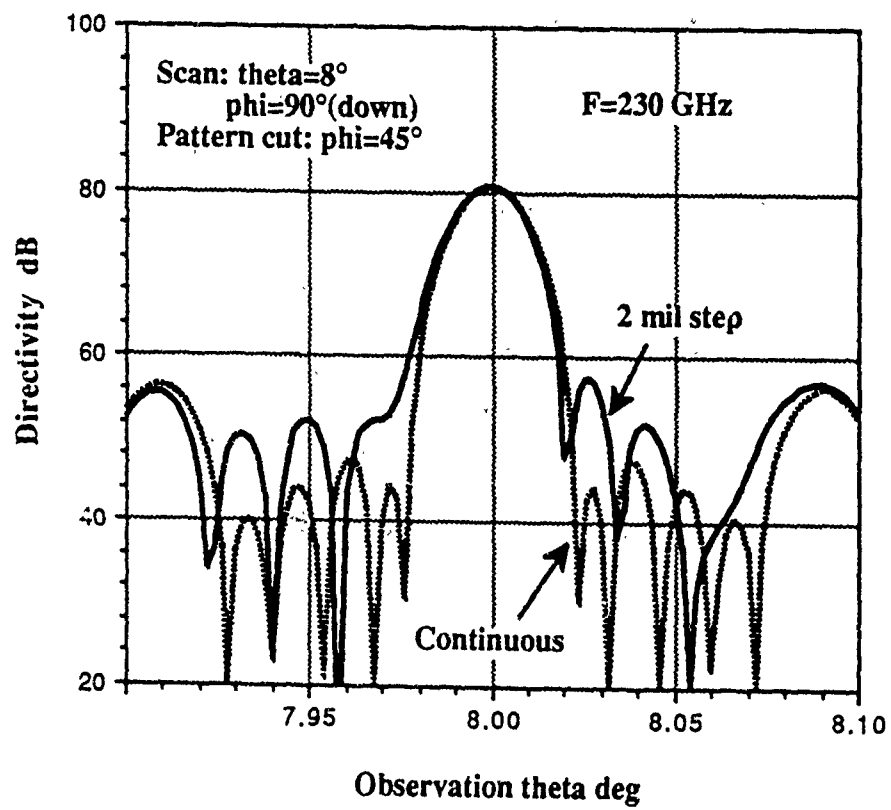


Figure 12. Same as Figure 11 except the beam scans to  $(\theta_0, \phi_0 = 90^\circ)$ .

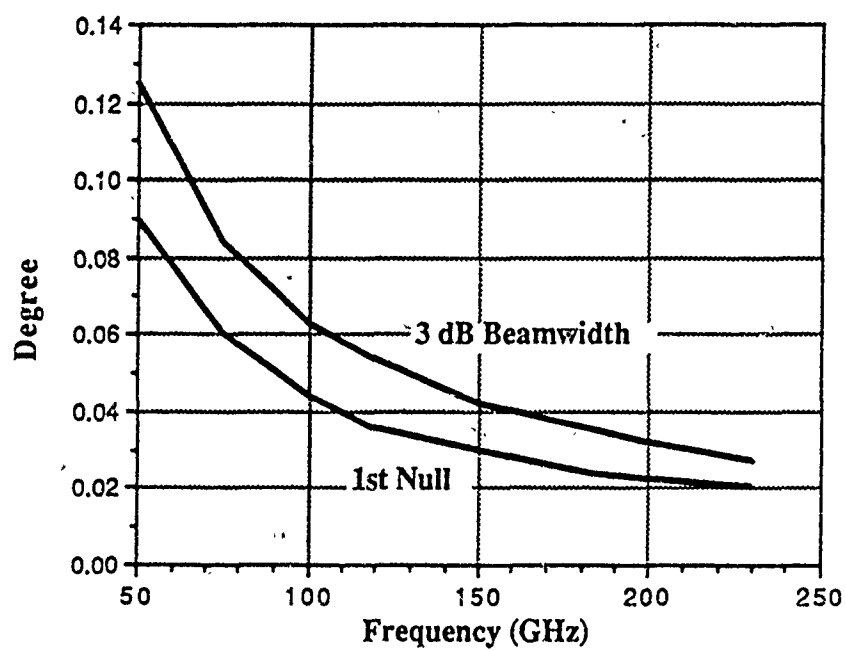


Figure 13. Beamwidth and the first null position for the boresight beam ( $\phi_0 = 0^\circ$ ).

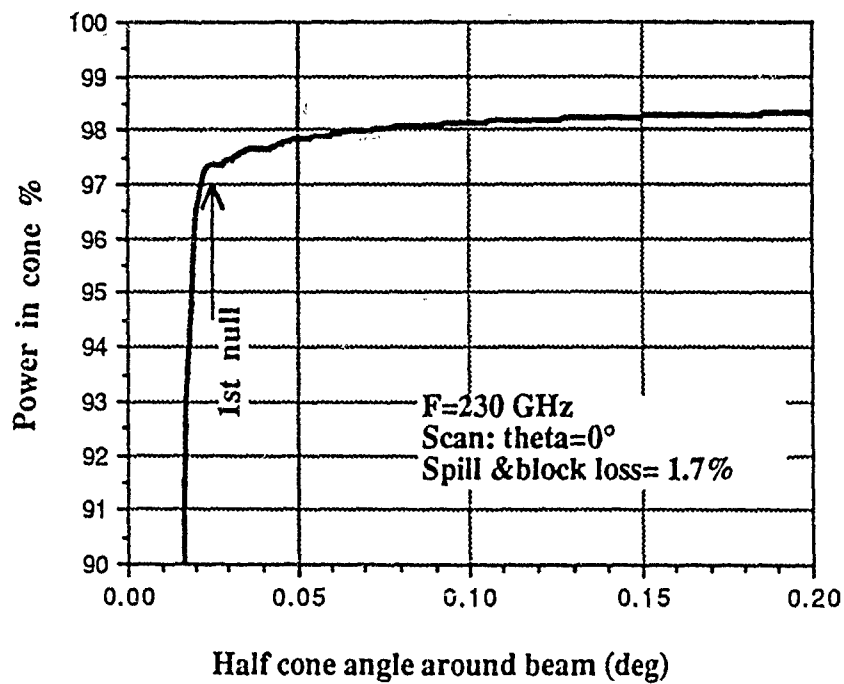


Figure 14. Percentage of power in a cone around the main beam normalized by the total power radiated from the feed.

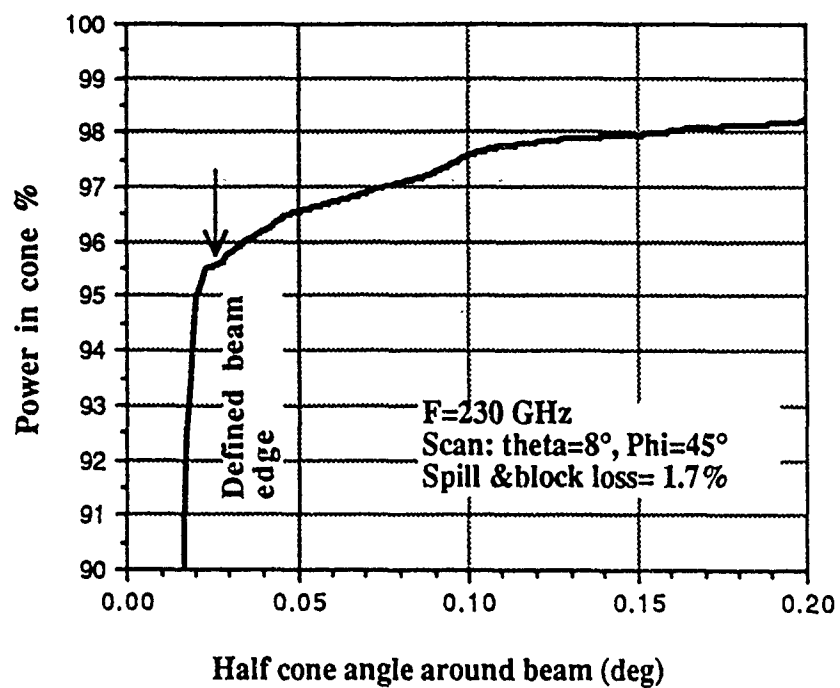


Figure 15. Same as Figure 14 except the beam is at ( $\theta_0 = 8^\circ$ ,  $\phi_0 = 45^\circ$ ). The sliding step size is 2 mils.

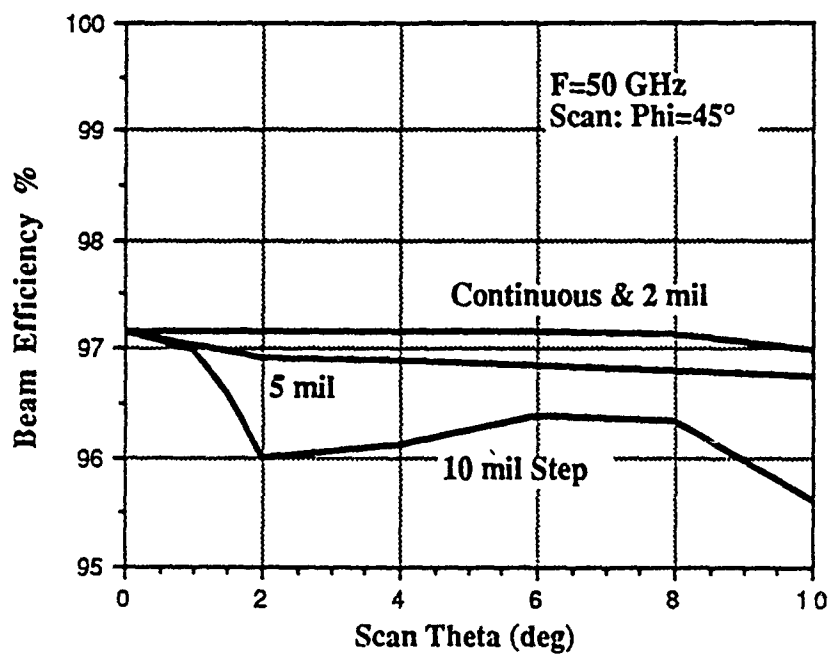


Figure 16. Beam efficiency as a function of scan angle in the diagonal plane for different sliding step sizes.  $F = 50$  GHz. Because the phase error due to discrete sliding is of 'hit and miss' nature, the curves are not monotonic.



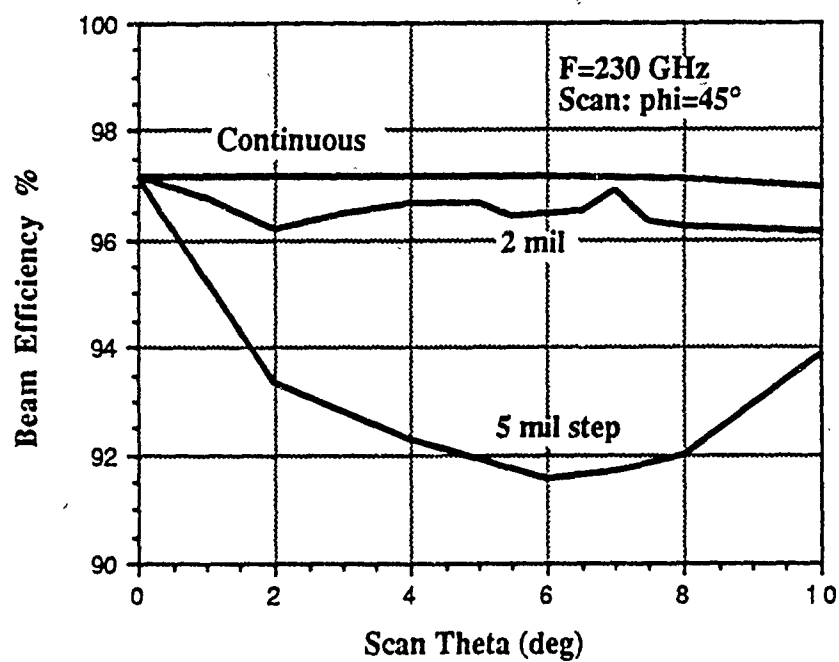


Figure 17. Same as Figure 16 except  $F = 230$  GHz.

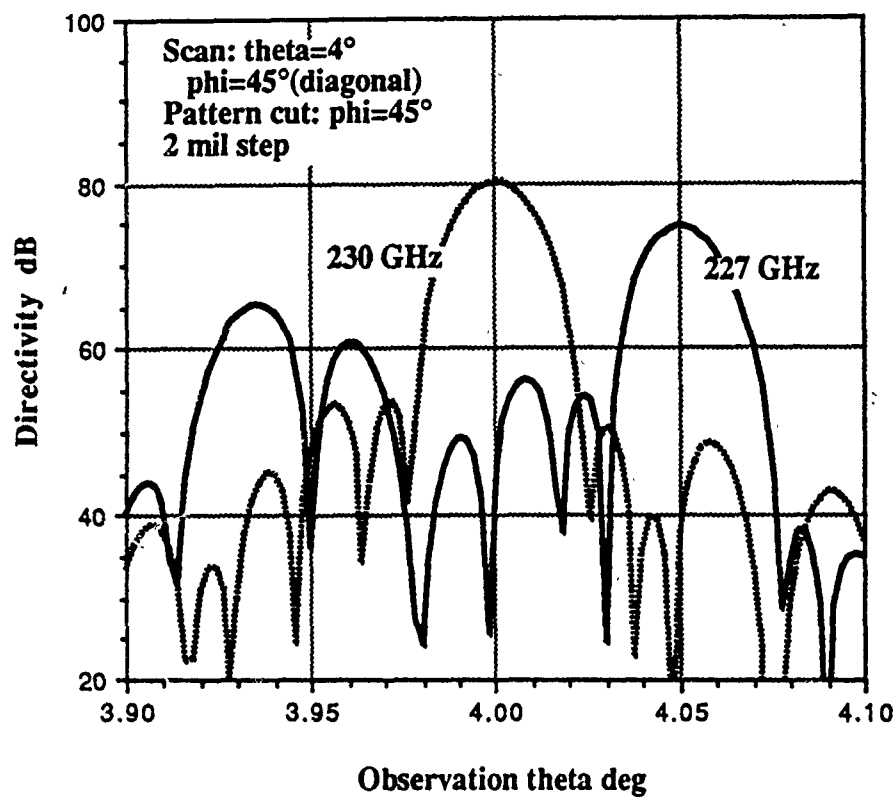


Figure 18. In the diagonal plane,  $4^\circ$  scanned secondary patterns at the central frequency 230 GHz, and at a nearby frequency 227 GHz. The mirror position is set for the central frequency.

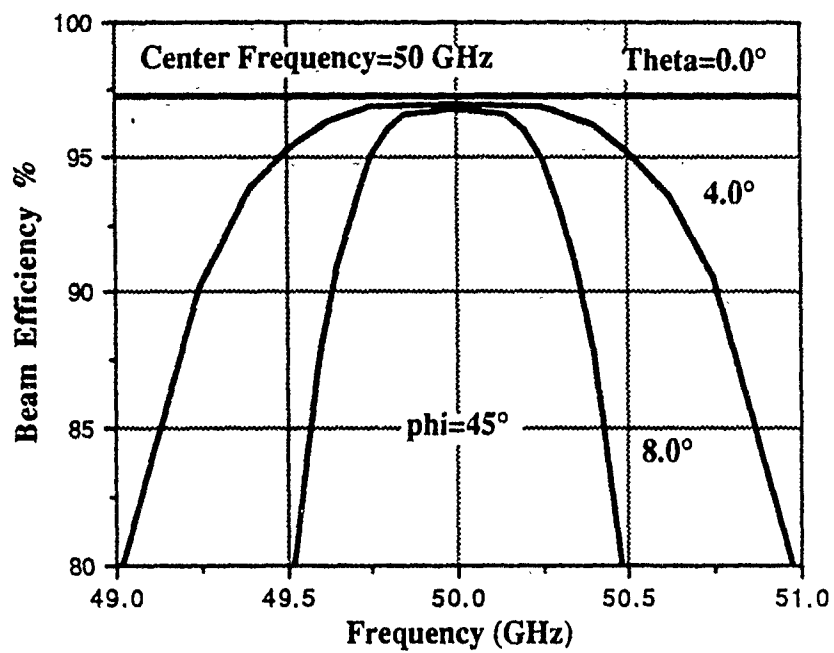


Figure 19. Beam efficiency of the segmented mirror antenna as a function of frequency. The plate position is set for  $F = 50$  GHz.

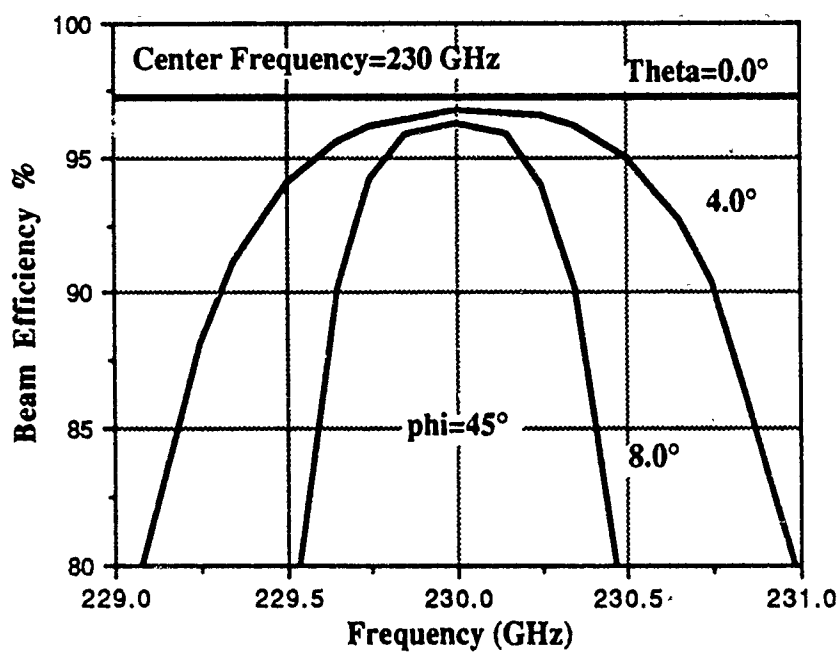


Figure 20. Same as Figure 19 except  $F = 230$  GHz.

## **REFLECTOR PERFORMANCE DEGRADATION DUE TO AN ARCJET PLUME**

H. Ling\*, G. A. Hallock\*, H. Kim\*, B. W. Birkner\* and A. Zaman\*\*

\* Department of Electrical and Computer Engineering  
The University of Texas at Austin  
Austin, TX 78712-1084

\*\* NASA Lewis Research Center  
Cleveland, OH 44135

### **ABSTRACT**

An arcjet thruster is an electrothermal propulsion device which heats a nitrogen-hydrogen mixture by means of a high temperature arc discharge. This device is an attractive candidate for auxiliary propulsion applications on satellites. One important issue which arises in the actual spacecraft integration of this technology is the environmental contamination caused by the arcjet plume, especially on microwave communication systems. In this study, the effect of an arcjet plume on the performance of on-board reflector antennas is addressed. The arcjet plume is modeled as a weakly ionized plasma. Spatial permittivity distribution of the plume is approximated based on the cold plasma model and the available measurement data of the electron density profile. Geometrical optics is applied to determine the ray path as well as the transmitted field strength through the inhomogeneous plume. The far field performance degradation of the reflector in the presence of the plume is calculated for simple two-dimensional geometries. As the electron density increases (corresponding to higher arcjet power), a gradual

degradation of the main beam in terms of both gain loss and beam broadening is observed. In addition, significant beam squinting can occur.

## **1. INTRODUCTION**

The use of electric propulsion for stationkeeping and attitude control could potentially extend the lifetime of modern communication satellites up to ten years. This represents cost savings in the tens of millions of dollars. An arcjet thruster is one such electrothermal propulsion device which heats a nitrogen-hydrogen mixture by means of a high temperature arc discharge. The heated propellant is then ejected through a nozzle to produce thrust. Current research indicates that specific impulse levels above 400 sec are attainable<sup>1</sup>, making arcjets a very attractive candidate. NASA and the Air Force are currently developing arcjet systems, with initial flight testing to begin in approximately 5 years.

For this technology to be accepted by the communication satellite industry, it is necessary to demonstrate an acceptable level of signal degradation to and from the spacecraft. The arcjet produces a weakly ionized plasma, which modifies the free-space dielectric normally surrounding the satellite. This causes both refraction and attenuation of the microwave signals. In this paper, the effect of an arcjet plume on the performance of on-board reflector antennas is studied (Fig. 1). The arcjet plume is modeled as an inhomogeneous scatterer with a smoothly varying refractive index. The spatial distribution of the refractive index is related to the measured electron density data based on the cold plasma model. Since the plume size of interest is more than several wavelengths in extent, geometrical optics is used to calculate the microwave propagation through the plume. The trajectory, phase,

amplitude and polarization of the high frequency ray field transmitted through the plume are computed numerically, and are verified against available closed form solutions in several special media. The far field performance degradation of the reflector in the presence of the plume is calculated. This information is crucial in determining realistic constraints on the location and maximum power output of the arcjet for spacecraft integration.

## 2. PLUME MODEL

Available experimental data<sup>2</sup> taken from Langmuir probe measurements indicate that the arcjet plume consists of a partially ionized plasma with a maximum electron density which ranges from  $10^6$  to  $10^{12}$  cm<sup>-3</sup>, depending on the ignition condition. These numbers correspond to a plasma frequency which ranges from Megahertz all the way up to the tens of Gigahertz regime. For plasma temperature below 1 eV, a cold plasma model is adequate for modeling the arcjet plume. The refractive index of the plasma depends only on the electron density for an unmagnetized plasma and is given by

$$N^2 = \frac{\epsilon}{\epsilon_0} = 1 - \frac{\omega_p^2}{\omega^2}, \quad \omega_p^2 = \frac{n_e e^2}{m \epsilon_0} \quad (1)$$

where  $\omega_p$  is the plasma frequency and  $n_e$  is the electron density. For the arcjet plume the spatial distribution of the electron density is found to be approximately

$$n_e = \frac{a_1}{r^2} \exp(-0.03 \theta) \text{ cm}^{-3} \quad (r \text{ in cm, } \theta \text{ in degrees}) \quad (2)$$

where  $r = \sqrt{x^2 + z^2}$  is the distance from the nozzle. Contour plots of the relative dielectric constant generated using the above model ( $a_1 = 3 \times 10^{12} \text{ cm}^{-1}$ ) are shown in Fig. 2. Figs. 2(a) and 2(b) are the plume profile at 3 GHz and 1 GHz, respectively. The contour levels are 0.02 apart. The outermost contour represents a relative dielectric constant of 0.98. It is observed that the physical size of the plume increases as the frequency of the microwave signal is decreased. However, the electrical size of the plume (measured in terms of the free space wavelength) remains essentially independent of the frequency.

### 3. RAY TRACING IN INHOMOGENEOUS PLUME

The solution of geometrical optics fields in an isotropic inhomogeneous medium was first derived by Luneburg more than thirty years ago and is documented in detail by Kline and Kay<sup>3</sup>, Born and Wolf<sup>4</sup> and most recently, Bremmer and Lee<sup>5</sup>. Most numerical implementations of the solution for arbitrary media have been associated with studies of radio wave propagation in the ionosphere<sup>6</sup> and have not been widely reported in the antenna community. Below we outline the relevant equations for determining the ray trajectories as well as the associated phase, amplitude and polarization of the ray field along the ray. The trajectory of a ray in space is governed by the vector differential equation

$$\frac{d}{ds} (N \hat{t}) = \nabla N \quad (3)$$

where  $\hat{t}$  is a unit tangent vector of the ray at a point in space and the arclength  $s$  is measured along the curved ray trajectory. For an arbitrary inhomogeneous medium



with index of refraction  $N(\vec{r})$ , the trajectory of a ray can be determined by solving the above equation numerically. By finite differencing, we obtain the difference equation

$$N(\vec{r} + \Delta\vec{r}) \hat{t}(\vec{r} + \Delta\vec{r}) - N(\vec{r}) \hat{t}(\vec{r}) = \Delta s \nabla N(\vec{r} + \Delta\vec{r}/2) \quad (4)$$

which allows us to solve for the subsequent ray trajectory once the initial direction  $\hat{t}$  of a ray at point  $\vec{r}$  is given. When the medium is homogeneous, the ray trajectory reduces to a straight line, as expected.

Once the ray trajectory is determined, the phase variation along the ray path is given by Fermat's relationship:

$$[S(P_1) - S(P_2)] = \int_{P_1}^{P_2} N \, ds \quad (5)$$

The complete geometrical optics field along the ray can also be determined. The field at point  $P_2$  on the ray path is related to that at  $P_1$  by the relationship

$$\vec{E}(P_2) = \hat{e}_2 E(P_1) \sqrt{N_1/N_2} (DF) \exp\{-jk_0[S(P_2)-S(P_1)]\} \quad (6)$$

The quantity (DF), or the so-called divergence factor, can be interpreted physically as a factor which accounts for the spreading of the differential ray tube such that the energy carried by the ray tube remains constant (Fig. 3). The divergence factor is derivable from the first order transport equation and is given by

$$DF = \exp \left\{ -\frac{1}{2} \int_{P_1}^{P_2} (\nabla \cdot \hat{t}) \, ds \right\} \quad (7a)$$

or

$$DF = \exp \left\{ -\frac{1}{2} \int_{P_1}^{P_2} \left( \frac{1}{R_1} + \frac{1}{R_2} \right) ds \right\} \quad (7b)$$

where  $R_1$  and  $R_2$  are the two principal radii of curvature of the wavefront along the ray. Because of its simple geometrical interpretation, equation (7b) is well suited for numerical implementation of the divergence factor.

The polarization vector  $\hat{e}_2$  is related to the polarization vector at  $P_1$ ,  $\hat{e}_1$ , in the following manner:

$$\hat{e}_2 = \hat{n} \cos(\theta_0 - \hat{\theta}) - \hat{b} \sin(\theta_0 - \hat{\theta}) \quad (8)$$

where

$$\theta_0 = \tan^{-1} \left( \frac{\beta_0}{\alpha_0} \right), \quad \hat{\theta} = - \int_{P_1}^{P_2} \frac{ds}{\tau}$$

$$\hat{e}_1 = \hat{n} \alpha_0 + \hat{b} \beta_0$$

$$\text{and } \tau = \frac{(\hat{t} \times \hat{t}') \cdot \hat{t}''}{|\hat{t} \times \hat{t}'|^2}.$$

In the above expressions,  $\hat{n}$ ,  $\hat{b}$  and  $\hat{t}$  are respectively the normal, binormal and tangent vectors along the ray.  $\tau$  is the "torsion" of the ray trajectory in space. It is a measure of the turning of the binormal vector. Note that the polarization vector depends on the torsion of the ray trajectory. For planar ray paths, the torsion is zero and therefore the electric field remains at a constant angle with respect to the normal and binormal vectors along the ray.

#### 4. COMPARISONS OF RAY OPTICS WITH EXACT SOLUTIONS

Based on the ray optics equations in the previous section, a two-dimensional and a three-dimensional ray-tracing program have been developed for arbitrary inhomogeneous media. Results of the programs have been verified against several exact solutions available for special media. One such medium is the so-called "Maxwell's fisheye" which has a refractive index described by

$$N(r) = N_0 / [ 1 + (r/a)^2 ] \quad (9)$$

Shown in Fig. 4 is a set of ray trajectories in Maxwell's fisheye. The results obtained by the numerical routine and by the exact solution (which are circles) agree very well. The divergence factor calculation is also checked against the exact solution derived by Bremner and Lee<sup>5</sup> and found to be accurate. Note that the rays tend to bend toward regions of higher refractive index (the origin in this example). This is easily seen in equation (4) as the ray direction is continuously altered by the direction of the refractive index gradient.

To further validate the geometrical optics calculations, the two-dimensional scattering of a plane wave by an inhomogeneous circular cylinder is next studied (Fig. 5). The formal solution to a class of inhomogeneous cylinders with refractive index profile

$$N(\rho) = \begin{cases} (\rho / a)^\beta & , \rho < a \\ 1 & , \rho > a \end{cases} \quad (10)$$

is available in the literature. This problem has been used to validate the low frequency moment method code by Gong and Glisson<sup>7</sup>. Shown in Fig. 6 is the ray trajectories inside the dielectric cylinder for  $\beta=0.25$ . The discontinuity in the gradient  $\nabla N$  at  $\rho=a$  is small and has been ignored. By invoking Huygen's principle, the scattered far field can be found by integrating the geometrical optics field on the scatterer surface at  $\rho=a$ . The detailed formulation is similar to that reported earlier by Ling, Chou and Lee<sup>8</sup>. Figs. 7(a)-(d) are comparisons of the scattering widths of the cylinder calculated using the ray formulation and those obtained from the exact series expansion solution for cylinders of different radii. It is observed that for scatterer diameter above  $3\lambda$ , the agreement between the two results is very good in the forward scattering region. The ray results predicts zero backscattered field. This is indeed the case as the backscattered strength of the exact solution is more than 40 dB below the forward scattered strength.

## **5. REFLECTOR PERFORMANCE DEGRADATION**

Two-dimensional results of reflector performance degradation in the presence of the plasma plume have been obtained. They provide good physical insights into the plume effect on antenna performance. Shown in Fig. 8 is the geometry of the case under study. The reflector is assumed to have a diameter of 60 cm ( $20\lambda$  at 10 GHz) and is designed to have a uniform aperture illumination. The antenna pattern in the absence of the plume has a 3-dB beamwidth of  $3^\circ$  and a first sidelobe of -13 dB. Using the plume model described in Sec. 2, the ray trajectories through the plume profile with  $a_1=1\times 10^{14} \text{ cm}^{-1}$  at 10 GHz is also plotted in Fig. 8. The initial ray bundle is assumed to be perfectly collimated (after

reflection from the reflector). The plume effect on the ray path at the bottom portion of the beam is apparent. The direction, phase, amplitude and polarization of the ray field transmitted through the plume are computed on an exit aperture plane  $x=50$  cm. Once the transmitted fields are found, the far field of the reflector in the presence of the plume can be found by integrating the geometrical optics fields over the exit aperture. Four antenna patterns are shown in Figs. 9(a)-(d). Fig. 9(a) is the reflector pattern in the absence of the plume. Figs. 9(b)-(d) are patterns corresponding to increasing electron density profiles, from an  $a_1$  value of  $3 \times 10^{12} \text{ cm}^{-1}$  to  $1 \times 10^{14} \text{ cm}^{-1}$ . We observe a gradual degradation of the main beam in terms of both gain loss and beam broadening. In addition, there is significant beam squinting in the degraded pattern. This can be easily understood from the ray tracing plots of Fig. 8 as all rays are bent away from the plume center (toward the positive angles). As a consequence, the sidelobe levels on the positive angle side are also higher than the negative angle side.

Figs. 10(a)-(d) show the pattern degradation for the same reflector and plume parameters when a 10 dB edge taper is introduced onto the reflector aperture. The sidelobe degradation is more apparent in this case.

## 6. SUMMARY

One of the most critical issues which arise in the actual spacecraft integration of arcjet technology is the environmental impact of the arcjet plume, especially on microwave communication systems. In this paper, the effect of an arcjet plume on the performance of on-board reflector antennas is studied. The arcjet plume is modeled as a weakly ionized plasma. Spatial permittivity distribution of the plume

is approximated based on the cold plasma model and the available measurement data of the electron density profile. Geometrical optics is applied to determine the ray path as well as the transmitted field strength through the inhomogeneous plume. The scattered field calculated from geometrical optics is verified against the exact closed form solution in several special media. Finally, the far field performance degradation of the reflector in the presence of the plume is calculated. As the electron density increases (corresponding to higher arcjet power), a gradual degradation of the main beam in terms of both gain loss and beam broadening is observed. In addition, significant beam squinting can occur. Modeling of more realistic antenna configurations in three dimensions are currently under way. The quantitative information generated will be crucial in determining realistic constraints on the location and maximum power output of the arcjet for spacecraft integration.

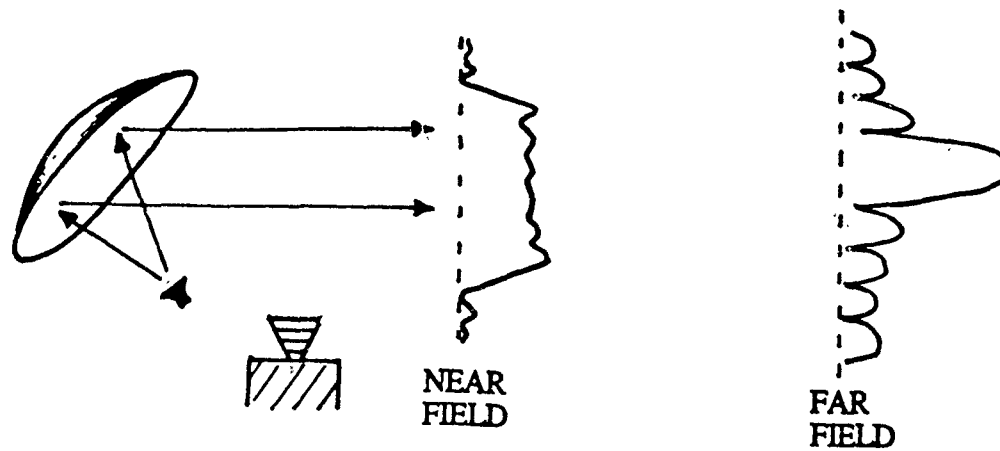
### **ACKNOWLEDGMENTS**

The authors would like to thank L. M. Carney for helpful discussions on the plume characteristics. This work is supported by the NASA Lewis Research Center under Cooperative Agreement NCC 3-127 and in part by the National Science Foundation under Grant ECS-8657524.

### **REFERENCES**

1. Knowles, S. C., Smith, W. W., Curran, F. M. and Haag, T. W. (1987) Performance characterization of a low power hydrazine arcjet, AIAA paper 87-1057.
2. Carney, L. M. (1988) An experimental investigation of an arcjet thruster exhaust using Langmuir probes, NASA Technical Memo, 1988.
3. Kline, M. and Kay, I. W. (1965) Electromagnetic Theory and Geometrical Optics, Wiley, New York, Chap. 5.
4. Born, M. and Wolf, E. (1964) Principles of Optics, MacMillan, New York, Chap. 3.
5. Bremmer, H. and Lee, S. W. (1984) Propagation of a geometrical optics field in an isotropic inhomogeneous medium, Radio Sci. 19: 243-257.
6. Budden, K. G. (1985) The Propagation of Radio Waves, Cambridge, London, Chap. 14.
7. Gong, Z. and Glisson, A. W. (1987) Electromagnetic scattering by circular two-dimensional dielectric cylinders with a specific class of permittivity profiles, IEEE Trans. Antennas Propagat. AP-35: 1315-1319.
8. Ling, H., Chou, R. C. and Lee, S. W. (1989) Shooting and bouncing rays: calculating the RCS of an arbitrarily shaped cavity, IEEE Trans. Antennas Propagat. AP-37: 194-205.

(a) Arcjet OFF



(b) Arcjet ON

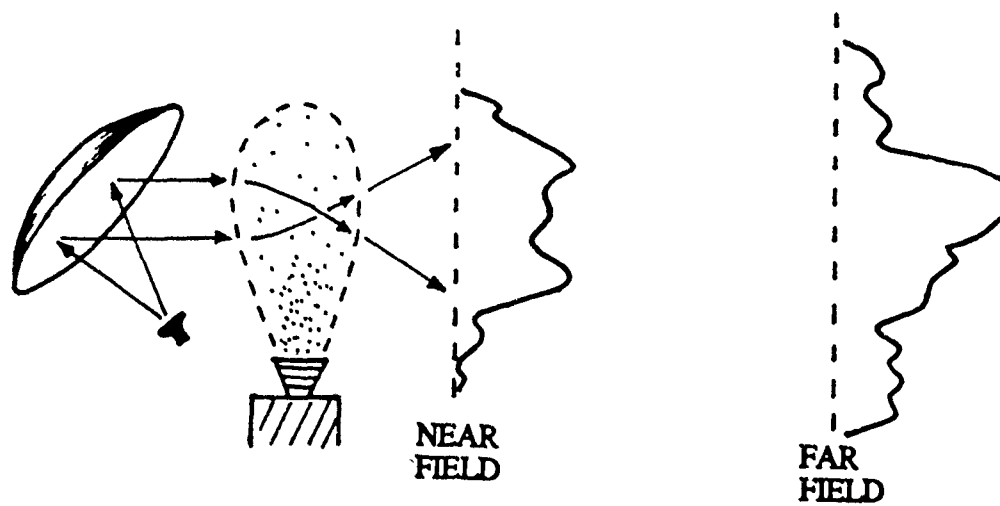


Fig. 1. Reflector performance degradation due to an arcjet plume.



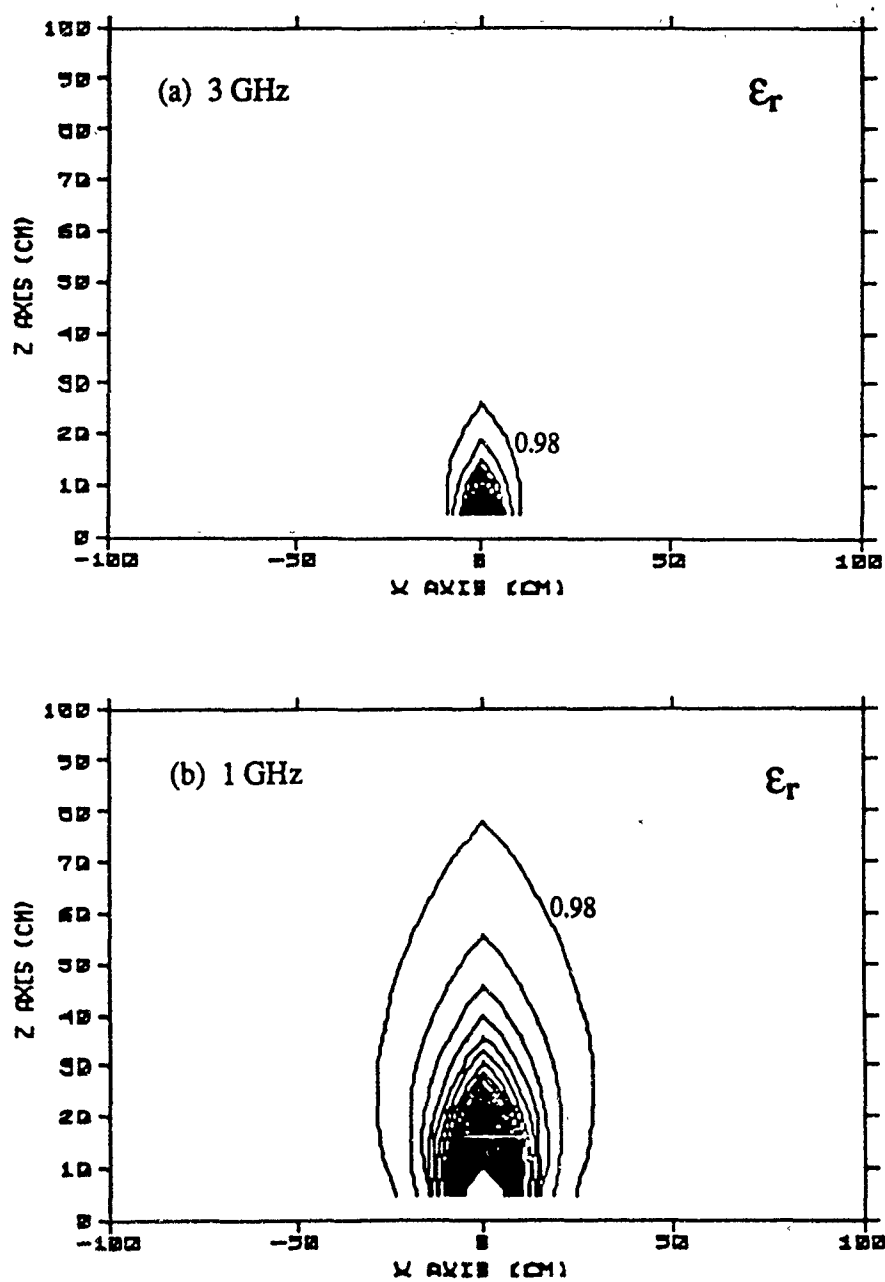
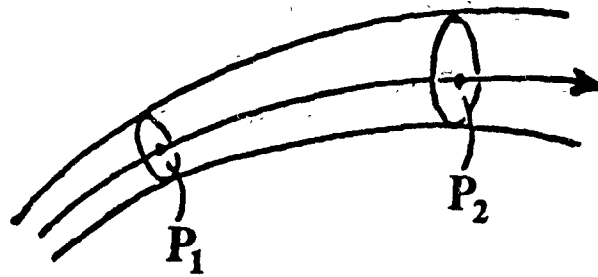


Fig. 2. Relative dielectric constant profile of the plume at (a) 3GHz, and (b) 1 GHz. The contour levels are 0.02 apart.



$$|DF|^2 = \frac{\text{Differential Ray Tube Area at } P_1}{\text{Differential Ray Tube Area at } P_2}$$

Fig. 3. Ray tube spreading is accounted for by the divergence factor (DF).

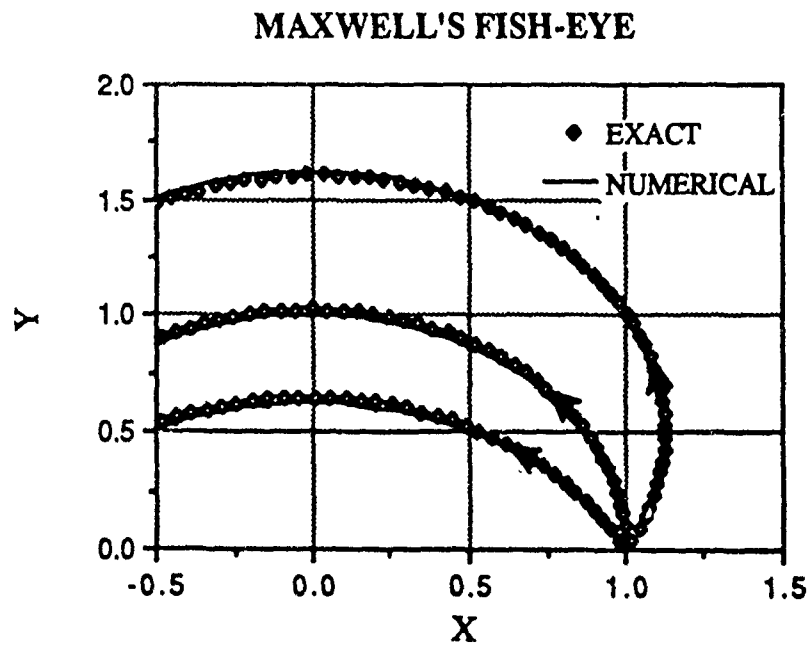


Fig. 4. Ray trajectories in Maxwell's fish-eye. The three rays shown in the figure originate from point (1, 0) with different initial directions.

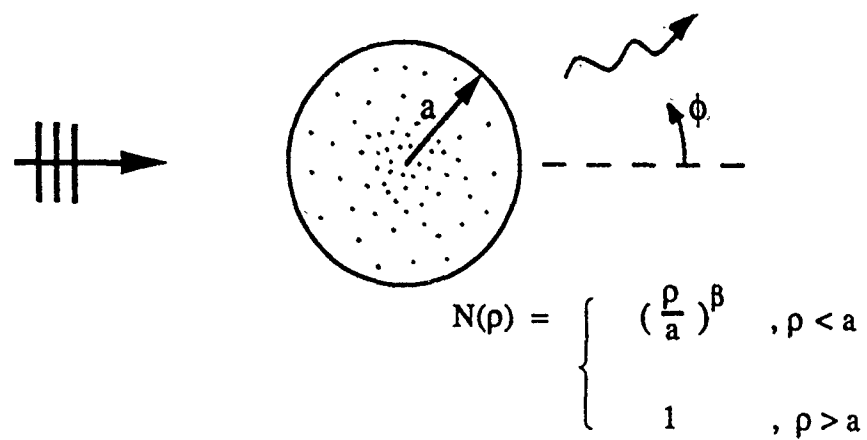


Fig. 5. Two-dimensional scattering of a plane wave by an inhomogeneous circular cylinder.

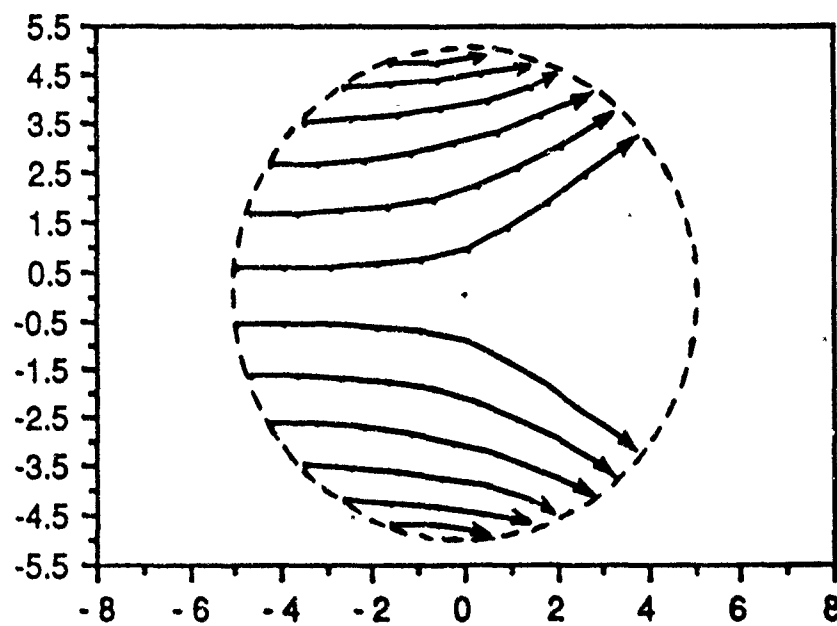


Fig. 6. Ray trajectories inside the inhomogeneous dielectric cylinder of diameter  $10\lambda$  with  $\beta = 0.25$ .

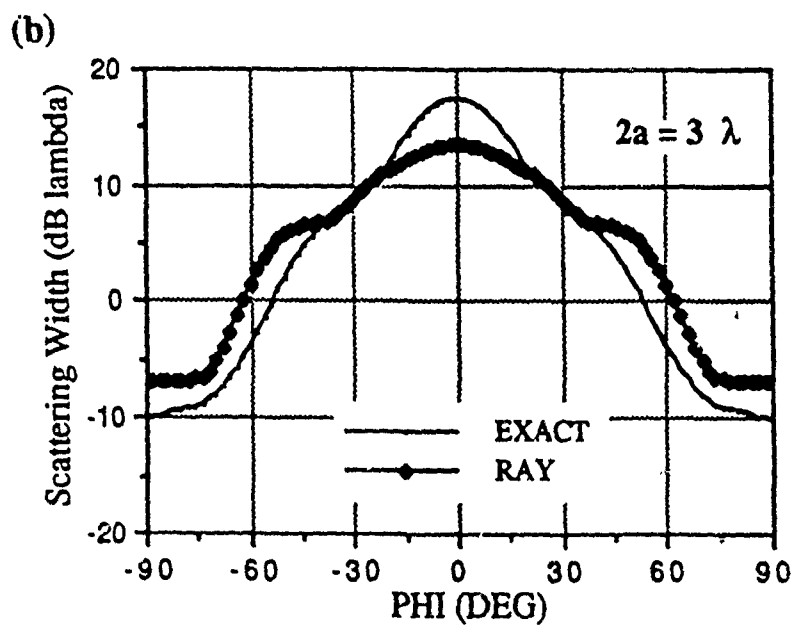
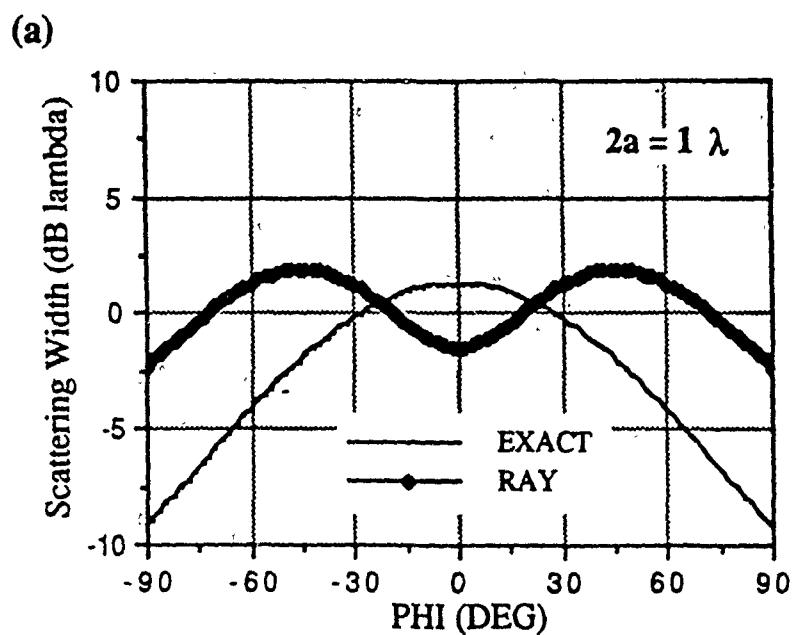


Fig. 7. Comparison of the scattering width of the inhomogeneous cylinder calculated using ray optics with the exact series expansion solution.  
(a)  $2a = 1\lambda$ . (b)  $2a = 3\lambda$ .

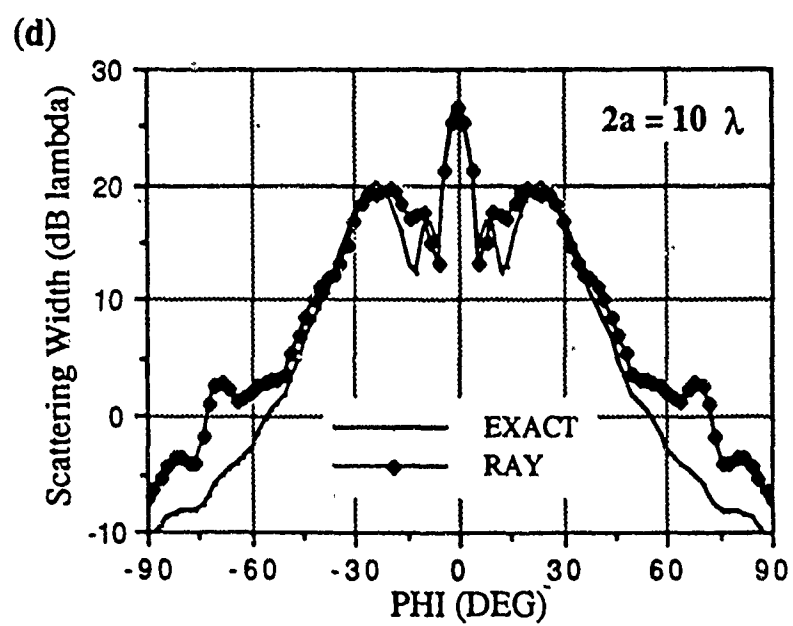
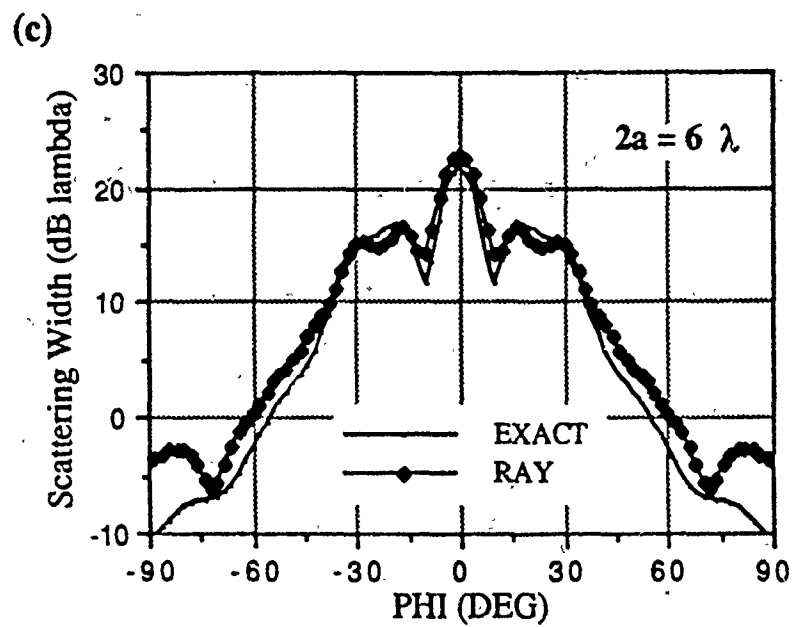


Fig. 7(Cont'd). (c)  $2a = 6\lambda$ . (d)  $2a = 10\lambda$ .

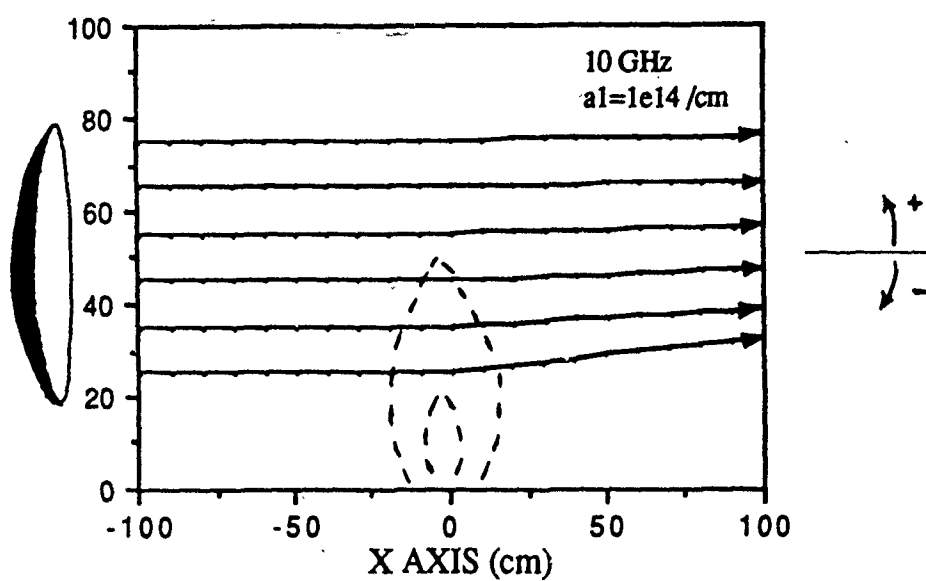


Fig. 8. Geometry of the reflector degradation study. The diameter of the reflector is 60 cm ( $20\lambda$  at 10 GHz). Also plotted are the ray trajectories through a plasma plume with  $a_1 = 1 \times 10^{14} \text{ cm}^{-1}$ .

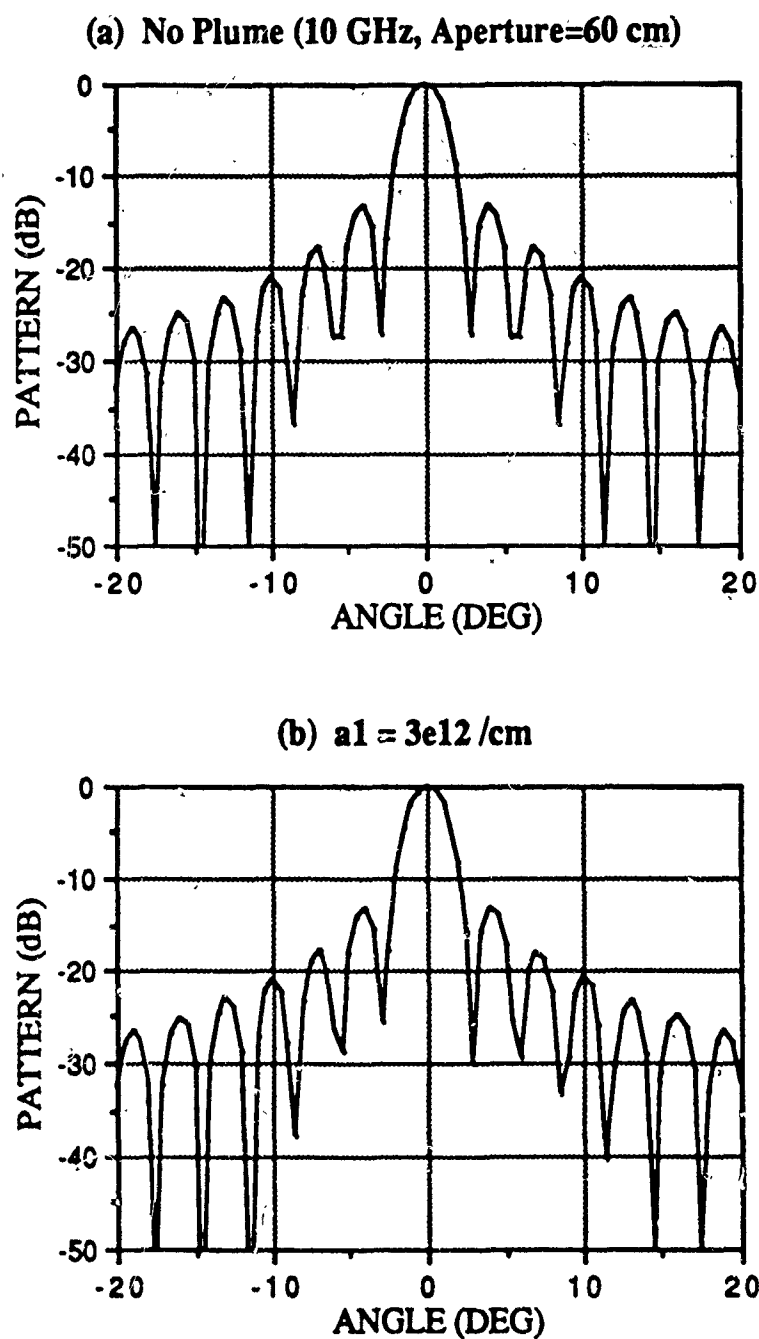


Fig. 9. Reflector patterns in the presence of a plasma plume. A uniform aperture illumination is assumed for the reflector.  
 (a) No plume case. (b)  $a_1 = 3 \times 10^{12} \text{ cm}^{-1}$ .

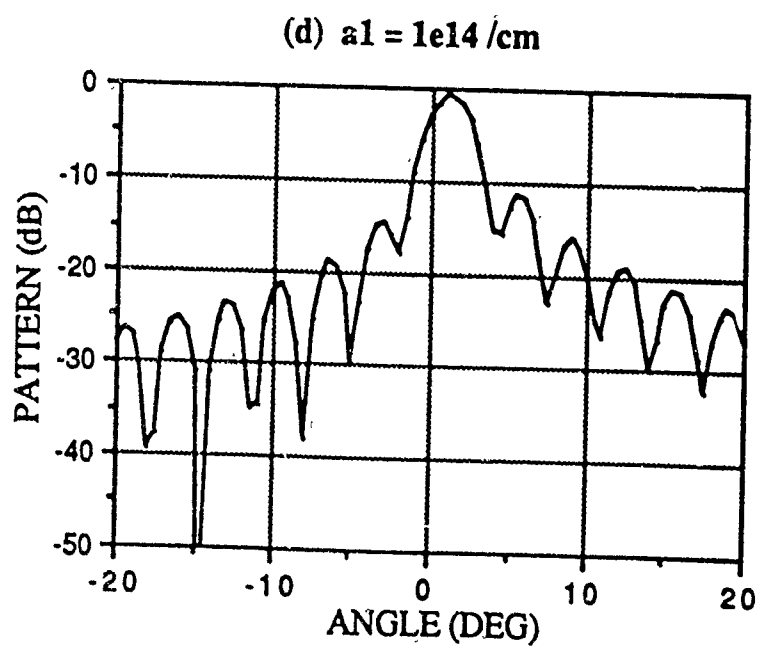
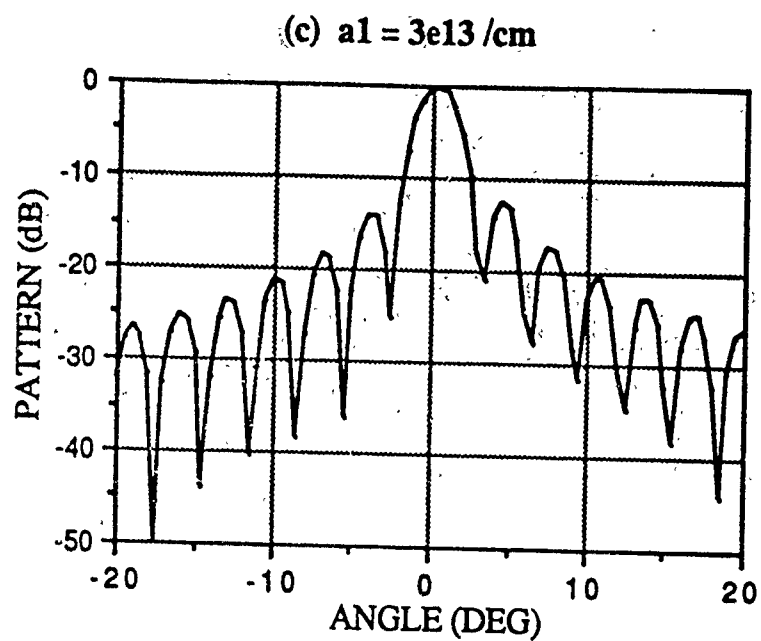


Fig. 9(Cont'd). (c)  $a_1 = 3 \times 10^{13} \text{ cm}^{-1}$ , (d)  $a_1 = 1 \times 10^{14} \text{ cm}^{-1}$



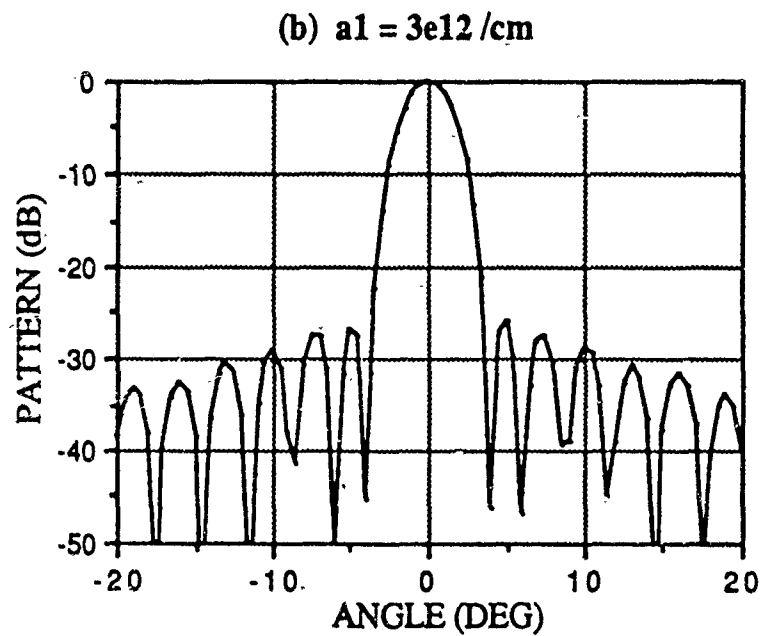
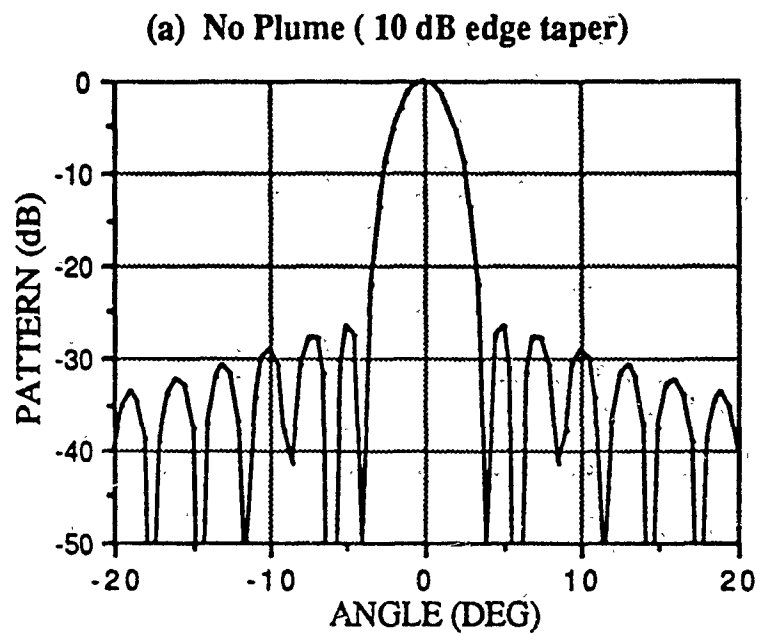


Fig. 10. Reflector patterns in the presence of a plasma plume. A 10-dB aperture edge taper is assumed for the reflector.  
 (a) No plume case. (b)  $a_1 = 3 \times 10^{12} \text{ cm}^{-1}$ .

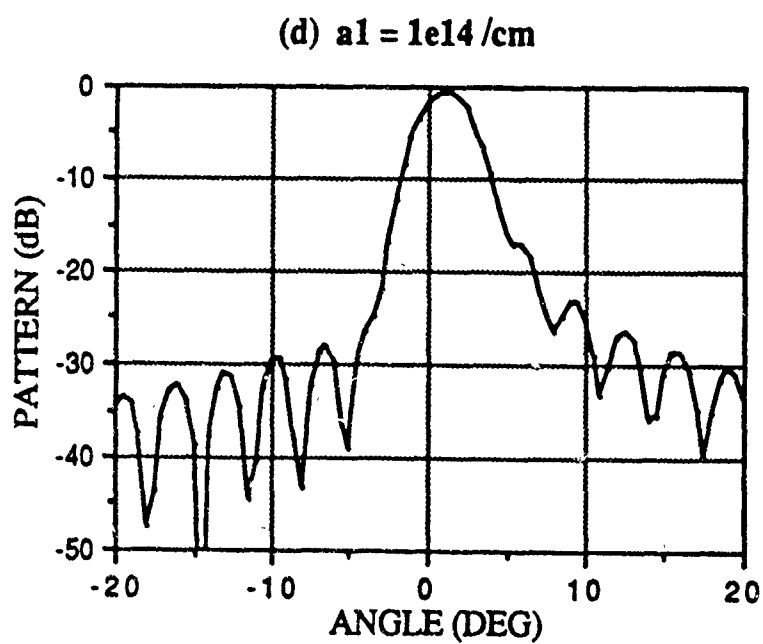
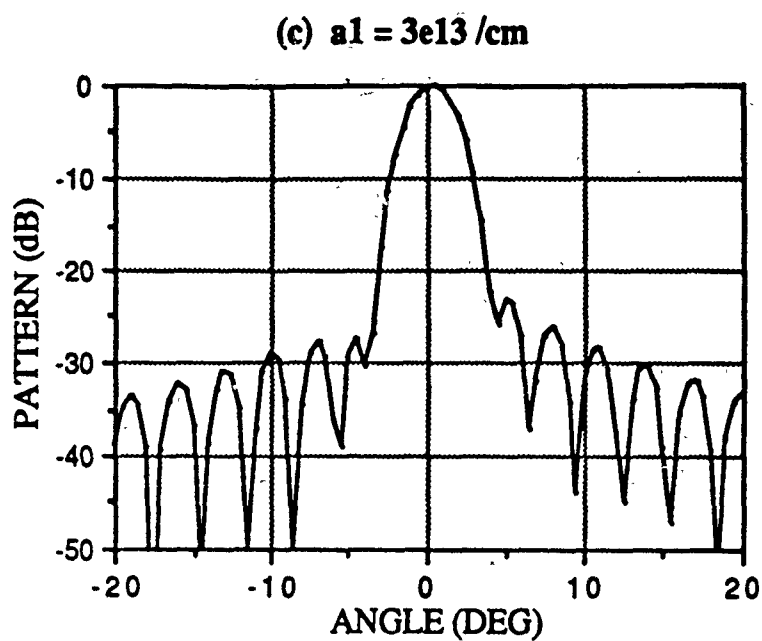


Fig. 10(Cont'd). (c)  $a_1 = 3 \times 10^{13} \text{ cm}^{-1}$ . (d)  $a_1 = 1 \times 10^{14} \text{ cm}^{-1}$

PARAMETRIC ESTIMATION OF THE J-BAND RADIATION  
PROPERTIES OF CYLINDRICAL FEEDS WITH OR  
WITHOUT EXTERNAL COAXIAL CUPS

Constantinos J. Papathomas  
Dept. of Electrical and Computer Engineering  
University of Massachusetts  
Amherst, MA 01003.

ABSTRACT

The radiation properties of cylindrical prime focus feeds with or without external coaxial cups in J-band satellite communications are investigated as functions of the geometrical parameters and the frequency of operation. Modeling schemes for circular waveguides with thick walls are discussed and it is concluded that a dual mode model provides a reasonable representation of their behavior. In addition, both the cross-polar level and beam symmetry of cylindrical feeds with external cups are linked, not only to the radii of the structure, but to the cup depths as well.

## 1. INTRODUCTION AND MODELING PRINCIPLES

One of the most important technical features of cylindrical prime focus feeds with or without external coaxial cups, which are used in connection with deep parabolic reflectors in satellite communication links, is their cross-polar performance; that is, their ability to distinguish and discriminate among signals of different polarizations. An equally important feature is the level of circular symmetry in the main beam, manifested by the equality of the E- and H-plane radiation patterns, as well as the bandwidth over which a certain level of circular symmetry and consequent low cross-polarization is maintained.

The desirable radiation properties, such as low level of cross-polarization, principal planes beam equality and an extensive bandwidth, are known experimentally to be very much dependent on the geometrical parameters of the feeds<sup>1,2,3</sup>. Therefore, an investigation of the influence exerted by the central waveguide and cup radii, cup depths and frequency on the radiation performance of these feeds, is fully warranted and is the main concern of this paper.

To achieve this goal, we used the modeling procedure recently proposed by Papathomas and Collin<sup>4,5</sup> for the determination of the radiation characteristics and the input mismatch of cylindrical satellite antenna feeds, with or without secondary coaxial-cup radiators of finite depth (Figures 1, 2).

The theory uses a multimode method of moments description of the aperture fields, that leads to improved predictions of the cross-polar properties over previously used single mode analyses. The main drawback of the single mode approach is that it predicts much lower cross-polarization levels than the actual levels observed<sup>6</sup>. An important feature of this procedure is that it allows for the modeling of feeds with finite cup depths. Cup depths are probably the most sensitive geometrical parameters involved in the design of such feeds<sup>7</sup>, therefore means to account for their influence are viewed as absolutely necessary.

The feed excitation is modeled after the dominant H-mode in the cylindrical waveguide. There is no need to consider excitation by higher order modes because, primarily due to its relatively small diameter, the waveguide produces a circularly symmetric pattern by

excitation with the dominant mode only. The overall incident field in the central waveguide is chosen as that of the  $TE_{11}$  mode with a short-circuit imposed on the waveguide free-space interface, in anticipation of a Love's equivalent principle type treatment of the radiating apertures. Therefore, the scattered field in the central region takes the form of a sum of evanescent  $TE_{1n}$  and  $TM_{1n}$  modes. Due to the circular symmetry of the problem, only modes with the same number of circumferential variations as the excitation are considered.

The radiated field component of the feeding waveguide excites parasitic fields in the cup sections, composed of a number of modified coaxial cylindrical waveguide modes that can be set as high as required. These modes can propagate or are attenuated, depending on the dimensions of the cup sections, while at the same time they provide for the tuning of the circuit by satisfying the boundary condition at the bottom of the cup. The various modal components radiated from any aperture, couple among themselves (mutual coupling), as well as with the modal components radiated from every other aperture (cross-

coupling), thus determining what portion of the power content of each single modal component is scattered or radiated.

The level of modal coupling, which is primarily controlled by the geometrical parameters of the feed, is computed numerically<sup>4</sup> and then translated into expressions for the far field radiation patterns<sup>5</sup>. Excellent pattern symmetry and very low cross-polarization is obtained, when at certain dimensions the coupling between the various modal components results in an almost linearly polarized field throughout the total aperture of the feed.

## 2. CYLINDRICAL FEEDS WITHOUT CUPS

The analytical results of the modeling procedure have been incorporated into computer codes in order to generate graphs of the desired feed characteristics, such as the E- and H- plane patterns and the 45° plane co- and cross-polarized patterns. For the pattern plots presented the following format has been adopted: two axes are used, namely X and Y, where Y represents the relevant field amplitude in dB (increasing from -60dB to 0dB in increments of 5dB), while X is the

angular displacement  $\vartheta$  from the  $z$ -axis in a spherical coordinate system (varying from 0 to 90 degrees in increments of  $10^\circ$ ).

We turn our attention first, to the case of the circular waveguide with thick walls in the absence of secondary radiators. The radiation properties of cylindrical waveguides with infinitely thin walls have been studied by both James et al<sup>8</sup> and Collin et al<sup>2</sup> through a Wiener-Hopf type of analysis. This model renders predictions very close to experimental data for waveguides with wall width in principle smaller than  $0.01\lambda_0$ . On the contrary, the behavior of circular waveguide radiators with thick walls has not received much attention, besides the experimental studies of James<sup>8</sup>.

When only the dominant  $TE_{11}$  mode is considered in the aperture field expansion, the four principal radiation patterns of interest for the circular waveguides with radii  $a_1 = 0.55\lambda_0$  and  $0.60\lambda_0$ , are presented in Figures 3 and 4, when the design frequency is 12GHz. The best E- and H- plane symmetry is obtained for a diameter of  $2a_1 = 1.077\lambda_0$ , where the cross-polarization level remains below -60dB for up



to, approximately,  $\theta = 50^\circ$ . This result is in very good agreement with the findings of Adatia, Rudge and Parini<sup>9</sup>, who reported minimum cross-polarization for an aperture diameter of  $1.15\lambda_0$  using a similar single mode theory.

If, on the other hand, both the  $TE_{11}$  and  $TM_{11}$  modes are allowed in the aperture field expansion, significant changes are observed. The cross-polarization levels are much higher from the ones predicted with the single mode model, as Figures 5 and 6 point out for the waveguides with radii  $a_1 = 0.55\lambda_0$  and  $0.60\lambda_0$  respectively. The two mode analysis turns out to be in good agreement with measurements of the cross-polarization from thick wall circular waveguides. As the waveguide wall thickness increases and exceeds 1.3 radii, the experimental results<sup>8</sup> follow closely the theoretical predictions via the two mode model.

A five mode analysis reveals that the radiation patterns change insignificantly in comparison with the patterns of the two mode model, as exhibited in Figures 7 through 10. The cross-polar patterns, in particular, remain always within 0.25dB from the respective curves of the two-mode case. Since the

computing time for the evaluation of the five-mode patterns is more than twice the CPU time required for the two-mode patterns, we maintain that the two-mode model represents an excellent compromise between accuracy and computational cost.

For the sake of completeness, an eight mode as well as a twelve mode analysis, has also been carried out for a variety of radii. The resulting patterns are again almost identical with the ones from both the two- and five-mode models.

### 3. CYLINDRICAL FEEDS WITH COAXIAL CUPS

Next we focus our attention to the cylindrical feed with external coaxial cups. The importance of each geometrical parameter can be singled out by varying this parameter alone, while keeping all the others constant.

Significant improvement both in cross-polar performance and principal planes beam symmetry can be achieved by proper selection of the cup depths alone. Namely, improvements of up to approximately 9dB in cross-polarization levels were observed, when the cup depth was allowed to scan a range of the order of half a wavelength. Figures 11 and 12 offer an example of

the strong influence of the position of the bottom of the cup radiator, relative to the mouth of the feeding waveguide, in the performance of the feed with one cup. The feed in both cases operates at a frequency of 10GHz and its radial dimensions are  $a_1 = 1.27\text{cm}$  and  $b_1 = 2.54\text{cm}$  respectively, while the cup depth changes, from  $l_1 = 0.2\lambda_0$  in Figure 11 to  $l_1 = 0.4\lambda_0$  in Figure 12. The beam symmetry of the later feed is superior, and the diagonal plane cross-polarization improves by approximately 4dB.

Variations of the cup depths were studied extensively within the range from  $0.05\lambda_0$  to  $1.3\lambda_0$  and it was found that the radiation properties change in a smooth and continuous fashion as supported by experimental evidence. This feature points out a potential advantage of this modeling procedure over the theory that represents the corrugations in an approximate manner through anisotropic surface impedances<sup>7</sup>. In the later, variations of only  $0.02\lambda_0$  in cup depth can generate differences in cross-polarization of the order of 20dB.

It was found that the dimensions of the feed radii play also an important role in the formation of

favorable conditions for satellite signal reception. Figures 13 and 14 illustrate the relevant changes in the performance of the feed with two cups, when the outer radius is increased from  $0.85\lambda_0$  to  $1.1\lambda_0$ . The remaining dimensions are  $a_1 = 0.45\lambda_0$ ,  $a_2 = 0.78\lambda_0$ ,  $l_1 = 0.48\lambda_0$  and  $l_2 = 0.53\lambda_0$ . Similar observations are supported by the change in the inner radius  $a_1$  of another dual cup feed with  $a_2 = 0.77\lambda_0$ ,  $a_3 = 0.92\lambda_0$ ,  $l_1 = 0.48\lambda_0$  and  $l_2 = 0.53\lambda_0$ . Figure 15 pictures the feed for an inner radius value of  $0.40\lambda_0$ , while in Figure 16 the inner radial dimension has been slightly increased to  $0.42\lambda_0$ . The frequency in both cases is 10GHz.

The radial dimensions control both the modal content of each radiating region and the level of coupling among modal components, thus being largely responsible for the amount of polarization purity of the resulting aperture field. On the other hand, the length of the secondary cup radiators determines the relative phase of the modes. Therefore, once the radii for a feed with acceptable properties have been obtained, varying the cup depth allows the best possible performance to be extracted from the original design.

## ACKNOWLEDGMENTS

This work was supported in part by the National Science Foundation under Grant No ECS-8307052. The author wishes to express his gratitude to Prof. Robert E. Collin for a number of enlightening conversations and for his continuous encouragement in this work.

## REFERENCES

1. Scheffer, H. (1975) Improvements in the Development of Coaxial Feeds for Paraboloidal Reflector Antennas, Proc. of Fifth European Microwave Conference, Frankfurt.
2. Collin, R.E., Schilling, H. and Hebert, L. (1982) Coaxial Prime Focus Feeds for Paraboloidal Reflectors, NASA Report CR 167934.
3. Keen, K. M. (1978) Beamwidth Variation with Aperture Diameter of the Choked Waveguide Feed Antenna, Electronics Letters 14 (No. 13):406-407.
4. Papathomas, C.J. and Collin, R.E. (1989) Coupling Effects in Microwave Antennas: Modeling and Computer Simulation", Proc. of Seventh Benjamin Franklin Symposium on Advances in Antenna and Microwave Technology : 71-74, Cherry Hill.

5. Papathomas, C.J. and Collin, R.E. (in press) Multi-mode Analysis of a Two Coaxial Cup Prime Focus Feed with an Infinite Flange, Electromagnetics.
6. Olver, A.D., Clarricoats, P.J.B., Hockham, G.A. and Parini, C.G. (1978) Design of Corrugated Feeds for Low Cross-Polarization, IEE International Conference on Antennas and Propagation - Part 1: Antennas (No. 169): 355-359.
7. Iskander, K.A., Shafai, L., Frandsen, A. and Hansen, J.E. (1982) Application of Impedance Boundary Conditions to Numerical Solution of Corrugated Circular Horns, IEEE Trans. on Antennas and Propagation 30 (No. 3):366-372.
8. James, G.L. and Greene, K.J. (1978) Effect of Wall Thickness on Radiation from Circular Waveguides, Electronics Letters 14 (No. 4):90-91.
9. Adatia, N.A., Rudge, A.W. and Parini, C. (1977) Mathematical Modelling of the Radiation Fields from Microwave Primary Feed Antennas, Proc. of Seventh European Microwave Conference, Denmark.

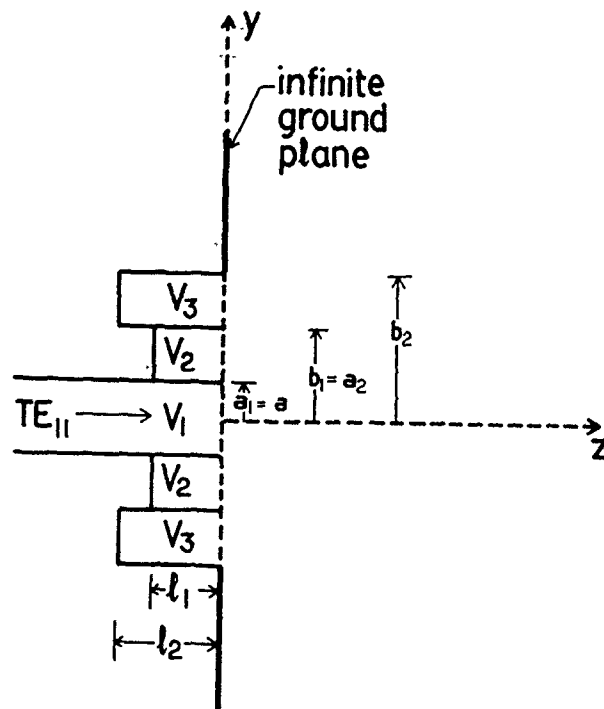


FIGURE 1: Cylindrical feed with cups.

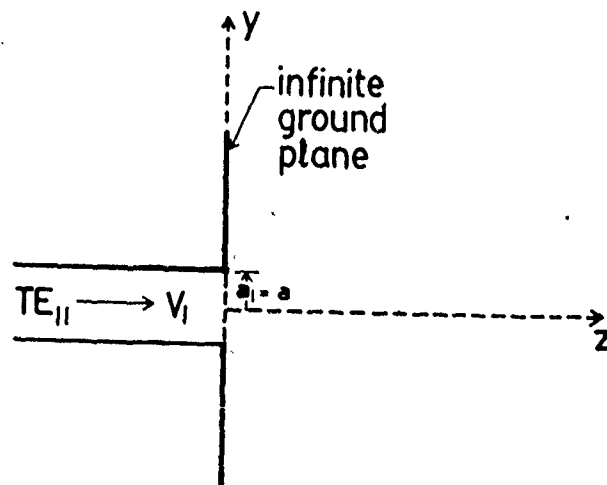


FIGURE 2: Cylindrical feed without cups.

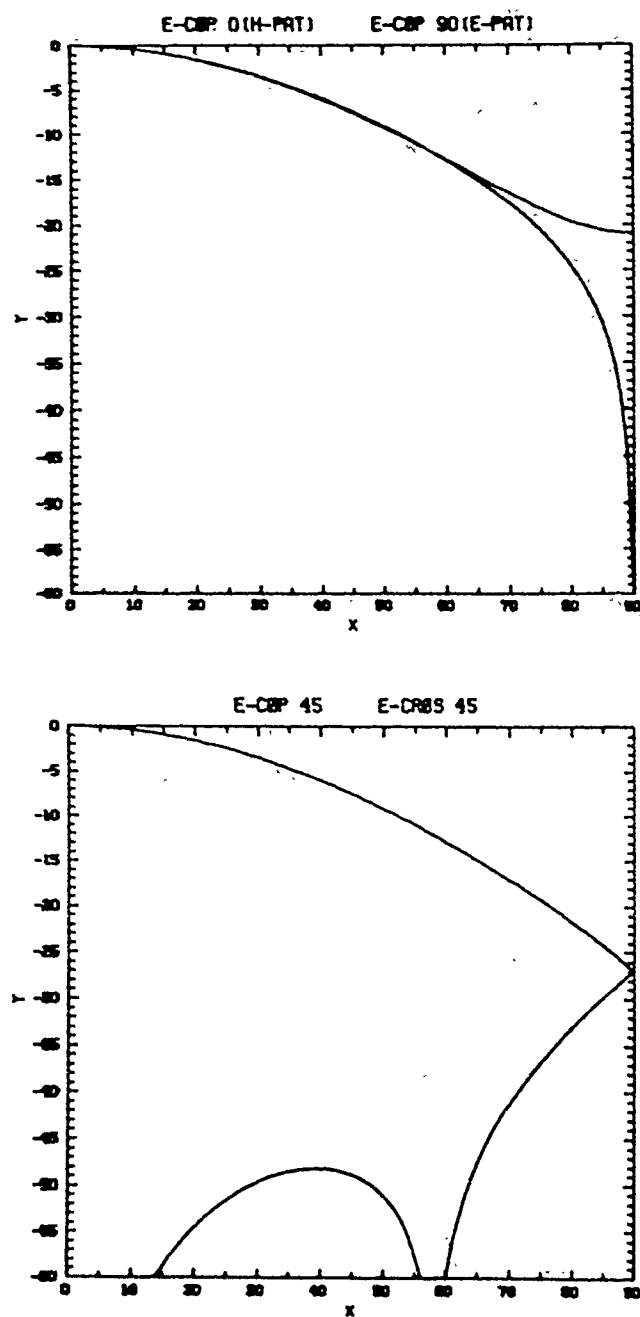


FIGURE 3: Principal radiation patterns for  
 $a_1 = 0.55\lambda_0$  (single mode model).



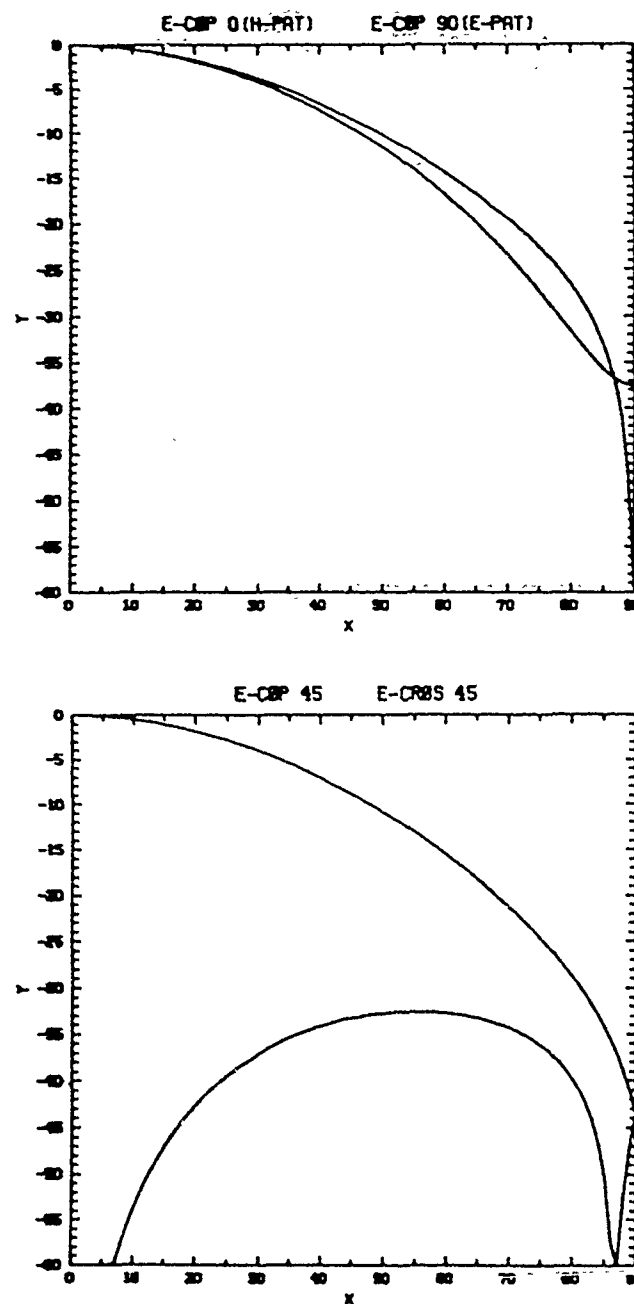


FIGURE 4: Principal radiation patterns for  
 $a_1 = 0.60\lambda_0$  (single mode model).

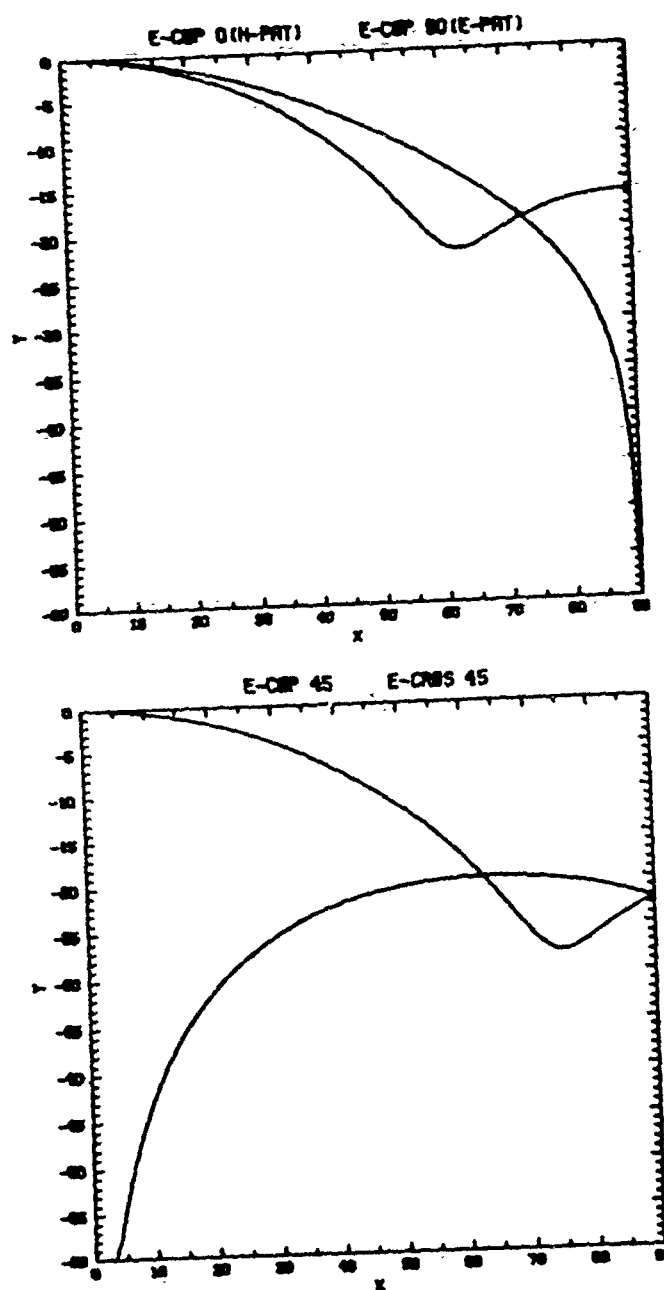


FIGURE 5: Principal radiation patterns for  $a_1 = 0.55\lambda_0$  (two mode model).

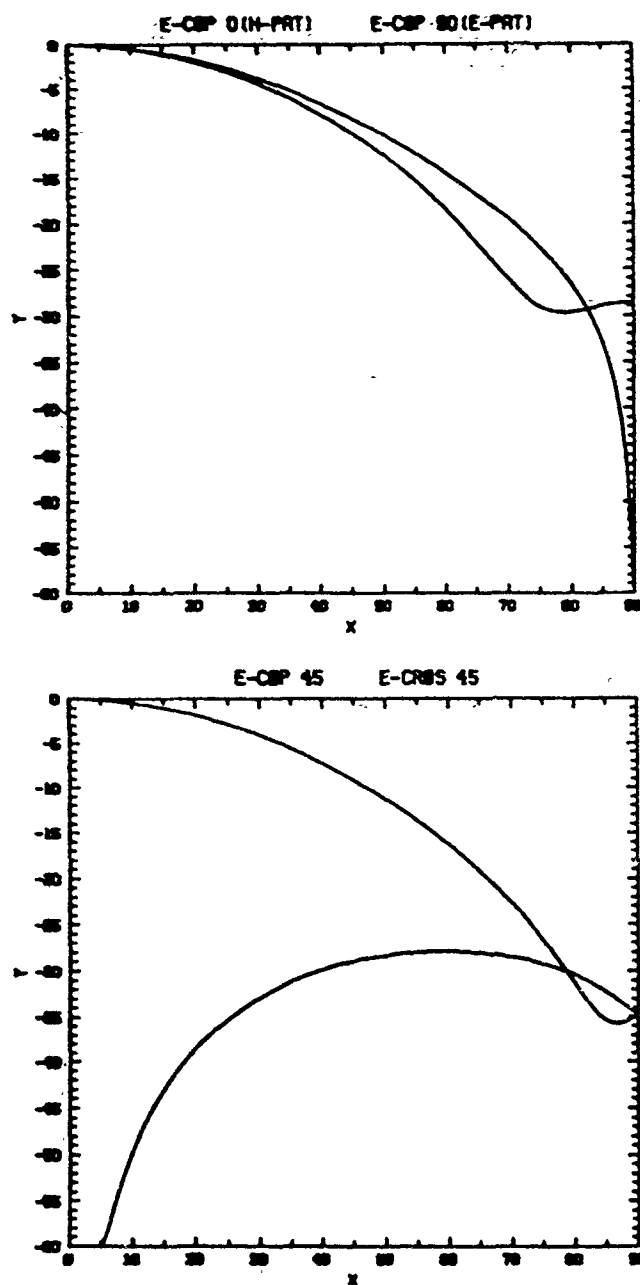


FIGURE 6: Principal radiation patterns for  $a_1 = 0.60\lambda_0$  (two mode model).

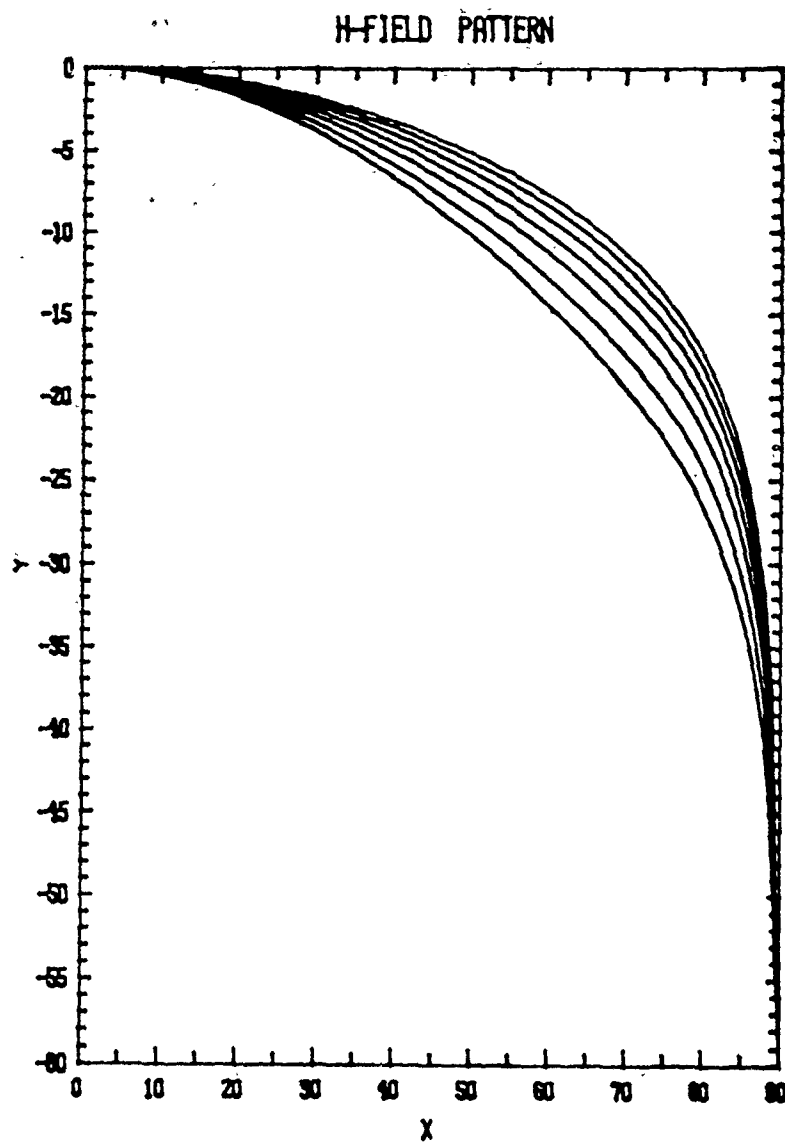


FIGURE 7: H-plane patterns of five mode model. From top to bottom curve, aperture radius increases from  $0.3\lambda_0$  to  $0.6\lambda_0$ , in increments of  $0.05\lambda_0$ .

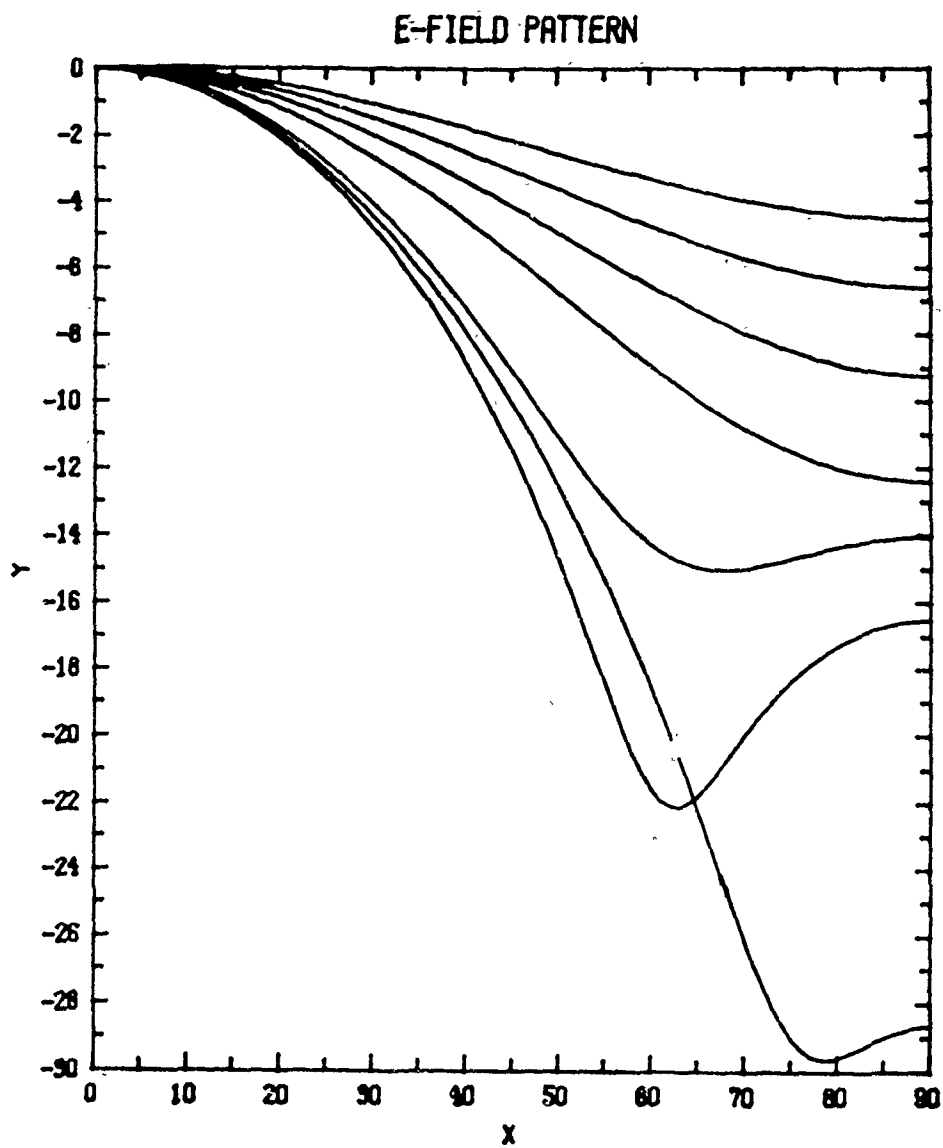


FIGURE 8: E-plane patterns of five mode model. From top to bottom curve, aperture radius increases from  $0.3\lambda_0$  to  $0.6\lambda_0$ , in increments of  $0.05\lambda_0$ .

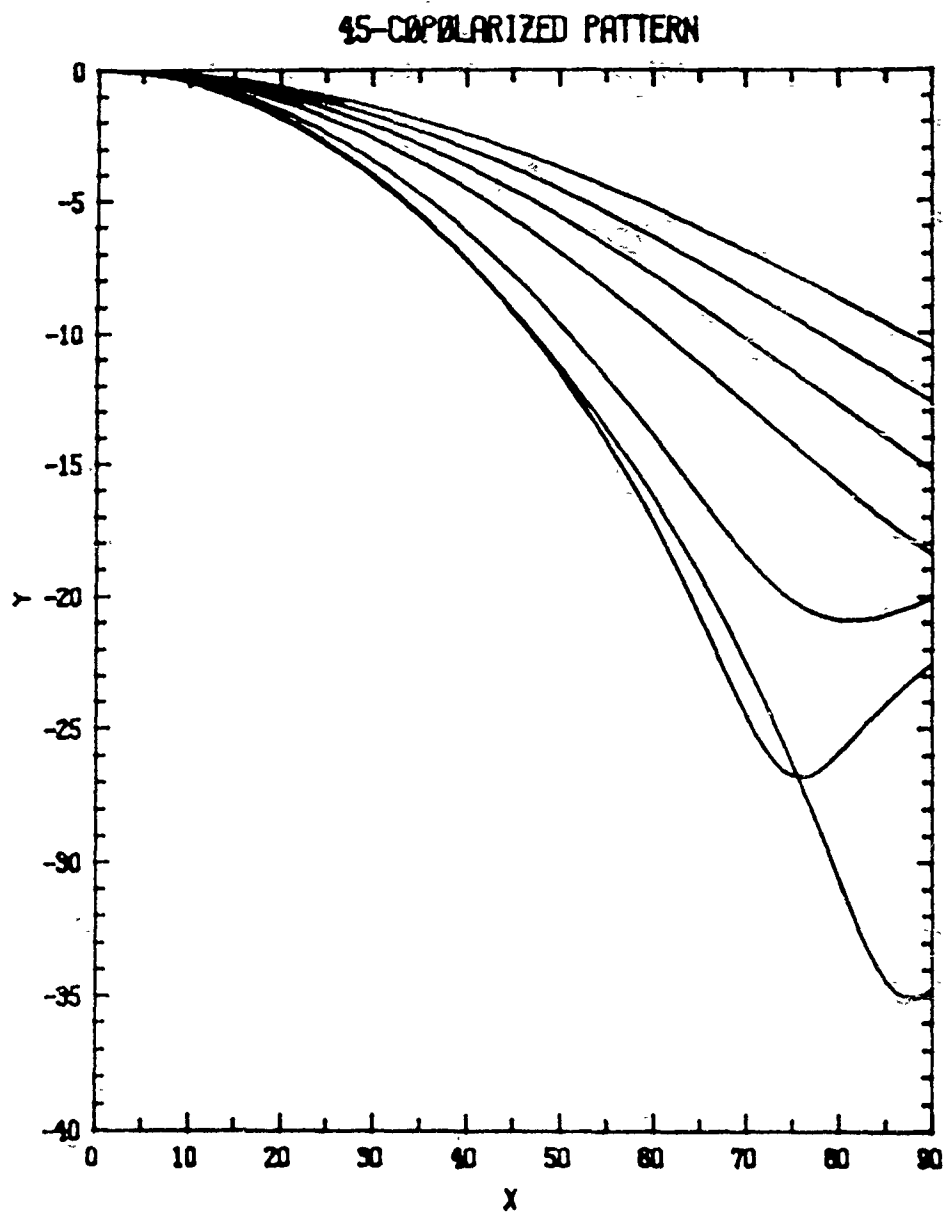


FIGURE 9: 45°-plane copolarized patterns of five mode model. From top to bottom curve, aperture radius changes from  $0.3\lambda_0$  to  $0.6\lambda_0$ , in increments of  $0.05\lambda_0$ .

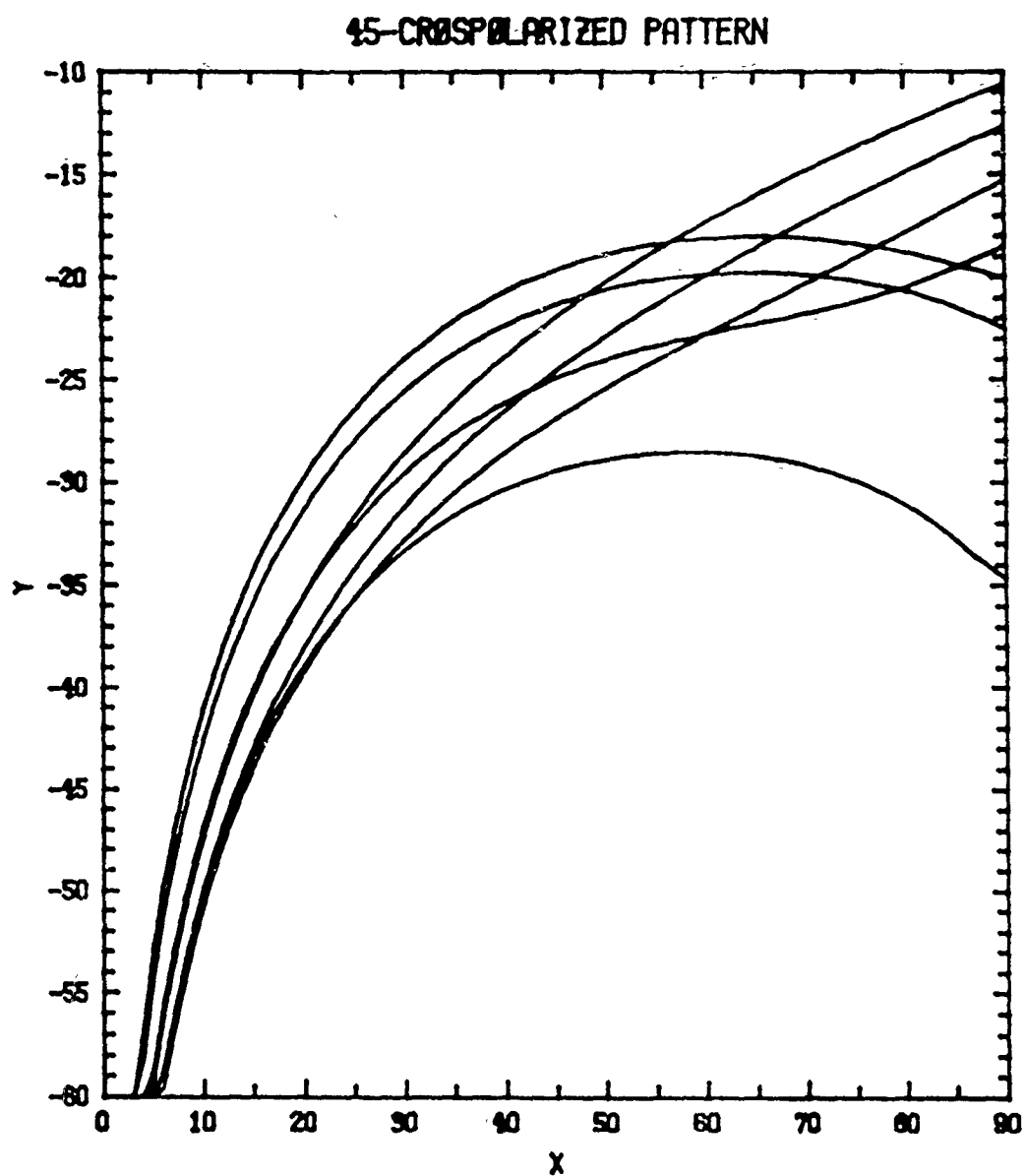


FIGURE 10: 45°-plane cross-polar patterns of five mode model. From top to bottom curve, aperture radius changes from  $0.3\lambda_0$  to  $0.6\lambda_0$ , in increments of  $0.05\lambda_0$ .

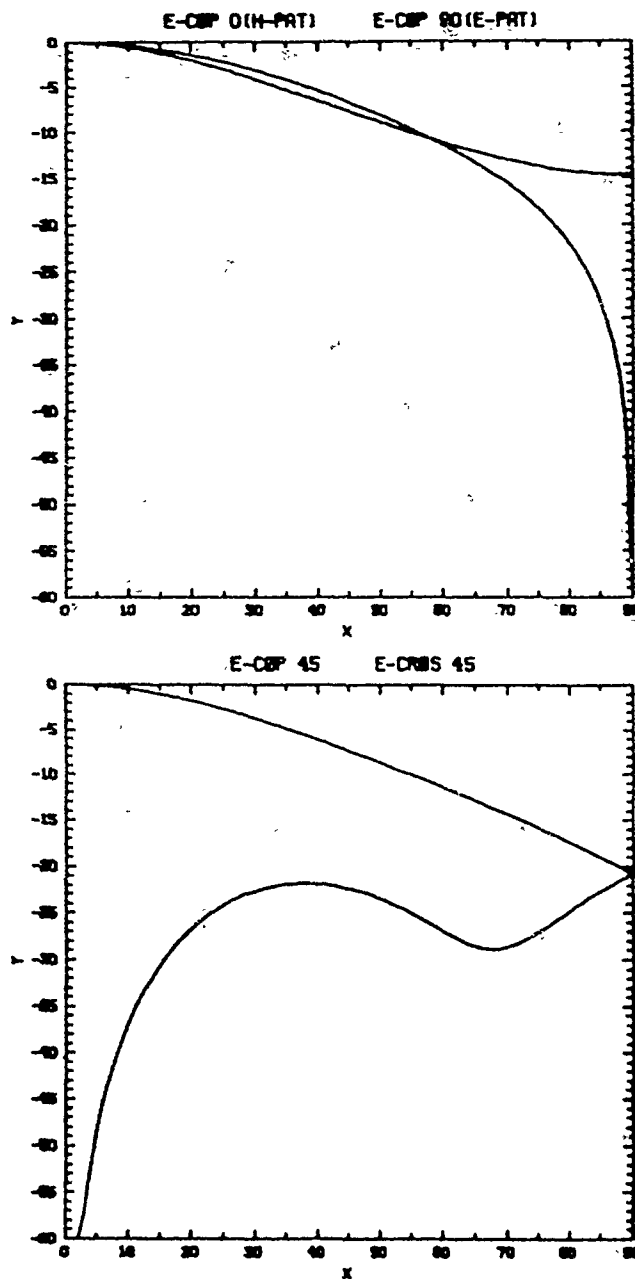


FIGURE 11: Single cup feed with  $a_1 = 1.27\text{cm}$ ,  
 $b_1 = 2.54\text{cm}$  and  $l_1 = 0.2\lambda_0$  at 10GHz.



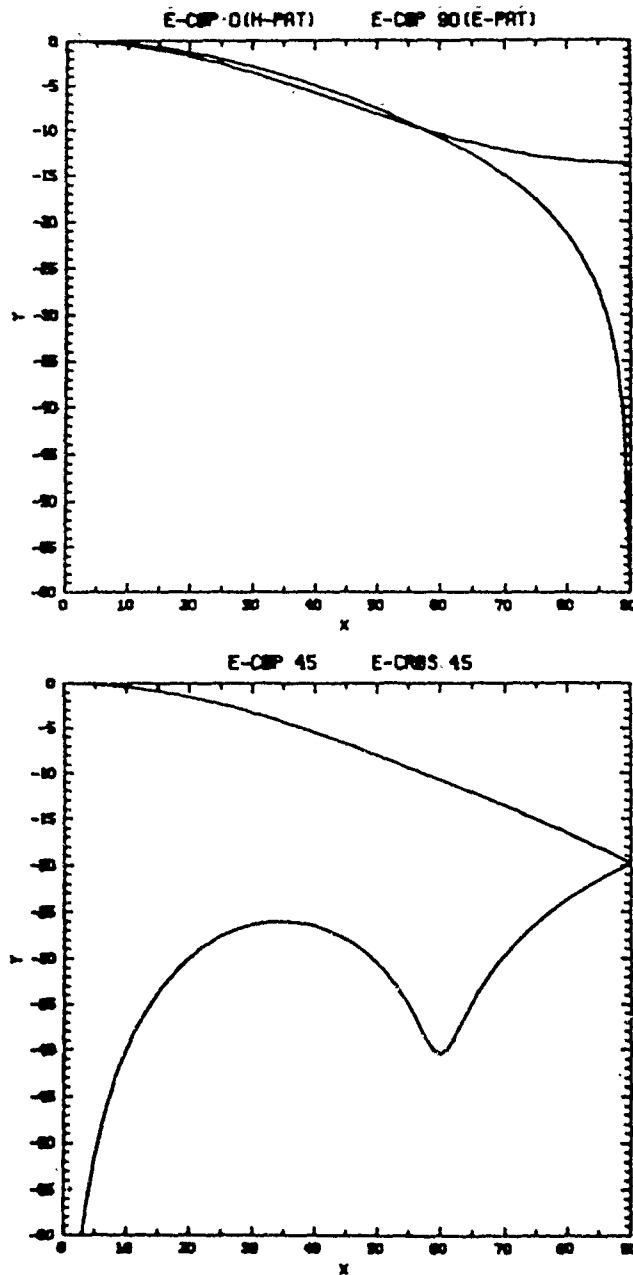


FIGURE 12: Single cup feed with  $a_1 = 1.27\text{cm}$ ,  
 $b_1 = 2.54\text{cm}$  and  $l_1 = 0.4\lambda_0$  at  $10\text{GHz}$ .

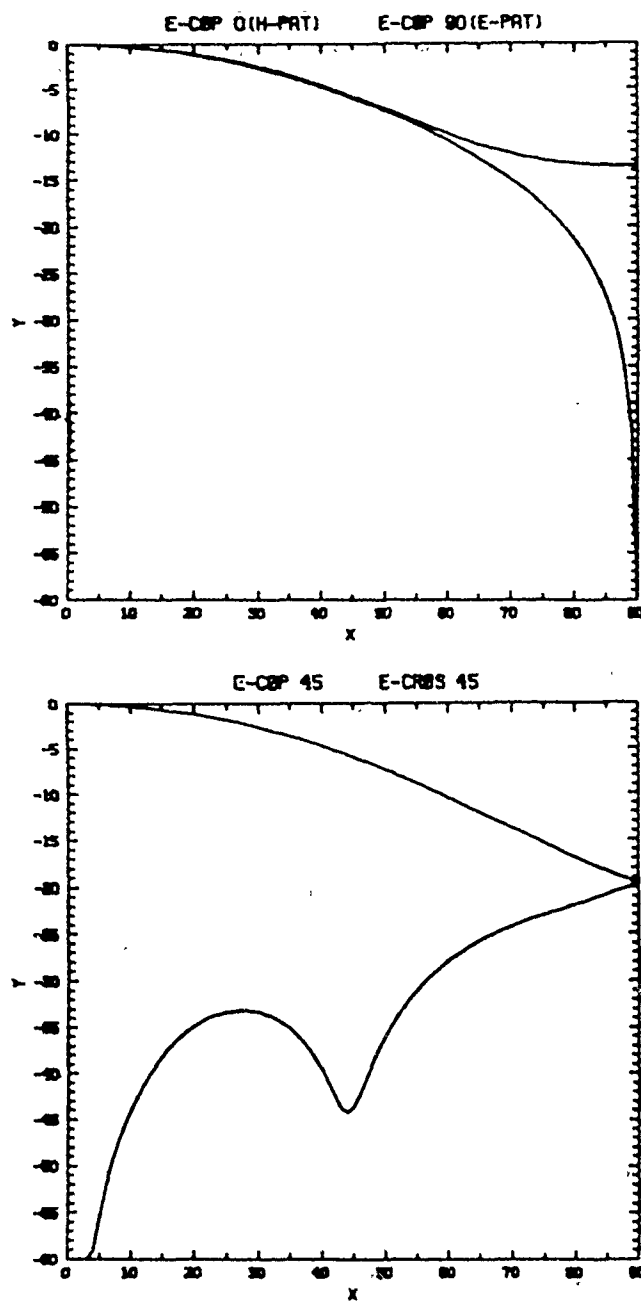


FIGURE 13: Outer cup radius  $a_3 = 0.85\lambda_0$ , in dual cup feed with  $a_1 = 0.45\lambda_0$ ,  $a_2 = 0.78\lambda_0$ ,  $l_1 = 0.48\lambda_0$  and  $l_2 = 0.53\lambda_0$ .

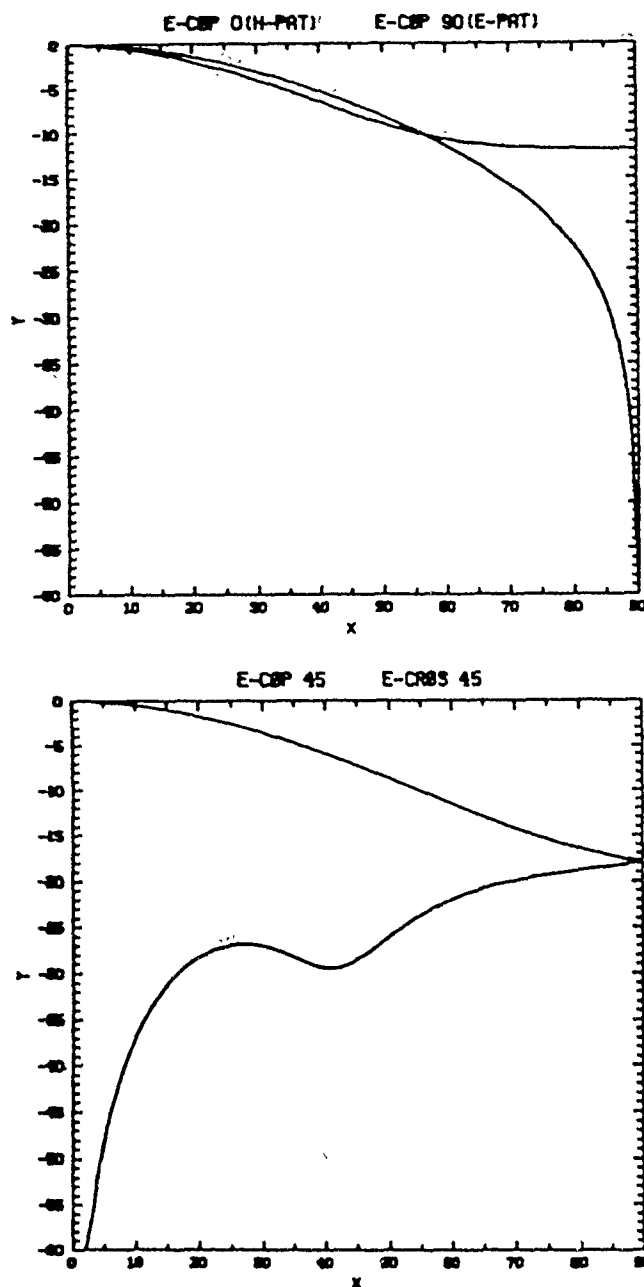


FIGURE 14: Outer cup radius  $a_3 = 1.1\lambda_0$ , in dual cup feed with  $a_1 = 0.45\lambda_0$ ,  $a_2 = 0.78\lambda_0$ ,  $l_1 = 0.48\lambda_0$  and  $l_2 = 0.53\lambda_0$ .

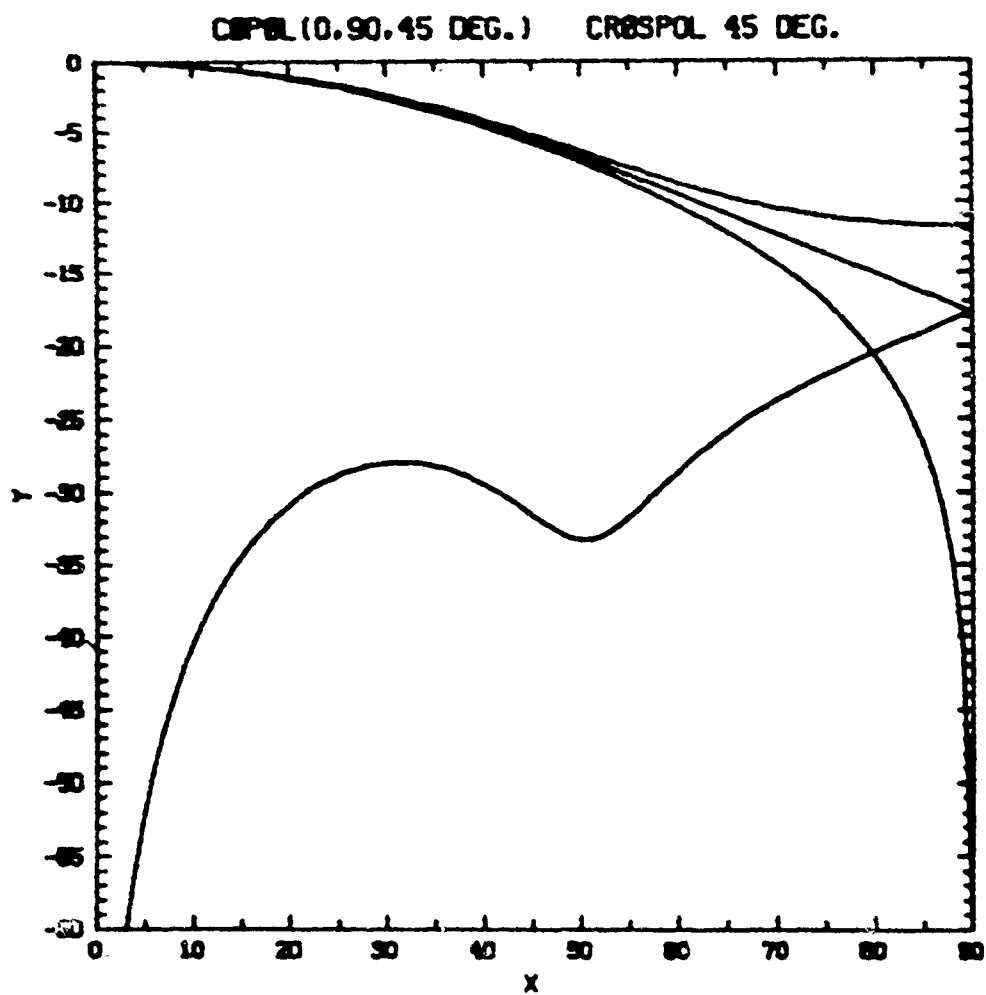


FIGURE 15: Inner radius  $a_1 = 0.40\lambda_0$ , in dual cup feed with  $a_2 = 0.77\lambda_0$ ,  $a_3 = 0.92\lambda_0$ ,  $l_1 = 0.48\lambda_0$  and  $l_2 = 0.53\lambda_0$ .

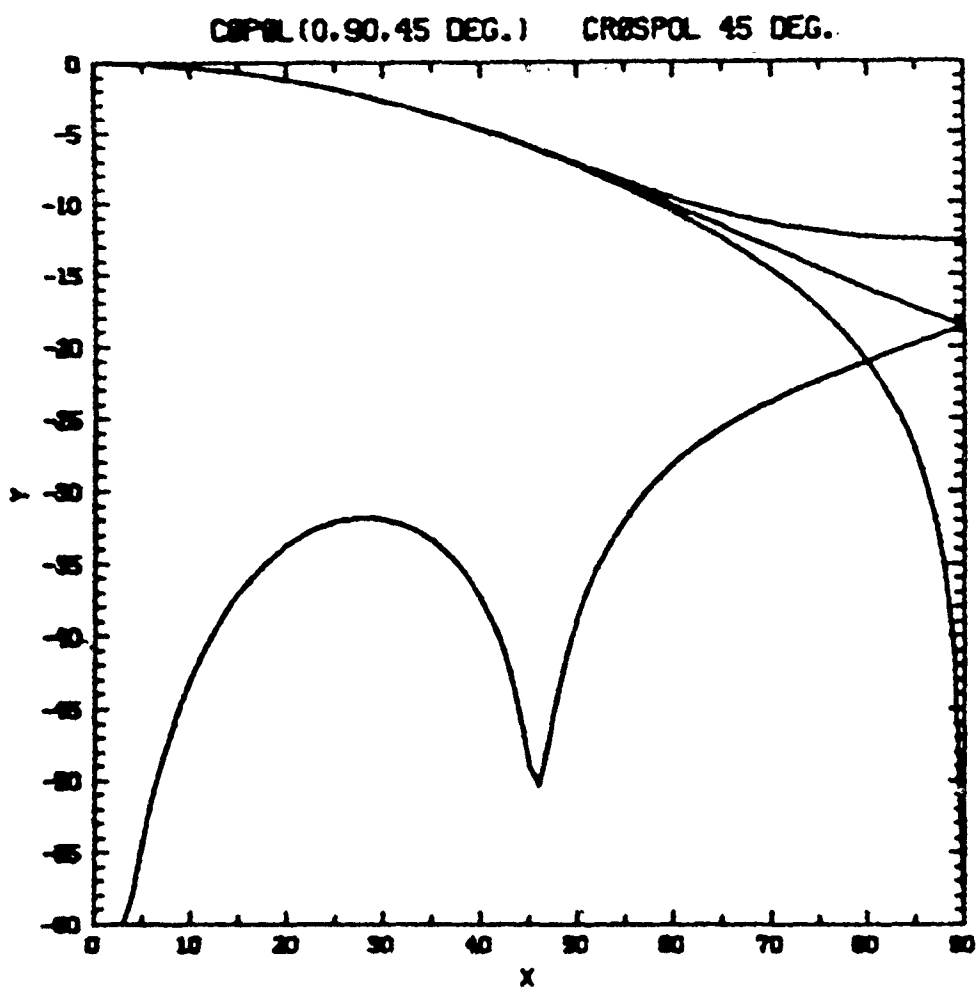


FIGURE 16: Inner radius  $a_1 = 0.42\lambda_0$ , in dual cup feed with  $a_2 = 0.77\lambda_0$ ,  $a_3 = 0.92\lambda_0$ ,  $l_1 = 0.48\lambda_0$  and  $l_2 = 0.53\lambda_0$ .

# **Impedance-Matched Coaxial-Probe Feed for a Rotman Lens-Fed Array with 4.5:1 Bandwidth and Sector Pattern Coverage**

Joseph A. Troychak  
Peter S. Simon

Raytheon Electromagnetic Systems Division  
Goleta, CA

1989 Antenna Applications Symposium  
Monticello, IL, Sept. 20-22, 1989

## **Abstract**

This paper discusses the analysis, design, and realization of a coaxial probe-fed microstrip Rotman lens for achieving a broad sector array factor pattern over a 4.5 to 1 frequency bandwidth (4-18 GHz). The probe location within the lens is chosen to provide the appropriate quadratic phase error at the linear array aperture that results in optimal array factor pattern sector coverage over the entire bandwidth.

Methods for using Rotman lenses for phased array synthesis have been described in the literature. Here, the addition of a coaxial shorted-probe network for sector coverage to a microstrip Rotman lens with normal fan-beam coverage is analyzed and developed.

The sector beam lens port is modeled as a shorted probe-fed radial waveguide. The corresponding first-order input impedance is computed, and a three section coaxial matching network is designed for broadband performance. The effect of mutual coupling between multiple probes on probe input impedance is included in the model.

Computed lens array factor sector patterns and measured lens array port aperture distributions are presented. Measured and computed data are compared for multiple probe mutual coupling and probe VSWR.

## **1 Introduction**

Synthesis of low-sidelobe constant beamwidth antenna patterns over ultra-wide bandwidths using the multiple port excitation of Rotman lenses has been demonstrated<sup>1</sup>. In addition, the use of a shorted coaxial probe-fed

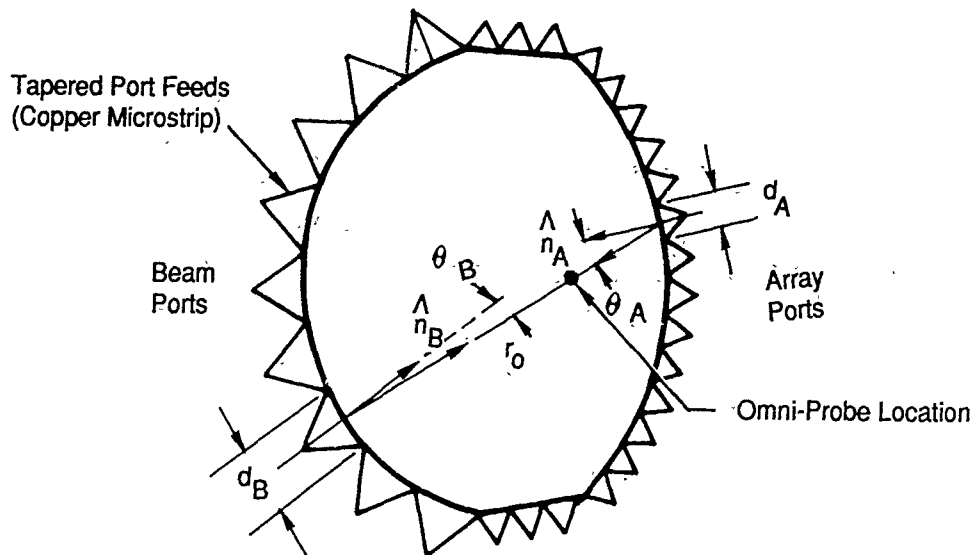


Figure 1: Rotman lens geometry, probe location, and port angle definition.

stripline Rotman lens for broad beamwidth sector coverage has been disclosed<sup>2</sup>. For sector coverage applications the lens parallel-plate region is excited at a location which provides an array port illumination with an approximately quadratic phase distribution. Figure 1 presents the lens geometry and defines the variables of interest for computing the port to port S-parameters. The direct ray path coupling from an array port to a beam port is given by

$$S_{B,A} = \sqrt{\frac{2\pi d_A d_B}{kr_0}} \frac{E(\theta_B, d_B) E(\theta_A, d_A)}{\lambda} e^{-jkr_0} \quad (1)$$

where  $E(\theta, d)$  is the radiation pattern into the parallel plate region of a feed port of width  $d$  at an angle  $\theta$  with respect to its pointing direction,  $\lambda$  is the wavelength in the dielectric, and  $k = 2\pi/\lambda$ . If a shorted coaxial probe is assumed to radiate an omni-directional pattern within the lens the array port to probe port coupling is given by

$$S_{P,A} = \sqrt{\frac{d_A}{2\pi r_0}} E(\theta_A, d_A) e^{-jkr_0} \quad (2)$$

By computing the array factor pattern produced by various probe locations one can iteratively determine an optimum probe location for a particular bandwidth. This design utilized a 0.020 inch probe radiating into a soft-substrate microstrip lens structure ( $\epsilon_r = 10.5$ ) and operated over a 4 to 18 GHz frequency range.

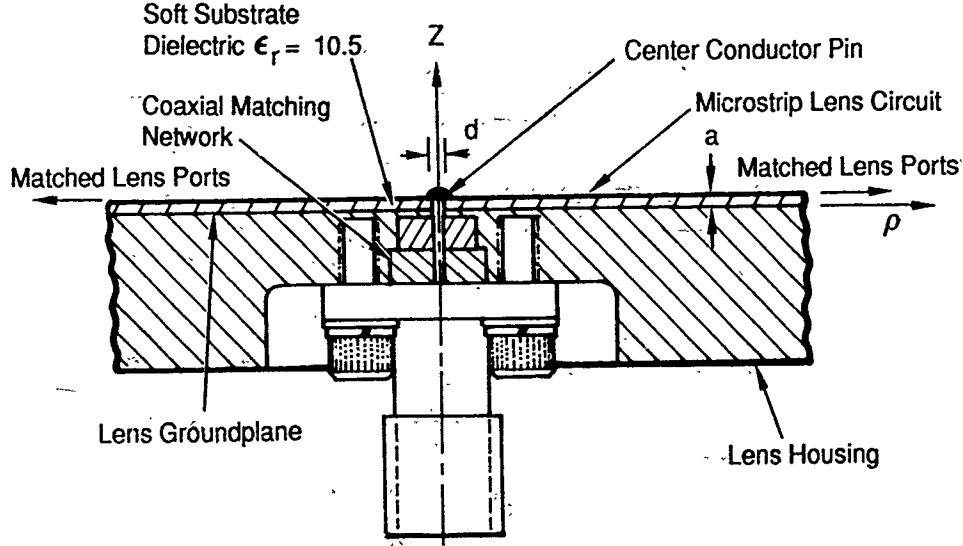


Figure 2: Probe-Fed Lens Configuration and Coordinate System.

## 2 Probe Modeling and Input Impedance

The excitation of a well-matched microstrip lens structure with a shorted probe can be modeled to first order as a perfectly matched probe-fed radial waveguide. The probe fed radial waveguide configuration and coordinate system are defined in Figure 2. A variational approach<sup>3</sup> yields an input impedance of

$$Z_{11} = -\frac{1}{I^2} \iint \mathbf{E} \cdot \mathbf{J} dS, \quad (3)$$

where  $I$  is the total input current,  $\mathbf{E}$  is the field radiated by  $\mathbf{J}$ , the assumed uniform surface current flowing on the coaxial center conductor. This probe excites a  $\text{TM}_z$  radial waveguide mode, and since  $a \ll \lambda$  the  $\text{TM}_{00}$  mode is dominant and all other modes can be neglected. Therefore,

$$E_z = -\frac{k\eta I}{4} H_0^{(2)}(k\rho), \quad (4)$$

with  $\eta$  the intrinsic impedance in the dielectric. Using the large argument formula for the Hankel function of the second kind, we obtain

$$Z_{11} = \frac{\eta}{4} ka \left( 1 - j \frac{2}{\pi} \ln \frac{\gamma kd}{4} \right), \quad (5)$$

where  $\gamma$  is Euler's constant.

Computed values of  $Y_{\text{in}} = 1/Z_{11}$  and the corresponding equivalent circuit for the case of  $d = 0.020$  in.,  $a = 0.025$  in.,  $\epsilon_r = 10.5$  are shown in Figure 3.

The equivalent circuit is a parallel RL load requiring a shunt capacitance of value  $C = 1/(\omega_0^2 L) = 0.324$  pF for resonance at 14 GHz. The capacitance



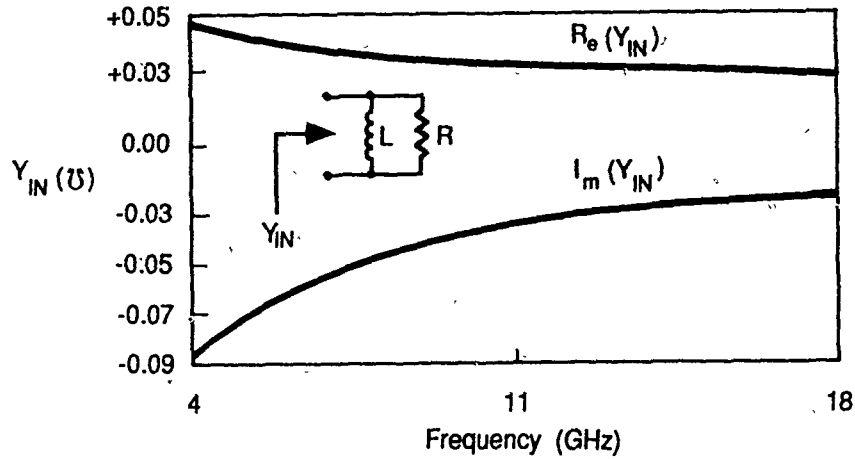


Figure 3: Computed Input Admittance and Equivalent Circuit.

is realized by using a short section of low-impedance coaxial line. The capacitance is given by  $C = Yl/v$ , where  $Y = 1/Z$  is the characteristic line admittance,  $l$  is the line length, and  $v$  is the wave velocity. For a resonant frequency of 14 GHz the proper length of  $10\Omega$  line is  $l = 0.038$  in. of air or  $l = 0.012$  in. for dielectric filled coaxial line (alumina,  $\epsilon_r = 9.9$ ). The resonant frequency was chosen at 14 GHz to maximize the lens array factor gain at the upper frequencies where the lens losses are highest. The  $10\Omega$  line impedance for the equivalent shunt capacitance was the lowest impedance value which could be easily realizable in coaxial line. At the resonant frequency, the  $50\Omega$  coaxial SMA connector is matched to the purely real load impedance ( $R = 1/G = 34\Omega$ ) using two alumina dielectric filled coaxial line quarter-wave sections of  $40.4\Omega$  and  $44.6\Omega$  respectively.

A second probe designed for the low band frequency range was matched at 10 GHz using a single teflon-filled ( $\epsilon_r = 2.1$ ) quarter-wave ( $l = 0.204$  in.) coaxial section of impedance  $Z = 30\Omega$ . For a probe impedance magnitude at 10 GHz of  $|Z_{in}| = 19.5\Omega$  the optimum line impedance to match to the  $50\Omega$  SMA connector is given by  $Z = \sqrt{(19.5)(50.0)} = 31.2\Omega$ . The design value of  $30\Omega$  was determined by optimizing over the 4 to 10 GHz frequency range on TOUCHSTONE. The value of the computed lens array factor gain was high enough at the low band frequencies to not require additional matching sections.

The resulting filter structures were modeled on TOUCHSTONE using transmission line sections of the appropriate impedances and lengths to compute the frequency responses. The filter designs loaded with the computed probe input impedances gave the responses of  $S_{11}$  shown in Figure 4 and

are compared to the corresponding  $S_{11}$  for an unmatched probe. Note that these plots do not include the effects of mutual coupling which is considered in the next section.

### 3 Multiple-Probe Modeling and Mutual Impedance

By assuming uniform, cylindrical currents on the probe surfaces one can derive an approximate expression for the mutual impedance between a pair of probes, neglecting reflections from the lens boundary. The result is

$$Z_{12} = \frac{\eta ka}{4} J_0(kd_1/2) J_0(kd_2/2) H_0^{(2)}(kR_{12}), \quad (6)$$

where  $d_1$  and  $d_2$  are the port diameters,  $J_0$  is the Bessel function of the first kind of order zero and  $R_{12}$  is the separation of the two ports. Of course,  $Z_{12} = Z_{21}$  for this reciprocal device. With Equations (5) and (6) we may compute the complete open-circuit impedance matrix,  $\mathbf{Z}$ , of the two-port network. The scattering matrix is then found using the standard formula

$$\mathbf{S} = (\mathbf{Z} - \mathbf{Z}_0)(\mathbf{Z} + \mathbf{Z}_0)^{-1} \quad (7)$$

where  $\mathbf{Z}_0$  is the identity matrix multiplied by  $Z_0 = 50\Omega$ .

Suppose now that the second probe is terminated in a load impedance  $Z_L$ . Under this condition, the current flowing in probe 2 is related to that in probe 1 by

$$I_2 = -\frac{Z_{21}I_1}{Z_{22} + Z_L} \quad (8)$$

and the input impedance seen at probe 1 is

$$Z_{in} = Z_{11} - \frac{Z_{12}Z_{21}}{Z_{22} + Z_L}. \quad (9)$$

The special case of probe 2 consisting of a shorting pin is treated by taking  $Z_L = 0$ . The above formulas are all easily generalized to include more than two probes.

### 4 Measured Results

Measurements of a two-probe microstrip lens were performed on an automatic network analyzer to determine probe mutual coupling and the resulting lens array port amplitude and phase distributions for individual probe

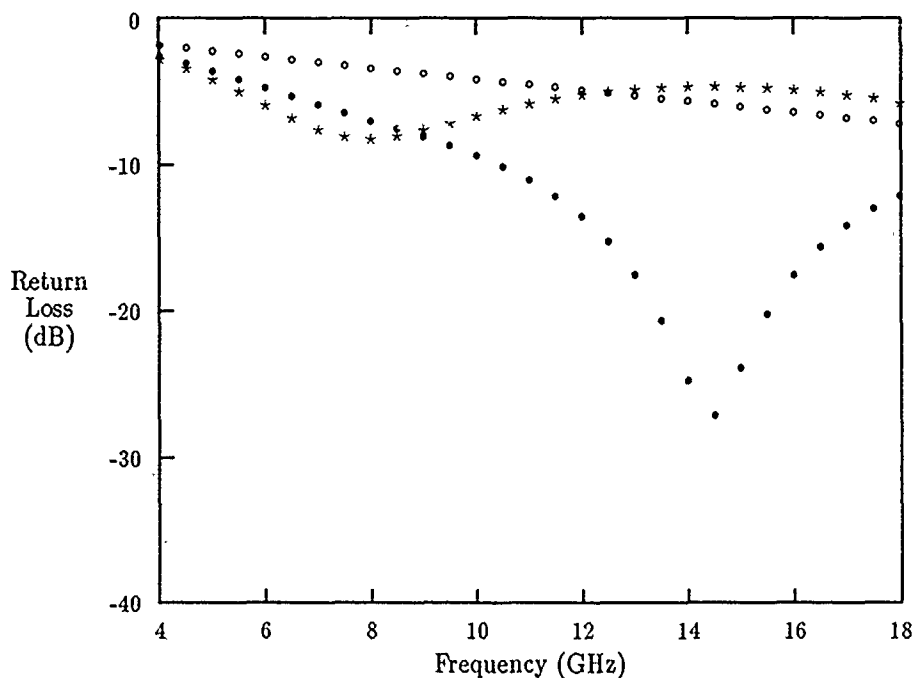


Figure 4: Computed return loss for the low band (\*) and high band (•) probes including matching sections compared to the computed return loss of a single probe (o) without matching network.

excitation. The computed and measured S-parameters of the two-port probe network are shown in Figures 5 and 6.

For each probe the measured and computed (both with and without mutual coupling) lens array port aperture distributions ( $S_{P,A}$ ) were then used to compute array factor patterns for an equally spaced (0.36 in.) linear eight element array. These patterns are compared at 10 GHz in Figure 7, which shows the importance of including mutual coupling.

It should be noted that a single three-section matched-probe provides the necessary array factor coverage over the entire 4-18 GHz bandwidth, and that the two-probe approach was developed for a particular system configuration.

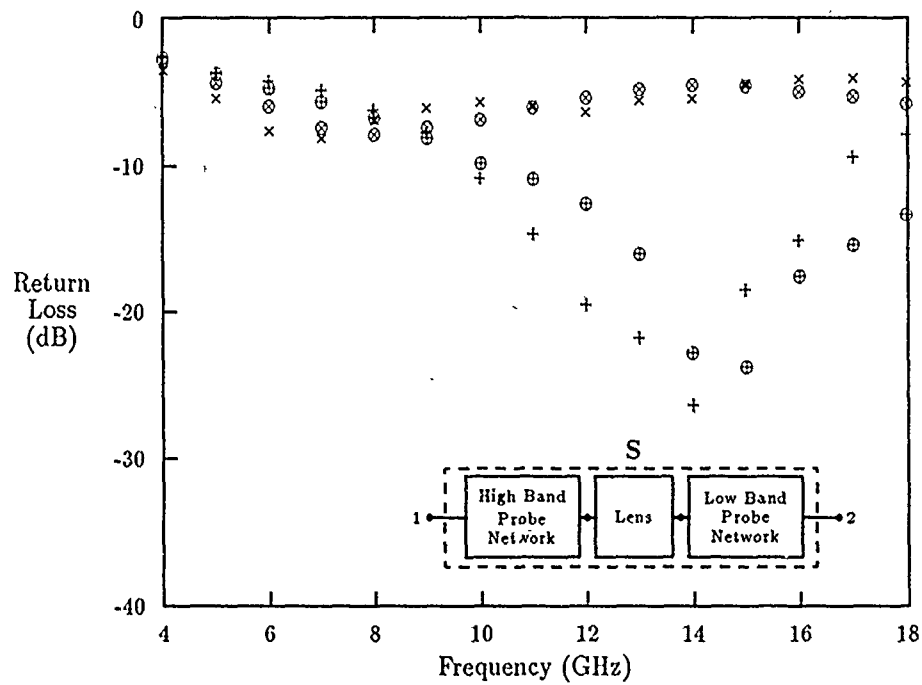


Figure 5: Computed and measured return loss for the two-port defined as shown.  $\oplus$  and  $+$  are used for computed and measured return loss at port 1, respectively, while  $\otimes$  and  $\times$  are used for the same quantities at port 2.

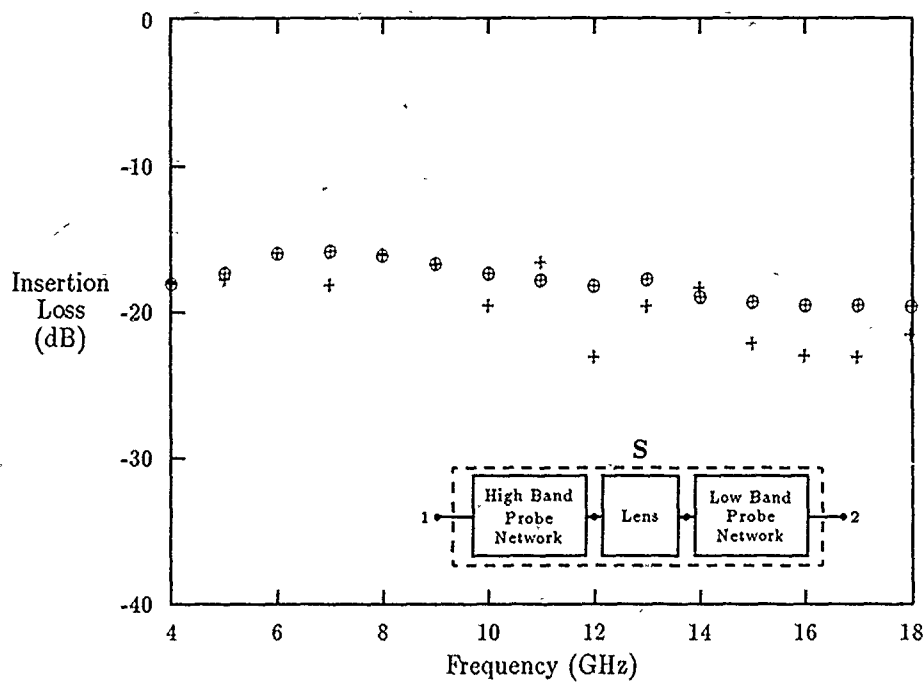


Figure 6: Computed and measured insertion loss for the two-port defined as shown.  $\oplus$  and  $+$  are used for computed and measured values, respectively.

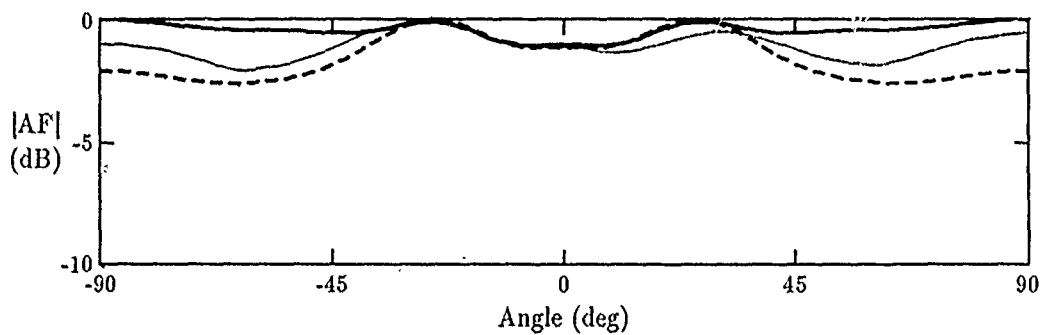


Figure 7: Low band probe array factor patterns at 10 GHz. Dashed line: computed taking into account mutual coupling; dark line: computed neglecting mutual coupling; light line: computed from measured lens  $S$ -parameters.

## 5 Conclusion

A two-probe microstrip Rotman lens has been analyzed and developed for synthesizing sector coverage array factor patterns. The probe array factor gain has been optimized for this configuration by utilizing a coaxial multiple section filter. The implementation of this approach for realizing a broadband (4–18GHz) wide sector synthesized array factor pattern has been demonstrated.

## References

- [1] J. A. Troychak, "Broadband Synthesis of Low-Sidelobe Antenna Patterns," *IEEE Int. Symp. Digest - AP*, Vol. 2, June 1987, pp. 1070–1073.
- [2] R. J. Prickett, "Broad Beamwidth Lens Feed," *U.S. Patent No. 4,641,144*, Feb. 3, 1987.
- [3] R. F. Harrington, "Time-Harmonic Electromagnetic Fields," *McGraw-Hill*, 1961, p. 378.

## KU-BAND ANTENNA FOR VSAT APPLICATIONS

Nicholas Moldovan  
Prodelin Corporation  
1700 N.E. Cable Drive  
Conover, North Carolina 28613

### ABSTRACT

Very Small Aperture Terminals (VSAT's) operating in the Ku-Band frequency range are gaining popularity for two way data communications via satellite. Today, over 10,000 VSAT antennas are in operation and market forecasts shows all the signs of continued high growth potential. For these networks, antennas in the 1.8 and 2.4 meter aperture sizes are typically used. The antennas are designed for high performance and low cost.

This paper discusses the development and production implementation of a 1.8 meter VSAT antenna and accessories. System performance parameters are presented along with novel component designs including: reflector, feed horn, and anti-icing provisions.

## 1.0 INTRODUCTION

During the past five years, there have been increasingly widespread applications for cost-effective satellite communication systems offering the end user 2 way high volume data transmission. This new business has been identified as Very Small Aperture Terminal (VSAT) and is currently in use by private industry and federal agencies. Typically, these remote antennas are 2.44 meters in aperture size or less and connect to a central antenna hub/computer facility to create the network.

A critical element of the VSAT network is the remote communication antenna. The short wavelengths of Ku-Band frequencies, high reliability and low cost requirements, and FCC regulations, place challenging requirements on the antenna. This paper describes a 1.8 meter prime focus offset antenna which has been specially developed for application in VSAT networks. To date over 10,000 antennas are currently in operation throughout the world. The paper is organized as follows: antenna system design and performance summary, component design and manufacturing technology, and radiation performance.

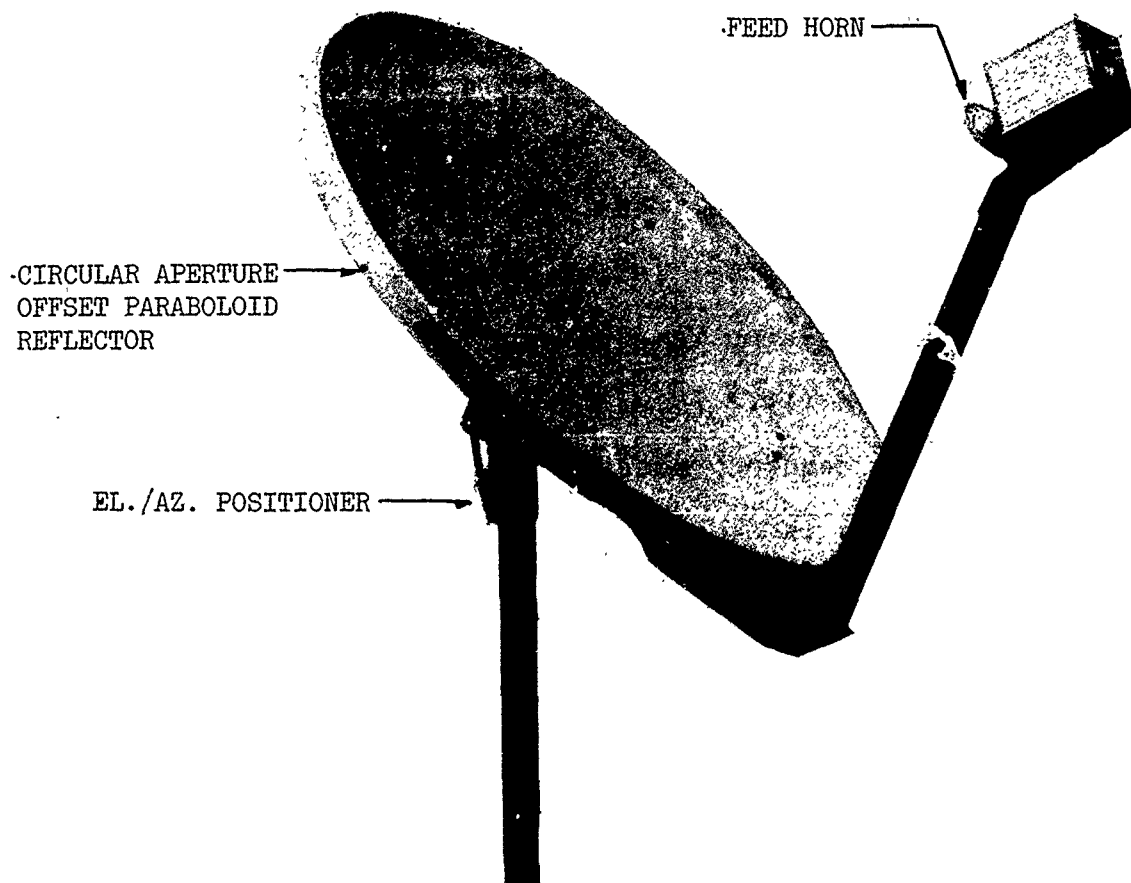


## 2.0 Antenna System Design and Performance Summary

The prime focus offset fed antenna system, shown in figure 2.0-1 is the baseline design. This antenna provides simultaneous operation across the domestic receive (11.7 - 12.2 GHz) and transmit (14.0 - 14.5 GHz) frequency bands with linear polarization. The antenna is compliant to the FCC Co-Polar sidelobe specifications along the geostationary satellite arc. Major components of the antenna system are a one piece reflector, feed horn and elevation over azimuth positioner. Optional components include anti-icing provisions for the reflector and feed horn.

## 3.0 Component Design and Manufacturing Technology

Product technical performance, product cost, and anticipated market share were of dominant importance in the design and selection of manufacturing technologies for the antenna system. Early VSAT network market forecasts estimated approximately 50,000 remote antennas would be utilized between 1986 and 1992. In addition, needs for Ku-Band receive-only antennas for video and audio applications were estimated at 30,000



#### 1.8 METER SPECIFICATIONS SUMMARY

##### ELECTRICAL

OPERATING FREQUENCY, Rx	11.7 - 12.2 GHz
Tx	14.0 - 14.5 GHz
MIDBAND GAIN, Rx	45.0 dBi @ 11.95 GHz
Tx	46.5 dBi @ 14.25 GHz
SIDELobe ENVELOPES, CO-POL (dBi)	
$1^\circ < \theta < 7^\circ$	29-25 LOG $\theta$
$7^\circ < \theta < 9.2^\circ$	+8
$9.2^\circ < \theta < 48^\circ$	32-25 LOG $\theta$
$48^\circ < \theta < 180^\circ$	-10

##### MECHANICAL

OPERATIONAL WIND LOADING	45 mi/h
SURVIVAL WIND LOADING	125 mi/h
CORROSION METAL PROTECTION	HOT DIPPED GALV.

FIGURE 2.0-1 1.8 ANTENNA SYSTEM AND PERFORMANCE

remote antennas over the same period. Since these satellite delivery networks are in direct competition with leased terrestrial data lines, cable networks, etc., system cost was of paramount importance. Therefore, at the start of the development, a close interface between RF, Mechanical, and Manufacturing Engineering was established. The following paragraphs describe the design and manufacturing technology selected for the 1.8 meter reflector, feed horn, and optional anti-icing provisions.

### 3.1 Reflector

The circular aperture, prime focus, offset fed optics were selected because of the simplicity and technical criteria such as: elimination of blockage and reduced impact caused by accumulating rain, ice, and snow on the reflector.

The selection of a material system and its associated manufacturing process for the reflector design go well beyond surface accuracy (rms) and stiffness requirements. Without due consideration of complex environmental conditions, susceptibility to handling damage, structural weight,

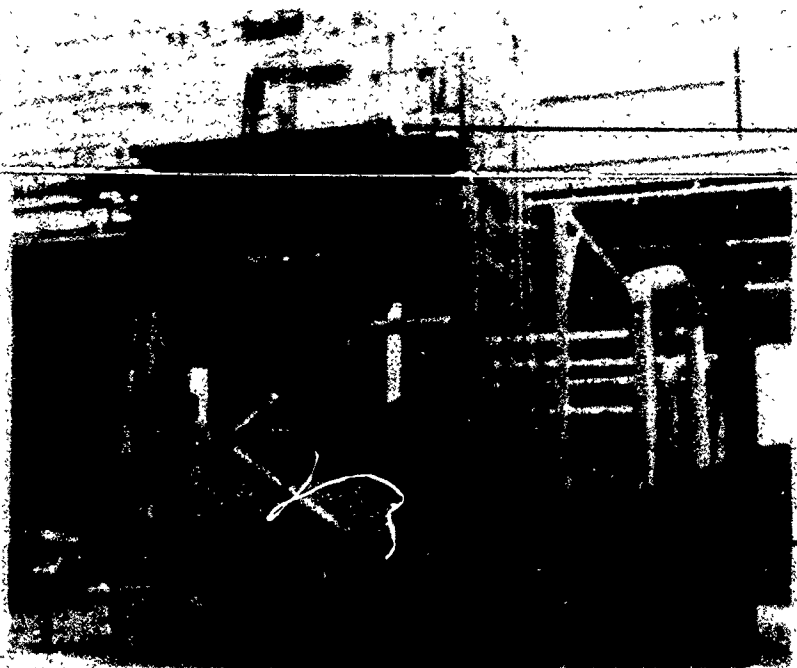
and appearance, a particular design may fall short of meeting its long term objective.

Light gauge metals have long been widely used for reflector manufacturing, principally because of their inherent microwave reflectivity and high tensile strength. Their cost performance is typically unsurpassed in structural applications involving low quantities (2,000 units/yr) and simple shapes. Typical manufacturing methods include stretch forming, stamping, and hydroforming.

Over the past 7 - 12 years, however, advanced composite materials have entered selected engineering applications in the aerospace and automotive industries. In applications where stiffness-to-weight and stiffness-to-cost are dominating criteria, they can be unsurpassed. As these materials relate to the design and manufacture of small aperture reflectors, properly engineered systems of compression molded glass/inorganic solids/polyesters can demonstrate the highest levels of dimensional accuracy and part-to-part uniformity. The added attributes of low thermal coefficient of expansion (approximately equal to steel), high impact strength, and low thermal conductivity make this class of material highly

suitable for microwave reflector applications. When properly designed and utilized, compression molded reflectors permit the integration of multiple parts through the material's complex shaping capabilities which can result in fewer separate parts, elimination of fasteners, secondary assembly steps, and lower production costs. For example, the reflector surface and back structure is molded in one operation. The inherent overall corrosion resistance of these composites have eliminated the need for costly coating systems. For small aperture reflectors in moderate-to-high quantities (5,000 to 25,000 units/year) the compression molding process utilizing sheet molding material (SMC) was selected. The SMC formulation (% by Wt.) for this application consists of 50%  $\text{CaCO}_3$  (limestone), 30% glass fiber, 17% Polyester resin, and 3% Modifiers & catalysts.

In summary, the selection of compression molding for the 1.8 meter reflector has proved to be the correct choice. Figure 3.0-1 shows the production facility where the reflector is molded. Reflector fabrication cycle time is 9 minutes.



2,500 TON  
PRESS



SMC  
MATERIAL  
IN  
REFLECTOR  
DIE



DEFLASHING  
AFTER  
MOLDING

FIGURE 3.0-1 REFLECTOR PRODUCTION FACILITY

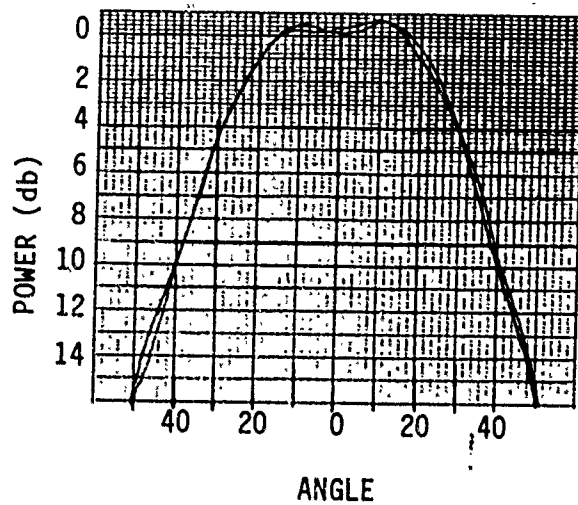
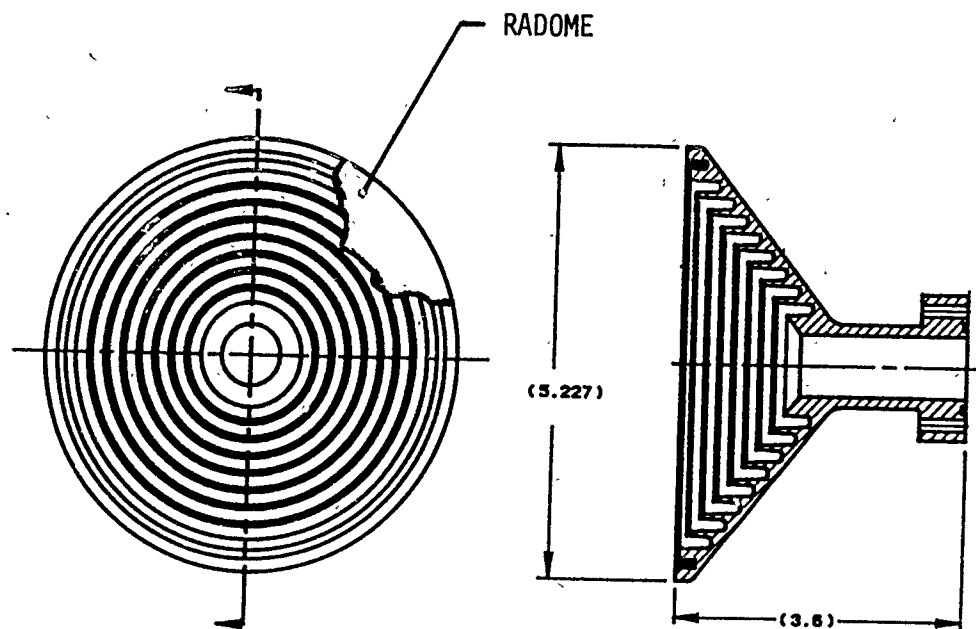
### 3.2 Feed Horn

High gain, low sidelobe, and low cost antennas present a significant design challenge in matching the reflector and feed. For this application, a conical corrugated horn was selected for the following reasons:

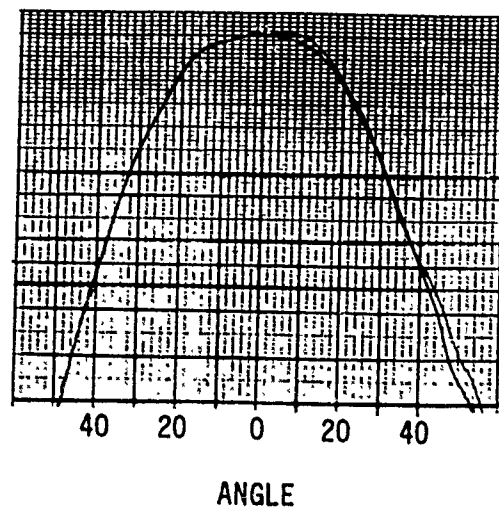
- High Efficiency
- Wide Band
- E & H Plane Symmetry
- Very Low Cross Polarization
- Optimum Reflector Illumination (10 db edge taper)
- Manufactured by Aluminum Die Casting Method

The feed horn configuration and primary radiation patterns are shown in Figure 3.2-1.

To facilitate volume production, corrugations are parallel to the boresight axis as opposed to more conventional approaches (i.e. perpendicular to wall or axis). To prevent moisture accumulation inside the feed horn, extensive development was performed on the material selection and assembly method of the radome. A polyester material with an ultraviolet absorber was



FREQUENCY = 14.25 GHz  
E & H PLANES



FREQUENCY = 11.95 GHz  
E & H PLANES

FIGURE 3.2-1 FEED HORN



selected for the radome material because of its outstanding rf and mechanical properties. Completing the assembly, the radome receives a hydrophobic coating which imparts extreme water repellency.

### 3.3 Optional Antenna Anti-Icing Provisions

In commercial applications in North America and Europe, antenna anti-icing has been found to be a necessity in most of the commonly used frequencies. In Ku-Band experience, where offset reflectors are incorporated, there is less tendency to accumulate large depths of snow, but a greater tendency for the signal to be attenuated in thin layers of snow or glaze ice. In order to meet high VSAT system reliability and antenna system performance specifications, A novel reflector and feed horn anti-icing system was developed. The reflector anti-icer (SoftHeat Radiant<sup>TM</sup>) consists of a self regulating radiant heating element, as shown in Figure 3.3-1. The radiant heating element is located in a backshell and is separated slightly from the reflector structure, enabling the uniform heating of

SoftHeat Radiant<sup>TM</sup> - Trademark of Raychem Corporation

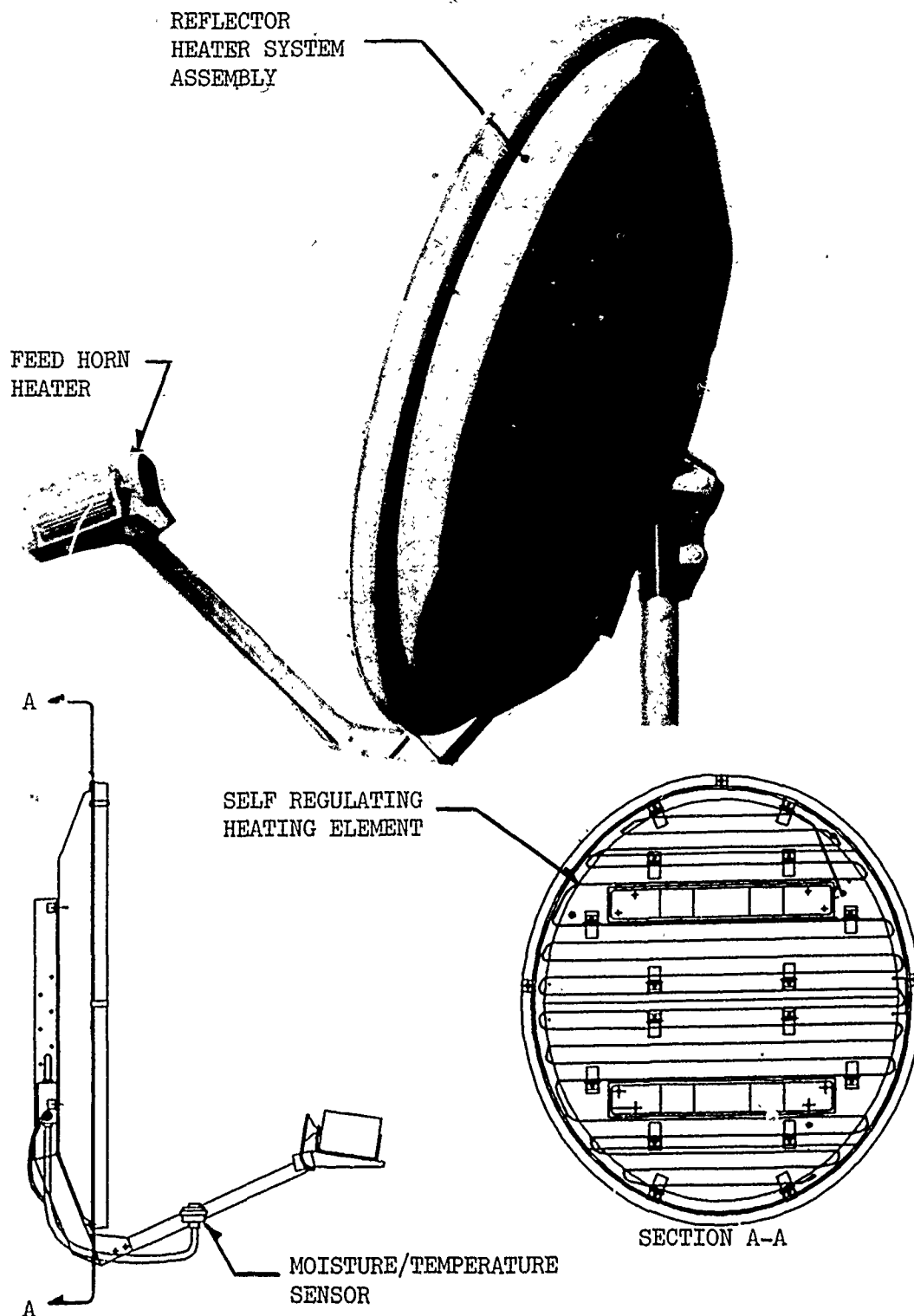


FIGURE 3.3-1 ANTI-ICING PROVISIONS

the reflector. Since the element utilizes self-regulating heating technology, they have been found to be extremely long-lived. In addition, the heat transfer mechanics of radiant heating, when combined with the self-adjusting power level of the heater in response to its environment, provide intensive heating for those areas of the antenna where anti-icing is needed. When the system is idling in the absence of peak storm conditions, less power is drawn. RF radiation measurements along with infrared thermal images have been obtained showing the even heating provided by the heating system. To provide anti-icing capability for the feed horn, a self-regulating heater is wrapped around the outer surface of the horn. The heater heats the internal air volume of the horn, gently warming the surface of the feed window. Controlling the heaters, the microcomputer-based SnoTrol<sup>TM</sup> saves energy by operating the antenna heaters during snow and for one hour thereafter. It detects snow by sensing both temperature and moisture. The SnoTrol<sup>TM</sup> provides an electronic bypass switch for testing and manual heater operation.

SnoTrol<sup>TM</sup> - Trademark of Environmental Technology, Inc.

#### 4.0 1.8 meter Antenna System Performance

To illustrate the performance characteristics of the antenna, midband co-pol and cross-pol secondary radiation patterns are presented in Figure 4.0-1.

#### 5.0 Conclusion

This paper discussed the development and production implementation of a Ku-Band, 1.8 meter antenna system for applications in Very Small Aperture Terminals (VSAT) networks. The antenna system has been specifically developed utilizing high volume/low cost manufacturing methods. Antenna system radiation performance is presented in addition to descriptions of reflector, feed horn, and anti-icing provisions.

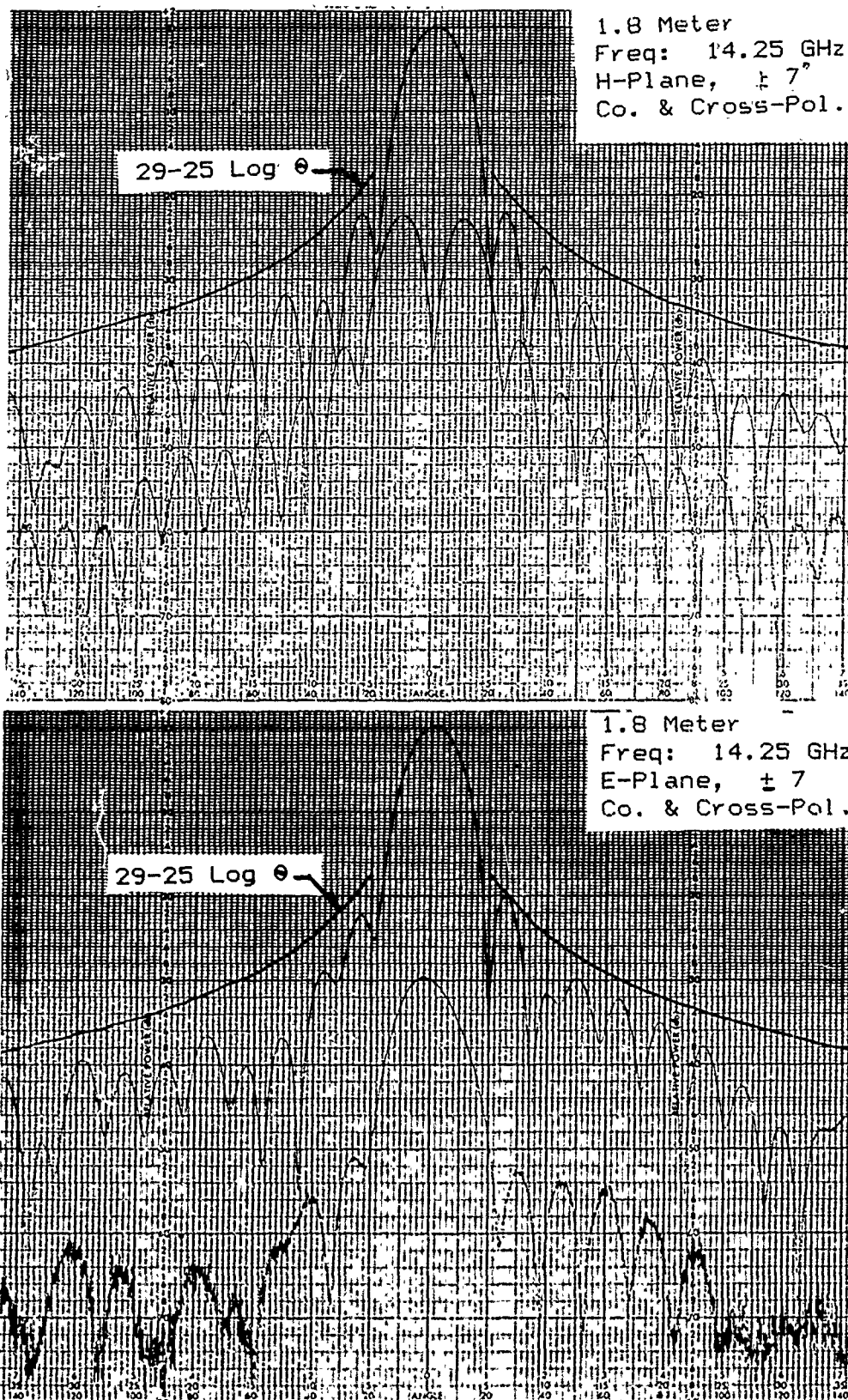


Figure 4.0-1 1.8 meter Radiation Patterns

## ELECTROMAGNETIC COUPLER

Peter R. Franchi  
Rome Air Development Center  
Hanscom AFB MA 01731

Nicholas P. Kernweis  
Rome Air Development Center  
Hanscom AFB MA 01731

### I. INTRODUCTION

Large conformal airborne phased arrays (Fig 1) are increasingly projected as a future Air Force need. While many of the ultimate characteristics cannot be accurately predicted at the present time certain features are clearly desirable. One of the features is minimum extrusion to keep added air-drag as low as possible. Because space inside a surveillance aircraft is also at a premium, minimum intrusion is also highly desirable. For these two reasons phased arrays are envisioned with multiple planar configurations, that is, at the outermost plane would be the radome surface, then, the radiating surface, the phase shifter or T/R module surface, finally the beamforming network layer and mixed in within these layers would be DC power and digital control layers. Figure 2 shows a sample configuration.

In this paper, the principle concern is the RF feed coupling the RF power distribution network to the active or phase shifter layer. If these feed-throughs are metallic pins and there are a great number of them both the difficulty of assembling the networks and the expected power long-term reliability are very serious problems. Furthermore, another set of transverse wire connectors is required for mode suppression making the network assembly even more complex (See Fig 3). An examination of the use of electromagnetic or proximity coupling has been undertaken to alleviate these problems.

### II APPROACH

The approach we have used involved the analytic solution and application of the weak coupler case from Mathei and Young to coupling between stripline with longitudinal slots (i.e. slots that have their maximum dimension in the direction of the stripline center conductors). This solution was extended to give complete coupling. From this base, an experimental model was built, tested and modified to overcome the problems of using weak coupler design for total coupling.

### III Derivation:

For the configuration shown in Figure 4 the following equations apply:

$$\frac{1}{Z_{oe}} = \frac{1}{2} \left[ \frac{1}{Z_{oo}} + \frac{1}{Z} \right] \quad (1)$$

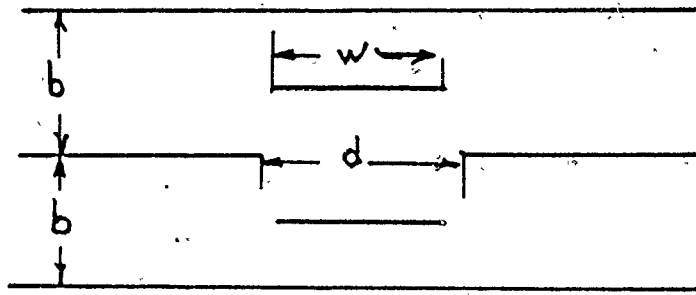


FIG 4

where  $Z_{oe}$  is the even mode characteristic impedance of the stripline,  $Z_{oo}$  is approximately  $Z_o$  the characteristic impedance of the stripline and

$$Z = \frac{30\pi}{\sqrt{Er}} \frac{K(k')}{K(k)}$$

$K$  is the complete elliptic integral of the first kind.

$$k = \sqrt{\frac{\cosh \frac{\pi w}{b} - 1}{\cosh \frac{\pi w}{b} + \cosh \frac{\pi d}{b}}} \quad (2)$$

$$\text{and } K' = \sqrt{1 - k^2} \quad (3)$$

If the length of the coupling section is  $\beta_o$ , maximum coupling occurs when  $\beta_o = \frac{\pi}{2}$ . This gives an impedance of  $Z_I$  in this region where

$$Z_I = \frac{Z_{oe} - Z_{oo}}{2} \quad (4)$$

$$\text{and } \beta_o = \frac{\lambda_o}{4}$$

Since  $Z_I$  will be smaller than  $Z_o$ , a quarter-wave matching

section is needed at the input and output lines.

$$Z_m^2 = (Z_1 Z_0) \quad (5)$$

where  $Z_m$  is the impedance of the matching section.

These equations together with Figure 5 are sufficient to determine the dimension of a coupler for a given  $\epsilon_r$  and ground plane separation,  $b$ .

#### IV EXPERIMENTAL RESULTS

A test coupler was built at S-Band ( $\lambda_0=3.5$  inches). It consisted of four layers of etched copper clad dielectric. The complete coupler is shown in Fig 6. The outside dimension of the test piece was 6" x 3.5 inches. Large aluminum plates were used to hold the four pieces together with nuts and bolts. Coax to stripline connectors linked the test piece to the network analyzer. A 50 ohm stripline with the same dimensions was made to account for the ohmic losses of the equivalent transmission line. Power applied to the test coupler, divides into power out the output connector ( $S_{12}$ ), power reflected back ( $S_{11}$ ), power absorbed by the stripline, ohmic loss, and power lost by radiation from the coupler. Since we have measured estimates of  $S_{11}$  and  $S_{12}$  the power absorbed, we can estimate the power lost by coupler radiation as the remaining power. This loss is the critical measure of the coupler since this energy is free to propagate throughout the stripline circuit.

By the use of tuning the reflection loss can be reduced to -20db or greater (less than 1% of reflected power). Low loss dielectric and thick copper coating can reduce the ohmic loss. For the 6 inch stripline section this loss is about .5db. Again, the loss that is critical is the coupler radiation loss. If this loss were much greater than .5db or 10% in power it would be an unacceptable loss for most practical applications. On the other hand a loss of .1db or 2% would be quite acceptable.

Figure 7 is the final measured result after several iterations. The return loss is 20db or greater over an 8% band. At the center the transmission loss is .24db. The loss, then, due to coupler radiation is only 4 or 5%. This result is the lowest coupler loss, obtained after several iterations. The initial design used a total stripline separation of .13 inches. The application of the design equations lead to a slot width of .35 inches. Because of the



assumption that the large slot width is the major cause of high coupler loss designs with narrower slots were found. These designs did appear to give considerably less coupling loss but the mismatch at the edges of the test piece with absorber prevent a well defined estimate of the coupling loss. The rough rule emerging is to keep the slot width less than 4 or 5% of a wavelength.

## V CONCLUSION

The use of the design equations of section III along with a slot width restriction of  $.04\lambda_e$  where  $\lambda_e$  is the wavelength in dielectric stripline gives low loss coupler performance. With the low loss, proximity or electromagnetic couplers become practical and for complex networks that require multiple layers of stripline for beamforming the need for blind pin connectors and mode suppressions is eliminated. Fabrication cost should be reduced and network reliability enhanced.

## REFERENCES

Mathei and Young and Jones Microwave Filters, Impedance Matching Networks, and Coupling Structures. McGraw-Hill

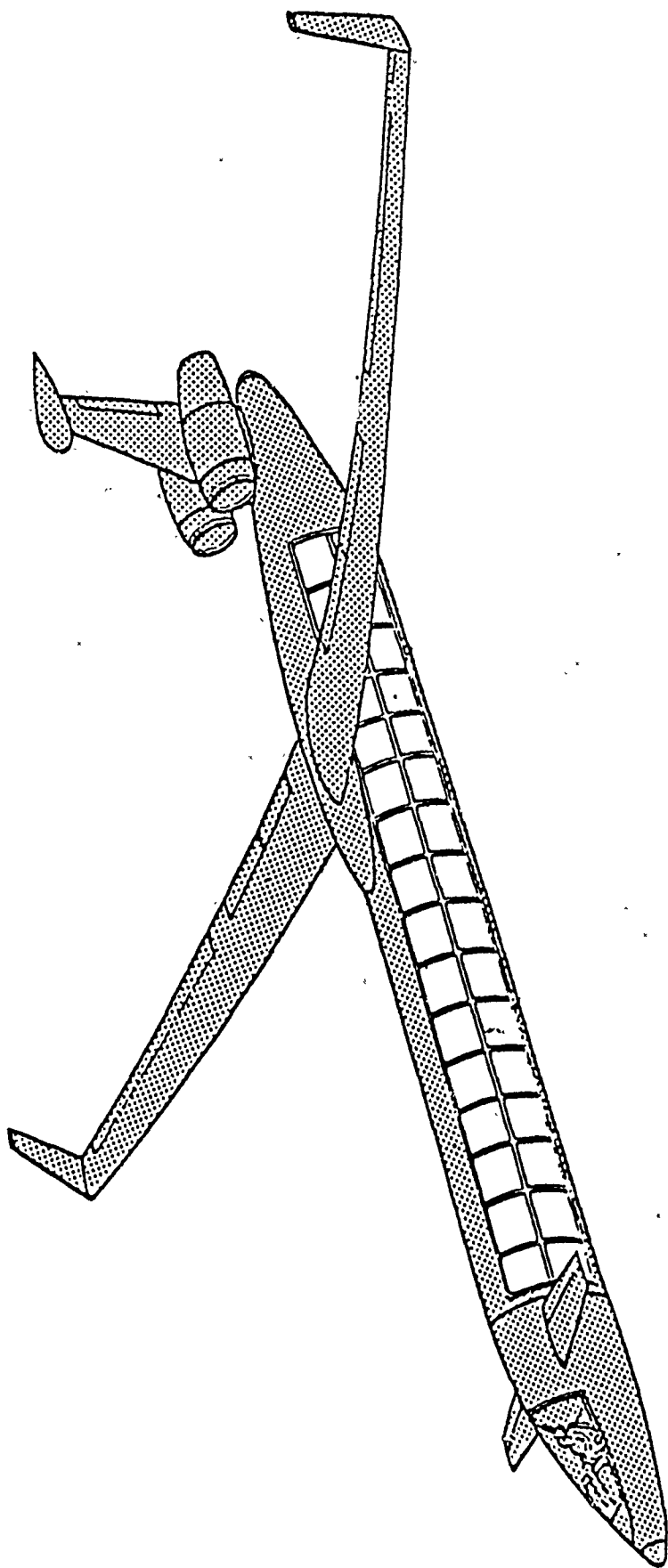


Figure 1 Large Conformal Array

# MULTI-LAYER CONSTRUCTION OF PRINTED CIRCUIT ARRAY

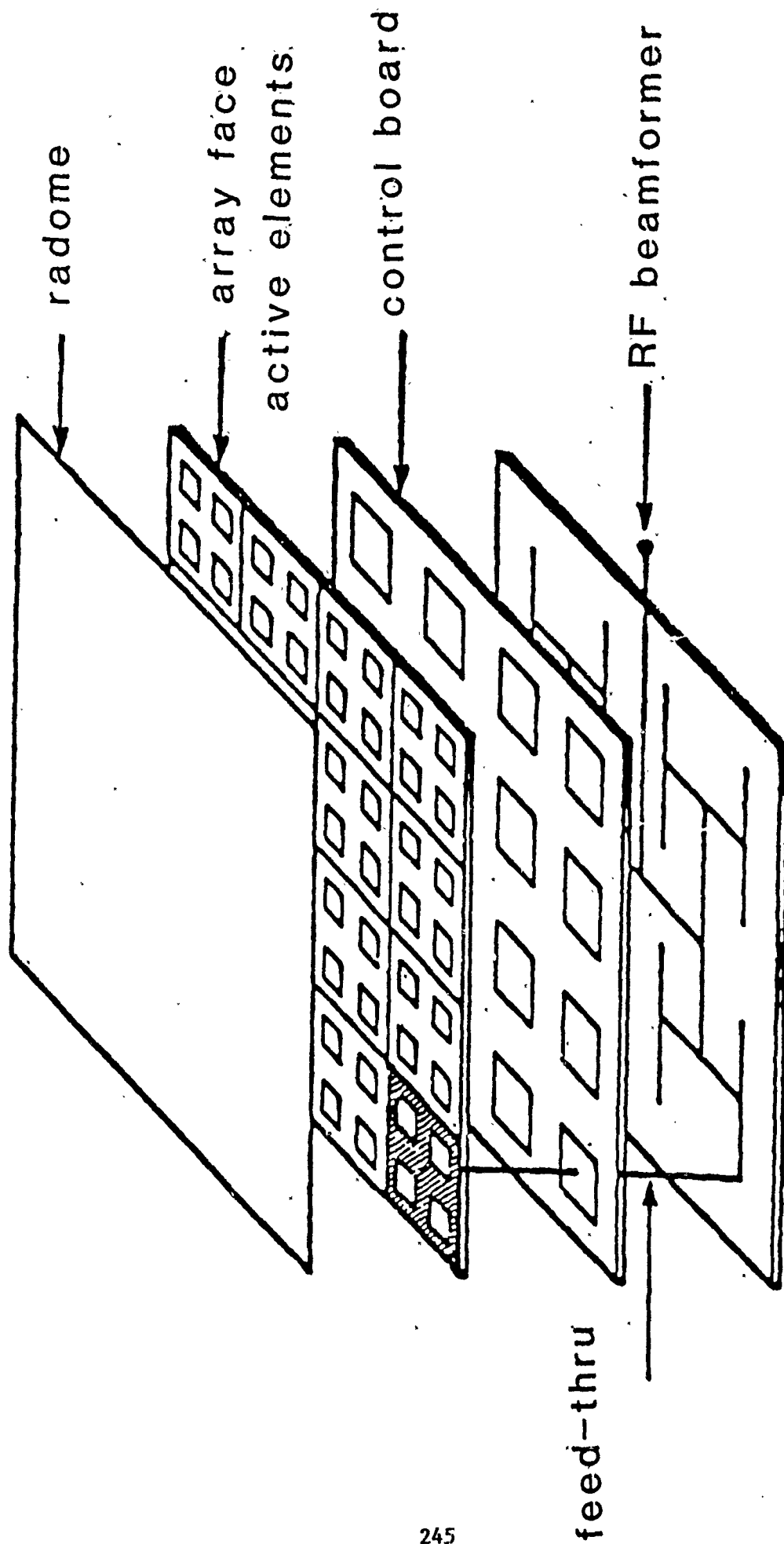


Figure 2. Possible Configuration

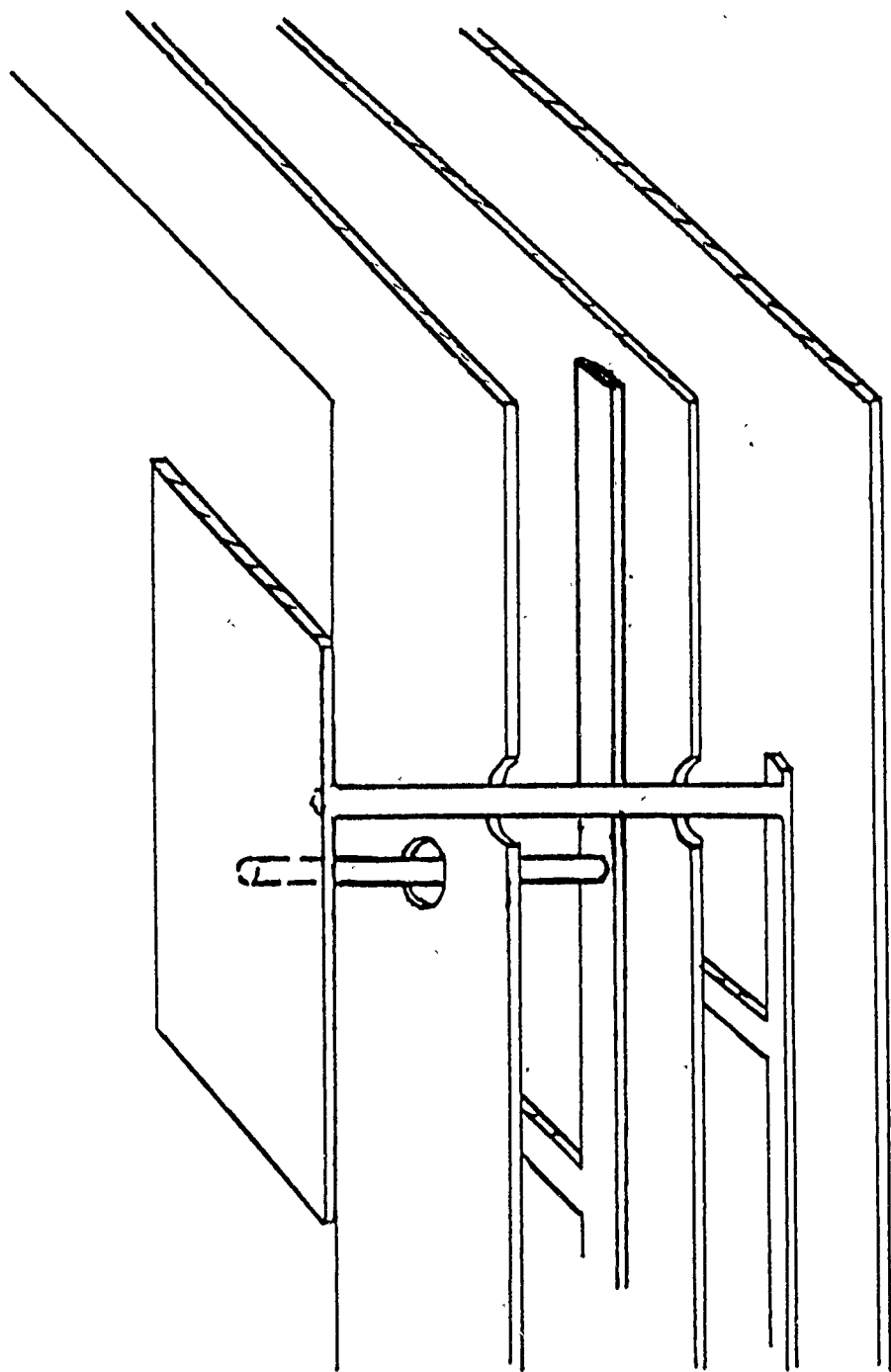
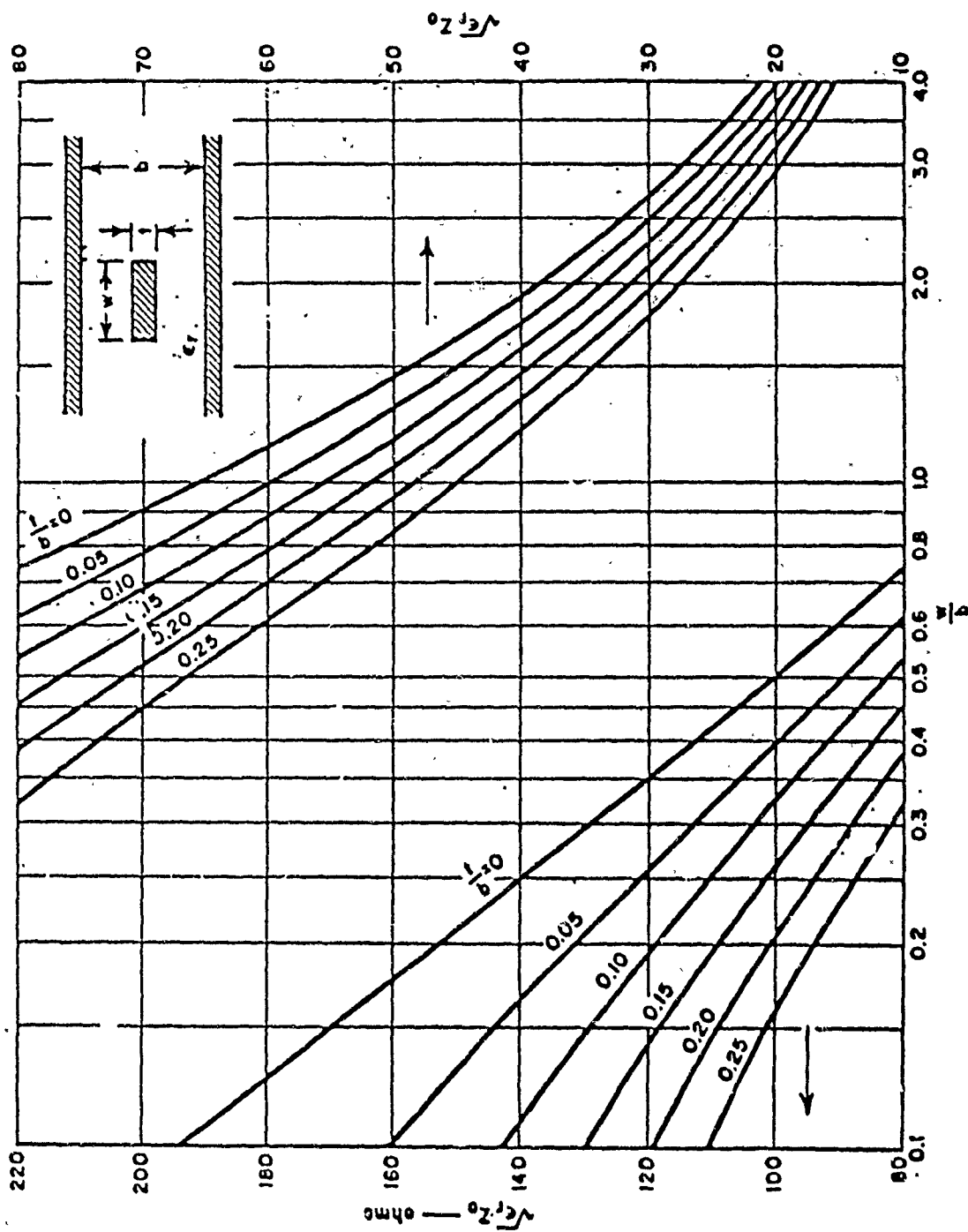


Figure 3 possible network  
cross-section



SOURCE: Final Report, Contract DA 36-039 SC-63232, SRI; reprinted in *IRE Trans., PGMTT* (see Ref. 2, by S. B. Cohn).

Figure 5  $Z_0$  versus  $w/b$

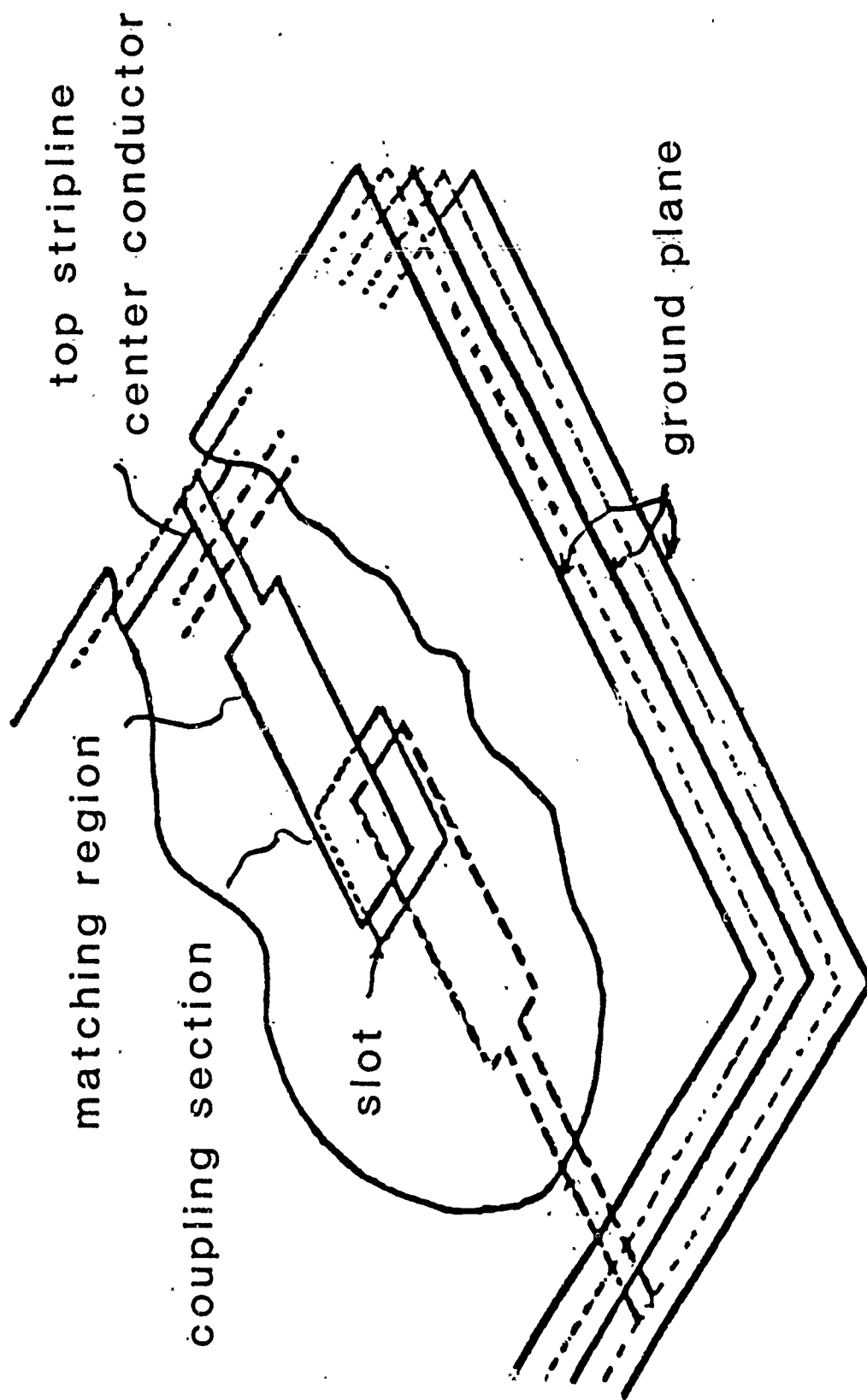
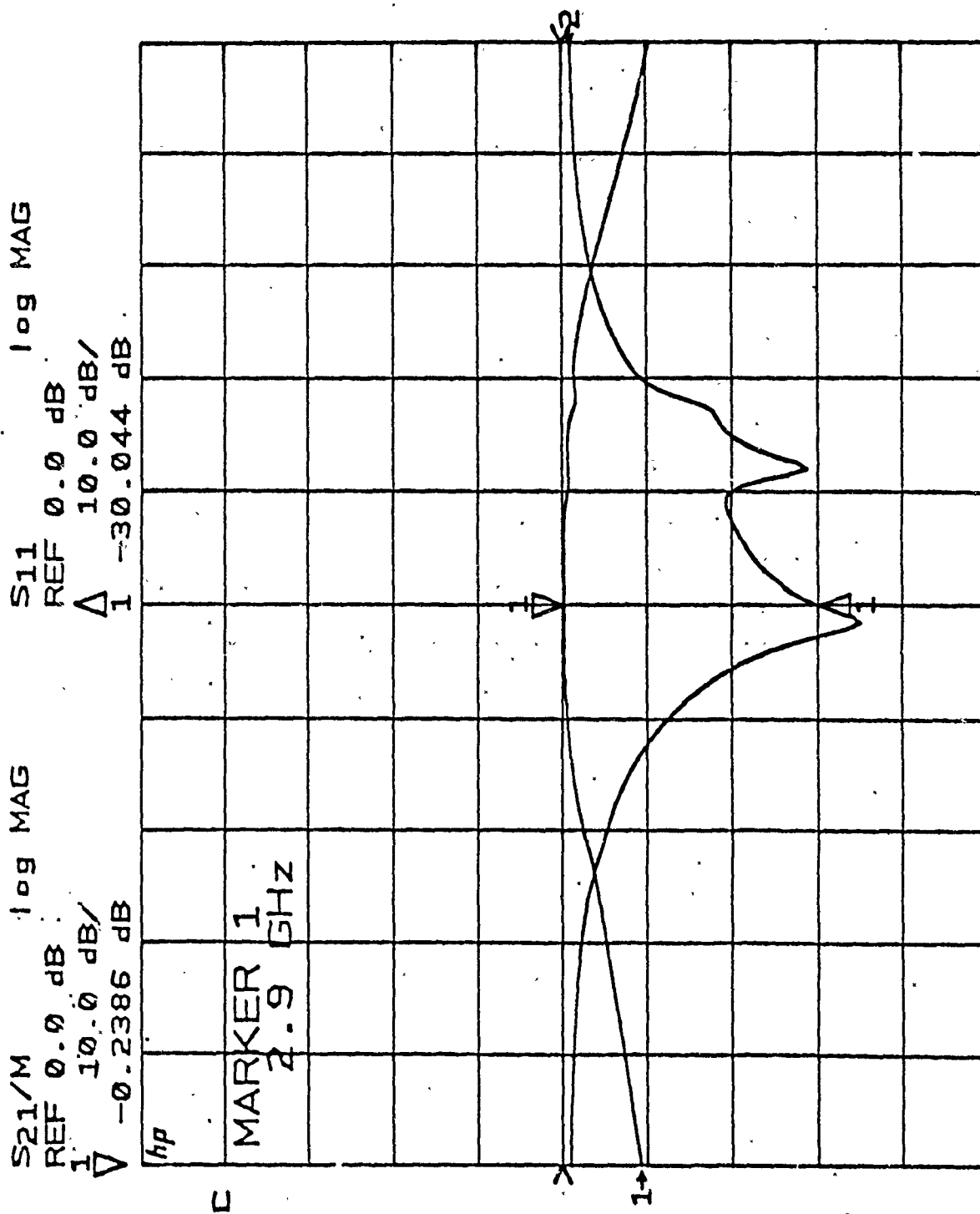


Figure 6 assembled coupler



START 2.30000000 GHz  
 STOP 3.50000000 GHz

Figure 7 coupler reflection and transmission behavior



## Design of a Planar Array of Parasitic Microstrip Patch Antennas

R.W. Shaw and J.K. Kovitz; Shason Microwave Corporation;  
Houston, Texas

Dr. I.Paz and L. Johnson; Lockheed Engineering and Sciences Company  
Houston, Texas

Dr. G.D. Arndt; National Aeronautics and Space Administration  
Johnson Space Center, Houston, Texas

### Abstract

The accumulation of space debris in low earth orbit (LEO) is expected to present an increasing threat to large space structures such as the planned Space Station "Freedom." Space borne radar systems will eventually be needed to detect and track debris of approximately 1 cm or smaller. Due to the small radar cross section of such debris and the high closing velocities of the particles, stringent constraints must be placed on the space borne system. The preliminary investigation of the antenna system required to perform in this application has been configured as a planar array of parasitic microstrip antennas. Benefits of the parasitic over the directly fed patch configuration include increased gain and impedance bandwidth. In addition, the reduction in number of fed elements in the array will simplify the design and improve the performance of the corporate feed network.

This paper will address the design of the rectangular patch subarray, the integration of the subarray with the feed network, the implementation of the microwave components (i.e. low noise amplifiers, power amplifiers, phase shifters, etc.) into the antenna system and review basic parameters required in the orbital debris scenario. The design process and the performance measurements of a partial array consisting of four electronically steered subarrays will be described and presented.

## 1.0 INTRODUCTION

Antenna arrays are finding wide applications in military and space-based systems which require rapidly scanned beams or simultaneous beams for numerous users. In these applications, and in most space requirements, the operating frequencies are specified in the higher microwave region including Ku, K and Ka bands (13 to 40 GHz). As a result of these higher frequencies, transmitter power levels and receiver noise figures become the main performance limiters on the system. A simplified block diagram for an active array system is shown in figure 1.

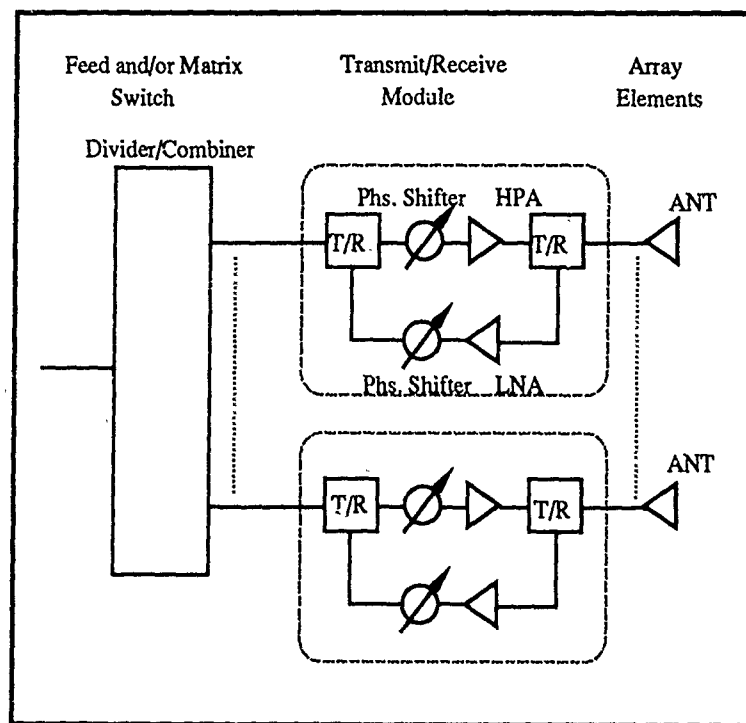


Figure 1: Simplified Active Array Antenna System

A significant advantage can be gained by the use of solid state power transmitters and low noise amplifiers embedded and distributed in the numerous elements which make up the aperture of the array. This

distributed architecture must physically and mechanically accommodate the active circuits as close to the array element as possible in order to achieve the optimum system performance. While recent work has extended the performance of Monolithic Microwave Integrated Circuits (MMICs), development of supporting technology has lagged. It can be shown in many applications that the distribution networks, feed networks, and most importantly, the antenna elements are constraining the performance enhancements associated with the use of MMIC components. The inability of most antenna element structures to achieve wide operating bandwidths and still be conducive to the electrical and mechanical requirements of MMIC integration is a major problem in higher frequency systems.

This work has developed a subarray of parasitic patch antennas which can be used as a basic building block element for a larger array. The parasitic subarray makes use of the natural integration of the planar microstrip patch antenna and the planar strip transmission lines used in the feed networks and associated active circuits. In addition, the use of parasitic patch antennas improves the gain and bandwidth over single element microstrip patches and reduces the complexity of the corporate feed structure. Similar developments of these structures at S-band and X-band frequencies have demonstrated bandwidth improvements of 3:1 when compared to single patch antennas.<sup>1,2,3</sup> The application of this antenna architecture at Ku, K, and Ka bands will allow a single array to operate in a full-duplex, frequency division multiple access (FDMA) communication system or in a wideband "chirped" radar.

## 2.0 SYSTEM APPLICATIONS

This parasitic array configuration will be demonstrated in a space debris detection and tracking radar system feasibility design. The Debris Radar System that triggered the need and provided the

justification for this work was described in detail in a previous paper.<sup>4</sup> We summarize here, for completeness, some of its architectural ingredients and required specifications.

## 2.1 System Block Diagram

A block diagram of the radar system is given in figure 2.

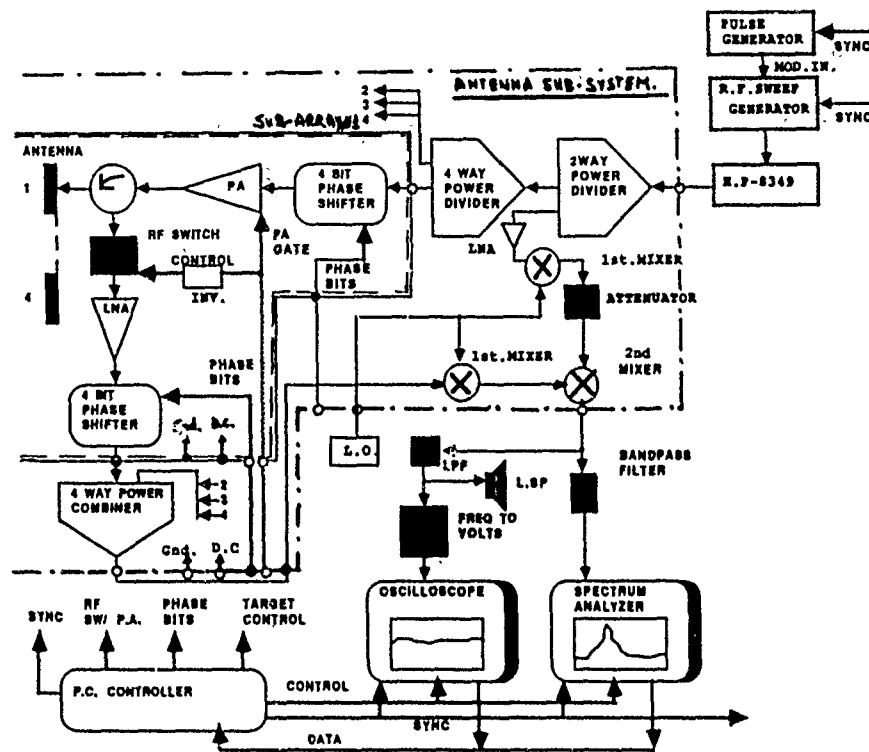


Figure 2: Debris Radar System Block Diagram

The purpose of this radar system would be to provide the necessary detection and tracking information to allow auxillary systems to protect the critical areas of the Space Station "Freedom" from the dangerous collision impacts with orbital debris. A feasibility radar system was therefore devised which shall easily be adaptable to perform the necessary proof of concept in different test environments. The decision to use a phased array antenna for the Debris Radar System followed

from the need for high beam scanning speeds and good maintainability over long periods of time.

The smallness of the radar cross section, the high velocities relative to the space station, and the large scan regions for the debris detection and tracking made the optimal design of the antenna subsystem of extreme importance.

## 2.2 Antenna System Considerations

Power budget requirements would apparently ask for as large an antenna as possible. This would imply, however, increasing the number of subarrays and power amplifiers and therefore, the costs. A large antenna would also lead to a sharper beamwidth and this will require an increase in the scan rate needed for providing the system with the necessary time to process the information provided by the detected echoes. Alternatively, one could try to increase the detection range for this purpose. An increase in range will require a significant increase in the "power budget" of the system. This increase in power budget could be achieved by: a) increasing the size of the antenna, b) increasing the power supplied to its subarrays or c) increasing the sensitivity of the receiver. Increasing the sensitivity of the receiver will require pulse-integration, or an increase in the number of echoes that can be obtained per beam position. An increase in the number of "hits" per beam position will actually require either: a) a slow down in the scanning rate or b) an increase in the beamwidth: (i.e., a smaller antenna, but a poorer possible tracking resolution).

The antenna system described in this paper provides a possible solution to the above conflicting requirements. It will be of a modular architecture with each module being based on 3 to 6 subarrays and independently controlled by a microprocessor using some prestored phase shifting and other necessary control sequences. This will save on

the otherwise large amount of cabling needed and reduce weight and complexity. Also, such a distributed modular approach will provide the system with a more robust performance, with only gradual performance degradation.

### 3.0 SUBARRAY DEVELOPMENT

#### 3.1 Concept

Antenna elements used in arrays must have the following characteristics known or specified before the system architecture can be determined:

Gain (dBi) compared to isotropic radiator

Bandwidth (%) usually specified by 2.0:1.0 VSWR

Radiation Pattern (Beamwidth and sidelobe response)

Although these characteristics are used to describe the antenna element, they depend also on the particular feeding circuit used to launch the electromagnetic energy into the radiator. At frequencies greater than 15 GHz, the interconnection between the active components and the antenna radiators becomes an integral part of the active array system and its performance.

The antenna design for the Orbital Debris Radar System consists of planar microstrip patch elements for the individually controlled subarrays. Each subarray has 3 antenna elements consisting of 3 rectangular patches, the center patch is directly fed and the two adjacent patches radiate the coupled energy. This arrangement, known as parasitic microstrip arrays, improves the gain and bandwidth over single element microstrip patches and reduces the number of active components. Figure 3 shows the layout of a three patch parasitic element.

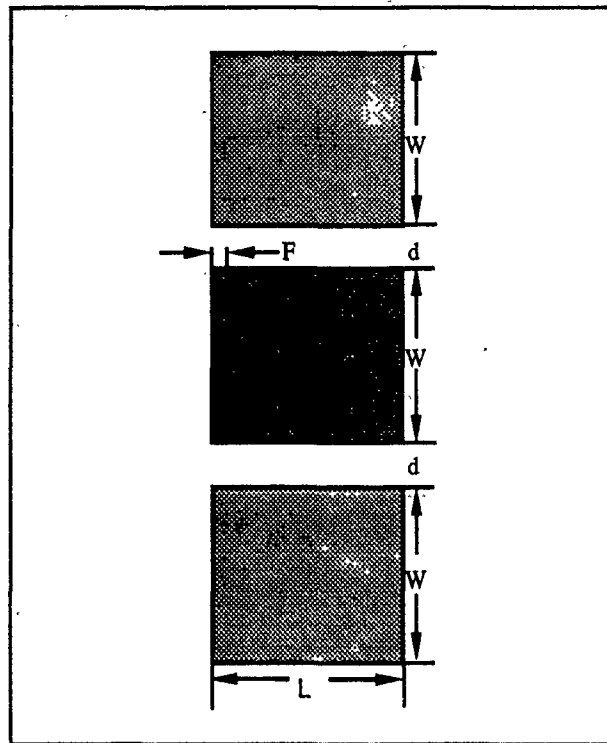


Figure 3: A Typical Layout of a Three Patch Parasitic Element

### 3.2 Center-fed Patch Design

The main areas of concern in the design of the parasitic element are the rectangular patch size, the feed design and location, and the parasitic patch spacing. The physical size of the microstrip patch has the geometry as shown in Figure 4. Several parameters that affect the length ( $L$ ) and width ( $W$ ) of the patches are:

- 1) substrate dielectric thickness
- 2) substrate relative dielectric constant
- 3) resonant frequency

$f_r = 14.5 \text{ GHz}$

$\epsilon_r = 2.21$

$h = 0.010" \text{ \& } 0.020"$

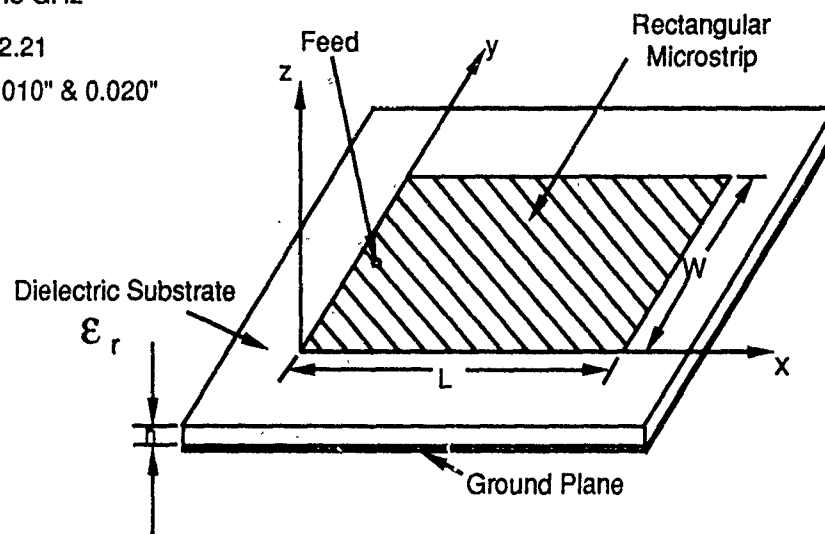


Figure 4: Microstrip Patch Geometry

For a rectangular patch of geometry shown in figure 4, the formulas used in the design are as follows:

$$W = \frac{C}{2 f_r} \left( \frac{\Sigma_r + 1}{2} \right) \quad (1)$$

$$L = \frac{C}{2 f_r \sqrt{\Sigma_e}} - 2 \Delta l \quad (2)$$

where:  $c$  = Speed of Light  
 $\Sigma_r$  = Relative Dielectric Constant  
 $f_r$  = Resonant Frequency  
 $\Sigma_e$  = Effective Permittivity  
 $\Delta l$  = Fringing length line extension



$h$  = height of substrate

and

$$\frac{\Delta l}{h} = 0.412 \frac{(\Sigma_e + 0.3) \left( \frac{W}{h} + 0.264 \right)}{(\Sigma_e - 0.258) \left( \frac{W}{h} + 0.8 \right)} \quad (3)$$

$$\Sigma_e = \frac{\Sigma_r + 1}{2} + \frac{\Sigma_r - 1}{2} \left( 1 + \frac{12h}{W} \right) - \frac{1}{2} \quad (4)$$

The resonant frequency of the single patch element is to be 14.50 GHz and will be fabricated on a 10 mil thick substrate (.010 inch) of dielectric constant 2.21. These parameters yield a rectangular patch of length 268.9 mils and width 321.5 mils.

The feed topology for the array is a coaxial pin launched from the back side of the substrate. This type of launch provides a stable mechanical design for the system but introduces electrical interface discontinuities into the patch. From previous results <sup>1</sup> the location of a single patch element feed is approximately  $0.3W$  ( $W$  = width), however, the resultant input impedance reduction due to the parasitic elements will cause a modification in the location to between  $0.15W$  to  $0.20W$ . Figures 5 and 6 show the measured return loss and radiation pattern for the single patch. The resonant frequency is 3 per cent low, as can be seen by the measured results. Adjustment in the length ( $L$ ) was made to move the frequency to 14.3 GHz. It has been shown in previous work <sup>1</sup> that the resonant frequency of the single patch will shift higher when coupled to adjacent parasitic patches, therefore, a single patch resonant frequency of 14.3 GHz will yield the desired parasitic resonance frequency.

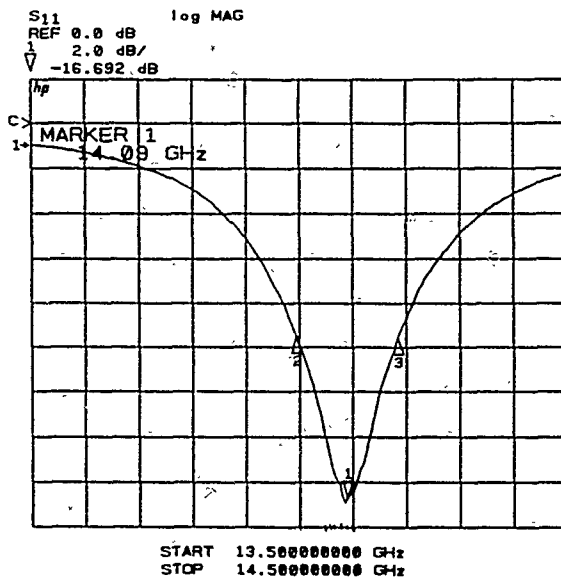


Figure 5: Input Return Loss of Single Patch

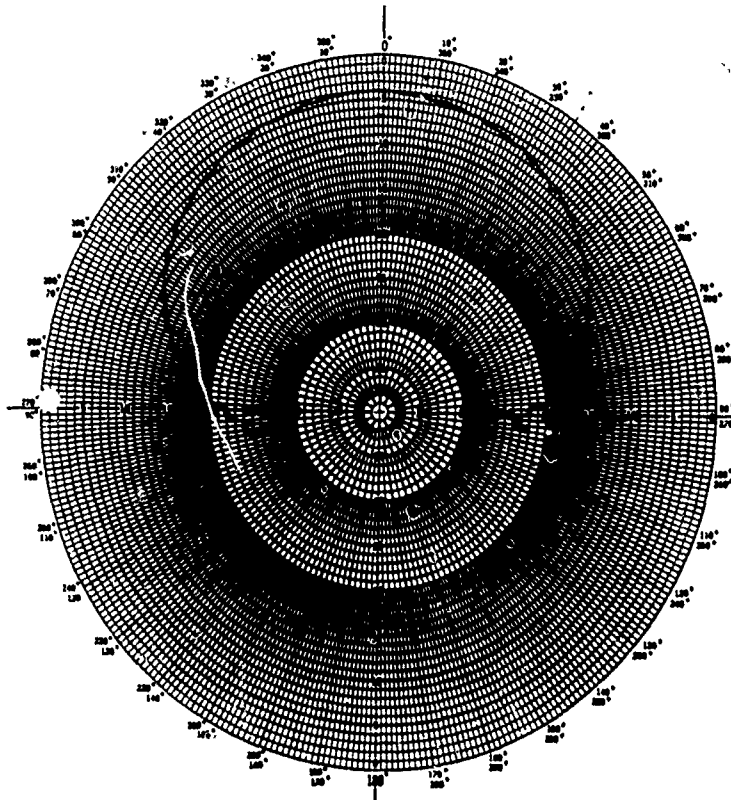


Figure 6: Radiation Pattern of Single Patch

### 3.3 Parasitic Element Design

The parasitic group as shown in figure 3 consists of a 3-patch linear array with the center patch being directly fed. The two parasitic

patches are coupled to the non-radiating edges of the center patch and were initially spaced at 0.05 wavelengths ( $0.05\lambda$ ). The return loss and radiation pattern of this parasitic structure is shown in figures 7 and 8. As can be seen in the plots, the parasitic group resonant frequency is higher than that of the single patch, however, the radiation pattern shows an undesired null at the antenna boresight. Subsequent parasitic patch spacings showed that the radiation pattern could be manipulated to give various responses. Of particular interest could be the result of figure 9 which shows an absolute boresight null at a spacing of .040 inches. This phenomenon leads to the assumption that specific desired radiation patterns may be tailored to an antenna by use of the parasitic structure. This phenomenon was not pursued by this project, but is mentioned here for reference.

The empirical tuning of the parasitic structure included adjustment in; patch length for both the fed and coupled patches, parasitic spacing, and the feed location. The gap spacing between the fed and two parasitic patches was varied from 190 to 4 mils. At 190 mils the radiation pattern was approximately the same as a single patch. As the gap spacing became smaller, a dip began to form in the radiation pattern at boresight. A spacing of 40 mils realized a deep null. Between 40 to 4 mils, three lobes were observed on the radiation pattern with the center lobe at boresight becoming higher with smaller spacing. However, adequate patterns were not achieved.

Radiation patterns were recorded at numerous frequencies to help discern if gap spacing was a function of wavelength or the substrate height. The results of this testing showed the element to radiate the desired pattern shape between 13.7 and 14.0 GHz. In an effort to shift this frequency up to the desired 14.5 GHz, the parasitic patches were trimmed. The desired pattern was achieved after 30 mils was removed from the radiating edge of each parasitic patch. Once the desired

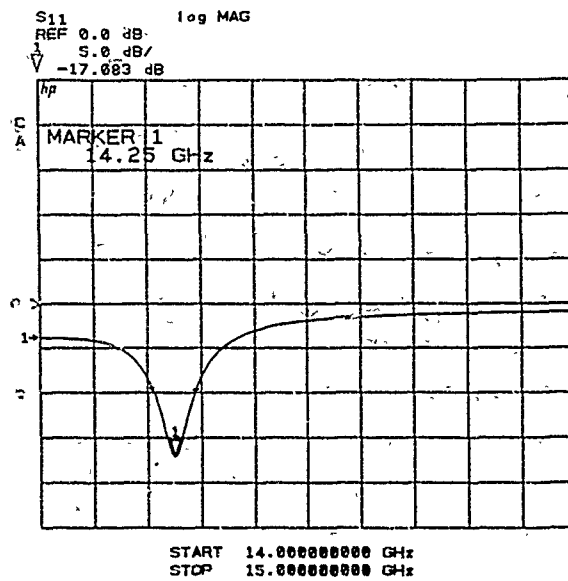


Figure 7: Return Loss of Preliminary Parasitic Element

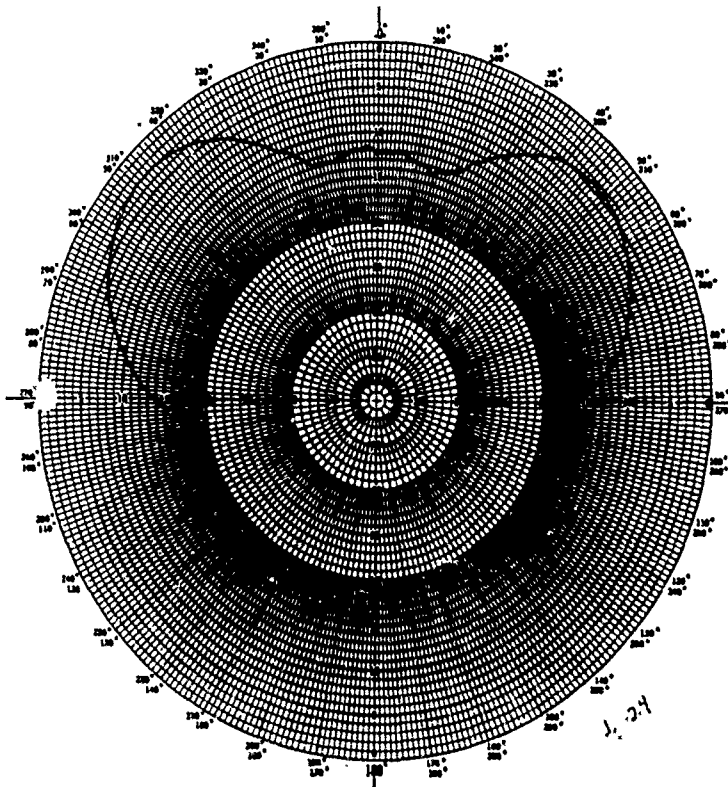


Figure 8: Radiation Pattern of Preliminary Parasitic Element

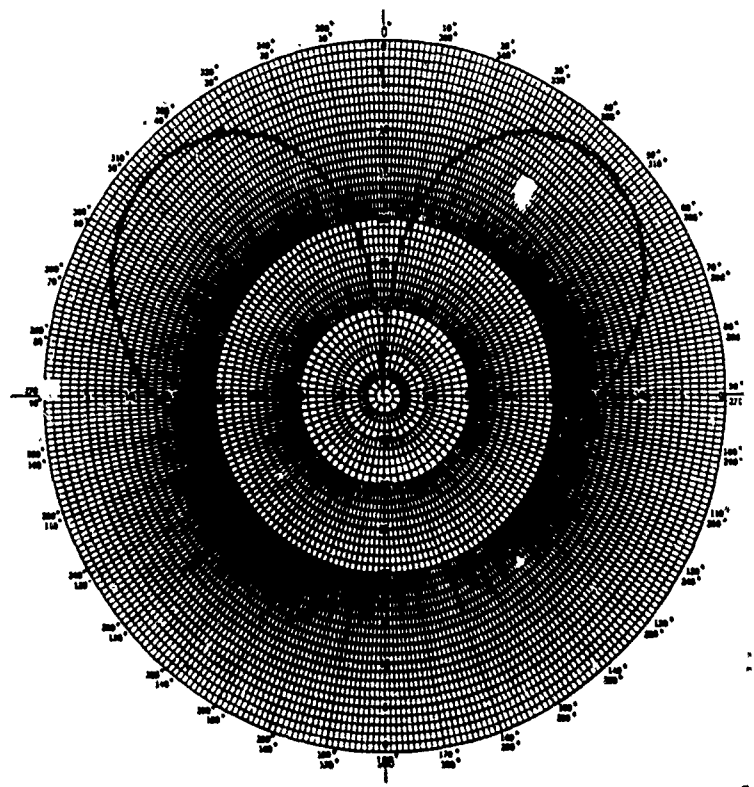


Figure 9: Radiation Pattern of .040 Inch Parasitic Element

radiation pattern was achieved, the feed location was moved closer to the edge so that an adequate 2:1 VSWR bandwidth was realized.

### 3.4 Mechanical Design

The mechanical design of the subarray must allow three parasitic patch elements to be fed from one transmit/receive unit. The required feed structure must split the signal into 3 paths of equal amplitude and phase. Figure 10 shows a block diagram of the feed network and antenna connection.

The connection to the microstrip patch from the microstrip feed network is made via a mounting plate with a glass coaxial K-connector bead. This can be viewed in figure 11 which shows a cross section of the mounting plate with the K-connector bead. The design allows complete electrical testing apart from the feed board or antenna board by sliding connector shells over the protruding pins.

The subarray/feed assembly and the transmit/receive unit are configured as shown in figure 12. The complete module is front loaded into the system chassis and has a center plate area for air flow cooling of the components.

## 4.0 SUBARRAY PERFORMANCE RESULTS

Electrical testing of the subarray and feed network assembly has been completed. The methodology was such that each part of the assembly could be individually tested and characterized for performance.

### 4.1 Feed Network

The results of the 3-way feed network measurements are shown in table 4.1.

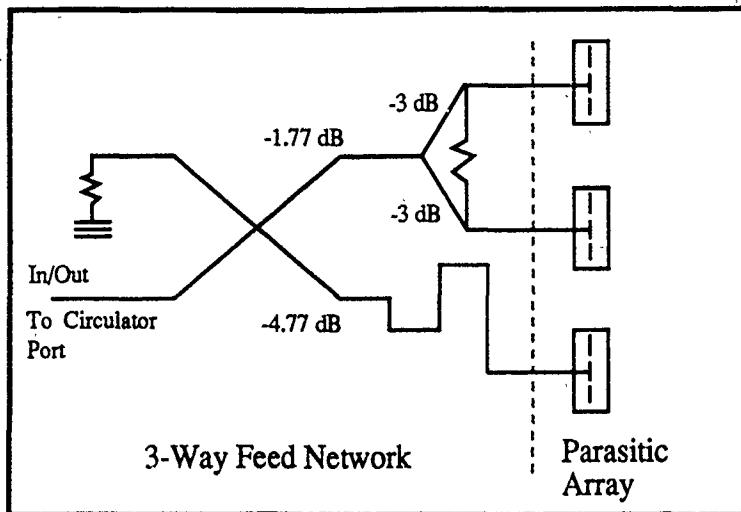


Figure 10: Feed Network Block Diagram

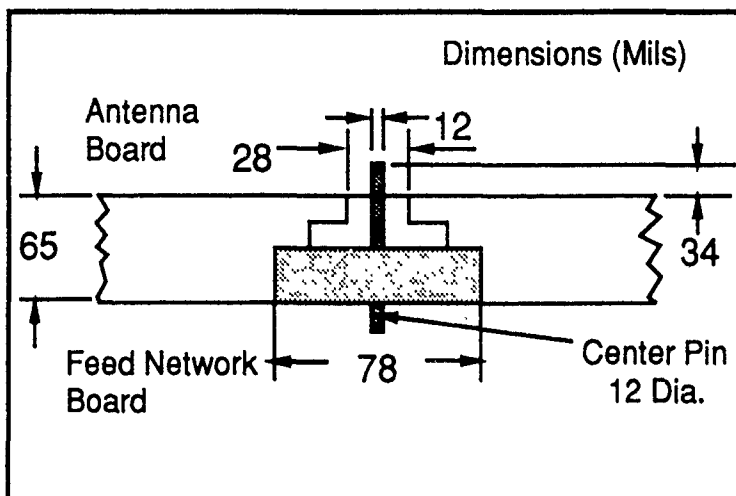


Figure 11: Cross Section of Antenna/Feed Mounting Plate

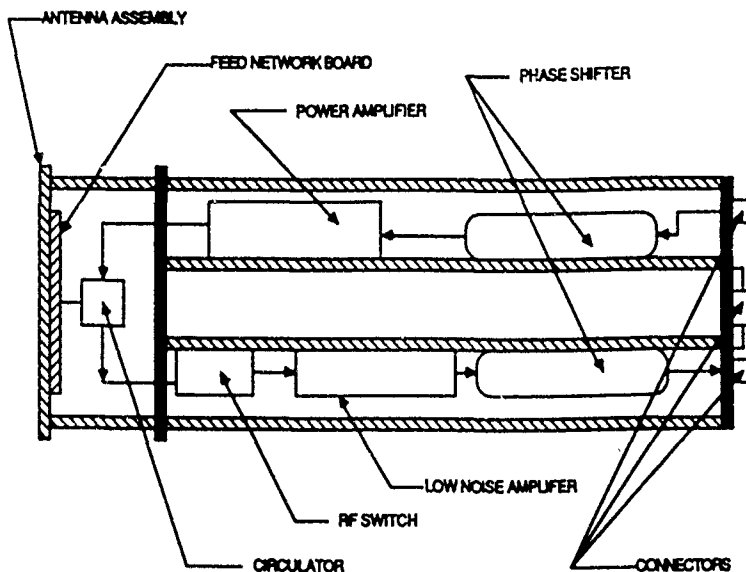


Figure 12: Subarray/Feed-Transmit/Receive Assembly

Parameter Measured	Port			Common
	1	2	3	
Return Loss	15.6 dB	14.7 dB	15.8 dB	20 dB
Insertion Loss	5.2 dB	7.2 dB	6.8 dB	
Transmission Phase	135.71 °	140.13 °	146.84 °	

Table 4.1: 3-Way Feed Performance at 14.5 GHz

These measurements show that the amplitude and phase balance between the feed ports are 2 dB and 11 degrees respectively. Further iteration on this network should improve these to 0.5 dB and 5 degrees.

#### 4.2 Parasitic Element

The three parasitic elements in the subarray were individually tested for VSWR, gain and radiation pattern. Table 4.2 shows the results of the measured performance. These measurements show an increased gain of approximately 3 dB from the single fed patch. The impedance bandwidth of a typical parasitic element is shown in figure 13. The bandwidth can be increased by further adjustment of the feed location to move the plot down and to the left on the Smith Chart.

#### 4.3 Subarray

The integrated subarray consisted of 3 parasitic elements and the 3-way feed network. Figure 14 shows the input return loss of the common port of the feed network with the antenna elements loading the output ports.

Parameter Measured	Parasitic Element			Frequency of Measurement
	1	2	3	
Return Loss	17.3 dB	18.1 dB	17.4 dB	14.5 GHz
Gain	9.2 dB	9.3 dB	9.0 dB	14.5 GHz
Beamwidth (3 dB)	54 °	49 °	56 °	14.2 GHz
	52 °	48 °	54 °	14.5 GHz
	45 °	44 °	49 °	14.8 GHz
2:1 VSWR Bandwidth	6%	2%	6%	

Table 4.2: Parasitic Element Performance

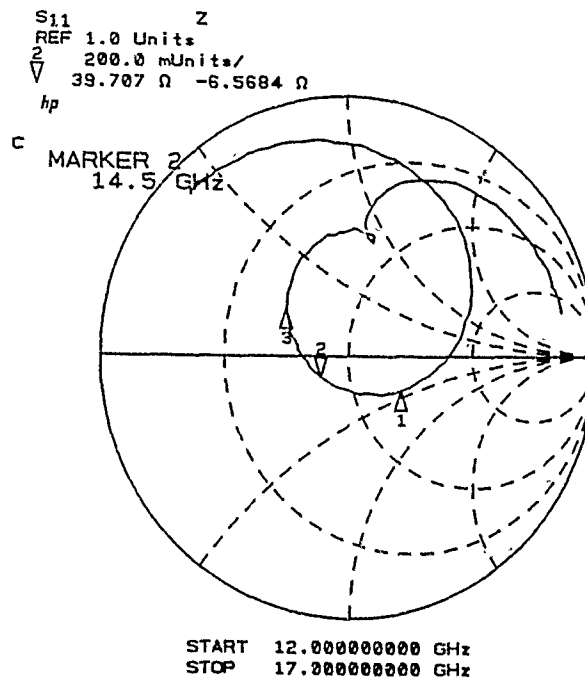


Figure 13: Typical Input Impedance of a 3-Patch Parasitic Element

Figure 15 shows the measured radiation pattern of the subarray assembly at 14.5 GHz and table 4.3 shows a complete summary.



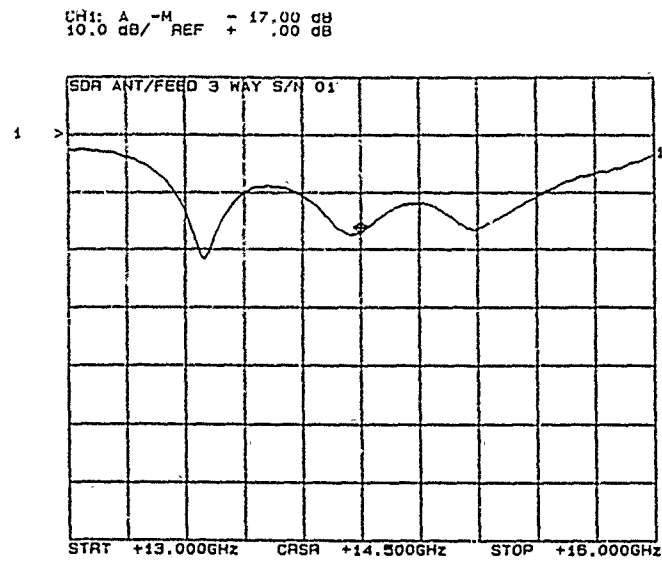


Figure 14: Return Loss of Feed Network

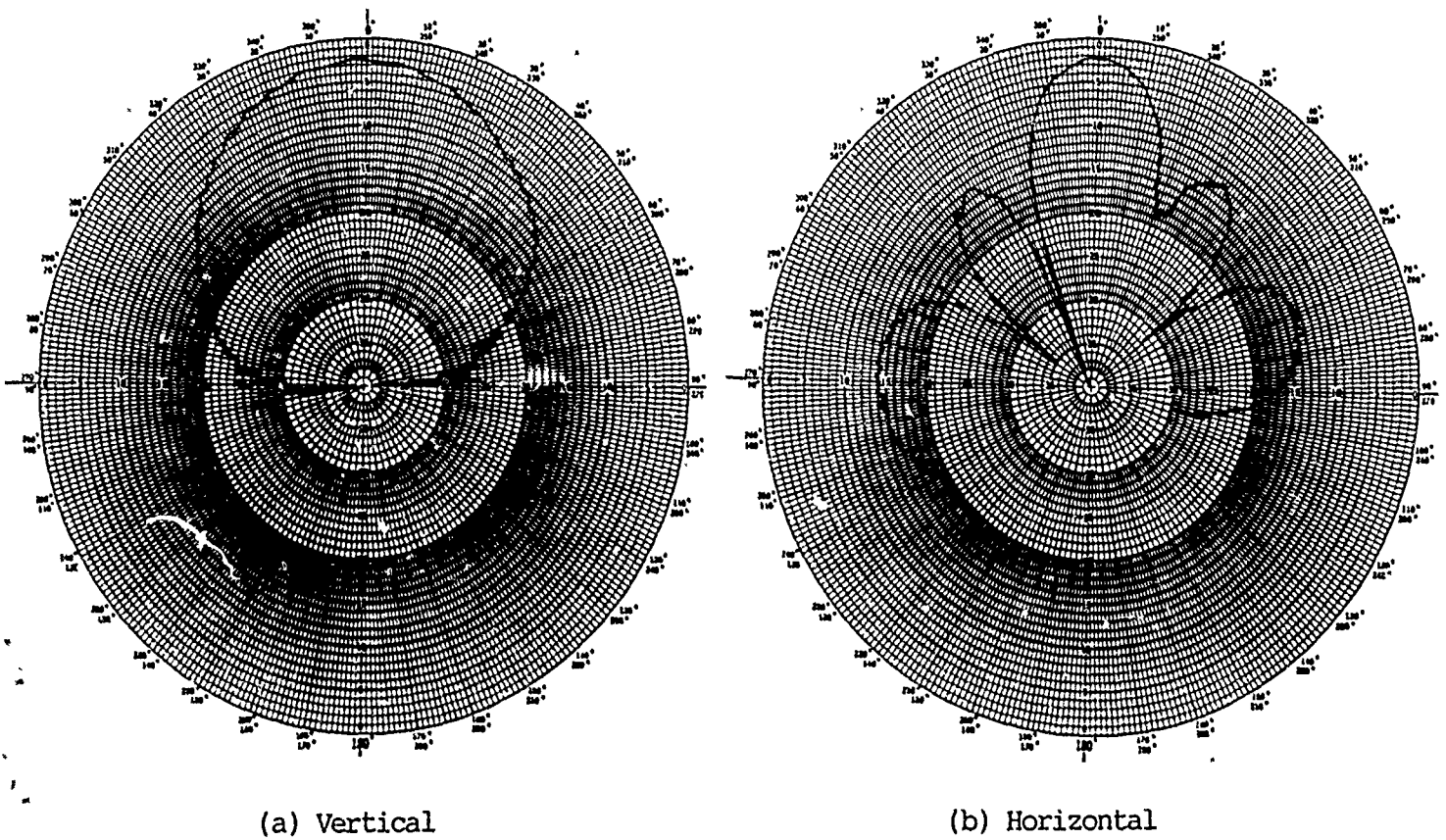


Figure 15: Radiation Pattern of Subarray

Measurement Frequency	Return Loss	Gain	Beam Width
14.2 GHZ	11.2 dB	13 dB	19°
14.5 GHz	17.0 dB	12.8 dB	20°
14.8 GHz	11.6 dB	12 dB	19.5°

Table 4.3: Subarray Performance

## 5.0 DISCUSSION

The 3 patch parasitic element layout which achieved the desired performance was empirically determined from an initial design approach. Although no analysis or synthesis program has been written to predict and verify the results, some basic guidelines have been discerned. These design guidelines for a linear three patch parasitic array include:

- 1) The fed center patch should resonate approximately two to three per cent below the desired parasitically coupled resonant frequency.
- 2) The feed point of the single fed patch will decrease in resistance when the patch is parasitically coupled. Therefore, the feed location will move toward the edge for input matching of the parasitic layout.
- 3) For widening the impedance bandwidth and preserving the integrity of the element radiation pattern, the parasitic patches should have a length (L) dimension five to ten per cent less than the fed patch.

- 4) The determination of the parasitic patch spacing should be based on the ratio of spacing to dielectric substrate height ( $S/H$ ). Typical values of the parasitic spacing to dielectric height ratio should be between 0.3 to 0.1.
- 5) The parasitic element impedance bandwidth is greater for thicker dielectric substrates. In addition, fewer radiation pattern anomalies are observed on thicker substrates (i.e. smaller  $S/H$ ).

## 6.0 CONCLUSION

It has been demonstrated by experimental fabrication and testing that a three patch parasitically coupled arrangement, with the center patch directly fed, can obtain higher gain, narrower beamwidth results when compared to a single patch element at Ku-band. Other benefits realized with this structure include a 3:1 increase in impedance bandwidth and an increase in backplate circuit area, which can be directly configured to MMIC integration. Three of these parasitic elements have been configured as a building block subarray to be used in a larger active array system. The ability of this configuration to enhance the microstrip patch performance at microwave and millimeter-wave frequencies, make it one of the few antenna elements applicable to a fully printed-circuit active array.

The successful implementation of these antenna structures and their ability to realize the MMIC benefits, demands that work be done to model and understand the coupling mechanisms. It is envisioned that a computer-aided design synthesis program could be used to design such parasitic arrays without the need for numerous empirical interpolations.

## ACKNOWLEDGEMENTS

The authors would like to acknowledge Wayne Cope, Larry Dolson and Cynthia Hightower of Lockheed Engineering and Sciences Company for their many efforts and support in this project. Mr. Cope was involved in the mechanical design and circuit board fabrication. Mr. Dolson and Ms. Hightower have been involved in the hybrid assembly and electrical testing of the numerous networks required in the project.

## REFERENCES

1. Lee, R.Q. , R. Acosta, J.S. Dahele, and K.F. Lee. (1987) An Experimental Investigation of Parasitic Microstrip Arrays. Paper presented at the 1987 Antenna Applications Symposium, Urbana-Champaign, Illinois.
2. Kumar, G. and K. Gupta. (1985) Nonradiating Edges and Four Edges Gap -Coupled Multiple Resonator Broad-Band Microstrip Antennas, IEEE Transactions on Antennas and Propagation AP-33 (No. 2):173-178.
3. Kumar, G. and K. Gupta. (1985) Directly Coupled Multiple Resonator Wide-Band Microstrip Antennas, IEEE Transactions on Antennas and Propagation AP-33 (No. 6):588-593.
4. Paz, I., J.R. Carl, R.W. Shaw, J.K. Kovitz, and G.D. Arndt. (1989) Design of an Orbital Debris Radar Ground Demonstration. Paper presented at the 1989 IEEE Aerospace Applications Conference, Breckenridge, Colorado.

## ADVANCES IN MONOLITHIC HORN-ANTENNA IMAGING ARRAYS

*Philip Stimson, Yong Guo  
Karen Lee and David Rutledge*

California Institute of Technology  
Pasadena, CA, 91125

*Abstract*—Monolithic horn arrays consist of arrays of pyramidal horns etched into a silicon block. Dipole antennas are suspended on  $5\text{ }\mu\text{m}$  thick silicon oxynitride membranes approximately half way down the horns. This approach leaves room for low frequency connections and processing electronics on the membrane surface between the horns. The devices fabricated in our laboratory are  $7\times 7$  arrays of  $1\lambda$ -square horns at 93 GHz. The horns have a  $71^\circ$  flare angle and couple efficiently to low  $f$ -number optical systems. This paper discusses an optical system designed for diffraction limited imaging measurements with the arrays. A Michelson interferometer using a swept frequency klystron source is used to measure the amplitude and phase of the radiation reflected from a target. We also discuss a quasi-optical thin film power density meter consisting of a 2-square cm bismuth film on a Mylar membrane. This device was developed to measure the power incident on the horn arrays, which is necessary for accurate efficiency measurements. Aperture efficiencies of approximately 60% have been obtained.

## 1. INTRODUCTION

The aim of the horn imaging array program at Caltech is to develop an efficient, monolithic imaging array sensor for frequencies up to 1 THz. Applications of these arrays include remote sensing through fog, smoke and dust which is opaque to optical and infrared radiation, astrophysical mapping of regions of star formation in the galaxy, atmospheric sensing of pollutants, for example, ozone and ClO, and in plasma diagnostics.

The devices consist of arrays of square pyramidal horns etched into a silicon block<sup>1</sup>. Half way down each horn, a membrane of silicon oxynitride a few microns thick is grown across it. Antennas, detectors and other circuitry are fabricated on the membrane. Incoming radiation is concentrated by the horn, received by the antennas and fed to the detectors. One advantage of using this configuration is that the membrane is so thin compared to a wavelength that the antennas radiate as if they were in free space, and coupling to substrate modes is avoided. Figure 1 shows a 93 GHz horn array. The horn apertures are  $1\lambda$  across. The horns are fabricated using anisotropic etching with ethylene-diaminepyrocatechol solution which naturally forms pits bounded by the (1,1,1) crystal planes of the silicon. This gives a horn flare angle of  $71^\circ$ . The membrane is fabricated by PECVD from silane, nitrous oxide and ammonia gases. A layer of the oxynitride is grown on the wafer, and the wafer etched to leave the free-standing membrane. The horns are built up from a number of wafers stacked and glued together. There is a large amount of space on the membrane between the individual horns for fabrication of mixing and IF circuitry. This can be produced at the same time as the antennas are defined. The antennas on the membrane surface are nominally half-wave dipoles. Recently, experiments have been conducted to determine the effect of different antenna lengths on array performance. Bismuth microbolometers are used as detectors for efficiency experiments as they can be calibrated in terms of absolute power. A quarter wavelength section of coplanar line acts as a low pass filter and prevents loss of millimeter-

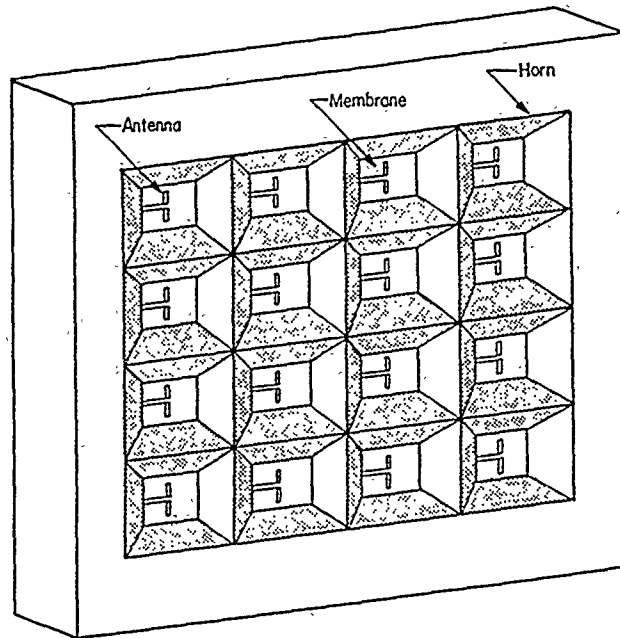


**Figure 1.** A 93 GHz horn imaging array.

wave power to the bias circuit. Experiments have also been conducted using beam-lead diode detectors. These are bonded to the membranes with gold epoxy.

The antenna patterns of the array elements are quite wide, due to the large horn flare angle. The 3 dB widths of patterns taken with  $0.235 \lambda$  antennas and bolometers, are  $50^\circ$  and  $60^\circ$  in the E- and H-planes respectively<sup>2</sup>. This produces optimum array coupling to  $f/0.7$  optical systems. Antenna patterns recorded with beam-lead diodes and  $0.2 \lambda$  antennas exhibit  $50^\circ$  3 dB widths in both planes. These patterns are very satisfactory for an imaging array.

## 2. EFFICIENCY MEASUREMENTS

The aperture efficiency of an individual element is defined as the ratio of the power received in the detector, to the power incident on the aperture of the horn when the device is illuminated by a plane wave. This is measured using an all DC technique requiring no frequency response or conversion

factors. The millimeter-wave power density in the plane of the array is measured using a thin film quasi-optical power density meter discussed in Section 3.

Element	Length	Resistance	Efficiency
1	$0.20 \lambda$	$86 \Omega$	57%
2	$0.20 \lambda$	$119 \Omega$	57%
3	$0.20 \lambda$	$97 \Omega$	67%
4	$0.25 \lambda$	$83 \Omega$	12%
5	$0.25 \lambda$	$74 \Omega$	11%
6	$0.25 \lambda$	$83 \Omega$	12%
Prev.	$0.235 \lambda$	$100 \Omega$	44%

Table 1. Aperture efficiencies of horn elements incorporating antennas of different (half) length. Recent measurements are compared with previous data.

Table 1 gives the result of recent aperture efficiency measurements. Results are given for three different antenna lengths, (the half-length of the antenna is specified). Each configuration has a different mismatch loss between the antenna and detector. The aperture efficiency of the elements with  $0.2 \lambda$  antennas is approximately 60%, and that with  $0.235 \lambda$  antennas is 44%. The efficiency of elements with  $0.25 \lambda$  antennas is about 10%. This antenna may have a large inductance as the antenna ends are very close to the metallized horn sidewalls. Measurements performed at 7 GHz on a model of the horn array indicate that the  $0.2 \lambda$  antenna should be resonant in the horn.

Table 2 gives the power loss mechanisms in the horn arrays. The largest components are mismatch loss and sidewall loss. The mismatch loss arises from the impedance mismatch between the antenna, which has an impedance of  $50 \Omega$ , and the  $100 \Omega$  bolometer. The sidewall losses are due to conduction currents induced in the silicon walls of the horn by the incoming radiation. Most of the walls are coated with gold but the walls in the neighborhood of



the membrane were not coated when these measurements were performed. Other minor losses include pattern loss (taper loss of the horn), loss to the cross polarized component and coupling loss to adjacent horns. These give a total calculated loss of 1.8 dB, close to the measured 2.2 dB (60%). There is further scope for improvement. We will try to reduce the mismatch and sidewall losses.

Intrinsic Pattern Loss	-0.2 dB
Mismatch Loss	-0.6 dB
Horn-Sidewall Loss	-0.7 dB
Cross-Polarization Loss	-0.2 dB
Horn-to-Horn Coupling Loss	-0.1 dB
Total Calculated Loss	-1.8 dB
Total Measured Loss	-2.2 dB

Table 2. Loss processes in the horn arrays.

### 3. LARGE AREA BOLOMETER

The large area bolometer is a simple design consisting of a metal film on a membrane effectively suspended in free space<sup>3</sup>. There are no windows or thick substrate, no chopping of the signal is required, and the device is easy to fabricate. Calibration is performed with DC measurements. The primary application for this device is absolute power calibration for antenna efficiency measurements. The bolometer is shown in Figure 2.

To fabricate the device, a thin bismuth film was evaporated through a metal mask onto the Mylar until the DC resistance of the 2 cm square was  $189 \Omega$  (250 Å thick). The geometry of the device allows for a four-point measurement which eliminates the resistance in the ohmic contacts. The biasing contacts are offset from the voltage sensing leads. Continuous flow of the DC current is in the same direction as the millimeter wave induced currents in the effective measuring area. The bolometer is much thinner than

a wavelength at millimeter wavelengths, resulting in a surface impedance the same as the DC resistance. This maximizes the amount of absorbed power relative to the incident power without the use of a back-shorting mirror. The absorption coefficient may be calculated from a transmission line equivalent circuit. For a surface resistance of  $189 \Omega/\text{sq}$ , the absorption coefficient,  $a = 0.5$ . The bolometer is embedded in styrofoam to prevent disturbance by local air currents. The attenuation at 93 GHz in the styrofoam is imperceptible, while thermal radiation (from human bodies) is blocked. By placing the structure in an absorbing pyramidal housing, reflections and other unwanted signals are minimized.

We calibrate the power density meter at DC by measuring the resistance as a function of DC power applied, and the slope determines the responsivity of the bolometer in ohms per watt. Measurements are made by determining the resistance without, then with, the millimeter wave power incident. We can assume that the change in resistance due to the addition of millimeter wave power is the same as that due to the addition of DC power, so the difference in the resistance under each condition and the slope of the R-P plot will accurately give the millimeter wave power applied.

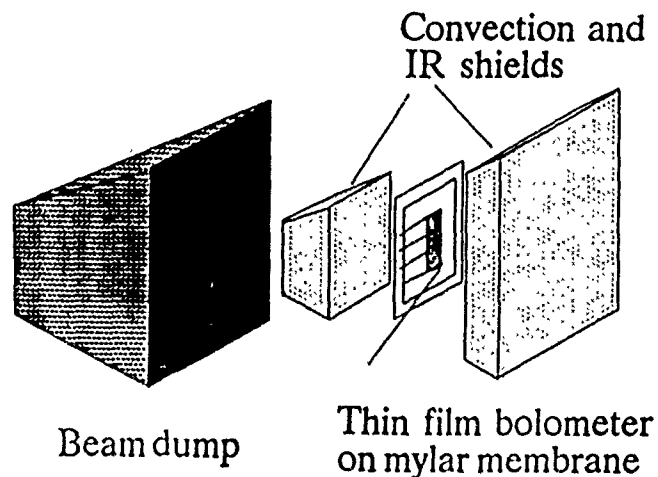


**Figure 2.** The large area bolometer power density meter.

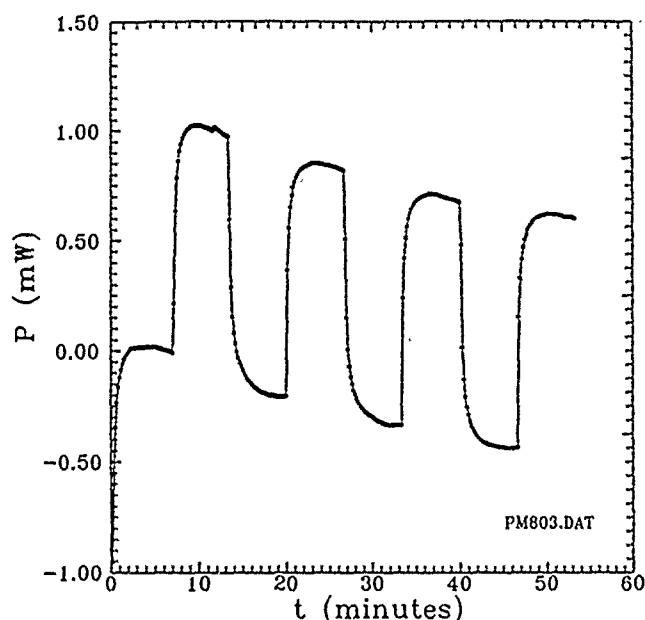


**Figure 3.** Signal recorded by a large area bolometer power meter during an aperture efficiency measurement. The millimeter-wave beam was alternately blocked and unblocked with absorber. The resistance drift is removed by subsequent processing.

Power density was measured at a fixed distance from a klystron source. Figure 3 shows the time response to turning the millimeter waves on and off over four cycles. By subtracting the downward slope caused by bolometer drift, one can obtain the power absorbed by the bolometer. We have measured absolute power densities of  $0.5 \text{ mW/cm}^2$  to an estimated accuracy of 2%.

#### 4. IMAGING

We hope to demonstrate diffraction limited imaging of incoherent objects using coherent sampling. There is presently some debate as to the validity of this idea, which is important for millimeter-wave imaging systems<sup>4,5</sup>. We believe that the image of an incoherent object can be reconstructed by sampling at the Nyquist spacing for the electric field (which is twice that for the intensity) provided that the sampling and interpolation is performed

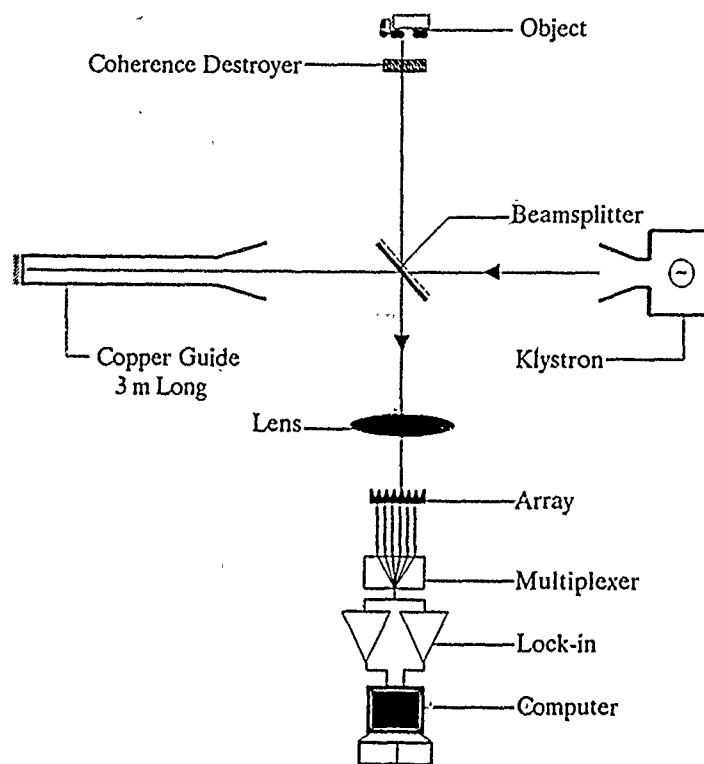


Figure 4. The optical system for imaging array measurements.  
instantaneously.

The optical system for the experiment is shown in Figure 4. The advantage of this configuration is that a low IF frequency may be produced electronically from the 93 GHz source<sup>6</sup>. If a ramp voltage is applied to the klystron reflector grid, a low frequency IF may be generated on the array. This is because the beams returning from the two interferometer arms to the beamsplitter have different frequencies due to the different travel times down the long and short arms. The coherence destroyer shown in the short arm of the interferometer is used to provide incoherent illumination of the object when desired. To record an image, a multiplexer circuit selects the first array element. The voltage across the bolometer is fed to a two-phase lock in amplifier which detects the magnitude of the signal and its phase with respect

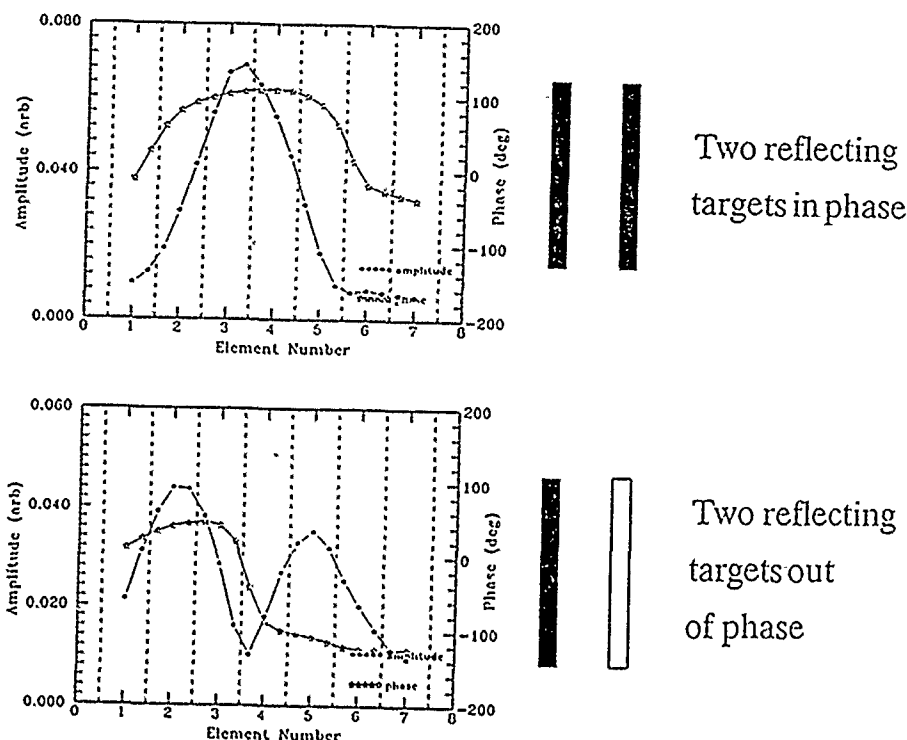


Figure 5. Measurements of the reflection coefficient of two illuminated copper strips when the reflections are in, and out of, phase. These data are one dimensional scans across the millimeter-wave beam.

to the reflector ramp. These are recorded by the computer and the process repeated until the entire array has been read. This gives a two-dimensional plot of the object reflection coefficient.

Calibration techniques for this imaging system have been developed. The calibration procedure is analogous to that for a microwave reflectometer. The system is modelled as an ideal reflectometer connected to a two-port error network which is connected to the (one port) device under test. The system output is measured when the device under test is replaced by a short, an open circuit and a matched load, and the scattering parameters of the fictitious error network determined. These are then used to correct the observed reflection coefficient when measuring an unknown device. For an optical sys-

tem, the equivalent of a short is a mirror, the equivalent of an open circuit is a mirror displaced by  $\lambda/4$  and the equivalent of a matched load is a sheet of absorber. The calibration procedure must be applied at the position of each array element. We have implemented this procedure using a diode detector scanned across the beam in one dimension. We will commence sampling measurements with the system soon.

## 5. FUTURE WORK

We want to increase the efficiency of the arrays still further by better impedance matching of the detector and complete gold coating of the horn walls. We will fabricate and test a back-to-back array (containing horns looking in opposite directions from the same silicon block) and investigate low-loss mixer configurations. We will also perform the imaging experiment to demonstrate reconstruction of diffraction limited images of incoherent objects using coherent sampling.

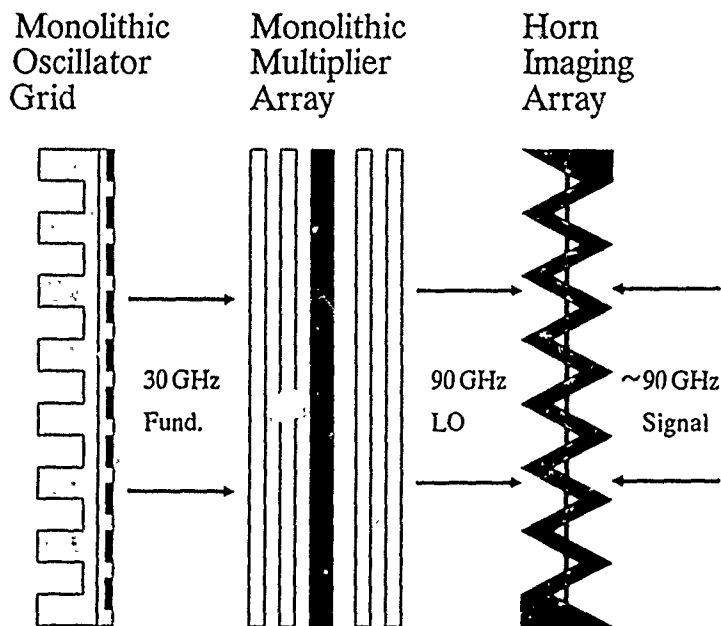


Figure 6. Possible configuration of a millimeter-wave TV camera.

One possible application of the horn arrays is the millimeter-wave TV camera shown in Figure 6. The front end sensor could be a modified horn array with elements facing in opposite directions, but sharing the same membrane wafer. One side would receive the 90 GHz signal and the other the LO. The LO could be produced by a monolithic grid (under development at Caltech<sup>7</sup>) and a monolithic grid tripler (UCLA and JPL<sup>8</sup>). Such a camera would be all solid state, compact and light.

#### ACKNOWLEDGEMENTS

This research was supported by the Department of Defense's, Terahertz Technology Program, contract F19628-87-K-0051 and Aerojet ElectroSystems Co.

#### REFERENCES

1. G.M. Rebeiz, D. Kasilingam, Y. Guo, P.A. Stimson and D.B. Rutledge, *Monolithic Millimeter-Wave Two-Dimensional Horn Imaging Arrays*, Accepted for publication in IEEE Transactions on Antennas and Propagation, January 1989.
2. G.M. Rebeiz, Y. Guo, P.A. Stimson and D.B. Rutledge, *Efficiency of MM-Wave Horn Imaging Arrays*, 13'th International Conference on Infrared and Millimeter Waves, Honolulu, Hawaii, USA, December 5-9, 1988.
3. Karen A. Lee, Kent A. Potter, Yong Guo, Phillip A. Stimson and David B. Rutledge, *Thin Film Power Density Meter for Millimeter Wavelengths*, In preparation.
4. David B. Rutledge, Dean P. Neikirk and Dayalan P. Kasilingam, *Integrated-Circuit Antennas*, in *Infrared and Millimeter Waves*, K.J. Button ed., vol. 10, 1983.
5. Joakim F. Johansson, Ph.D. Thesis, Chalmers University of Technology, Goteborg, Sweden, 1988.
6. M.A. Heald and C.B. Wharton, *Plasma Diagnostics with Microwaves*, John Wiley, N.Y., 1965, pp 206-210.
7. R.J. Hwu, L.P. Sadwick, N.C. Luhmann, Jr., D.B. Rutledge, M. Sokolich and B. Hancock, *Quasi-optical watt-level millimeter-wave monolithic solid-state diode-grid frequency multipliers*, IEEE MTT-S International Microwave Symposium, June 13-15, Long Beach CA, 1989, pp 1069-72.
8. Zoya B. Popovic, Robert M. Weikle, Moonil Kira, Kent A. Potter and David B. Rutledge, *Bar-Grid Oscillators*, submitted to IEEE MTT, August 1989.

# **WIDEBAND DUAL POLARIZED APERTURES UTILIZING CLOSELY SPACED PRINTED CIRCUIT FLARED SLOT ANTENNA ELEMENTS FOR ACTIVE TRANSMIT AND RECEIVE PHASED ARRAY DEMONSTRATION**

**Mark J. Povinelli**

**GE Aerospace  
Aerospace Electronic Systems  
Utica, New York 13503**

## **ABSTRACT**

The continuing proliferation of threat radars, both airborne and surface, throughout the electromagnetic spectrum, coupled with the deployment of high-g, high-velocity missiles, requires modern protective systems to cover both wide frequency bandwidths and wide ranges of aspect angles. The limited number of acceptable antenna sites available on tactical aircraft places a premium on multifunction (or shared aperture) antenna systems which can be programmed to serve radar functions as well as both electronic countermeasure (ECM) and electronic support measure (ESM) functions. Only phased arrays have the requisite scan angle coverage, frequency bandwidth, and computer-controlled flexibility to meet the needs of shared aperture systems, while also meeting the severe environmental and space limitations of tactical vehicles. Providing dual polarization capability in the antenna aperture along with close interelement spacings can increase function selectability and improve antenna performance. Wide bandwidth in a dense aperture is achieved by using printed circuit flared slot (notch) antenna elements with flare lengths and widths that are a fraction of a wavelength long. A reduction in the number of active transmit/receive (T/R) modules can be achieved by subarraying antenna elements in the aperture while maintaining a close element spacing for grating lobe suppression, reduced active voltage standing wave ratio (VSWR) variation with scan, and minimization of cross-polarization radiation pattern levels in all planes.

## **1.0 INTRODUCTION**

This paper will address the problem of providing an aperture (array of antenna elements) consistent in its operational bandwidth and grating lobe requirements and configurable as a phased array of transmit/receive (T/R) modules. The required frequency coverage has progressively widened until the typical frequency bandwidth now exceeds several octaves. As the bandwidth coverage increases, the types of radiating elements that could be considered have progressively decreased. At present, with frequency bandwidths exceeding three octaves, only endfire elements such as the log-periodic antenna and the exponential notch or flared slot can be considered viable radiating elements.



A major limitation in aperture performance is the active scanning VSWR that the aperture presents to the rest of the array. Aperture mismatch (high active VSWR) degrades radar performance by introducing mismatch and load pull losses along with reflections. Solutions to this problem include use of a circulator or active matching networks. Other possible solutions include varying the element, thereby changing the impedance, and non-uniform spacing. One problem with nonuniformly spaced elements in the array is their effect of noncommonality on the rest of the antenna system (i.e., it might be necessary for unique modules to fit the nonuniform spacing). The array active element impedance presented to the T/R module is determined by element type, element size, element lattice spacing, frequency of operation, mutual coupling, and beam scan angle. Generally, the reflection coefficient of the active antenna element increases with increasing scan angles and decreases with decreasing element spacing. These reflection coefficient changes can be severe, especially at large scan angles where the antenna impedance may present mismatches corresponding up to a 4.0:1.0 VSWR, resulting in an output power loss. The approach for wideband array apertures is to use closely spaced elements to reduce active VSWR variations with scan and restrict transmit and Bragg grating lobes. The aperture discussed here uses close element spacings ( $0.19 \lambda$  at low end) to reduce active VSWR with scan and restrict grating lobes. An absorber load is used between elements to optimize array embedded element performance and eliminate backlobe reflections.

Multifunction applications for phased array systems require the aperture to possess horizontal, vertical, circular, or full polarization diversity in a densely packed volume. A mockup of a full planar dual polarized phased array with over 4,000 discrete radiating elements is shown in Figure 1. A breakaway view (Figure 2) of the removable tray section assembled into the planar array illustrates the modularity of the design. A close-up of the antenna element's four-channel T/R module, cooling, and RF distribution is given in Figure 3. To prove these types of planar array concepts, a line array section of the planar array was designed and fabricated.

In these types of phased arrays, the reduced grating lobe requirements at the upper frequencies drive the array-element spacings closer, thereby limiting the array-element area. Given the reduced area and the wide frequency coverage needed, only endfire antenna elements can be considered. Two printed circuit antenna elements which meet these requirements are the log-periodic and flared slot (notch) antennas. The behavior of these two elements has been investigated as the element width becomes exceedingly narrow with respect to the lowest frequency of operation. A printed circuit version of a microstrip fed log-periodic element which has folded back arms to achieve a lower frequency of operation with less than optimal ( $\lambda_0/2$ ) element arm lengths is shown in Figure 4. Through empirical investigation, log-periodic antennas have been found to have inherent limitations when arrayed, which make them less useful for planar phased arrays. First, because the individual element arms occupy a large portion of the total element width, coupling interaction between adjacent elements can result in high cross-polariza-

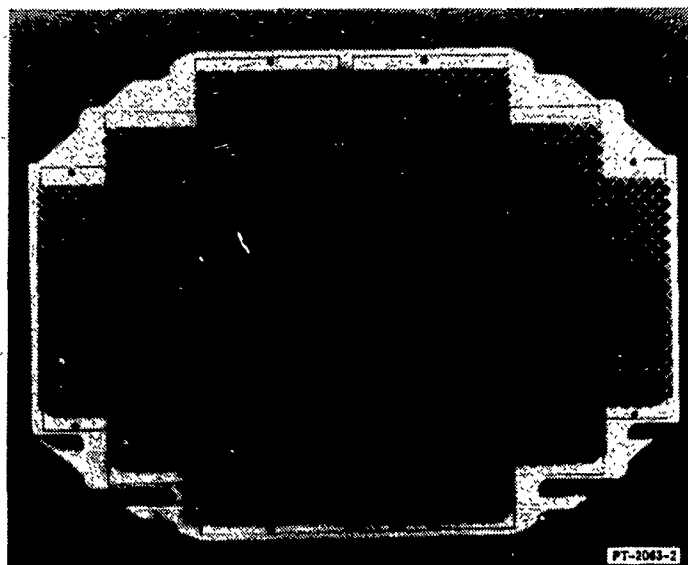


*Figure 1. Mock Up of Full Planar Phased Array Antenna*

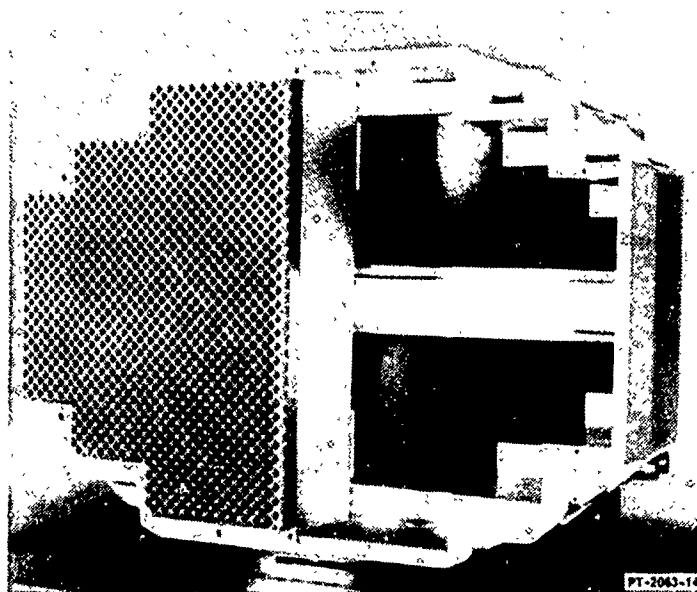


*Figure 2. Mock Up View Showing Modular Section Design*

tion pattern. Second, the necessity of a closely confined element spacing (area) restricts the low frequency arm lengths beyond the point of their optimal performance (half-wavelength). Fortunately, the printed circuit stripline fed flared slot antenna shown in Figure 5 offers a viable alternative. While the nominal low frequency limitation of a free space half-wavelength in element width still exists, the reduction in performance at the low end

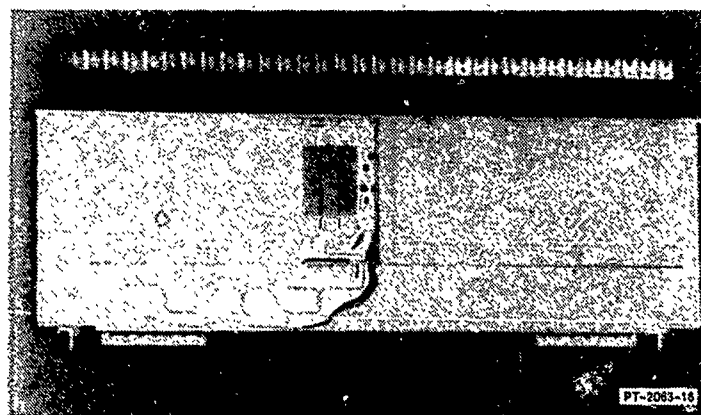


Figure 3. Breakaway View of Mock Up

of the frequency band is not as severe. For flare lengths less than  $\lambda_{\epsilon_r}/4$  ( $0.15 \lambda_0$  in this design) and widths less than or equal to  $\lambda_0/2$ , the possibility of a more resonant antenna exists. Selection of the array-element is based on performance over the 6.0 to 18.0 GHz band. Of the two element types, the stripline fed flared slot antenna has the best performance over the frequency band.

The printed circuit flared slot or notch antenna with a stripline feed has become popular and is extremely useful as a planar multioctave phased array-element. An overview of the development of the flared slot (notch) antenna was given by Povinelli [1]. The design and performance of wideband phased-array apertures with as many as 1792 elements and 192 element line array suited for multifunction planar array systems applications will be discussed.

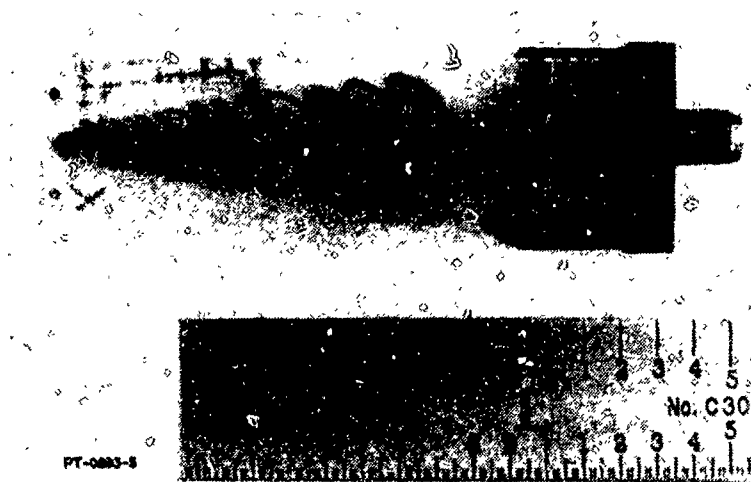


Figure 4. Microstrip Fed Log-Periodic Antenna Element with Low Frequency Folded Arms

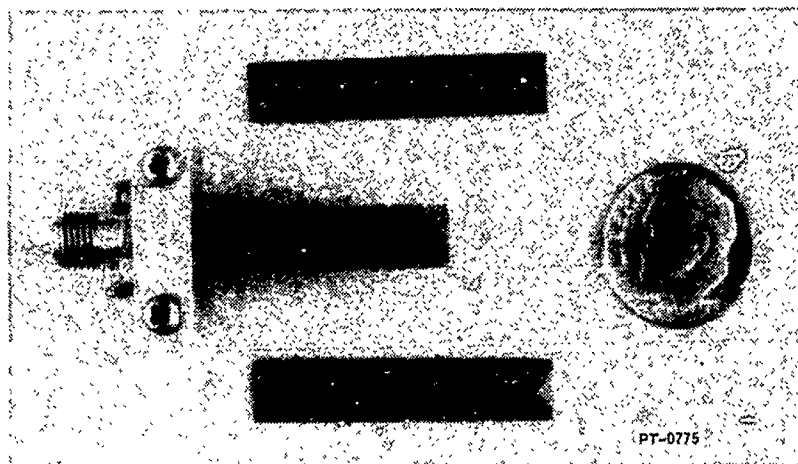


Figure 5. Printed Circuit Flared Slot (Notch) Antenna Element

## 2.0 LATTICE SELECTION AND APERTURE CONSTRUCTION

For 70-degree grating lobe free scanning at 11.0 GHz operating frequency, the array lattice must have a maximum interelement spacing of 0.530 inch. Both of these requirements include allowance for beamwidth. The line array aperture phase center spacing was selected at 0.530 inch with like-polarized discrete element spacing of 0.375 inch for Bragg grating lobe restriction. A layout of the lattice is given in Figure 6 showing the intercardinal (azimuth) and principle planes (E and H) for this aperture. A rotated square lattice was chosen to maximize on the allowable space for the T/R module, coolant and RF feed.

The printed circuit antenna element used to populate the aperture consists of a stripline feed terminating in a radial stub crossing over to excite (couple energy to) a flared slotline (terminated in a slotline open circuit) etched on both sides of the metallized ground planes of the dielectric substrates as depicted in Figure 7. A fifty percent reduction in the number of transmit/receive modules (circuits) in the phased array is achieved by subarraying every two like-polarized elements with a Wilkinson power divider as shown in Figure 8. This figure shows the two-stage Wilkinson stripline power divider with a radial stub termination etched on one half of the printed circuit element with the other half detailing the flared slot using a modified Dolf-Tchebycheff taper design ( $0.15 \lambda_0$  long at 6.0 GHz) terminated in a slotline open circuit. The modified Klopfenstein (the Dolf-Tchebycheff transmission line taper is given by Klopfenstein[2]) taper was designed to shorten the length of the element flare. The subarray used in this design is etched on two 0.020-inch low loss Duroid substrates ( $\epsilon_r = 2.2$ ), resulting in an overall element thickness of approximately 0.04 inch. Two orthogonal polarizations (with common phase centers) are realized by joining (colocating at right angles) a pair of subarrays through use of

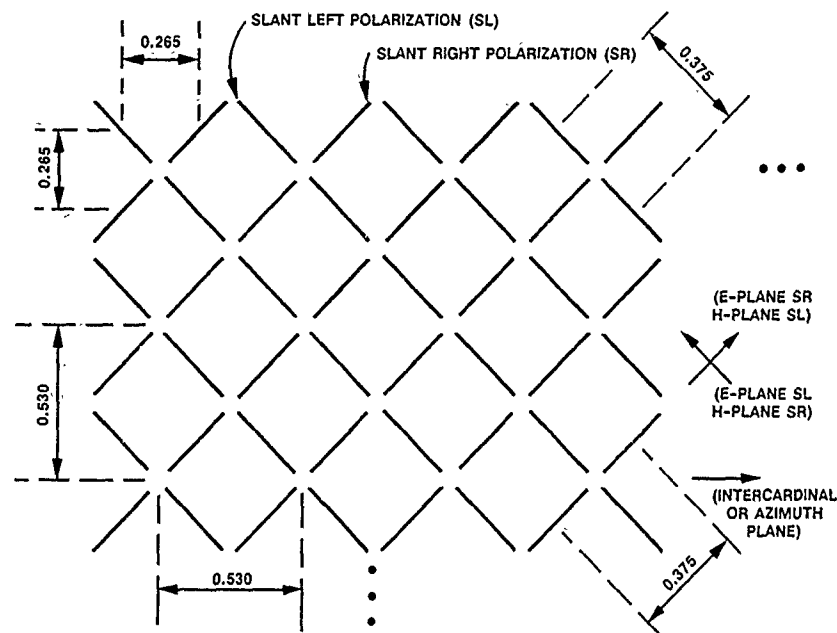


Figure 6. Dual Polarized Rotated Square Lattice

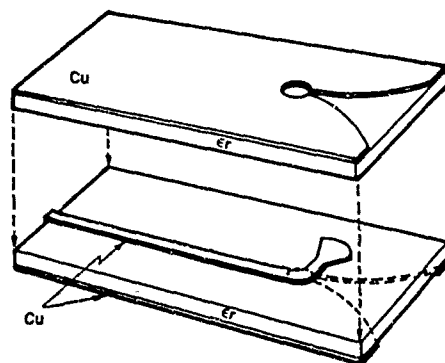
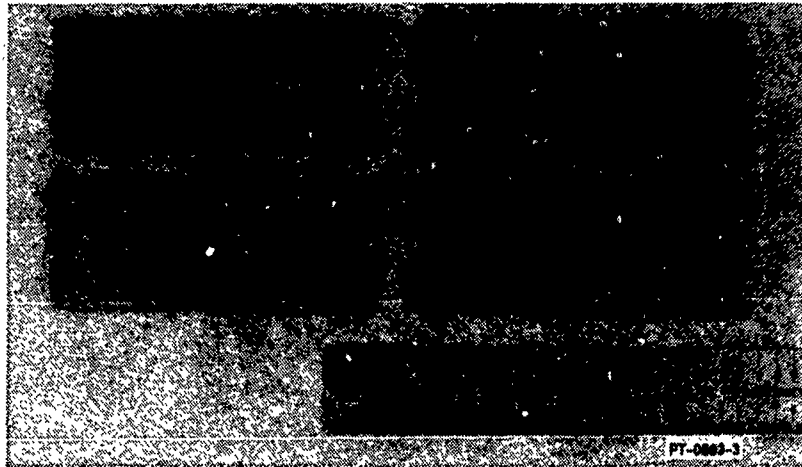


Figure 7. Stripline Fed Flared Slot (Notch) Antenna Element

a mechanical slot cut in the top of one subarray and the bottom of the other subarray as shown in Figure 9. The orthogonal subarray element pair with common phase centers and absorber loading on the base is shown in Figure 10. The subarray element with the colocation slot in the top is designated as a slant left polarization and the subarray with the slot in the bottom is the slant right polarization. This orthogonal subarray element (dual element) was then used to populate the line array aperture with full polarization diversity.

Eight dual elements were assembled onto a holder with push/pull connectors as shown in Figure 11. The eight dual element holder assembly has an inverted tapered absorber cone molded onto its base as shown in Figure 12 to enhance the array element performance. Six of these bar assemblies were used to form the 48 dual elements in the active portion of the line array aperture. The active portion of the line array aperture has three



*Figure 8. Wilkinson Stripline Fed Flared Slot Subarray Element Pairs*

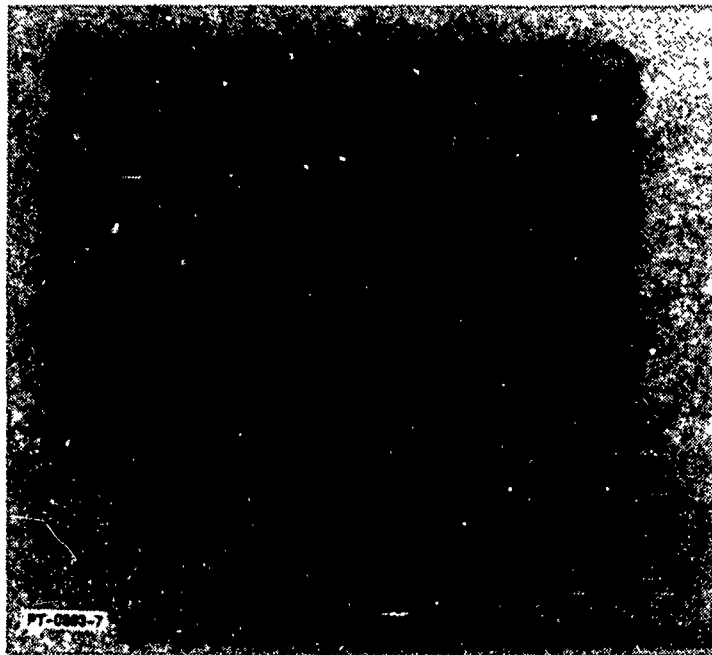


*Figure 9. Subarray Element Pairs with Mechanical Colocation Slot*

rows of terminated (loaded) dual elements (18 bars) on top and bottom and seven bars of dual elements on a side as depicted in Figure 13. The final line array assembled aperture is shown in Figure 14. A close-up view of the line array aperture is shown in Figure 15, showing the absorber loading in three of the central rows.

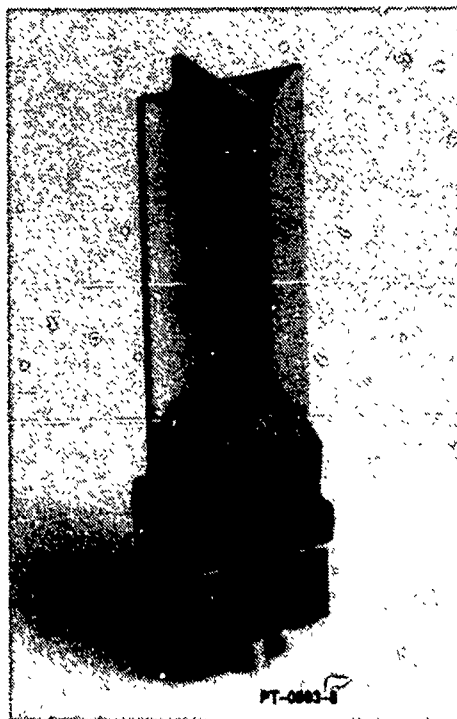


*Figure 10. Orthogonal Subarray Element Pair*



*Figure 11. Eight Orthogonal Subarray Element Pair Bars with Push/Pull Connectors*

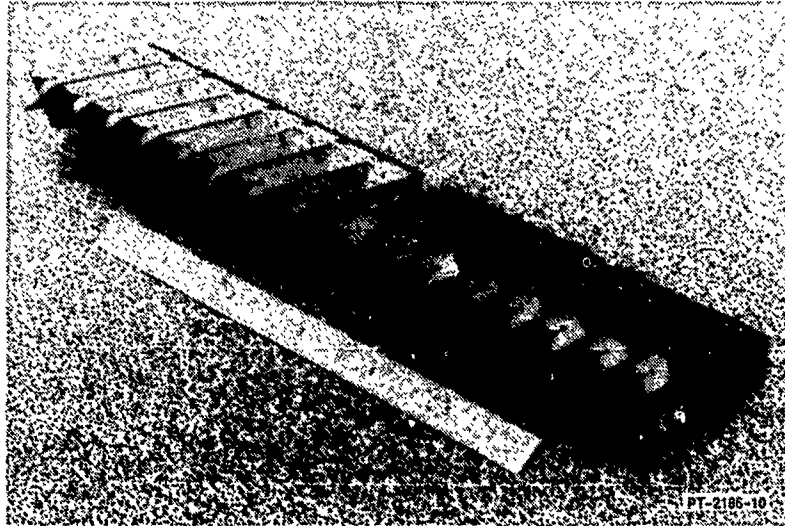


Figure 12. Eight Orthogonal Subarray Element Pair Bars With and Without Absorber Treatment.

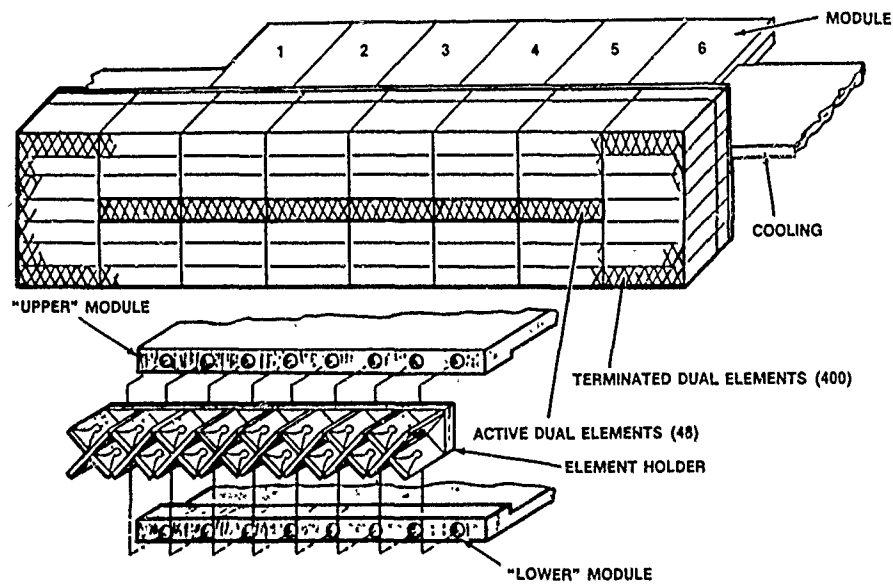
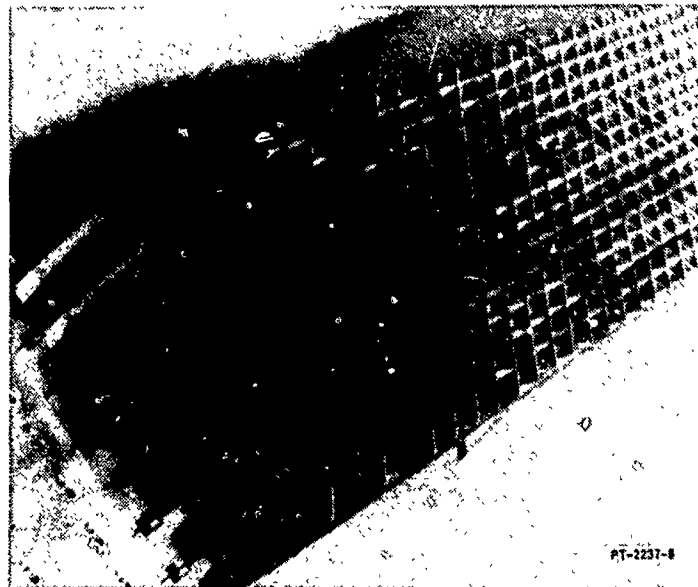


Figure 13. Schematic of Active Line Array Configuration





*Figure 14. Dual Polarized Planar Line Array Aperture*



*Figure 15. Close-Up View of Dual Polarized Planar Line Array Aperture*

### 3.0 ARRAY-ELEMENT PERFORMANCE

Array-element performance was characterized using a central element pair in the 7 x 64 dual element populated aperture [3]. This performance is determined in part by the mutual coupling between elements in the array environment. A short flare length (at low frequencies) was used to reduce array mutual coupling interactions and to optimize array-element patterns. To prove out the empirical design of this dual element, an 8 x 8 aperture was built and completely characterized as a phased array aperture [1]. The typical passive return loss of a slant right subarray is shown in Figure 16 from 2.0 to 20.0 GHz. The array-element performance optimization achieved with the absorber loading in between dual elements is given for the gain improvement of both polarization slants in Figures 17 and 18 and for E- and H-plane beam width enhancement in Figures 19 through 22. The typical gain response is shown in Figure 23 over the 6.0 to 18.0 GHz band along with the ideal theoretical directivity.

The co- and cross-polarized radiation pattern performance for a central dual element in the line array aperture was measured in the two principal planes and in the azimuth and elevation intercardinal planes. The H-plane co- and cross-polarized radiation patterns for a central slant right and slant left polarized dual element is shown at 10.0 and 14.0 GHz in Figures 24 and 25. The average 3 dB beamwidth in the H-plane is 110 degrees, slightly less than  $\cos\theta$ . Four typical E-plane radiation patterns are given in Figures 26 and 27 for the two subarray slants. The average 3 dB beamwidth is slightly below  $\cos^2\theta$  due to the element subarraying in the E-plane. The azimuth intercardinal co- and cross-polarized patterns for the two subarray slants are given in Figures 28 and 29 at 10.0 and 14.0 GHz. The average 3 dB beamwidth is better than  $\cos^2\theta$ . Intercardinal elevation plane patterns are shown in Figures 30 and 31 for the two slants. Overall the co-polarization radiation patterns were very symmetric and did not exhibit any holes or ripples. The cross-polarization radiation patterns were at an extremely low level (-25 dB typical) not only in the two principal planes but in the intercardinal planes as well.

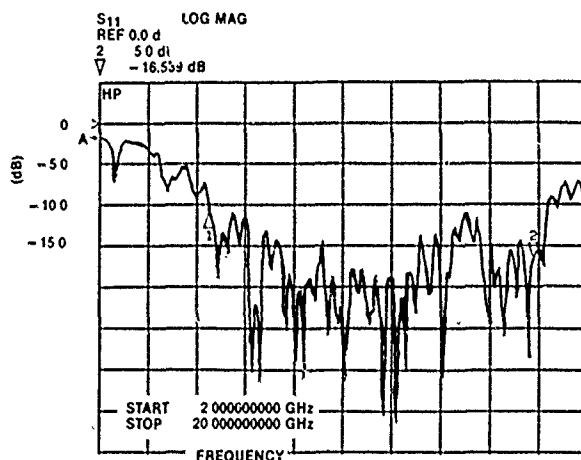


Figure 16. Embedded Slant Right Subarray Passive Return Loss

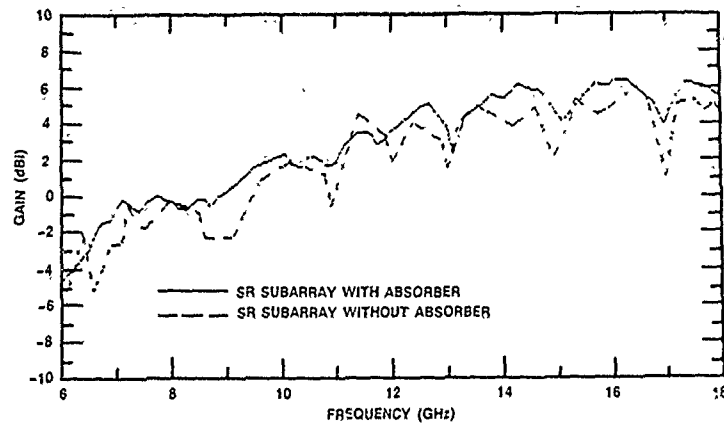


Figure 17. Comparison of Embedded Slant Right Subarray Gain With and Without Absorber

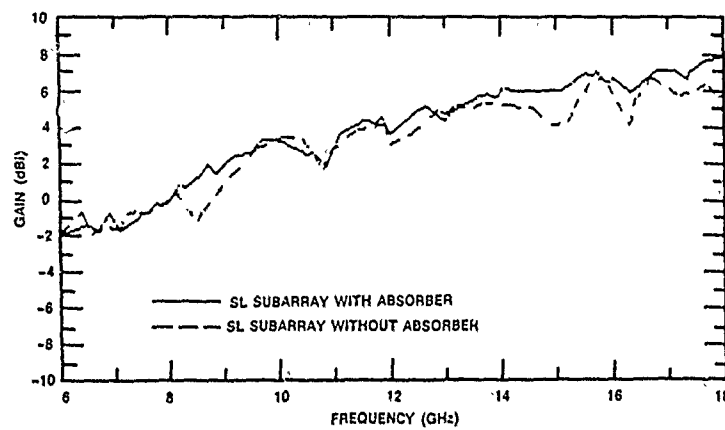


Figure 18. Comparison of Embedded Slant Left Subarray Gain With and Without Absorber

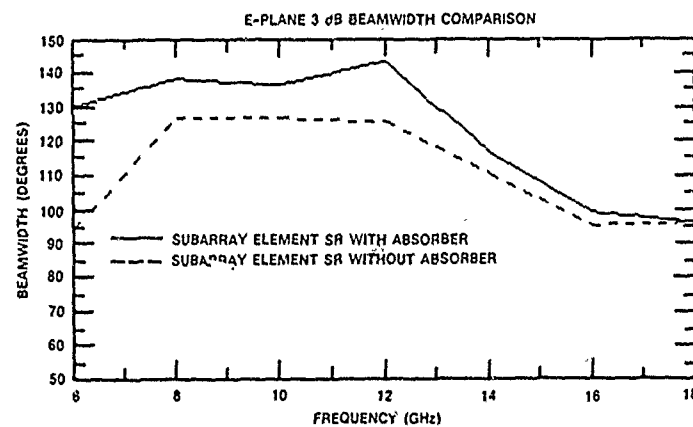


Figure 19. Comparison of Embedded Slant Right Subarray E-Plane 3 dB Beamwidth With and Without Absorber

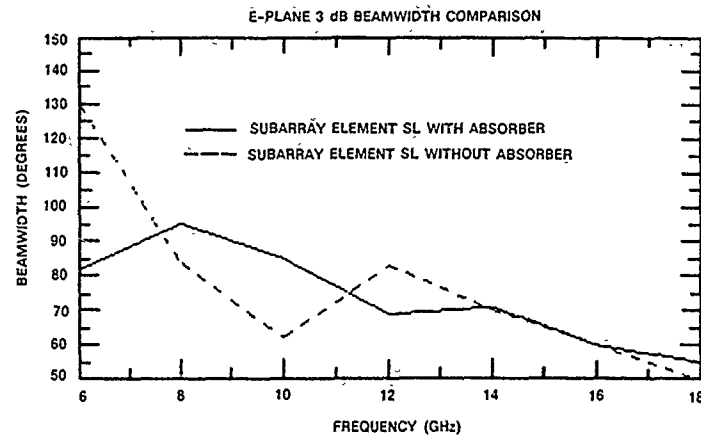


Figure 20. Comparison of Embedded Slant Left Subarray E-Plane 3 dB Beamwidth With and Without Absorber

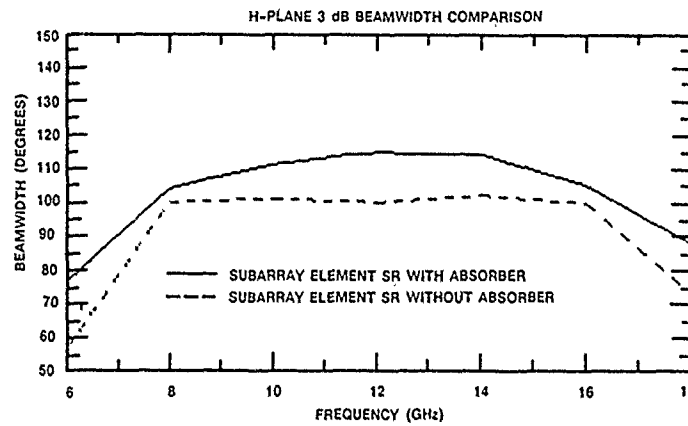


Figure 21. Comparison of Embedded Slant Right H-Plane 3 dB Beamwidth With and Without Absorber

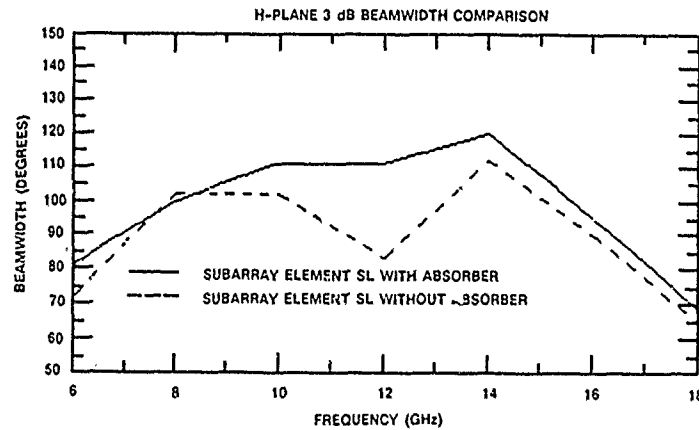


Figure 22. Comparison of Embedded Slant Left H-Plane 3 dB Beamwidth With and Without Absorber

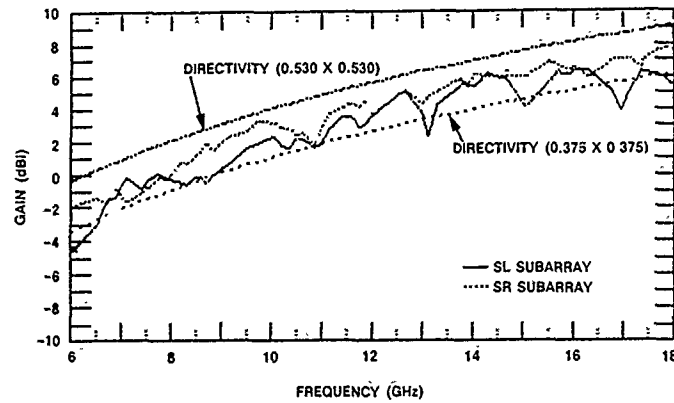


Figure 23. Typical Embedded Slant Right and Slant Left Subarray Gain

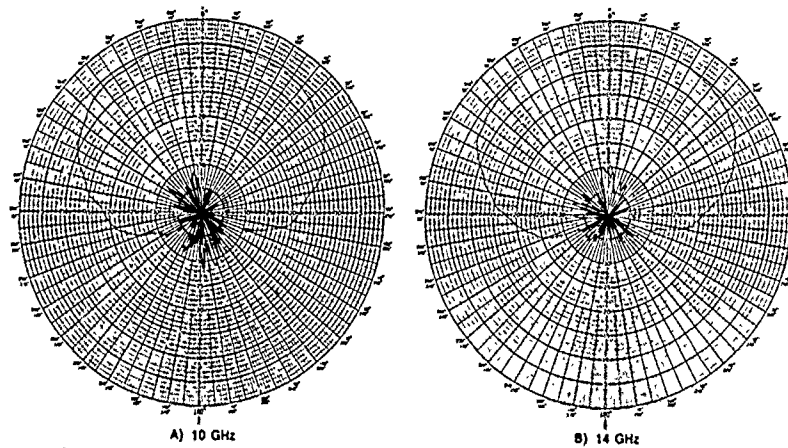


Figure 24. Line Array Aperture Embedded Slant Right Subarray H-Plane Radiation Patterns

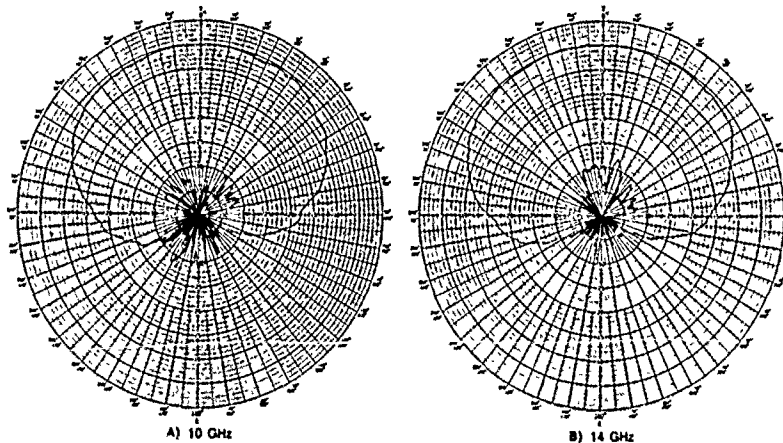
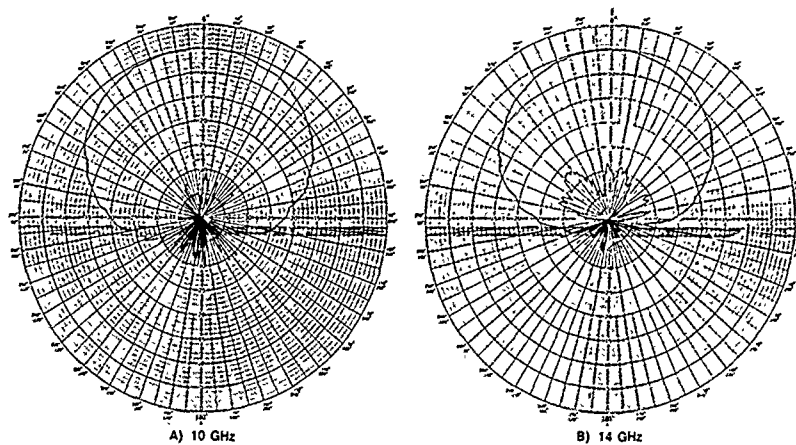
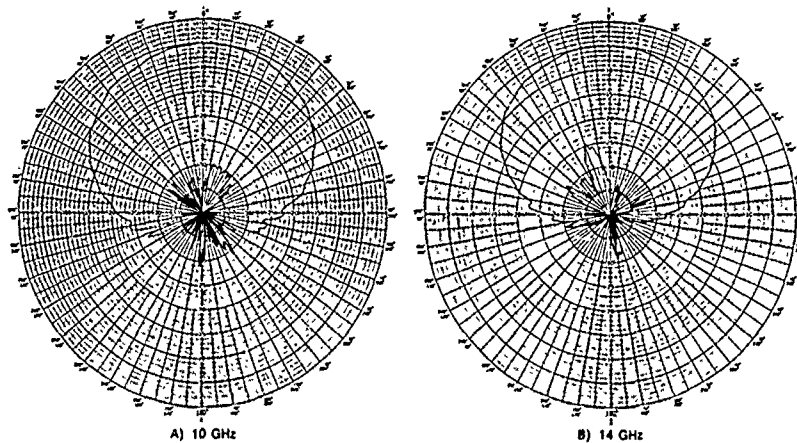


Figure 25. Line Array Aperture Embedded Slant Left Subarray H-Plane Radiation Patterns



*Figure 26. Line Array Aperture Embedded Slant Right Subarray E-Plane Radiation Patterns*



*Figure 27. Line Array Aperture Embedded Slant Left Subarray E-Plane Radiation Patterns*

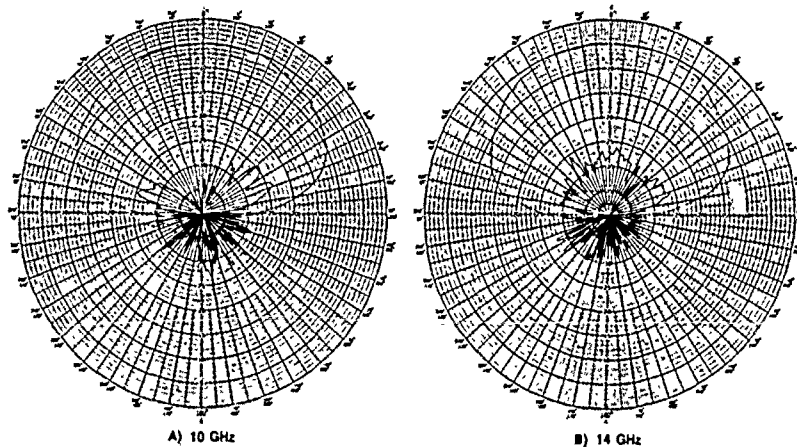


*Figure 28. Line Array Aperture Embedded Slant Right Subarray Intercardinal Azimuth-Plane Radiation Patterns*

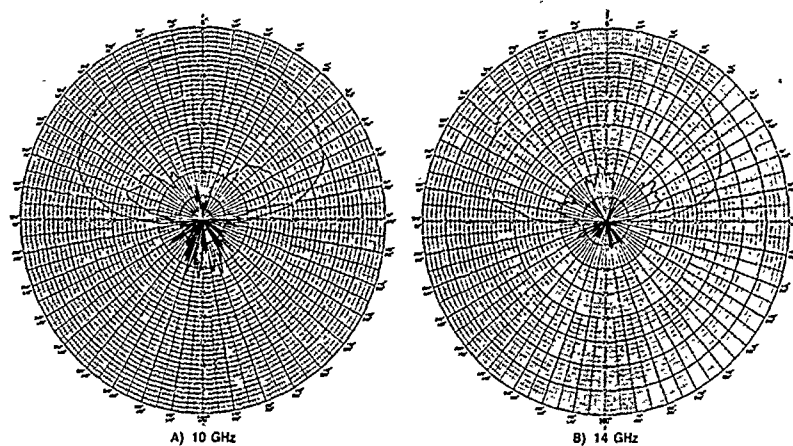


Figure 29. Line Array Aperture Embedded Slant Left Subarray Intercardinal Azimuth-Plane Radiation Patterns

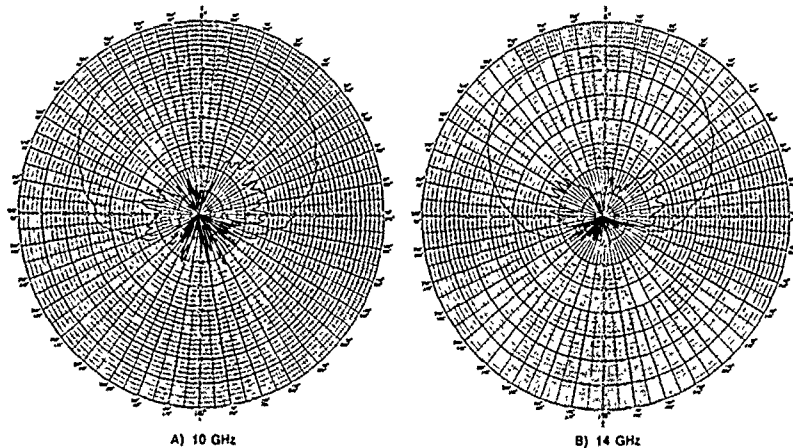


Figure 30. Line Array Aperture Embedded Slant Right Subarray Intercardinal Elevation-Plane Radiation Patterns

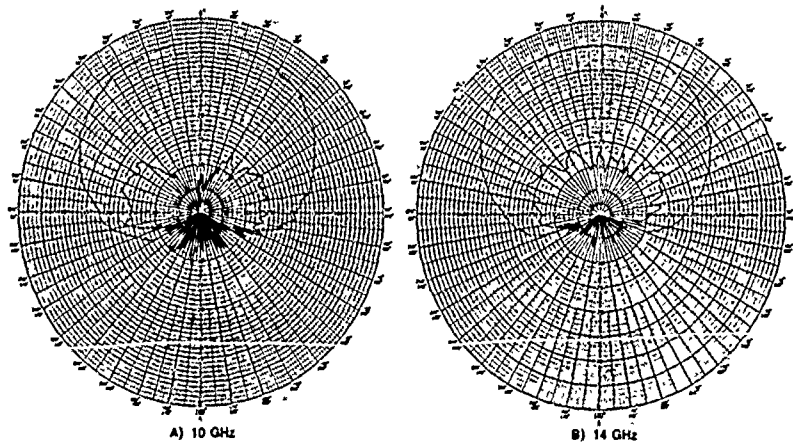


Figure 31. Line Array Aperture Embedded Slant Left Subarray Intercardinal Elevation-Plane Radiation Patterns

A simulation of active VSWR with azimuth scan on the line array was performed using a central row of an 8 x 8 arrangement of orthogonal subarray element pairs. The active VSWR with scan over all radiating half-space has previously been investigated for this type of lattice [1]. Using the mutual coupling measurements from a central subarray element pair to all other elements in the central row (all other rows terminated in 50 ohms), the active VSWR was calculated over the 6.0 to 18.0 GHz band for azimuth scan. The method used in this analysis is the free excitation (method) of radiating elements to measure mutual coupling and calculate active VSWR [4]. Figure 32 shows the active VSWR with azimuth scan ( $\pm 90$  degrees) from 6.0 to 18.0 GHz for a central slant right subarray. The number of occurrences for all values of active VSWR from 7.0 to 11.0 GHz are plotted in Figure 33 for a 60-degree scan volume for the central slant right subarray. The mean active VSWR is a 1.92:1.0 from 7.0 to 11.0 GHz in a  $\pm 60$  degree scan. The active VSWR with azimuth scan ( $\pm 90$  degrees) for the orthogonal slant left subarray element is shown in Figure 34 from 6.0 to 18.0 GHz. The number of occurrences for all values of active VSWR from 7.0 to 11.0 GHz in a 60-degree scan volume are plotted in Figure 35 for the central slant left subarray. The mean active VSWR is 1.91:1.0 from 7.0 to 11.0 GHz in a  $\pm 60$ -degree azimuth scan. The standard deviation in both cases is below

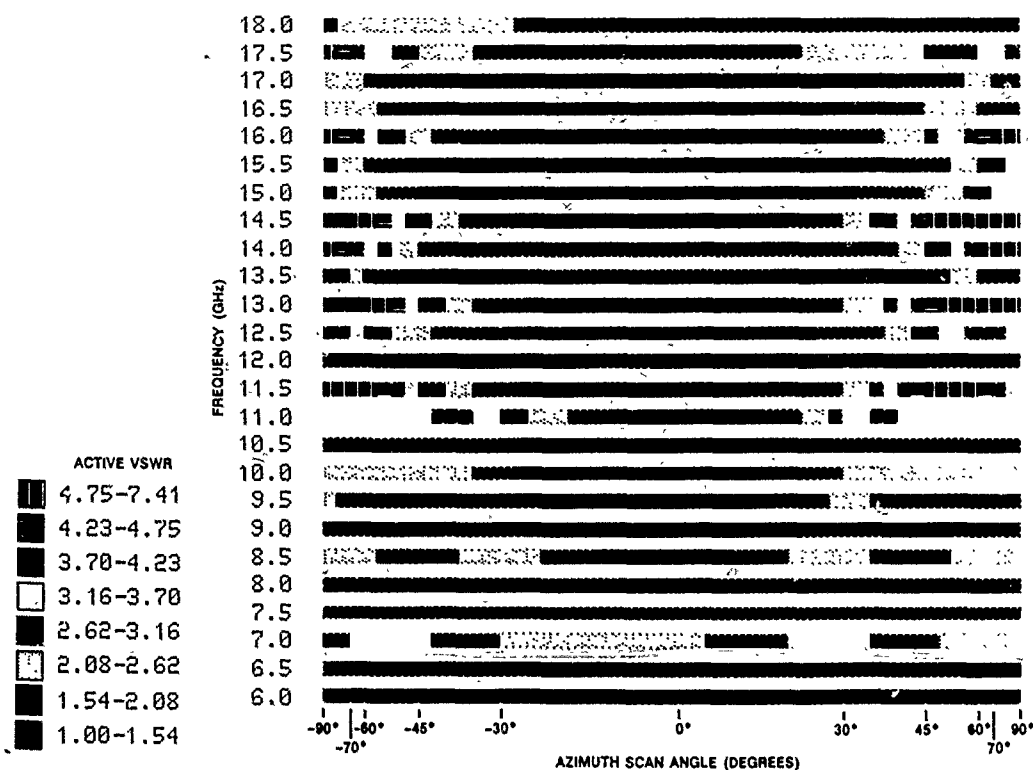


Figure 32. Active VSWR with Azimuth Scan versus Frequency for Central Slant Right Subarray



0.61. Over the full 6.0 to 18.0 GHz band, the mean active VSWR is below 1.93:1.0, the median is 1.76:1.0, and the standard deviation is below 0.93 for the orthogonal pair. The active VSWR is particularly low even scanning out past 70 degrees at 11.0 GHz where the grating lobe appears and at frequencies above 11.0 GHz where the grating lobe comes in from 70 degrees. At lower frequencies where the element spacing is on the order of  $0.19 \lambda_0$ , the active VSWR is extremely low over the entire  $\pm 90$ -degree scan.

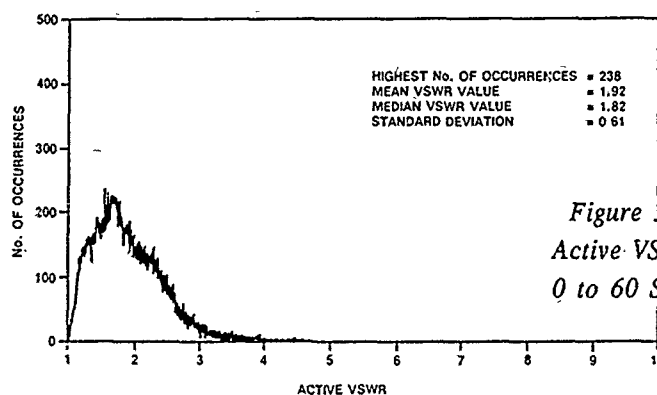


Figure 33. Number of Occurrences of Active VSWR over 7.0 to 11.0 GHz from 0 to 60 Scan for the Central Slant Right Subarray

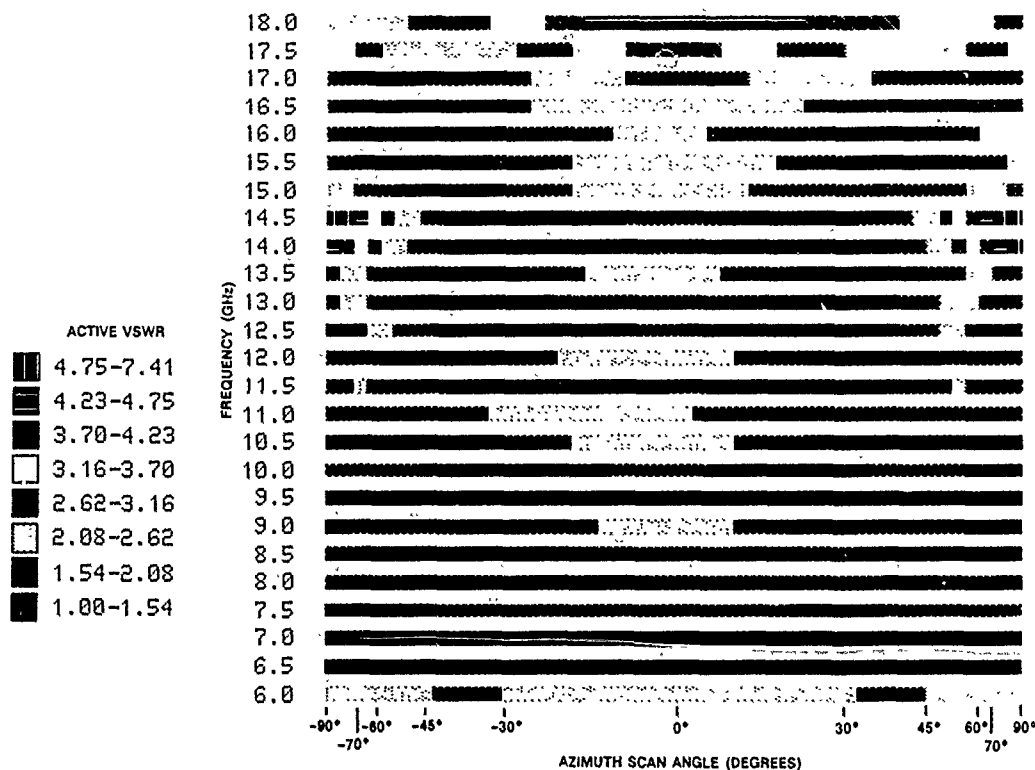


Figure 34. Active VSWR with Azimuth Scan versus Frequency for Central Slant Left Subarray

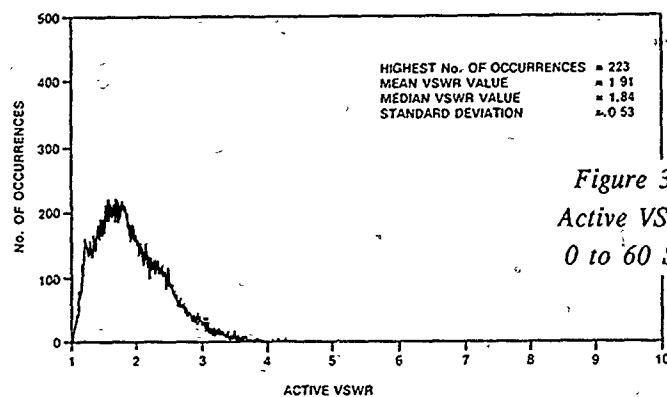


Figure 35. Number of Occurrences of Active VSWR over 7.0 to 11.0 GHz from 0 to 60 Scan for the Central Slant Left Subarray

#### 4.0 LINE ARRAY AND T/R MODULE CONSIDERATIONS

The active line array was designed, built, and measured to demonstrate the azimuth scan characteristics of a full planar active-phased array and to provide insight into the design of the next generation of phased arrays. The active line array assembly shown in Figure 36 consists of a corporate multilayer stripline feed network, six eight-channel Transmit/Receive (T/R) modules, a cooling manifold, and the dual polarized aperture consisting of 192 active and 1600 terminated subarray elements. The six T/R modules feed the active row of slant left polarized subarrays. The layout of the aperture showing the connection of the element bars with the module and the cooling manifold is given in Figure 13.

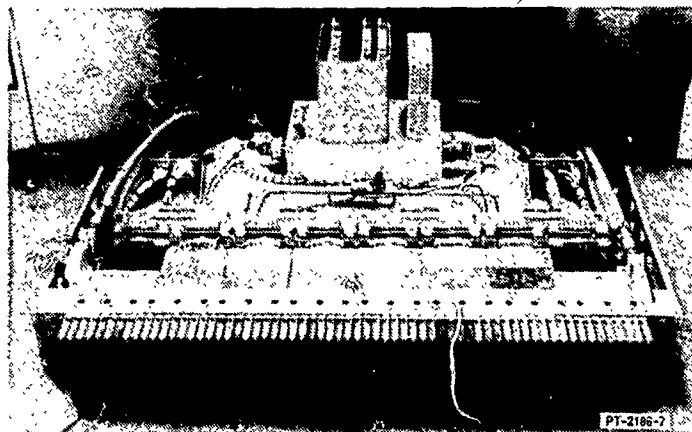


Figure 36. Assembled GaAs Active Monolithic Multifunction Line Array

The array lattice spacings described previously limited the area available for each T/R circuit to 0.53 inch horizontally by 0.265 inch vertically. The horizontal dimension accommodates the circuit and necessary module walls. The vertical dimension accommodates the circuit, module housing, and cold plate. With this spacing, full polarization diversity is possible; that is, each orthogonal subarray pair is driven by two full T/R circuits.

The eight-channel T/R module is shown in Figure 37. Each T/R circuit is laid out in a common leg configuration. This common leg design shares a five-bit phase shifter, attenuator, and driver amplifiers in transmit and receive modes as shown schematically in Figure 38. Each T/R circuit was constructed using four submodules; the Monolithic Microwave Integrated Circuit (MMIC) chips are 1985 technology. The low noise amplifier is limited to X-band performance; all other chips are designed for the 6.0 to 18.0 GHz band. Each channel also incorporates a calibration path from the array input to the circuit/radiating element interface. The eight inner module channel walls are made up of the multilayer stripline feed network consisting of the summation, difference, and calibration ports feeding the four submodules as depicted in Figure 13.

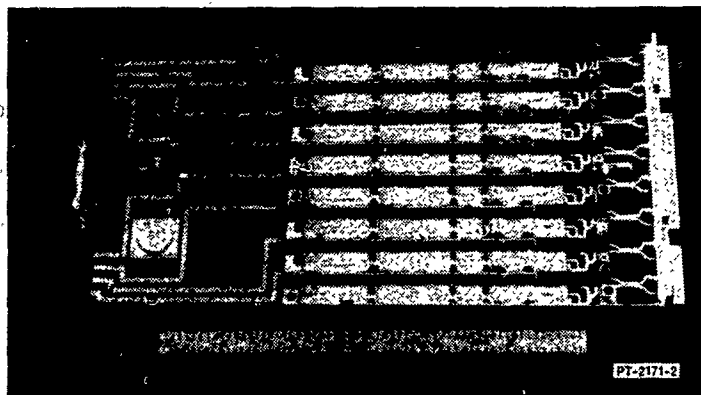


Figure 37. Eight-channel T/R Module with Sum, Delta, and Calibration Ports

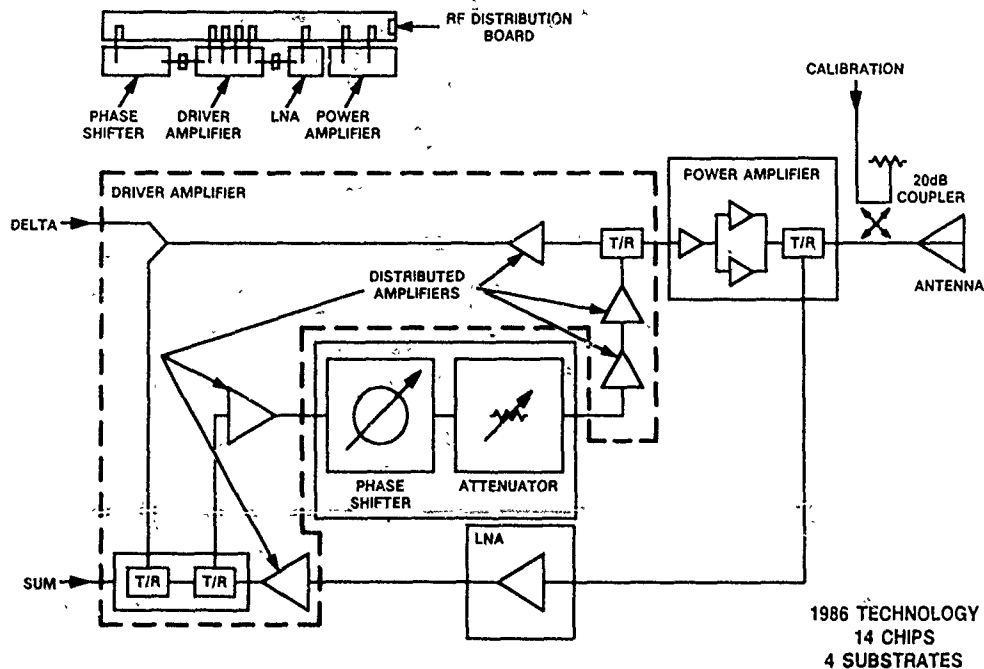


Figure 38. Schematic of T/R Module Channel Showing Common Leg Configuration

The RF and DC manifolds are organized into quadrants, with the upper two quadrants feeding one row of slant right polarized subarrays and the lower quadrants feeding the other row of slant left polarized subarrays. Independent RF feeds are provided for summation receive/transmit, difference receive, and calibration for each quadrant. These ports can be interconnected to provide sum and difference for a full array or partial functions. The active line array uses a liquid cooling plenum manifold for controlling the temperature of the eight channel T/R modules containing the four submodules of MMICs. The cooling manifold is centered between a top (slant right) T/R module and bottom (slant left) T/R module as depicted in Figure 13 to maximize use of cooling surfaces.

## 5.0 ACTIVE LINE ARRAY PERFORMANCE

Active line array performance was initially tested in the receive mode focusing on the 7.0 to 7.5 GHz frequency band. An initial frequency of 7.3 GHz was chosen for detailed testing to develop amplitude and phase calibration data for different scan angles and amplitude weightings. After the calibration data sets were obtained, the aperture was integrated and assembled on the line array and tested on an outdoor antenna range.

Only the slant left polarization of the aperture is active and the other is terminated in the configuration shown in Figure 13 and tested. The center row of the aperture (as depicted in Figure 13) includes the active dual elements, while the other dual elements are all terminated in 50 ohms and are included to simulate the environment of a full planar aperture.

Lab calibration was carried out with amplitude and phase bounds of +0.5 dB and  $\pm 5$  degrees selected as the alignment windows. The calibration procedure consists of a beam steering computer commanding the phase and attenuator state of individual T/R circuits one at a time with all other T/R circuits effectively off. The phase and amplitude were determined by injecting the RF source into the T/R module where the antenna elements connect, and then measuring the output of the line array at the receive summation port. This calibration takes all circuit interactions into account except the aperture effects. An iterative process of phase and amplitude adjustments to converge to the desired amplitude and phase responses (uniform, Taylor, Bayliss, scanned, etc.) within the established amplitude and phase bounds was used.

Antenna range radiation patterns were measured in the receive mode. Pattern measurements were obtained over the 7.0 to 7.6 GHz band, with primary emphasis at 7.3 GHz. In conjunction with the lab calibrated conditions, measurements were made for uniform, Taylor, and Bayliss amplitude tapers for the broadside ( $0^\circ$ ) and  $4.6^\circ$  angles. Additional scan angles were investigated, under uncalibrated conditions. The majority of the testing addressed the array azimuth intercardinal plane. The pattern obtained for calibrated 0 scan, uniform amplitude illumination at 7.3 GHz is shown in Figure 39.

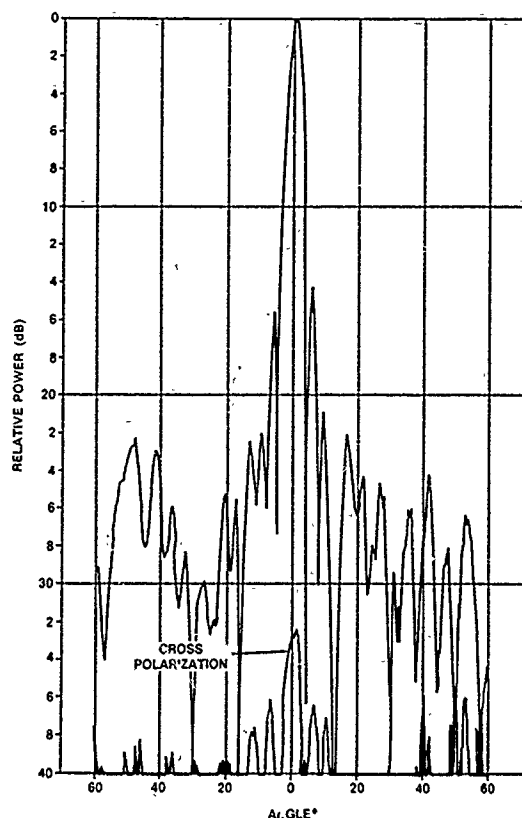


Figure 39. Collimated Azimuth Sum Pattern at  $0^\circ$  Scan Uniform Amplitude at 7.3 GHz

The first sidelobes levels are less than 14 dB and the sidelobe structure departs from a sine  $x/x$  roll-off in the outer region, in which the test environment (outdoor chamber enclosure) affects become dominant. The antenna gain is approximately 22 dB. The cross-polarization signal level is extremely good, being less than -32 dB down. The 3 dB beamwidth is  $3.6^\circ$ . Broadside patterns for the Taylor and Bayliss amplitude tapers are shown in Figures 40 and 41. A low amplitude and phase rms error for the former is evidenced by the lower inner region sidelobes, the result of a more precise laboratory alignment. Uniform, Taylor, and Bayliss weighted patterns for a  $4.6^\circ$  scan angle (lab calibrations) are shown in Figures 42 and 43. Principal E-plane patterns for the slant right subarray are shown in Figure 44 for uniform illumination. An azimuth scan pattern for  $19.9^\circ$  is shown in Figure 45, illustrating that the beam pointing angle correlates well with the commanded angle. Higher sidelobe levels are observed (i.e., broadside) as expected, due to increased rms errors in the uncalibrated case.

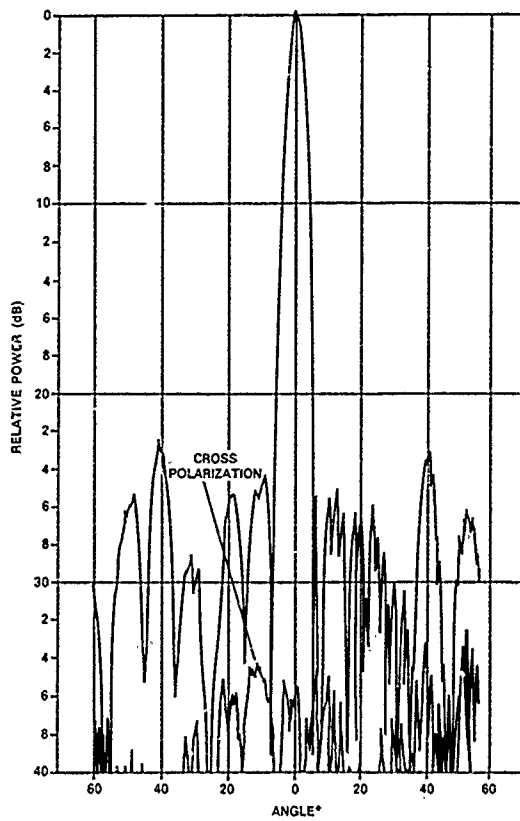
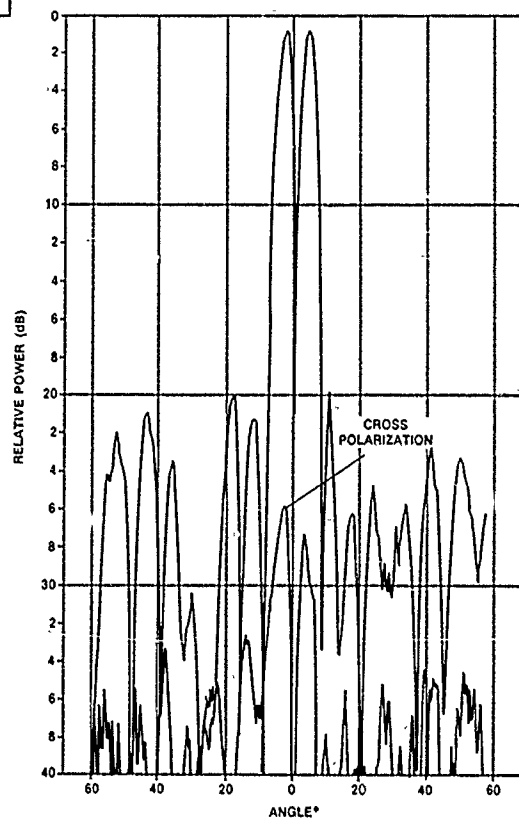


Figure 40. Collimated Azimuth Sum Pattern at 0° Scan, Taylor Taper at 7.3 GHz

Figure 41. Collimated Azimuth Difference Pattern at 0° Scan, Bayliss Taper at 7.3 GHz



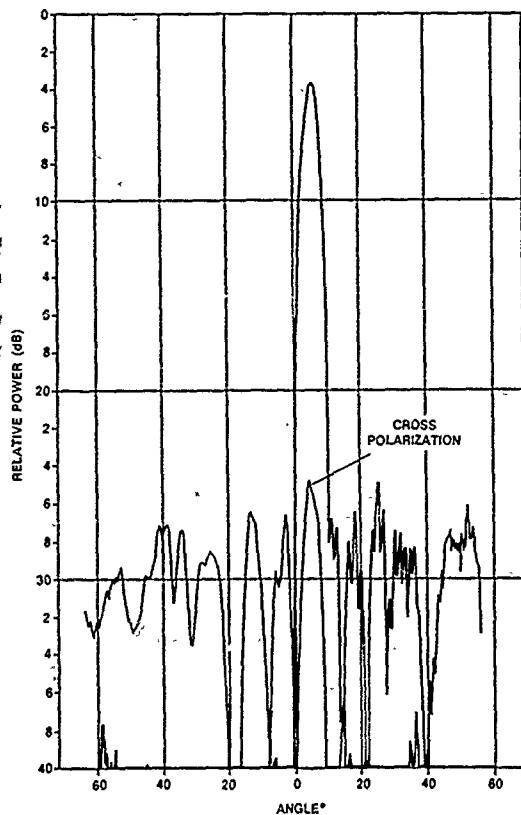
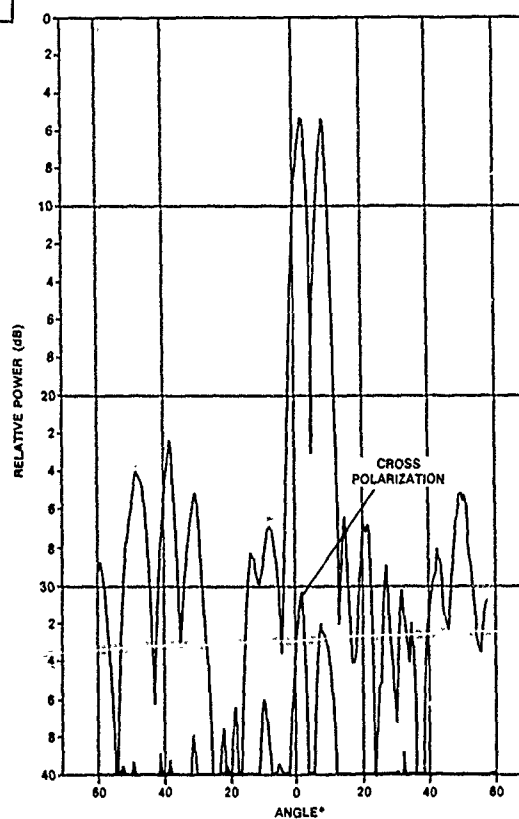


Figure 42. Collimated Azimuth Scan Pattern at 4.6° Scan, Taylor Taper at 7.3 GHz

Figure 43. Collimated Azimuth Difference Pattern at 4.6° Scan, Bayliss Taper at 7.3 GHz



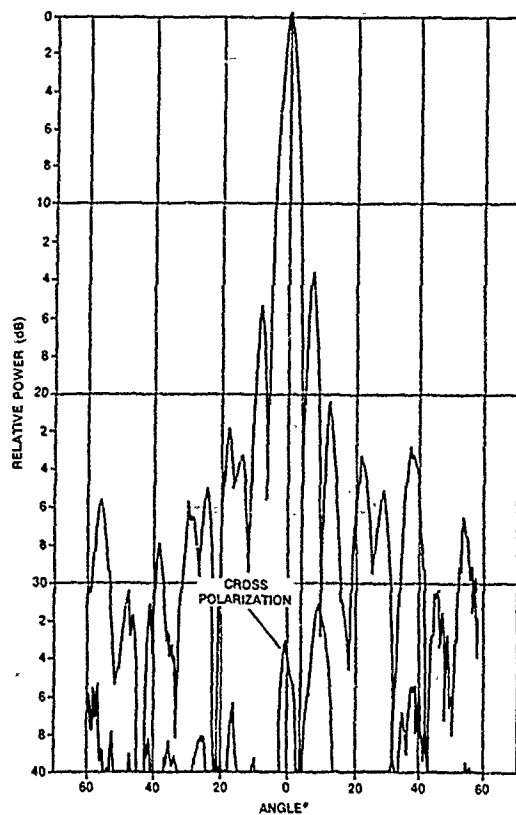
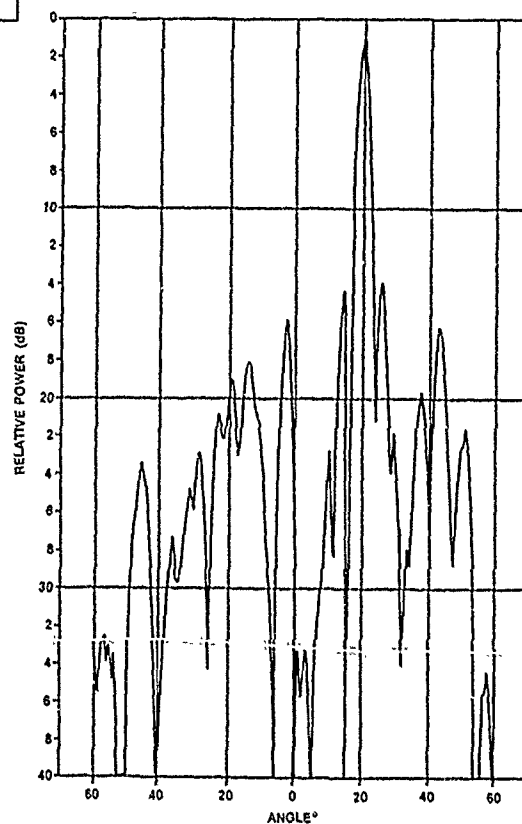


Figure 44. Collimated E-Plane Sum Pattern at 0° Uniform Amplitude at 7.3 GHz

Figure 45. Uncalibrated Azimuth Sum Pattern at 19.9° Scan, Uniform Amplitude at 7.3 GHz





Narrowband swept gain measurements were also conducted for the Taylor amplitude illumination. Gain is approximately 3.5 dB lower than that computed with uniform illumination, as a result of the additional dissipative loss required to fit the desired aperture amplitude taper. Additional testing at more frequencies both in transmit and receive are needed to further characterize module performance.

## 6.0 CONCLUSIONS

Significant progress has been made in the design of dual polarized wideband planar phased array apertures. The aperture was constructed using a printed circuit flared slot antenna element having a modified Klopfenstein taper (flare) a fraction of a wavelength long with a stripline feed transmission line. The subarraying of elements in the aperture directly decreases the cost of the phased array by reducing the number of T/R modules (circuits) in the array by half. Combination of subarrays into orthogonal element pairs allows for multiple polarization capability in the line array. Characterization of the antenna performance of these closely spaced ( $0.19 \lambda_0$ ) printed circuit orthogonal subarray element pairs over a wide bandwidth was obtained.

Exceptional array-element performance was measured over the 6.0 to 18.0 GHz band. The average embedded subarray E-, H-, and intercardinal plane radiation pattern beamwidths were between  $\cos\theta$  and  $\cos^2\theta$ . The subarray element radiation patterns were very symmetric and did not exhibit any holes. Intercardinal subarray radiation patterns with extremely low cross-polarization level were demonstrated for this aperture over the 6.0 to 18.0 GHz band. The cross-polarization pattern levels were also extremely low in the two principal planes. Overall, the polarization properties of the antenna elements are well-behaved when arrayed in a dual-polarized aperture. The typical embedded subarray gain was on the average only 0.8 dBi less than the ideal directivity, showing an extremely efficient element. The embedded subarray return loss was below -10 dB across the frequency band. The use of inner element absorber loading was shown to provide array-element performance optimization and increased mechanical stability. Close element spacing was achieved for restricted transmit and Bragg grating lobe operation, while maintaining a consistent level of antenna performance across an octave bandwidth.

Closely spaced elements for reduced (low) active VSWR with scan have been demonstrated with a mean plus standard deviation value below 3.0:1.0 over a full 6.0 to 18.0 GHz band with a  $\pm 60$ -degree scan. Radar performance in multifunction phased array systems with dual polarized apertures can yield active VSWR which is on the average below 2.0:1.0 over a  $\pm 60$ -degree scan in X-band. The mean active VSWR over the 6.0 to 18.0 GHz band scanning beyond 60 degrees (60 to 70 degrees) is below 3.3:1.0.

It has been demonstrated that full polarization diversity can be accomplished and that the T/R circuit can be packaged in densities consistent with 18.0 GHz performance. Fi-

nally, this aperture characterization and line array demonstration provided useful insight and experience for the design of next generation active phased arrays.

## 7.0 ACKNOWLEDGEMENT

We would like to express our thanks to the General Dynamics Corporation, Fort Worth Division, for their support in the development of the Line Array Hardware under the GAMMA (GaAs Active Monolithic Multifunction Array) program, General Dynamics purchase order no. 1060895/item 05.

## 8.0 REFERENCES

- [1] Povinelli, M. J., "Experimental Design and Performance of Endfire and Conformal Flared Slot (Notch) Antennas and Application to Phase Arrays: An Overview of Development", *1988 Antenna Applications Symposium*, Allerton Park, University of Illinois, September 1988, pp. 1-25.
- [2] Klopfenstein, R.W., "A Transmission Line Taper of Improved Design", *Proceedings of the IRE*, Vol. 44, No. 1, January 1956, pp. 31-35.
- [3] Povinelli, M. J., and Grove, C. E., "Wideband Apertures for Active Planar Multifunction Phased Arrays", *Proceedings of the 1989 IEEE AEES National Radar Conference*, March 30, 1989, pp. 125-128.
- [4] Debskin, T. R. and Hannan, P. W., "Complex Mutual Coupling Measured in a Large Phased Array Antenna", *The Microwave Journal*, pp. 93-96, 1965.

**DESIGN, PERFORMANCE CHARACTERIZATION AND HYBRID FINITE  
ELEMENT BOUNDARY ELEMENT ANALYSIS OF A LINEARLY POLARIZED  
PRINTED CIRCUIT TAPERED NOTCH ARRAY**

**Mark J. Povinelli**

**GE Aerospace**

**Aerospace Electronic Systems**

**Utica, New York 13503**

**and**

**John D'Angelo**

**GE Corporate Research and Development**

**Schenectady, New York**

**ABSTRACT**

The flared slot or tapered notch antenna has become the mainstay element for advanced wideband phased arrays. The flare design allows for a diversity of shapes which can impact pattern (main polarization and cross-polarization), input impedance, and gain. Tapers used in the past include exponential, circular, Dolf-Tchebycheff (Klopfenstein), stepped, and linear. This along with the use of mutual coupling fences is shown to have a direct impact on co- and cross-polarization pattern response in the intercardinal and principal planes of the element. The use of fences or mutual coupling post and close element spacings along with subarraying can impact active voltage standing wave ratio (VSWR) with scan and aid in the enhancement of antenna radiation performance.

The prediction of RF scattering or radiation of realistic objects by computer codes has always been encumbered by the complex nature of the antenna itself. The antenna can be complex in shape, electrically large in wavelengths, and have elaborate design and element-to-element interactions. This paper presents a method which can be used for determining the scattering or radiation results from objects with realistic characteristics based on a frequency-domain finite element solution for modeling the antenna and near-field region with absorbing boundary conditions or integral equations representing the exterior region. The application of this analysis on the design of a linearly polarized flared slot or notch array will be discussed. A linearly polarized array was designed with close element spacings to restrict transmit grating lobes. The array is constructed using printed circuit stripline fed tapered notch antenna elements. The elements are driven in subarray pairs through use of stripline Wilkinson power dividers and have flare lengths on the order of a fraction of a wavelength. The understanding of near-field radiation and coupling interactions is an important design aid. Physical phenomena are observed in the predicted near-field results.

## 1.0 INTRODUCTION

Advances in phased-array module technology and mission specifications require a new generation of antenna apertures which operate over a multioctave frequency range (2.0 to 18.0 GHz). The need for both wideband linearly-polarized arrays for traditional radar functions and wideband dual-polarized arrays for multifunction applications predicates the need for versatile design in the wideband aperture arena. The radiating element which makes up this aperture must operate as such over this extremely wide bandwidth. Grating lobe restrictions at high frequency further require the aperture to have closely spaced elements. This makes the effective element aperture width electrically small. Antenna elements and apertures of this type must improve in performance if they are to be used in wideband active phased arrays. Further development of two- and three-dimensional analysis methods and computer programs which can help predict the performance from these types of three-dimensional antenna element and aperture designs would be extremely useful. The design, analysis, and characterization of wideband linearly polarized arrays will be discussed in this paper.

The required frequency coverage has progressively widened in these phased arrays until the typical frequency bandwidth now exceeds several octaves. As the frequency coverage increased, the types of radiating elements that could be considered have progressively decreased. At present, with frequency bandwidths exceeding three octaves, only end-fire elements such as exponential notch or flared slot can be considered viable radiating elements.

The aperture discussed here uses a close element spacing ( $0.17 \lambda$  to  $0.19 \lambda$  at low end) to reduce active VSWR with scan and restrict grating lobes. The gain, return loss, radiation pattern, and active VSWR performance of linearly polarized flared slot arrays will be given. Predictions based on finite element and boundary element method analysis will be shown to provide useful insight into the design and operation of this antenna element type.

This antenna can be built using standard low cost printed circuit technology. Currently, design methods for analysis of multioctave, electrically small printed circuit radiating elements and apertures are limited. Design of this element (when its width approaches a tenth of a wavelength) in the past relied on experimental iterations due to a lack of dynamic electromagnetic analysis and computer-aided engineering (CAE) computer routines to predict radiation and scattering performance from three-dimensional printed circuit elements and antenna aperture structures. Analyses which include effects from the three-dimensional volume of the element are underway.

The two-dimensional Hybrid Finite Element/Boundary Element Method (FEM/BEM) has proven to be a very dynamic analysis tool for electromagnetic computation for antenna and scattering problems. The Finite Element Method (FEM) has been used for over a decade in mechanical stress and thermal analysis as a feasible and efficient compu-

tational method. The combination of Finite Elements with a Boundary condition for modeling the far-field is yielding a very dynamic analysis tool for electromagnetic field computation. The extension of this method for modeling full three-dimensional objects including lossy dielectrics is extremely promising.

## 2.0 DESIGN OF A WIDEBAND EIGHT-ELEMENT LINE ARRAY

To enable multifunction active arrays to perform over a multioctave frequency range, the aperture must have wideband performance (6.0 to 18.0 GHz) [1]. This wideband coverage requires frequency independent type behavior in the antenna element design. These types of modern active arrays are further specified to have reduced transmit grating lobes up to 18.0 GHz in some applications. For the line array demonstration, a 0.35-inch spacing was chosen to restrict transmit grating lobes up to 15.0 GHz with a plus or minus 60° scan capability. This requirement includes an allowance for beamwidth. This close element spacing was imposed to simulate similar future planar array requirements.

An antenna element that provides frequency independent type operation and is suited for phased array apertures is the stripline fed flared slot element. This element is built using standard printed circuit technology and provides workable element sizes for phased array applications. The line array can be configured with respect to the arrayed element's polarization as either an E- or H-Plane array. For an H-Plane array, the element will provide the necessary frequency independent type behavior with no restriction placed on its width. The criteria for choosing a suitable design would depend on the mutual coupling effects of the embedded array element and its active impedance with scan. In order to support future planar array concepts, a configuration was chosen which would restrict the element width in both the E- and H-Plane to 0.35 inch. This reduction of element width to 0.35 inch was found to lend itself readily to the flared slot or stripline fed notch design in both the E- and H-Planes.

The stripline notch element design was selected and is directly applicable to a planar array concept. This element exhibits multioctave performance when no restriction is placed on its width. When the element width is reduced to 0.35 inch, a reduction in element gain and a higher input impedance is observed at lower frequencies. This reduction in efficiency is overcome by connecting the elements end-to-end in an E-Plane line array which is etched on a copper clad Teflon substrate board as shown in Figure 1. Connecting all elements allows the element widths to be continuously merged into the adjacent elements. This connection overcomes the abrupt discontinuity of a 0.35-inch wide element and allows each element to increase in effective width. This increase in arrayed element width, while maintaining 0.35-inch spacing, directly improves the low frequency performance of an arrayed element. The measured data also suggests that no severe mutual coupling effects occur when connecting the elements together in this manner.

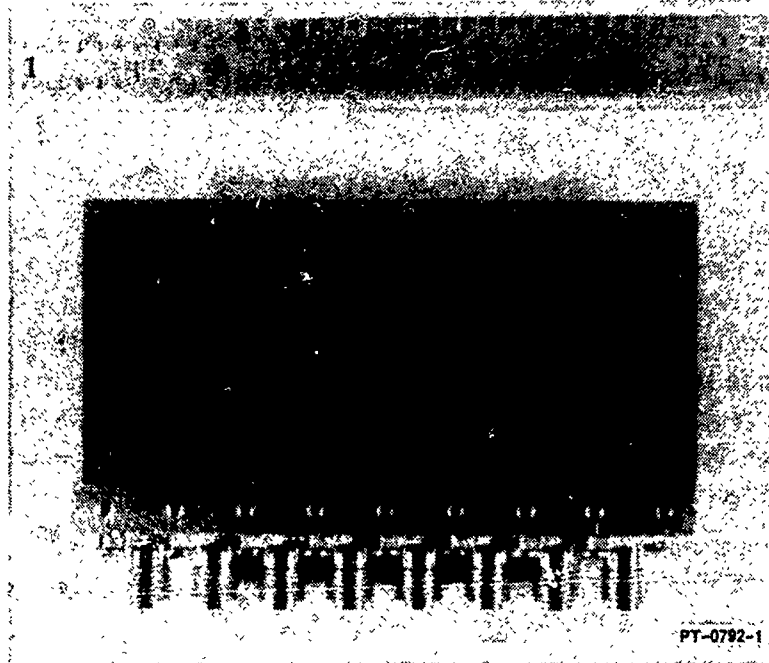


*Figure 1. Eight-Element Stripline Fed Flared Slot Aperture*

The stripline notch antenna element is realized by combining three printed circuit components into a single radiating element. A 50-ohm stripline is etched on a 0.031-inch copper-clad Teflon substrate. This 50-ohm line then feeds across a slot etched on the opposite side of the 0.031-inch thick board and across a similar slot on the opposite ground plane side to form a stripline to slotline coupling transition. This transition has an input return loss of -15 dB across the 6.0 to 18.0 GHz band. This wideband coupling from the 50-ohm line to the slotline is achieved by terminating the stripline in a radial stub and the slotline into an open circuit termination.

The launched quasi-TEM fields of the slotline radiate when the guide wavelength is greater than approximately 40 percent of the freespace wavelength. Therefore, the phase center of the point of radiation moves up the flare with decrease in frequency. This results in a low frequency limit based on element width. This low frequency limitation in width occurs at a freespace half-wavelength where a moderate roll-off can be obtained down to a tenth of a freespace wavelength. For shorter length flares ( $\lambda_0/4 \leftrightarrow \lambda_0\epsilon_r/4$ , and widths  $< \lambda_0/2$ ), the possibility of a more resonant antenna exists. A first-order approximation to the gain is given by the ideal theoretical directivity of the element area in the array where the gain increases as roughly the square of the frequency. Modification of the flare shape can result in beam broadening, pattern shaping, and impedance matching. The stripline notch array shown in Figure 1 uses a modified Klopfenstein taper on the flared slot to achieve a shorter aperture length ( $0.17 \lambda_0$  long at 6.0 GHz). This circuit is then repeated eight times on a single circuit board to create the eight-element, E-Plane line array.

A series of measurements was performed on a central element in the eight-element line array with all other elements terminated in 50 ohms. The return loss of this central element is shown in Figure 2 from 6.0 to 18.0 GHz. The return loss is less than -10 dB (VSWR 1.92:1) across the majority of the band. All elements in the array exhibit very similar return loss plots.

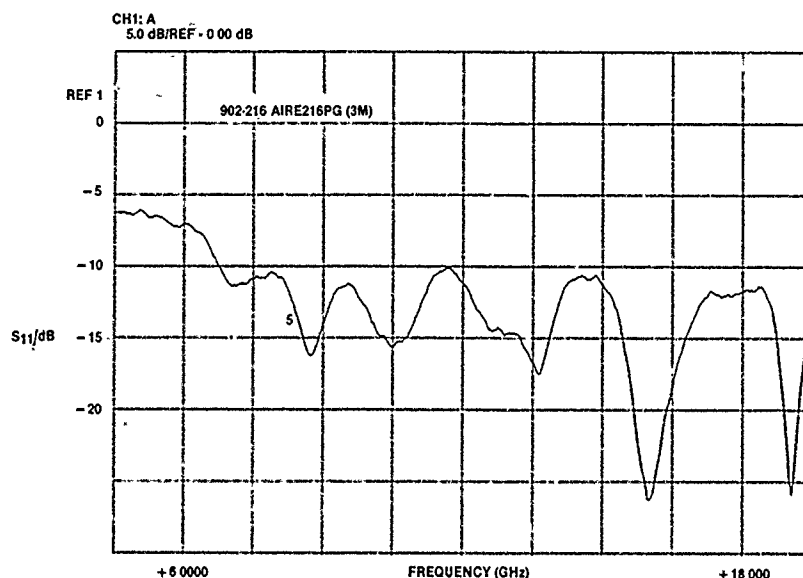


Figure 2. Return Loss of Center Element

The E- and H-Plane patterns are very symmetric and exhibit no holes over the 6.0 to 18.0 GHz band. The average E-Plane half-power beamwidth is 138 degrees, and the average H-Plane beamwidth is 128 degrees. Typical E- and H-Plane radiation patterns at 10 GHz are shown in Figure 3. The cross-polarization pattern is approximately -20 dB down from the main-polarization pattern over plus or minus 90 degrees.

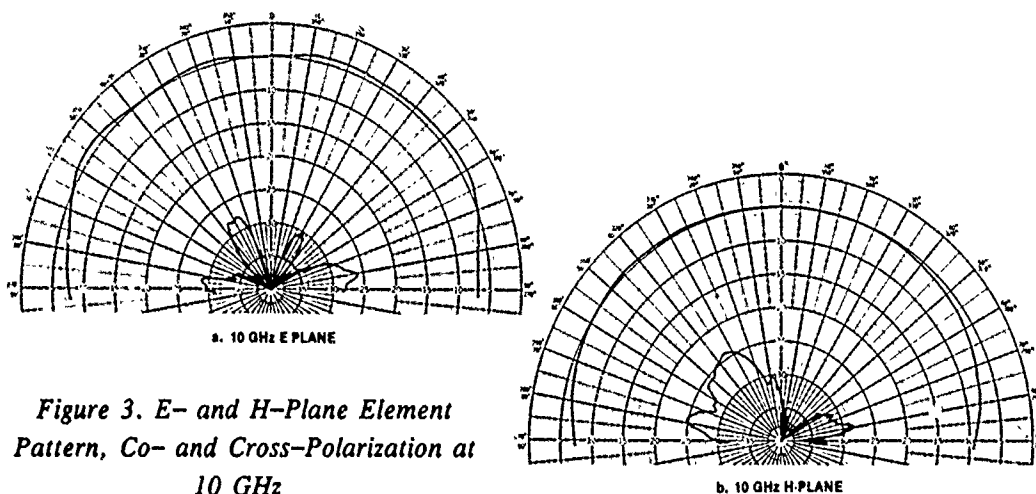


Figure 3. E- and H-Plane Element Pattern, Co- and Cross-Polarization at 10 GHz

The gain of this central element from 6 to 18 GHz is shown in Figure 4 along with the directivity for a 0.35-inch square. The gain is very smooth and approximately equal to the cell area directivity from 8.8 to 16.5 GHz. At lower frequencies, the E- and H-Plane patterns exhibit a higher backlobe radiation level. The variation in gain observable from 6.0 to 8.8 GHz is believed to be due to forward reflection from the back radiation incident on the ground plane block. The mutual coupling level from a central element to an adjacent element is -10 dB or lower across the band and is -20 dB to an end element. The reduction in active VSWR due to the close element spacings (less than  $0.2 \lambda$  at low frequencies) is observed in the computed data.

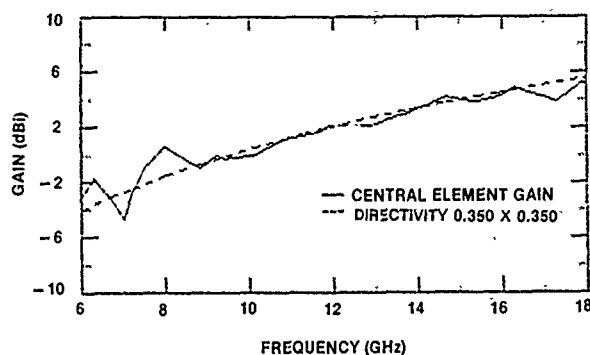


Figure 4. Central-Element Gain

The active VSWR with  $\pm 90$  degree scan over the full 6.0 to 18.0 GHz frequency band is shown in Figure 5. At 6.0 GHz where the element spacing corresponds to a  $0.17 \lambda$  spacing the active VSWR is extremely low over the entire  $\pm 90$  degree scan. As the element spacing increases up to a half-wavelength at 16.8 GHz, the active VSWR increases, starting approximately where the grating lobe appears in the  $\pm 90$  degree scan. At 15.0 GHz, the active VSWR is low from 0 to 60 degrees where the grating lobe appears.

### 3.0 ANALYSIS AND MODELING OF FLARED SLOT ANTENNAS

A hybrid finite element/boundary element method analysis computer code was developed and used to solve a number of antenna problems. The two-dimensional code was used to model an actual phased array aperture and a radome antenna configuration. This section presents the results of a two-dimensional finite element/boundary element time harmonic analysis of a phased array antenna including a radome[2,3]. The Hybrid FEM/BEM method can be used for both near and far field radiation and scattering analysis. In this technique, the boundary element method is used for the exterior far field region and the finite element method is used for the near field antenna/scatterer region. Predictions are given for the antenna's radiation pattern with and without the radome. Examples are also shown for an active phased array/radome configuration and predictions are compared to measured results for a steered pattern.

This method is unique in that complicated, high aspect ratio geometries can be modeled accurately and iteratively. Objects to be modeled can simultaneously contain con-



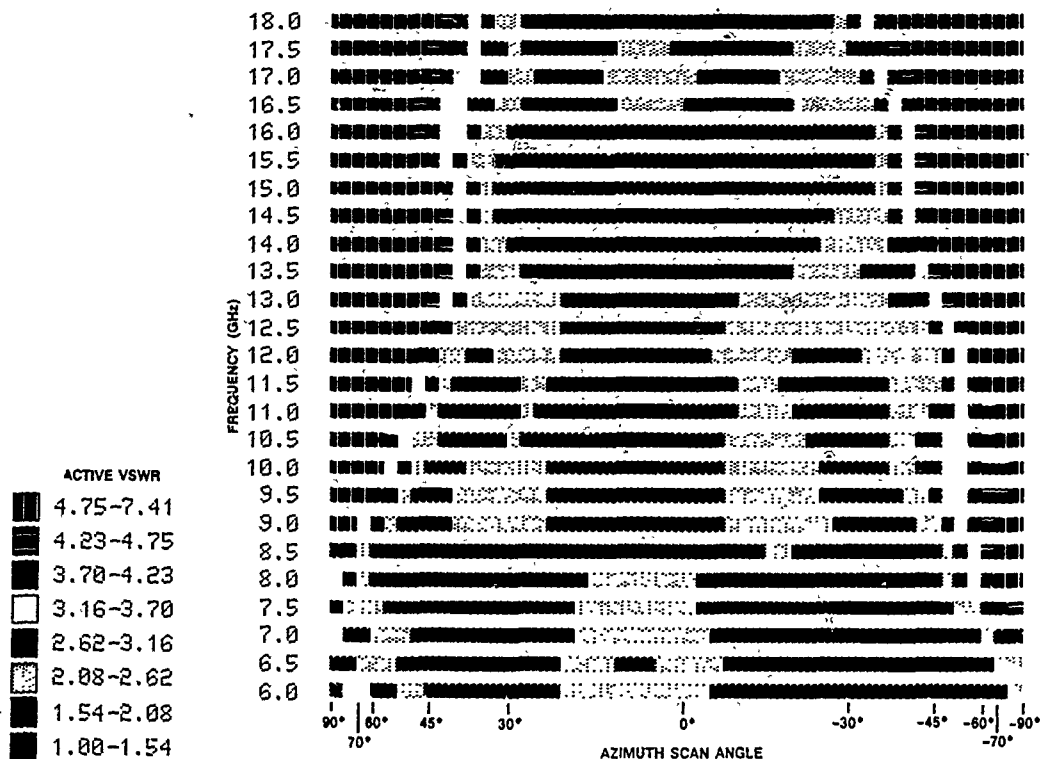


Figure 5. Active VSWR with Scan Over 6.0 to 18.0 GHz Band of Central Array-Element

ductors, lossy dielectrics, and lossy magnetic materials. This ability is facilitated by the use of the finite element method for the near field modeling. The boundary element method, in turn, is used for modeling the exterior open region. Objects of up to 20 wavelengths in dimension have been analyzed by this method. The same computer model and code can be used for both radiation and scattering analysis.

Scattering and radiation predictions are also shown for a constant thickness radome and a variable thickness radome. Comparisons can be made to the antenna array with no radome. The active phased array is also modeled with a multimaterial radome; shown are the near field interactions and the resulting far field pattern. This method is useful for solving the total electromagnetic antenna problem, including the radome's effect on pattern, impedance, and gain. The following is a brief discussion of the Hybrid FEM/BEM method.

The Vector Helmholtz's equation for the radiating field using a H polarization and an applied electric polarization, P, as the forcing function is:

$$\nabla \times \frac{1}{j\omega\epsilon} \nabla \times H + j\omega\mu H = \nabla \times P \quad (1)$$

To insure proper boundary conditions at material interfaces, the curl-curl formulation is used in (1) instead of the vector Laplacian. The use of an electric polarization as the input forcing function to the notch antenna is a novel idea presented here. The finite element formulation is obtained here by the Galerkin-Weighted Residual method[4].

$$\int_V \left[ (\nabla \times W) \cdot \left( \frac{1}{j\omega\epsilon} \nabla \times H \right) + W \cdot j\omega\mu H - W \cdot \nabla \times P \right] dV = \int_S W \cdot (n \times E) dS \quad (2)$$

$W$  in (2) is an arbitrary vector weighting function and  $E$  is the electric field. Normally in the finite element method, the surface integral in (2) is set to a constant or zero value. In the Hybrid technique, this surface integral is retained. The tangential component of the electric field ( $n \times E$ ) is an additional unknown on the exterior surface.

The boundary element equations are obtained directly from the Stratton-Chu formula[5,6].

$$\alpha H = \int_S [(n \times j\omega\epsilon E)G - \nabla G (n \cdot H) - (n \times H) \times \nabla G] dS \quad (3)$$

$\alpha$  is the integrated value of the singularity and  $G$  is the Green's function. (2) and (3) respectively become matrix equations by standard finite element and boundary element projection techniques[7,8]. Equations (2) and (3) together represent the electromagnetic field in the entire region of space, from the near field to infinity. The finite element matrix notation for (2) is:

$$[S][H] + [T][E_t] = [F] \quad (4)$$

The matrix  $[S]$  is obtained from the first two terms in the volume integral of (2), the matrix  $[F]$  is a column matrix from the third volume integral term containing the known polarization term, and  $[T]$  is from the surface integral term. The following matrix equations for the unknowns  $H$  and  $E_t$  are obtained from (3).

$$[U][H] + [V][E_t] = 0 \quad (5)$$

To solve for the entire space, (4) and (5) are solved simultaneously. This results in a sufficient number of equations to solve for the unknowns.

$$\begin{bmatrix} S & T \\ U & V \end{bmatrix} \begin{bmatrix} H \\ E_t \end{bmatrix} = \begin{bmatrix} F \\ 0 \end{bmatrix} \quad (6)$$

The eight element line array aperture discussed in Section 2.0 (shown in Figure 1) was assembled into a six transmit module phased array as shown in Figure 6. The phased array scanned pattern was measured with six central elements driven by transmit modules and the two edge elements terminated with 50-ohm loads. Predictions are given and compared with measured results of array-element pattern, gain versus frequency, and array scanned pattern.

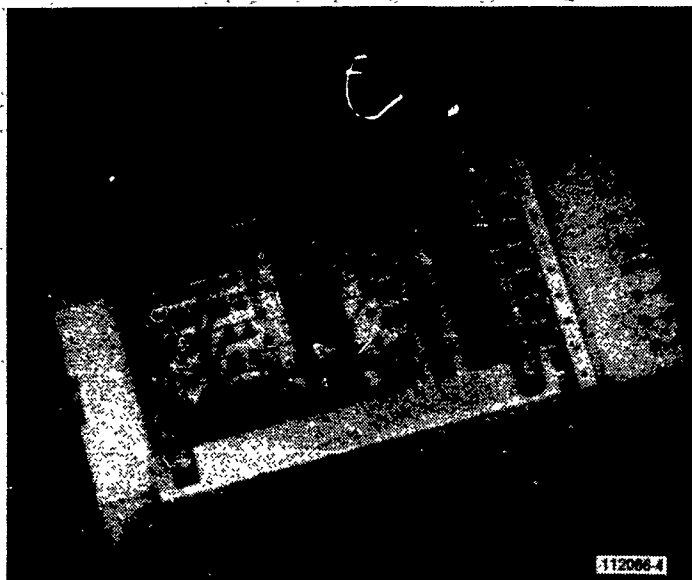


*Figure 6. Assembled Wideband Line Array with Stripline Notch Radiating Elements*

As an example of FEM/BEM modeling, the actual eight element line array shown in Figure 7 was modeled. Figure 7 shows the discretized model and Figure 8 is a zoomed-in section showing in detail the finite elements and boundary elements (elements are shrunk towards their centers for better visibility). In this model, much more airspace was modeled than needed. Usually, one or two layers of airspace finite elements are required before the boundary elements are placed on the surface.

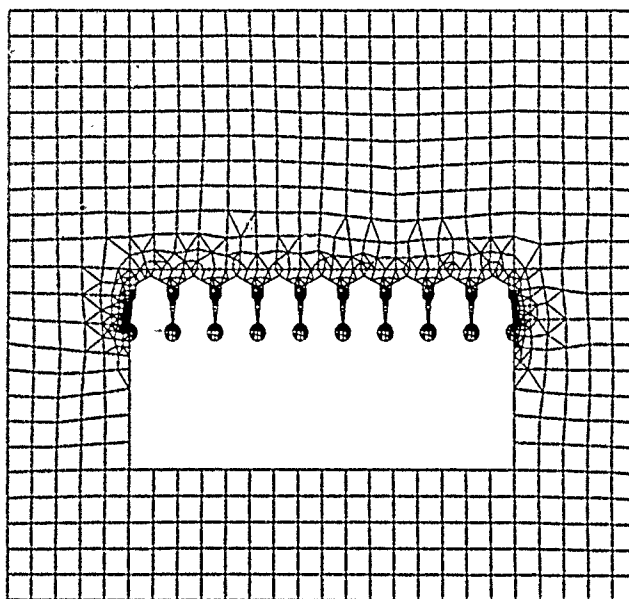
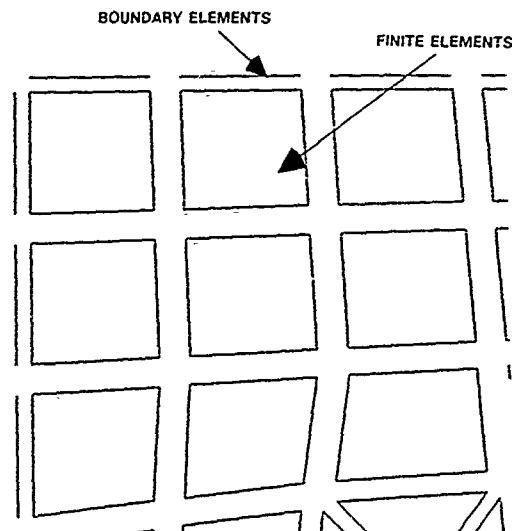


*Figure 7. Finite Element/Boundary Element Mesh*

Figure 8. Zoomed-In Section of Mesh



An electric polarization function is defined over the notch-gap region with specified amplitude and phase as shown in Figure 9. Figure 10 shows the outline of the line array aperture and the predicted near field radiation pattern (contours of Hz) at 10 GHz when the elements are phased to steer the beam +30 degrees. The edge elements were terminated with a 50-ohm junction at the bottom of the notch. A comparison of the predicted and measured phased array patterns steered to 30 degrees is shown in Figure 11. A comparison of sidelobe levels shows a 2 dB level difference. The half-power beamwidths are 27.2 degrees for the predicted and 31.0 degrees for the measured.

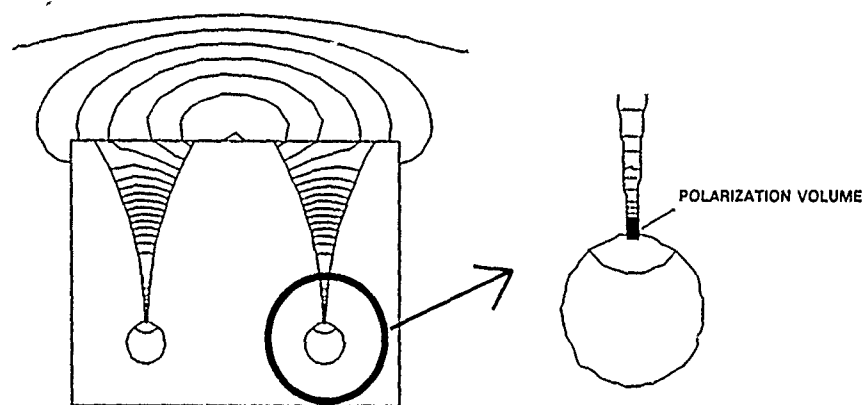
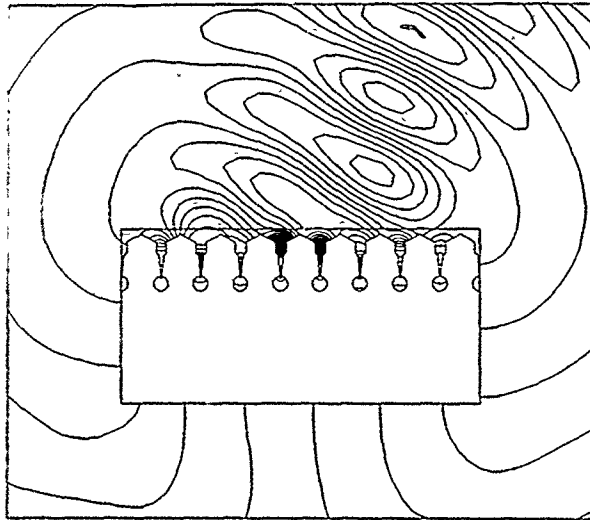


Figure 9. Forcing Function in Finite Element Region

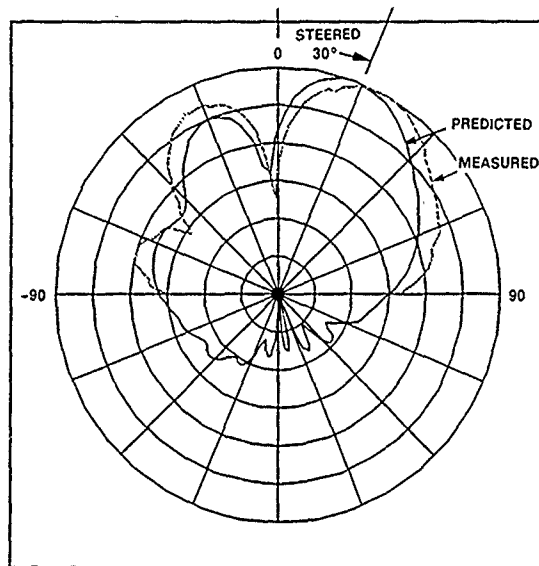
Results of the predicted and measured patterns show reasonable agreement in beam-width, sidelobe level, and overall shape. The null depth in the predicted pattern is not as deep due to two-dimensional approximations. The array-element E-plane pattern at 10 GHz is shown in Figure 12 for the predicted and measured results. The half-power beam-

width of the measured and computed results are 180 and 139 degrees, respectively. This difference in beamwidth is believed to be due to modeling error in the 50-ohm load termination. The measured array-element gain is shown in Figure 13 from 6 to 18 GHz



*Figure 10. Contour Map of E-Field Lines for Steered Array*

*Figure 11. Far-Field Predicted and Measured E-Plane Pattern Steered +30 Degrees at 10 GHz*



and compared with the normalized predicted gain from the Hybrid FEM/BEM solution. As previously mentioned, arbitrarily complex models can be analyzed with this method. Further extensions of this Hybrid method allow for combined antenna and constant thickness radome analysis as shown in Figures 14 through 16. The same radome/antenna models can also be used for scattering analysis. Figure 17 shows a near-field plot of the scattered field for the constant thickness radome. The incident plane wave is an angle of 45 degrees from the horizontal axis. Figure 18 shows the far-field, bistatic RCS patterns.

Figure 12. Array Element Predicted and Measured E-Plane Patterns

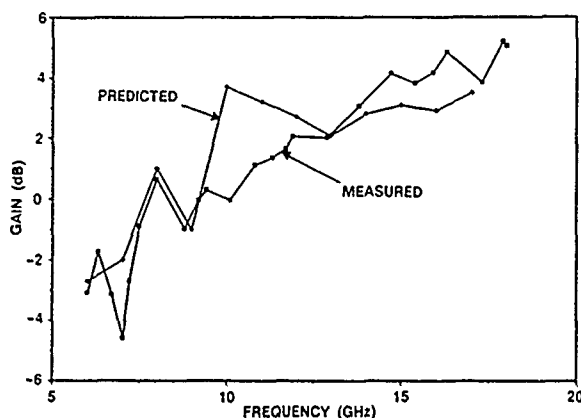
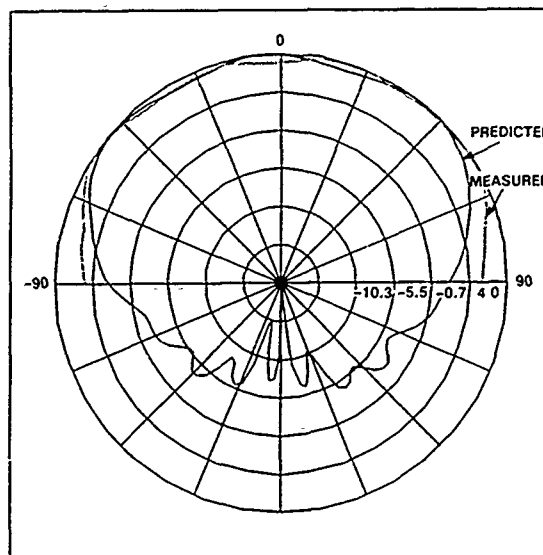
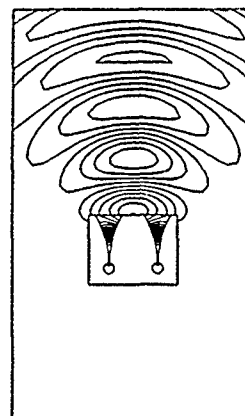


Figure 13. Array Element Gain versus Frequency at Boresight

Figure 14. Two-Element Array Near-Field Without Radome at 10 GHz



A curved, composite multiband radome design is added to the previously mentioned line array for the combined antenna radome analysis are shown in Figure 19. The inner and outer layers of the radome are made of a low loss dielectric material ( $\epsilon_r = 2.3 - j 0.05$ ). The inner layer is modeled as a low loss ( $\epsilon_r = 1.0 - j 0.1$ ) approximation to the honeycomb structure. The near-field pattern of the array-radome configuration is shown in Figure 20. The far-field pattern obtained for this case is shown in Figure 21. This figure shows the ability of the code to model the total interaction problem created by the introduction of the radome.

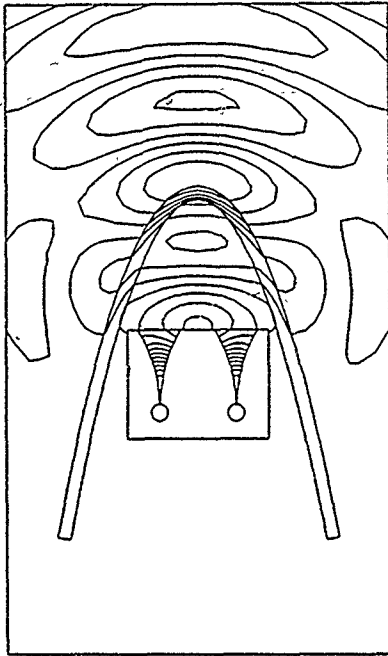


Figure 15. Two-Element Array  
Near-Field with Radome ( $\epsilon_r = 4.0$ ) at  
10 GHz

Figure 16. Far-Field E-Plane Pattern  
With and Without Radome at 10 GHz

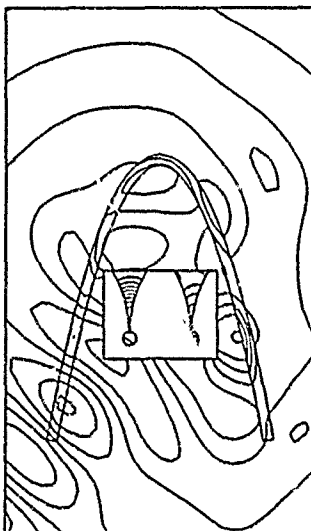
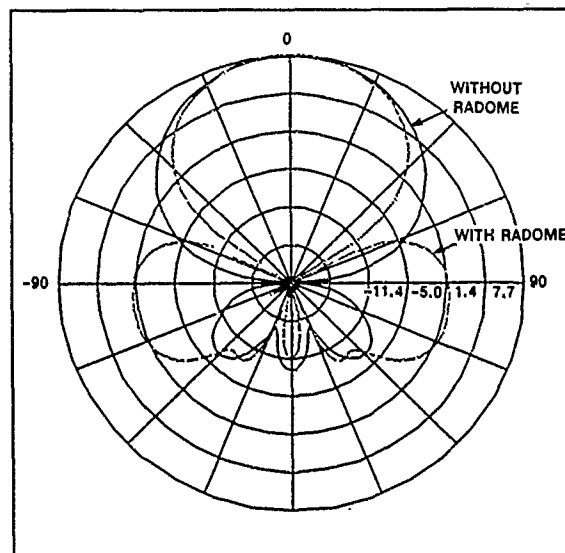


Figure 17. Scattered Near-Field Pattern  
(Incident Angle = 45 Degrees)

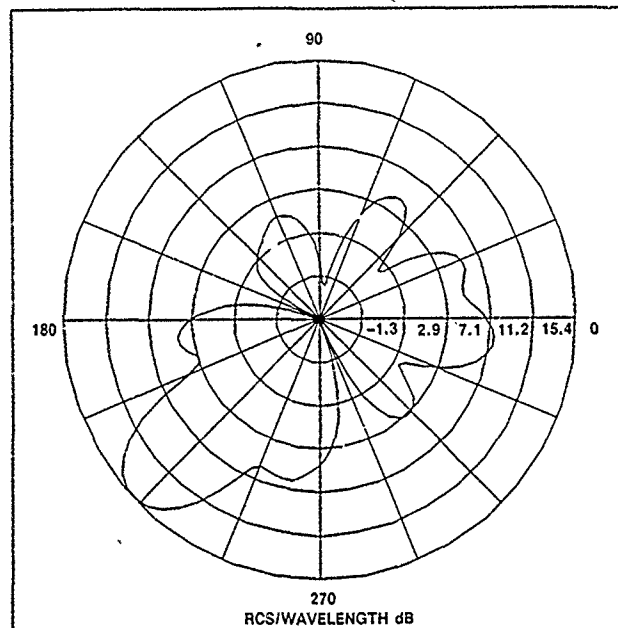


Figure 18. Bistatic Scattering from Antenna/Radome System at 10 GHz

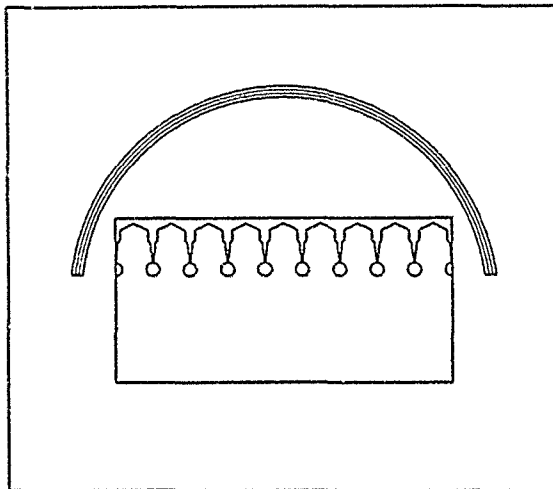


Figure 19. Array/Radome Model

Radiation predictions are also shown for a variable thickness radome with a two-element array in Figure 22. Comparisons can be made to the antenna array with no radome. The far-field pattern of the radome is shown in Figure 23. The variable thickness radome has the effect of splitting the main lobe into five lobes of nearly equal magnitude; the constant thickness radome creates two side lobes.

Hybrid finite element/boundary element methods (FEMs/BEMs) yield dense matrices for the exterior region, since every point on the region boundary is tightly coupled to every other point. Even if the interior region is modeled by the finite element method which yields sparse matrices, the boundary nullifies the advantages of the sparse system. It



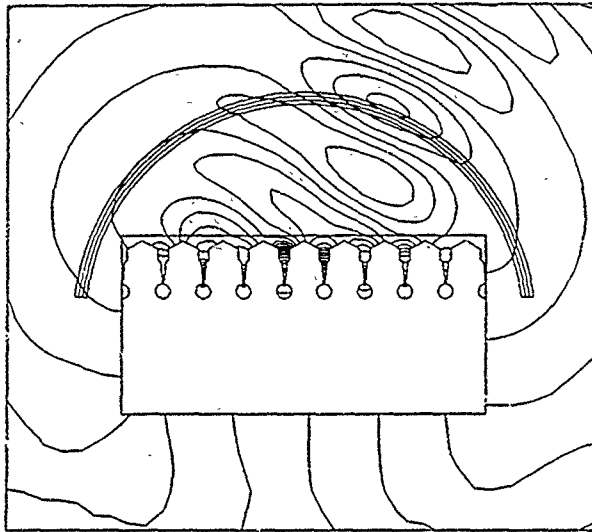


Figure 20. Contour Map of E-Field Lines for Steered Array with Radome

Figure 21. Predicted Far Field E-Plane Gain Pattern of Steered Array with Radome

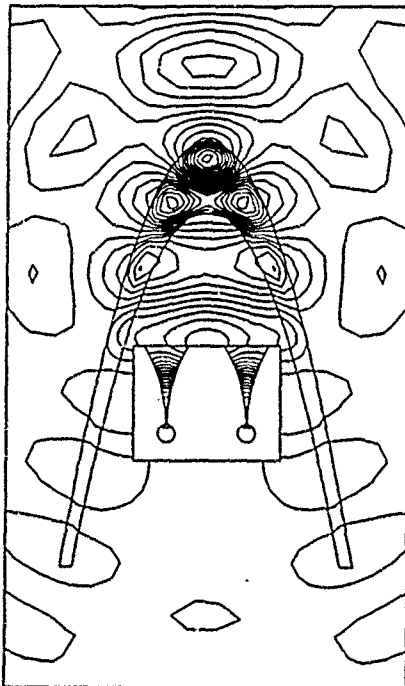
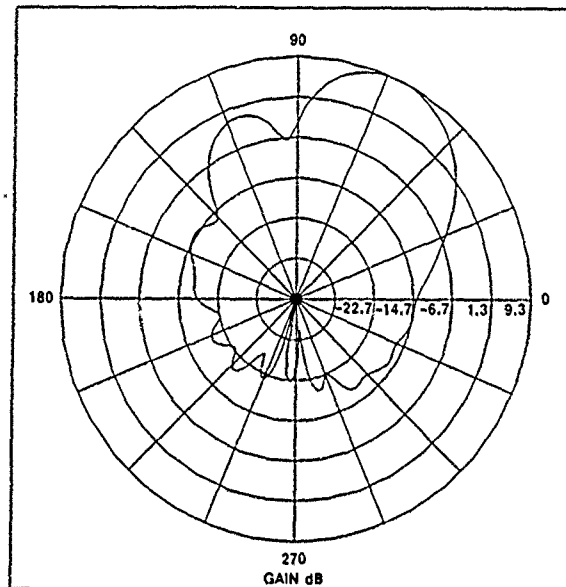


Figure 22. Two-Element Array with Variable Thickness Radome

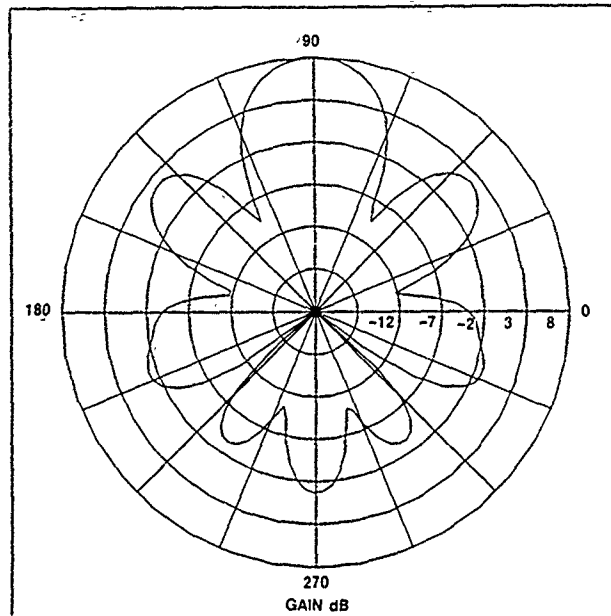


Figure 23. Far-Field E-Plane Pattern of Variable Thickness Radome

has become evident to engineers and numerical analysts that a more economical and effective method had to be found to eliminate dense matrices which require large computer memory and result in slow execution. One of these methods is to develop a hybrid boundary condition that yields sparse matrices but preserves solution accuracy. This type of boundary condition is called the absorbing or radiation boundary condition.

The results of the combination of the finite element method with two types of absorbing boundary conditions, the Engquist-Majda[9] and the Bayliss-Turkel[10], will be shown and compared with closed form solutions or with hybrid techniques. Both absorbing boundary conditions used in this discussion are of the second order. All of the examples will be for two-dimensional frequency domain scattering problems.

The objective of absorbing boundary conditions is to truncate a differential equation solution region with boundary conditions that cause minimum reflections of an outgoing wave. These absorbing boundary conditions should provide small, acceptable errors while minimizing the distance from the object of interest to the outer boundary. This minimal distance is required to reduce the number of unknowns in the problem for computational efficiency.

The second order Engquist-Majda absorbing boundary condition has the following form:

$$-k^2 \phi + jk \frac{\partial \phi}{\partial n} - \frac{1}{2} \frac{\partial^2 \phi}{\partial \tau^2} = 0 \quad (7)$$

where

$k \equiv$  wavenumber

$\phi \equiv$  unknown field value

$n \equiv$  normal direction

$\tau \equiv$  tangential direction

The second order Bayliss-Turkel absorbing boundary condition for two dimensions is derived from the Wilcox expansion and can be represented as follows:

$$\left( \frac{3}{4r^2} - k^2 - j \frac{3k}{r} \right) \phi + \left( \frac{5}{2r} - jk \right) \frac{\partial \phi}{\partial r} + \frac{\partial^2 \phi}{\partial \tau^2} = 0 \quad (8)$$

where

$r \equiv$  radial distance

Both ABCs can be easily implemented in a finite element formulation for the Helmholtz equation.

The following is the two-dimensional Galerkin Form for TE polarization:

$$\int_V \left\{ \nabla W \cdot \frac{1}{j\omega\epsilon} \nabla H + j\omega\mu W H \right\} dV - \int_S W \frac{1}{j\omega\epsilon} \frac{\partial H}{\partial n} dS = 0 \quad (9)$$

where

$W \equiv$  weighting function

$H \equiv$  magnetic intensity

$\omega \equiv 2\pi \times$  frequency

$\epsilon \equiv$  electric permittivity

$\mu \equiv$  magnetic permeability

To implement the absorbing boundary conditions, the normal derivative of the field is determined by either equation (7) or (8) and is substituted in the surface integral term of equation (9). Subsequent finite element discretization of the obtained Galerkin form is standard.

An example was solved with both absorbing boundary conditions and by using a third, hybrid finite element/boundary element analysis method. The geometry consists of two conducting wedges,  $5\lambda_0$  long, with the area between the two wedges filled with the  $\epsilon_r = 2$ ,  $\mu_r = 2$  material. The incident angle of the incoming plane wave is zero degrees.

Figure 24 shows the contour plot of the E-field. Figure 25 shows a comparison of the Engquist-Majda ABC versus the hybrid-finite element/boundary element bistatic results including the differences between the two. Figure 26 shows a similar comparison between the Bayliss-Turkel and the hybrid results.

Figure 24. Near E-Field Contour Plot

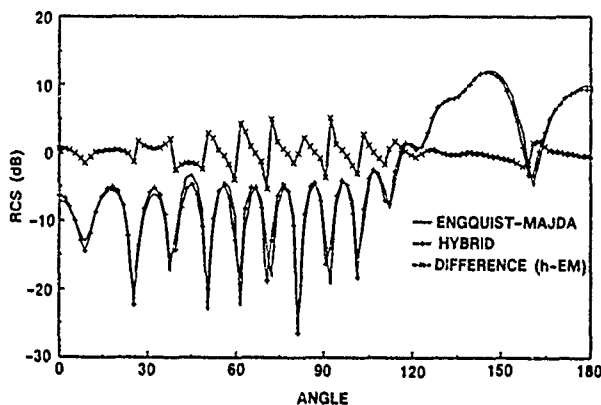
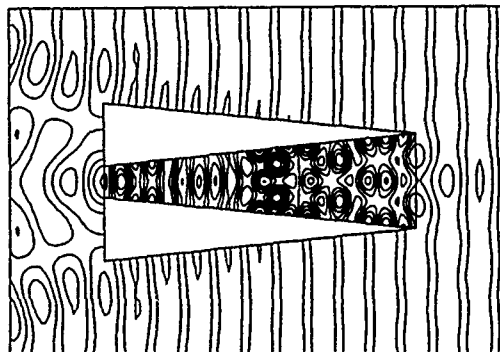
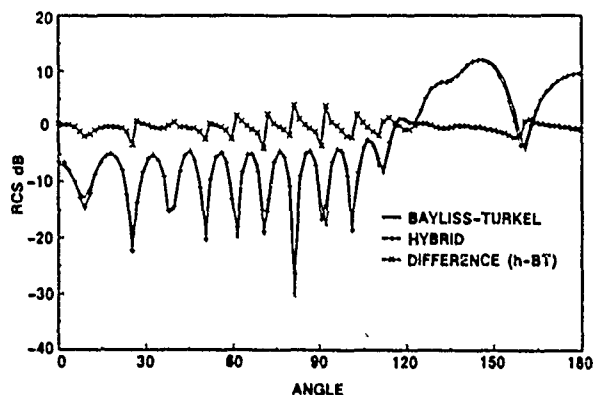


Figure 25. Bistatic Scattering Comparison of Engquist-Majda Absorbing Boundary Conditions and Hybrid FEM/BEM Solution

Figure 26. Bistatic Scattering Comparison of Bayliss-Turkel and Hybrid FEM/BEM Solution



In the above example, the absorbing boundary conditions yielded results of similar accuracy to the FEM/BEM method, but with tenfold improvements in computational efficiency both in terms of memory requirements and speed of execution.

#### 4.0 LINEARLY POLARIZED ARRAY DESIGN AND PERFORMANCE

A linearly-polarized array was designed, built, and tested for antenna radiation performance. Throughout this design the FEM/BEM electromagnetic analysis code was used to model designs and predict performance. The task of designing and building a linearly-polarized array which used the FEM/BEM analysis code and created a solution to the antenna radiation and mechanical design was undertaken. To provide a realizable solution to the aperture problem as a whole, a producibility study of the array aperture was also carried out. This includes analysis and experimentation to resolve potential problems concerning the producibility of elements, their mechanical integrity, and cost. Several approaches to ground plane design were evaluated for proper radiation, thermal, and interface performances. Other considerations for producibility, such as thermal, element alignment, and manufacturing tolerances, were also addressed.

A linearly-polarized array using subarray element pairs was designed, built, and tested. The goal of this effort was to develop an array with wideband radiation performance over the 6 to 18 GHz band and optimized performance over the 6 to 12 GHz band. Close element spacings were used to reduce grating lobes. In the E-plane, subarray pairs are spaced 0.736 inch apart (0.368 discrete element spacings), with H-plane spacing of 0.331 inch. The array consists of 169 subarray element pairs. The lattice is arranged with the phase centers in the E-plane sticks offset from each other. Figure 27 shows the final assembled array. A close-up view of the array is given in Figure 28.



*Figure 27. Wideband Linearly-Polarized Array using Subarray Stripline Notch Elements*



*Figure 28. Close-Up View of Array*

An example of a subarray element pair stick is shown in Figure 29. The array was constructed using an existing stripline notch ( $0.15 \lambda$  long at 6.0 GHz) design modified for a thicker dielectric material. The elements were etched on CuClad 233, a low-loss Teflon-woven glass substrate with a dielectric constant of 2.33. The thickness of the elements was increased from previous designs to a 0.062-inch ground plane spacing to increase mechanical rigidity. Subarraying is achieved by combining every two elements with a Wilkinson stripline power divider. The height of the elements could be reduced to a minimum of one inch. A margin of bare dielectric was left on the element sticks to allow for shaping to possibly enhance element performance.

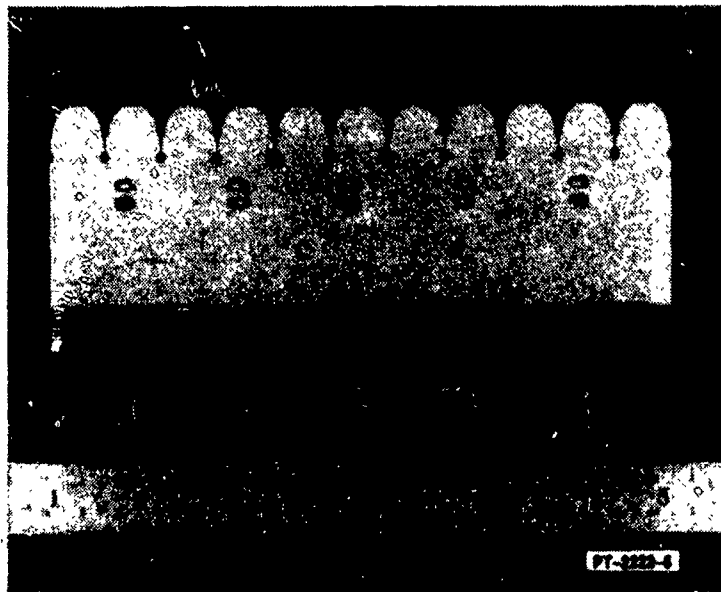


*Figure 29. Six Subarray Element Stick Showing Wilkinson Power Divider Isolation Resistors*

The gain of a five-element stick from this array was measured. This is plotted in Figure 30 with the theoretical area directivity curve. The element is highly efficient with gain at, or close to, the cell area directivity. Figure 31 shows the embedded element return loss of the array. The return loss is less than -10 dB over the majority of the 6 to 18 GHz bandwidth. The performance of this array was characterized in three different configurations. Measurements of the array were made in the baseline case (no mutual coupling fences between E-plane subarrays in the array), with absorber fences (Figure 32), and with resistive fences. For all three of these cases, the embedded element gain, linear and spin linear antenna patterns, and mutual coupling were measured and the active impedance was calculated. The embedded element gain of the array is shown in Figure 33, plotted with the directivity curve for the cell area. The two cases with fences have smoother gain with higher nulls and lower peaks. In all three cases, the measured gain matches very well with the directivity for the 6 to 12 GHz band, showing that the element is highly efficient. The average losses calculated over the 6 to 18 GHz band are 0.44 dB for the baseline case, 0.6 dB for the absorber fences (wedges) cases, and 0.6 dB for the resistive fence (card) case.

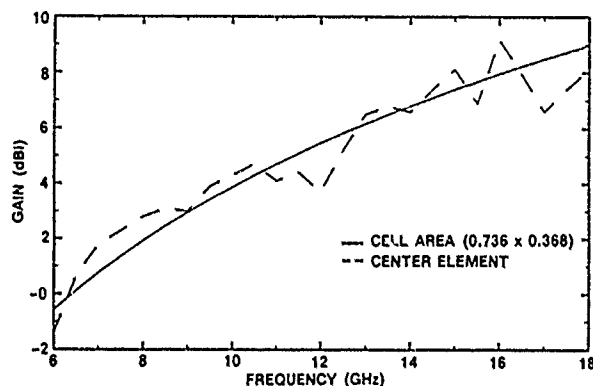


Figure 30. Central Embedded Element Gain in Five Subarray Element Stick

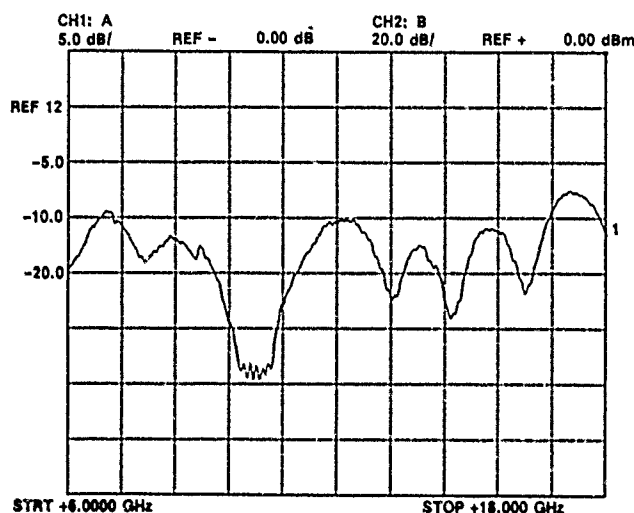


Figure 31. Embedded Subarray Element Return Loss from 6.0 to 18.0 GHz

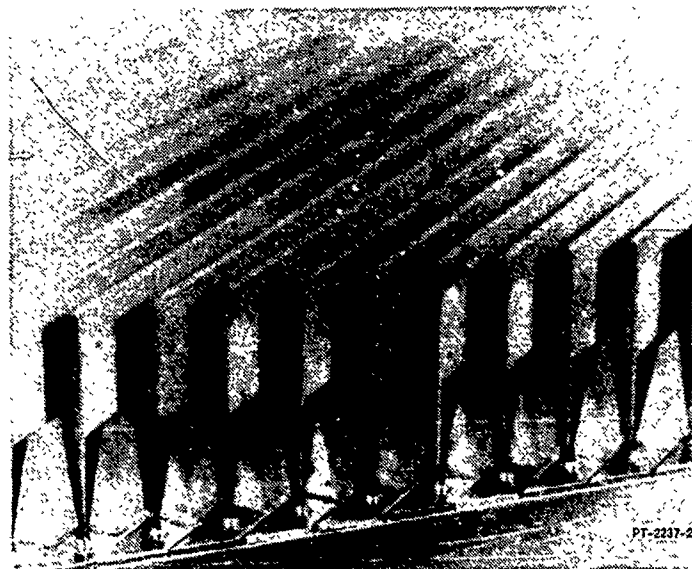


Figure 32. Close-Up View of Array with Absorber Mutual Coupling Fence

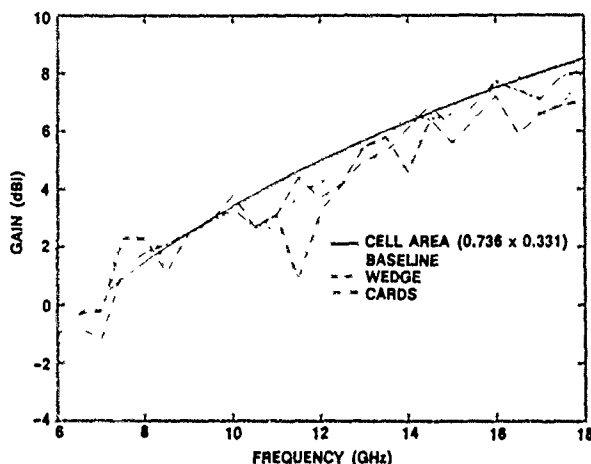


Figure 33. Central Embedded Subarray Element Gain in the Linearly-Polarized Array

Two typical E- and H-plane patterns at 8 GHz for the absorber fence case are shown in Figure 34. In the E-plane, the baseline patterns have a 2- to 3-dB ripple. Both the absorber fence and resistive fence patterns are smoother than the baseline case. The cross-polarization levels are about 5 dB higher in the baseline case than the other two cases. The H-plane patterns are smooth for all three cases, although the beamwidth of the baseline case is about 20 degrees below the other two. Figure 35 shows the E-plane half-power beamwidths of an embedded element. The baseline case has smaller beamwidths at the lower frequencies due to the ripple in the patterns. The ripple decreases after 10 GHz, by which time the beamwidths for all three cases are similar. The pattern of the absorber fence and resistive fence case is approximately that of a two-element array with each element having a  $\cos^2\theta$  field pattern at the low end which rolls off to  $\cos^5\theta$  at



the high end. The H-plane half-power beamwidths are shown in Figure 36. The wide variations in beamwidth present in the baseline case are eliminated by the mutual coupling fences. The patterns for the absorber fence and resistive fence are narrow at the low end of the band, broadening to  $\cos \theta$  for most of the band.

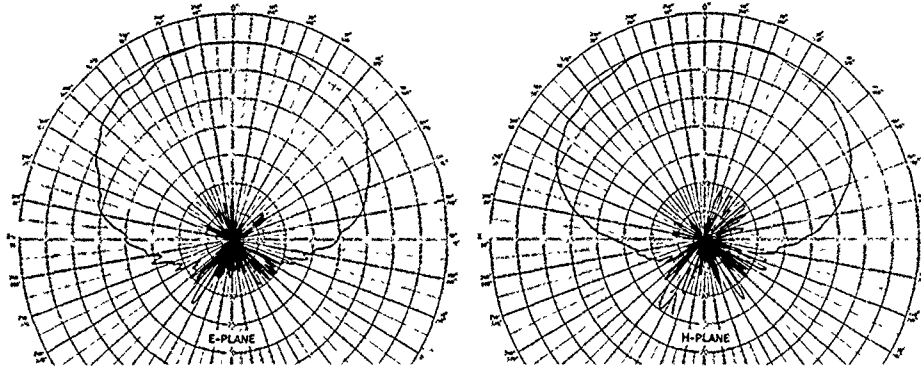


Figure 34. E- and H-Plane Central Embedded Subarray Element Patterns at 8.0 GHz in the Linearly-Polarized Array

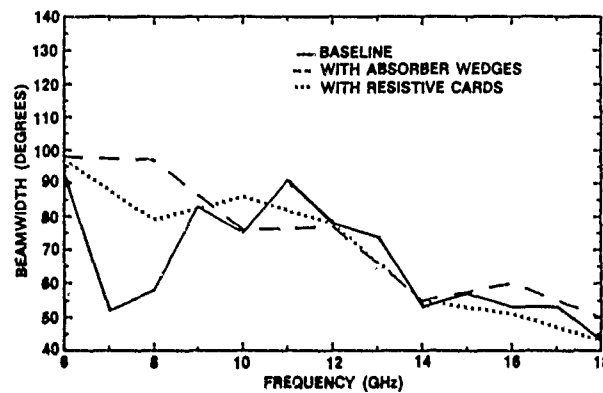


Figure 35. Central Embedded Subarray Element E-Plane Beamwidths in the Linearly-Polarized Array

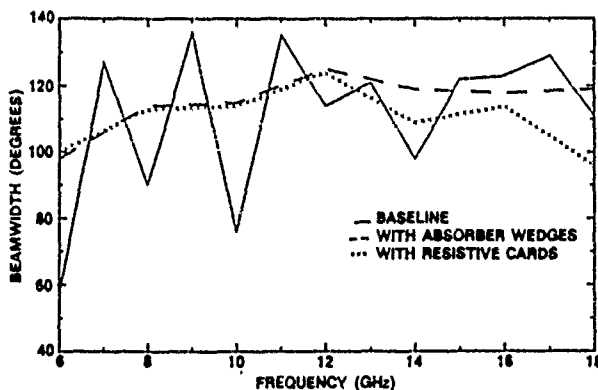


Figure 36. H-Plane Central Embedded Subarray Element Beamwidths in the Linearly-Polarized Array

Figure 37 shows a typical intercardinal ( $42^\circ$ ) spin linear pattern for the resistive fence cases. The resistive fence case has lower cross-polarization levels and less ripple. The active VSWR was calculated for the center element using mutual coupling data from the aperture. The active VSWR is plotted in sine space from 6 to 18 GHz in 0.125 GHz steps over all radiating half-space. The data points are taken in three-degree increments for a total of 1961 points per plot. Figure 38 shows a typical active VSWR plot in the midband for the resistive fence case with 30-, 45-, 60-, and 70-degree scan volume rings superimposed on the plot. The active VSWR in this plot is less than 2.0:1 for a 60-degree scan volume. Figure 39 shows the active VSWR in the E-, H-, and intercardinal planes for the baseline case at 10 GHz. The active VSWR is less than 2.0:1 for all but a few scan angles. The maximum number of occurrences for any value of VSWR from 6 to 18 GHz for a 60-degree scan volume is in Figure 40. For the baseline case, the mean VSWR, median VSWR, and standard deviation are 2.45, 2.27, and 0.89, respectively; for the absorber fence case, the values are 2.44, 2.41, and 0.61; and for the resistive fence case, the values are 2.23, 2.15, and 0.68. Figure 41 shows the maximum number of occurrences for a 60-degree scan volume from 8 to 12 GHz. For the baseline case, the mean VSWR, median VSWR, and standard deviation are 1.72, 1.62, and 0.45, respectively; for the absorber fence case, they are 2.13, 1.86, and 0.78; and for the resistive fence case, they are 1.72, 1.61, and 0.59.

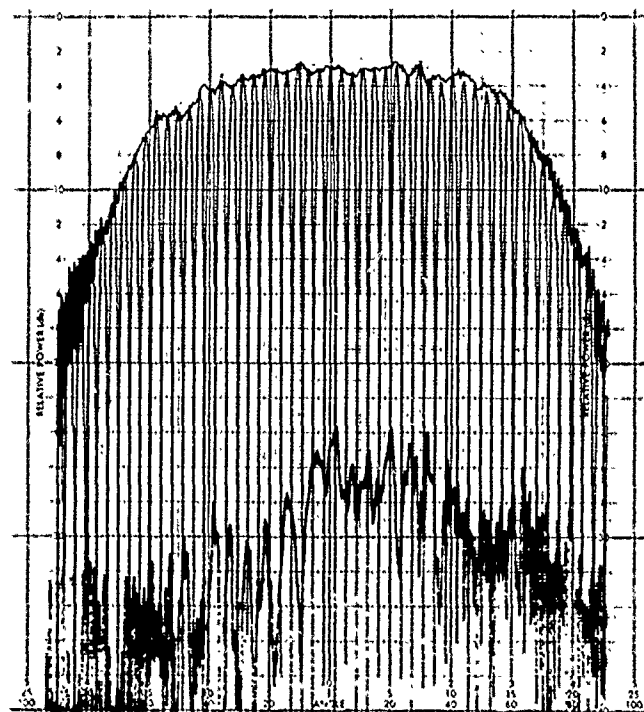


Figure 37. Intercardinal Plane Central Embedded Subarray Element Pattern at 12 GHz

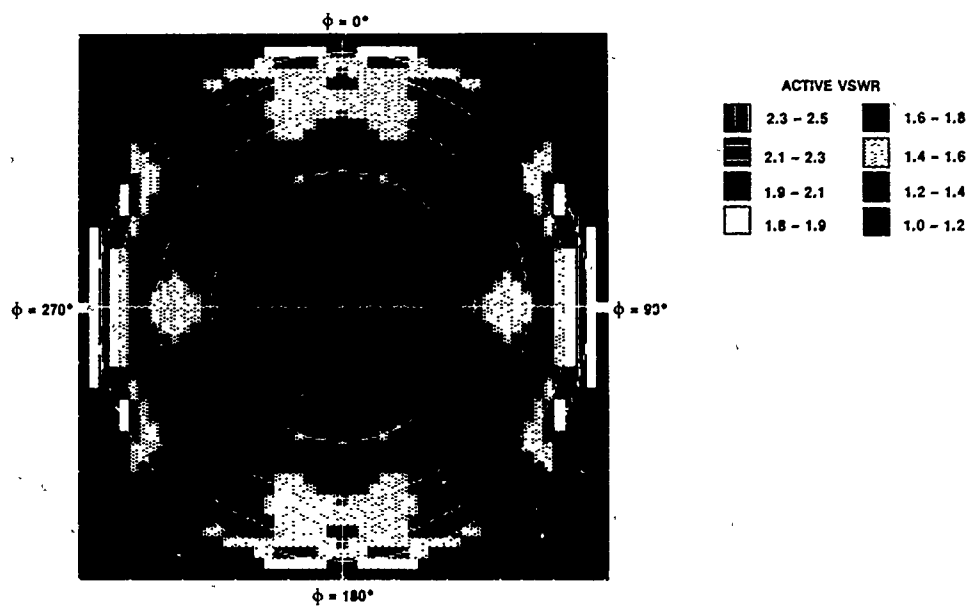


Figure 38. Active VSWR with Scan Over All Half-Space for Central Embedded Subarray Element at 9.0 GHz

Figure 39. Active VSWR at 10 GHz for Principal Scan Planes

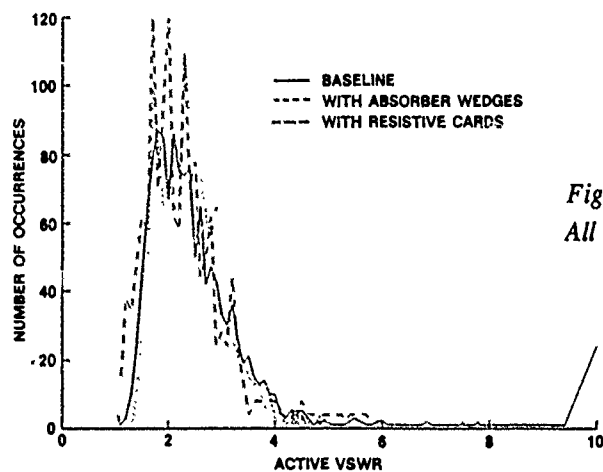
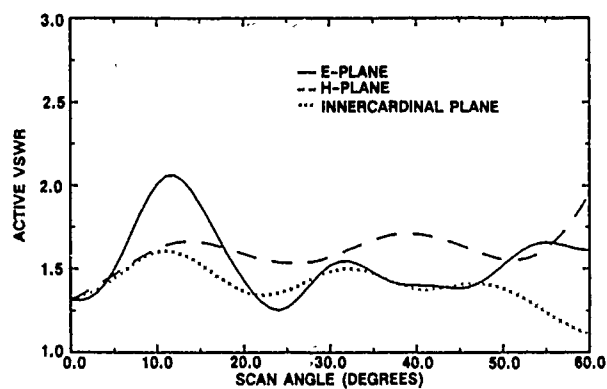


Figure 40. Number of Occurrences Over All Half-Space of Active VSWR from 6.0 to 18.0 GHz

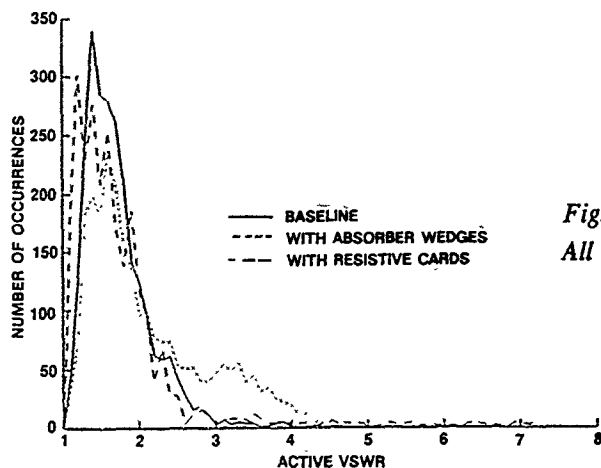


Figure 41. Number of Occurrences Over All Half-Space of Active VSWR from 8.0 to 12.0 GHz

Figure 42 shows the maximum number of occurrences for any value of VSWR from 12 to 18 GHz for a 60-degree scan volume. For the baseline case, the mean VSWR, median VSWR, and standard deviation are 1.96, 1.73, and 0.93, respectively; for the absorber fence case, the values are 2.19, 2.17, and 1.57; for the resistive fence case, the values are 1.90, 1.75, and 0.76. In the low band, the resistive fence case has the best VSWR performance, although performance in all three cases is similar. At midband frequencies, the baseline and the resistive fence performed best. In the high band, the resistive fence case has the best VSWR performance. Overall then, the VSWR performance is best in the resistive card case and highest with the absorber fence. The mean plus one sigma active VSWR over the entire 6.0 to 18.0 GHz band is still extremely low (3.34:1.0 over a 60-degree scan volume).

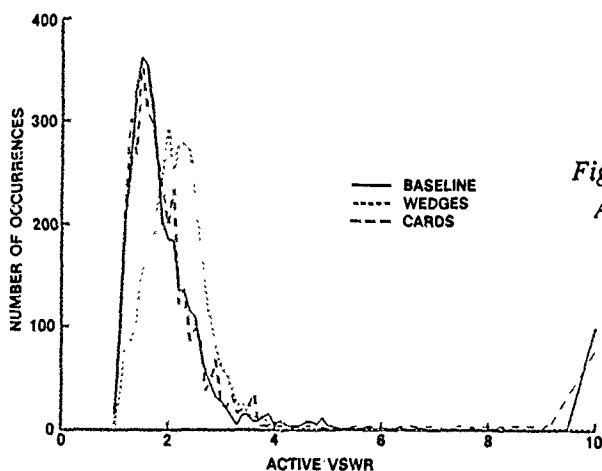


Figure 42. Number of Occurrences Over All Half-Space of Active VSWR from 12.0 to 18.0 GHz

Based on the measurements done on this array, performance is improved with the use of mutual coupling fences. Array gain and patterns are moderate in roll-off when fences are present and the cross-polarization pattern level is decreased. The active impedance performance of the array is improved by the use of the resistive fences, although it is not

improved dramatically by the use of absorber fences. Efforts are underway to iterate the design of the mutual coupling fences to further improve radiation performance. These iterations include changing the shape and height of the fences. The array element is also being iterated to optimize array performance over the 6 to 12 GHz band.

In order to verify that the dielectric margin on the elements was not causing a surface wave effect which was degrading performance, the active impedance of a 12-element stick was computed. The active impedance was calculated from mutual coupling measurements made with the full dielectric, half dielectric, and all the dielectric removed from the top of the element stick. The active VSWR with scan was computed for the central subarray with full dielectric in this E-plane stick over the full 6.0 to 18.0 GHz band and is shown in Figure 43. The absence of high active VSWR where the grating lobe appears in visible space ( $70^\circ$  at 8.27 GHz) indicates a possible design benefit in subarraying elements in an aperture. The use of closely spaced ( $0.186 \lambda$ ) elements combined into subarrays shows a reduction in active VSWR with scan. Figure 44 shows the results of this experiment at 11 GHz. The presence or absence of dielectric does not appreciably affect the active element performance. This result held true over the entire frequency band.

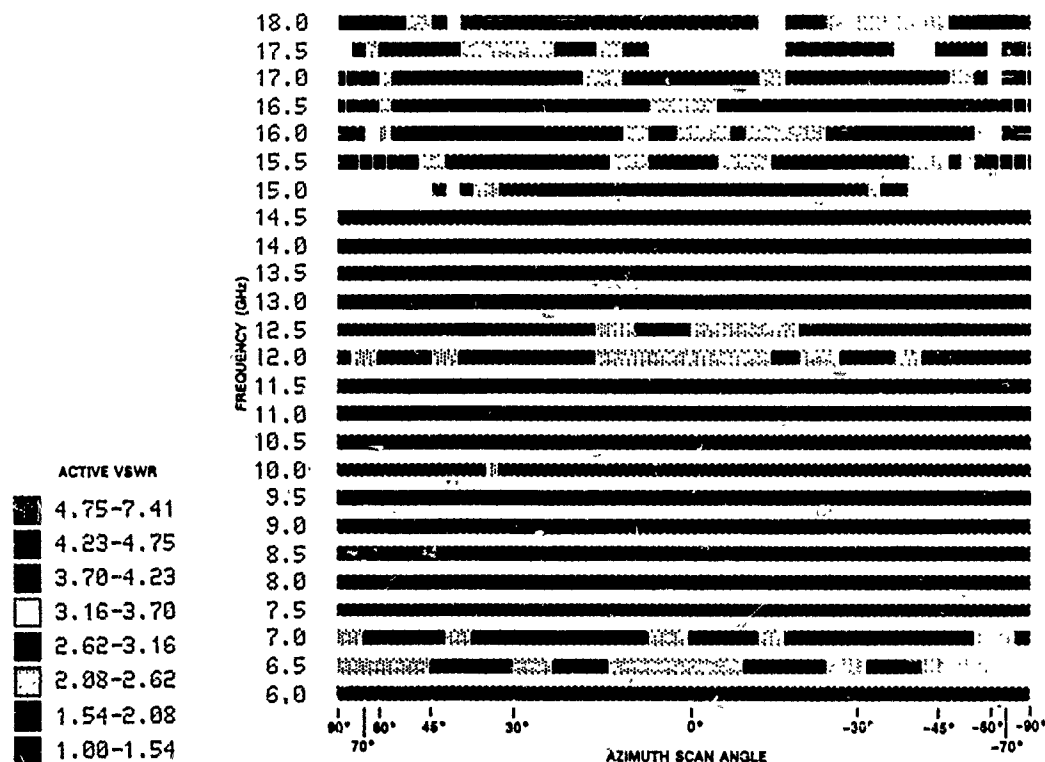


Figure 43. Active VSWR with Scan for Central Subarray in a 12-Element Stick over a 6.0 to 18.0 GHz Band

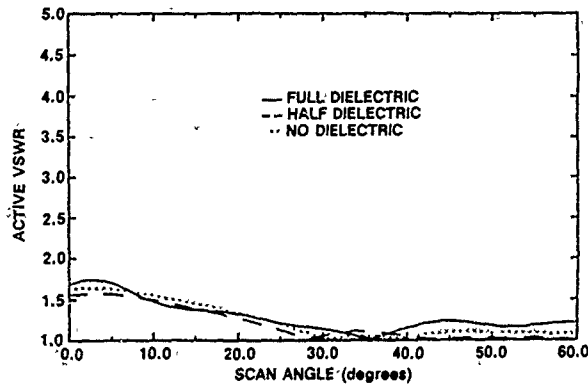
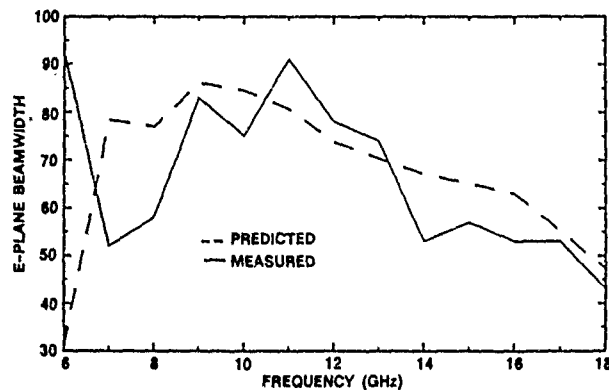


Figure 44. Active VSWR of 12 Subarray Element Stick with Various Heights of Dielectric Top

The hybrid analysis modeling code was used to model sticks of the array. Figure 45 shows the predicted beamwidth plotted with the measured array beamwidth. Based on Figure 45, the FEM/BEM predictions closely match the array performance. This is due to the two-dimensional FEM/BEM assumption that the elements are infinite in the y-plane (H-plane) and an array would more closely correspond to this infinite approximation than an isolated strip.

Figure 45. Predicted RF2D Beamwidths of Five-Element Stick Compared to the Embedded Subarray Element Beamwidths



A FEM/BEM analysis of a cross-section of the array was also modeled to verify the presence of resonant frequency spikes found in the mutual coupling interactions. These spikes are due to a waveguide coupling effect which is occurring within the dielectric of the printed circuit element.

The predictions of Figure 46 show a relatively small amount of reflection in the vicinity of the mutual coupling fence, while a large field exists within the dielectric of the element. Therefore, the energy coupled into the dielectric and rereflected out can be expected to add to coupling interaction. Furthermore, the plot of Figure 47 shows that this waveguide effect between the parallel plates of the feed element causes spikes in the frequency domain.

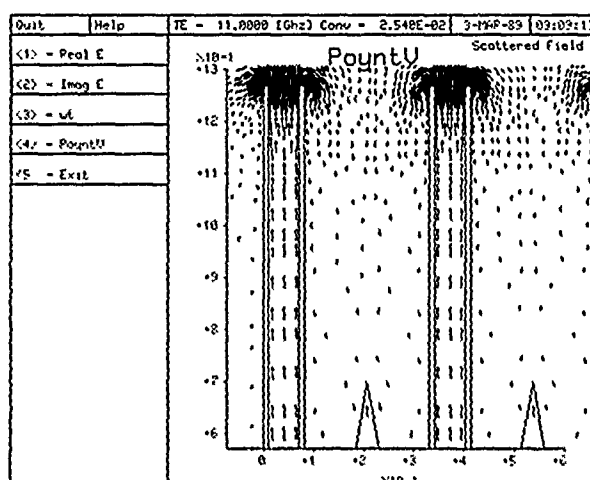
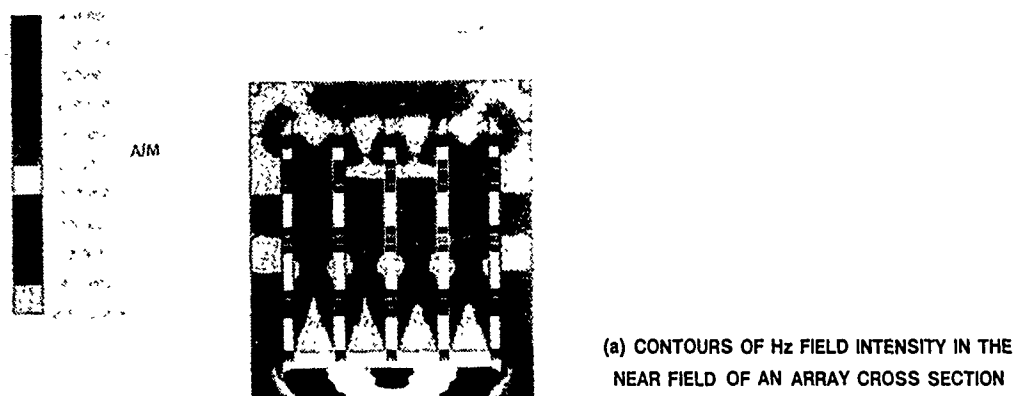


Figure 46. Field Intensity and Close-Up of Pointing Vector

An approach to reduce or eliminate the resonance and waveguide effect was to place plated-through holes along the element flare and between the element feeds as shown in Figure 48. This will reduce the energy being coupled into the dielectric and thereby eliminate spikes and secondary effects at the higher frequencies. This is shown in the mode suppression predictions in Figure 47 where the dielectric has been enclosed in metal. This will alter the mutual coupling in the array, thereby possibly reducing the array-element gain.

A detailed study of the vibrational effects of this element with temperature was also measured. A five subarray element bar was measured over the temperature range of -60 to 95 degrees Celsius with an input of 1, 3, and 5-G sinusoidal sweep with a frequency of 100 through 2500 Hz. The woven glass is stable up to 260 degrees Celsius and the rms

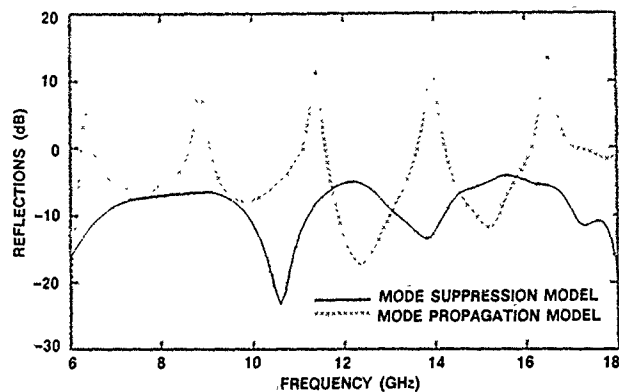


Figure 47. Mode Suppression Prediction of Cross-Sectional Model of an Array

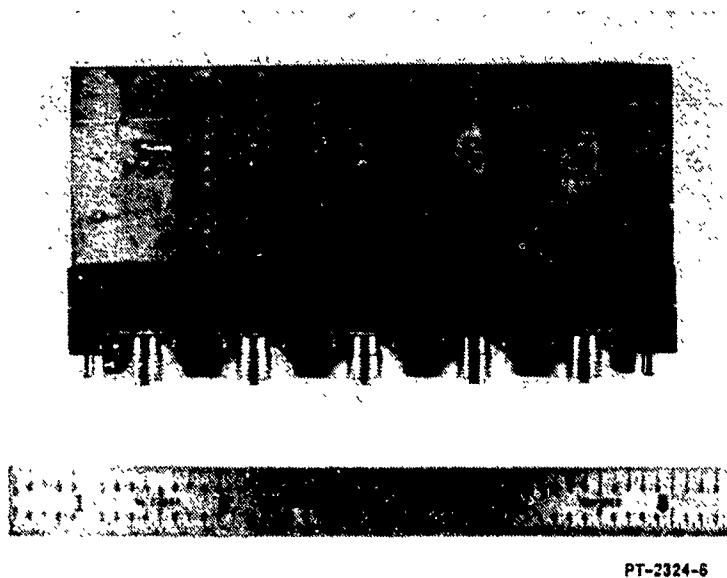


Figure 48. Five Subarray Stick with Mode Suppression Fills

deflection at the notch was under 0.0018 inch for the above mentioned loading. Tolerances on front to back registration were held to plus or minus three mils.

## 5.0 CONCLUSIONS

Significant progress has been made in the design and analysis of wideband linearly polarized phased array apertures. The combination of element pairs into subarrays reduces the number of transmit/receive modules in the array and also has been shown to reduce the active VSWR with scan versus frequency. The use of mutual coupling fences in between E-plane polarized rows of closely spaced flared slot antenna elements can reduce the level of the cross-polarized radiation pattern in the intercardinal and principal



planes. The co-polarized radiation pattern has also been shown to exhibit less ripple with the introduction of mutual coupling fences. Exceptional array-element performance was obtained using a stripline fed flared slot antenna element in both the single density and double density arrays.

The Hybrid finite element/boundary element is a powerful tool for the analysis of electromagnetic fields in flared slot antennas, radomes, and arbitrary complicated geometries. Splitting the region of analysis into two parts, the finite element and boundary element regions, allows for each method to be used where it is best suited. In the near field region, the finite element method allows for multimaterial, complex structures to be easily modeled, a necessary characteristic for a computer-aided design tool. The boundary element method, when added to the finite element region, extends the region of analysis to infinity with a surface integral term. The two-dimensional Hybrid analysis code used here is a good preliminary design tool neglecting the three-dimensional effects. With it, a user can analyze a number of design factors in rapid succession and with great detail.

For an increase in computational time, the absorbing boundary conditions (ABC), specifically those of second order, can be easily implemented and can be an effective method for modeling the unbounded fields in a finite element wave propagation problem. The advantages of ABCs are:

- They are local in nature.
- They do not spoil the sparsity of discretized equations.
- They are computationally efficient.

Combining these advantages with the observed accuracy makes ABCs much more productive to use than global representations of the exterior wave.

Through the use of finite element method analysis, progress is being made on a design tool suitable for performance predictions on wideband printed circuit antenna elements and linearly polarized arrays with element spacings and flare lengths on the order of  $0.2 \lambda$ .

## 6.0 REFERENCES

- [1] Pepe, C.D., Povinelli, M.J., and Komiak, J.J. (1987) Wideband Active Phased Array. *1987 Antenna Applications Symposium*, Allerton Park, University of Illinois, pp. 1-24.
- [2] D'Angelo, J., Povinelli, M.J., Palmo, M. (1988) Hybrid Finite Element/Boundary Element Analysis of a Stripline Notch Array. *IEEE AP-S, Symposium Digest*, Vol. 3, pp. 1126-1129.
- [3] D'Angelo, J., Povinelli, M.J., and Palmo, M.A. "Hybrid Finite Element/Boundary Element Analysis of a Radome/Phased Array Antenna Configuration", *19th*

- Symposium on Electromagnetic Windows*, Georgia Tech Research Institute, Atlanta, GA, 1988, pp. 26-42.
- [4] Huebner, K.H., *The Finite Element Method for Engineers*, John Wiley & Sons, 1975.
  - [5] Stratton, J.A., *Electromagnetic Theory*, McGraw-Hill, 1941.
  - [6] Paulsen, K.D., *Finite, Boundary, and Hybrid Element Solutions of the Maxwell Equations for Simulating Hyperthermic Treatment of Cancer*, Ph.D. Dissertation, Dartmouth College, 1986.
  - [7] Huebner, K.H., *Ibid.*
  - [8] Brebbia, C.A., *The Boundary Element Method for Engineers*, Pentech Press, 1979.
  - [9] Engquist, B. and Majda, "Absorbing Boundary Conditions for the Numerical Simulation of Waves," *Math. Comp.*, Vol. 31, pp. 629-651, 1977.
  - [10] Bayliss, A. and Turkel, E. "Radiation Boundary Conditions for Wave-like Equations," *Comm. Pure Appl. Math.*, Vol. 33, pp. 707-725, 1980.
  - [11] D'Angelo, J. and Manergoyz, I.D., "On The Use of Local Absorbing Boundary Conditions for RF Scattering Problems," *IEEE Transactions on Magnetics*, 1989.



# MISSION of Rome Air Development Center

*RADC plans and executes research, development, test and selected acquisition programs in support of Command, Control, Communications and Intelligence (C<sup>3</sup>I) activities. Technical and engineering support within areas of competence is provided to ESD Program Offices (POs) and other ESD elements to perform effective acquisition of C<sup>3</sup>I systems. The areas of technical competence include communications, command and control, battle management information processing, surveillance sensors, intelligence data collection and handling, solid state sciences, electromagnetics, and propagation, and electronic reliability/maintainability and compatibility.*